UNIVERSITY OF KENT

Faculty of Sciences

School of Physical Sciences (SPS)

Symbiotic Supramolecular self-association and the effects on antimicrobial activity

By

Stilyana Nikolaeva Tyuleva

Thesis for Masters of Science by Research

17 October 2018

UNIVERSITY OF KENT

17/10/2018

School of Physical Sciences (SPS)

Thesis for Masters of Science by Research

Abstract

SYMBIOTIC SUPRAMOLECULAR SELF-ASSOCIATION AND THE EFFECTS ON ANTIMICROBIAL ACTIVITY

by Stilyana N. Tyuleva

In this research the self-assembly and self-association processes occurring between supramolecular aggregates and surfactant structures were studied. Three amphiphilic molecules have been presented in this thesis. Two of which are novel and one which has been previously synthesised and characterised. The characterisation, self-association, binding modes and antimicrobial activity of these amphiphiles have been explored and reported. These amphiphiles containing tetrabutylammonium (TBA) countercation and anionic hydrogen bond donor/hydrogen bond acceptor unit have been observed in the solid, solution and gas states using a combination of scientific techniques. Observing these molecules in different solvent systems (DMSO and EtOH: H_2O (1:19) and at various concentrations has shown the ability of the anionic monomer to self-associate in solution, thus resulting in the formation of dimeric (in DMSO) and extended aggregate species (in EtOH/H_2O). A series of three mixture combinations containing the compounds were also studied. In addition, these mixtures of these amphiphilic salts showed their ability to self-sort which resulted in the increase of their antimicrobial activity and decrease in critical micelle concentration.

Table of content

Publications:

"*Towards the Prediction of Global Solution State Properties for Hydrogen Bonded, Self-Associating Amphiphiles*" – Lisa J.White, Stilyana N.Tyuleva, Ben Wilson, Helena J.Shepherd, Kendrick.K.L.Ng, Simon J.Holder, Ewan R.Clark and Jennifer R.Hiscock. Chem.Eur.J. 2018, vol 24 (30), pp.7761-7773.

Acknowledgements

I would like to express my gratitude to my supervisor Dr Jennifer R. Hiscock who gave a lot of guidance, support and encouraged me to not give up despite the difficulties. She made me realise that there is so much more that a person can do and pushed me in developing my skills and knowledge further. I would also like to thank my second supervisor Dr. Dan Mulvihill for his support and help throughout the year. My academic journey has been an inspiring one which taught me a lot more about myself and gave me a lot of confidence.

I would like to also thank the Hiscock group and all of my friends for their advice, amazing friendship and memories which will stay with me when we part ways.

I would also like to thank the NHS for the funding for this project.

I wish to thank Dr. Helena Shepherd, Dr. Kevin Howland, Dr. Paul Saines, Nyasha Allen, Tara Eastwood and Dr. Dan Mulvihil for their help in interpreting the single crystal - XRD, ESI-MS data, Microscopy data and plate reading data.

Last but not least I would like to thank my amazing family which have been experiencing everything with me throughout my academic journey. They have been my emotional support and have done nothing but have my back throught-out everything that happened this year.

Abbreviations

Å	Angstrom
A-T	Adenine – Thymine
AIEM	Aggregation induced enhanced emission
ATP	Adenosine triphosphate
ADP	Adenosine diphosphate
B.pumilus	Bacillus pumilus
br t	Broad triplet
CMC	Critical micelle concentration
C-G	Cytosine-Guanine
CAC	Critical aggregation concentration
CWA	Chemical warfare agent
CFP	Cyan fluorescent protein
CUR	Curcumin
^{13}C	Carbon (NMR)
cfu/mL	Colony-forming unit per millilitre (measuring viable cells)
DCM	Dichloromethane
DMSO	Dimethyl sulfoxide
d	Doublet (NMR characterisation)
DLS	Dynamic light scattering
DNA	Deoxyribonucleic acid
DOSY	Diffusion-ordered spectroscopy
D_2O	Heavy water
DMSO-d_6	Deuterated DMSO
d_H	Hydrodynamic diameter

DAPI	4’,6-Diamino-2-phenylindole (dye)
EtOH	Ethanol
E.coli	Escherichia coli
ESI-MS	Electron spray ionization- mass spectrometry
FTIR	Fourier transform infra-red spectroscopy
g	Grams
Gram -ve	Gram negative
Gram +ve	Gram positive
Hz	Hertz
HBD	Hydrogen bond donor
HBA	Hydrogen bond acceptor
^{1}H	Proton (NMR)
hrs	Hours
HepG2	Liver hepatocellular carcinoma (cells)
IUPAC	International Union of Pure and Applied Chemistry
J	Coupling constant (NMR characterisation)
kV	Kilovolt
K_a	Association constant
K	Kelvin
λ	Lambda
mg	Milligrams
m.p	Melting point

m/z	Mass to charge ratio (mass spectrometry)
m	Multiplet (NMR characterisation)
mV	Millivolt
mA	Milliampere
µ*g*	Microgram
mM	Millimolar
MCF-7	Human breast adenocarcinoma cell line
MPEG	Polyethyleneglycol monomethyl ether
NMR	Nuclear magnetic resonance spectroscopy
nm	Nanometre
ppm	Parts per million
pH	Acidity
pK_a	Acid dissociation constant
q	Quartet (NMR characterisation)
RNA	Ribonucleic acid
RUB	Rubusoside (diterpene glycoside - natural sweetening agent)
RES	Resveratrol
TBA	Tetrabutylammonium
TMA	Tetramethylammonium
TEA	Tetraethylammonium
TPA	Tetrapropylammonium
TFA	Trifluoroacetic acid

TLC	Thin layer chromatography
t	Triplet (NMR characterisation)
UV-Vis	Ultraviolet – visible spectroscopy
XRD	X-ray powder diffraction
µL	Micro-litres
EtOH	Ethanol
°	Degree
π	Pi

1. Aims

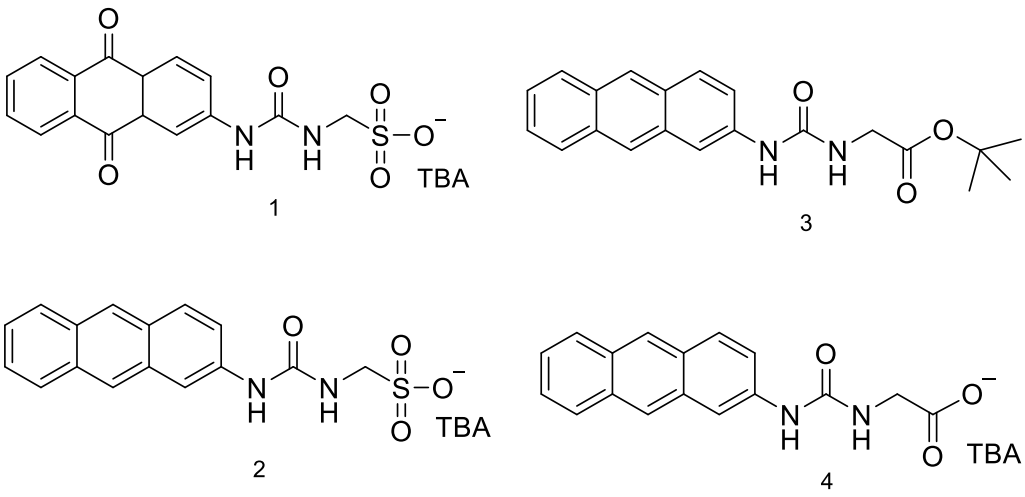

Figure 1: Compounds **1- 4** synthesised and explored.

1.1 The aim of this project is to synthesise a series of amphiphiles (Figure 1) characterise and explore their self-association properties using various techniques in the gas, solid and liquid phases. Some of the techniques which were used to observe the formation of large aggregate complexes, selectivity and self-association properties were as follows: DLS, quantitative ^{1}H NMR experiments, DOSY (NMR experiment), X-ray powder diffraction and single crystal x-ray diffraction. These molecules were then visualised and their global properties were observed using microscopy and surface tension measurements (determining the CMC values). These amphiphiles were also tested against clinically relevant bacteria Gram +ve Methicillin-resistant *Staphylococcus aureus* (MRSA USA300) and Gram -ve Escherichia coli (*E.coli*) in order to explore their antimicrobial activity, thus determining whether they can be used as potential novel antibiotics. The non-covalent interactions will be looked at when considering the properties of the developed amphiphiles, more specifically hydrogen bond interactions as they are key interactions that drive the self-assembly and molecular complex formation processes.

1.2 The series of synthesised amphiphiles have low molecular weights and contain a urea functional group which is covalently linked by a spacer and an anion substituent, as well as HBD/HBA moieties.[1] This has proven to be of great significance when looking at self-assembly and hydrogen bonding interactions.

1.3 Some of the amphiphiles synthesised by the Hiscock group[2] bear similarity with the main structures shown in Figure 1. Along with that, they have also been tested and shown to have antimicrobial activity against the same types of bacteria used in this research +ve *S.aureus* and –ve *E.coli*. Preliminary data of a similar series of compounds developed by the Hiscock group and co-workers have shown that some of the amphiphiles associate and can disrupt the bacterial plasma membranes, and once inside the bacterial cell are thought to disturb its metabolism. Resistance studies have shown that by affecting important components of the bacterial cell wall, this could prevent the bacteria from developing resistance. This alone shows how important and effective these amphiphiles are for clinical testing as novel antibiotics.

2.Introduction

2.1 Supramolecular chemistry and non-covalent interactions

Supramolecular chemistry was first introduced to the world of science in 1969 by Jean Marie-Lehn who also defined it as "*chemistry beyond the molecule*".[3] In 1987 along with Charles Pederson and Donald Cram, he won the Nobel Prize which showed their contribution and research carried out in this scientific field.[3] Supramolecular chemistry, known also as the "chemistry of the non-covalent bond"[4] focuses on complex molecular structures which can be formed as a result of two or more components and that are being held together by non-covalent intermolecular interactions.[5]

Being able to understand the nature of these interactions aids scientists exploring the molecular composition of complex building blocks and the way they associate. This can bring scientists one step closer to then being able to control and further use these complex structures in chemical and biological applications.

Gilbert N. Lewis, an American chemist[6] proposed in 1913 the theory of "valence" by introducing the Lewis structures, also known as Lewis diagram or dot structures, in which dots are used to show the lone pair of electrons, as well as the bonding occurring between the atoms of the molecule (Figure 2).[7]

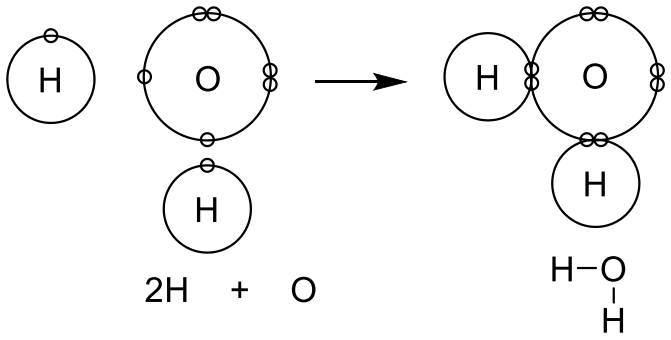

Figure 2: Example of covalent bonding of a single water H_2O molecule.[8]

There are two types of covalent bonds – polar and non-polar. Non-polar covalent bonds do not have any electron transfer, whereas polar bonds are formed by the transferring of electrons.[8] Non-covalent bonds, compared to covalent, are an area of study which is continuously researched and has provided scientists with a satisfactory understanding and definitive results on how complex structures using non-covalent interactions work.[9] There is no sharing of electrons in a non-covalent interaction, compared to a covalent one.

They are formed as a result of the electromagnetic interactions that occur due to the electron distribution process between two different molecules, or within only one individual molecule. This can lead to self-assembly, thus resulting in extended structure formation such as dimers, trimers or polymers. There are several different types of non-covalent interactions such as Van der Waals interactions, which are known to be one of the weakest non-covalent interactions with bond energies weaker than 5 kJ mol^{-1} depending on the distance between the molecules.[10, 11] This type of interaction is based on electrostatic interactions which are created due to the closeness of a neighboring nucleus which causes the polarisation of the electron clouds.[11] Individual bonds are pretty weak, however having more than one interaction can easily result in stronger molecular interactions.[10,12] The second type are ion-ion interactions which is one of the three main electrostatic interactions. In terms of bond strength, they are very similar to covalent bonds. Their bond energy varies between 100 and 350 kJ mol^{-1}.[11] An example of an ion-ion interaction would be sodium chloride, where we have a cation (Na^+) and a Cl^- anion group, thus showing the way an ion-ion interaction can be fully maximised (Figure 3A).[11,10] Then there are ion-dipole interactions which are formed using a polar molecule, which has a partial charge and an ion.[10] An example of such interactions is the bonding of an ion Na^+ with water (a polar molecule).[10,13] The bond strength of these interactions ranges between 50 and 200 kJ mol^{-1} (Figure 3B).[11] Another type of electrostatic interaction is dipole-dipole interactions, which are the weakest interactions with bond strength ranging between 5 and 50 kJ mol^{-1}.[11] The interactions form when dipoles that carry a partial charge are aligned, resulting in a stronger attraction between the molecules (Figure 3C).[7,10] Then there are π-π interactions, which are interactions occurring between an electronegative π-cloud of and the positively charged π-cloud of two neighbouring aromatic systems.[11] They are split into two main types and are distinguished based on the ways the aromatic systems interact, with the first one being face to face[14] (Figure 3.E.1) (corner of one system to the centre of the other) and the second one being edge to face[15] (Figure 3.E.2) (perpendicular orientation of an H atom from one system to the centre of another).[11]

Other interactions include anionic-π interactions,[16] which involve interactions occurring between an anion (Cl^-, F^-) and electron poor aromatic systems and cation-π interactions,[17] occuring between a cation (Fe^{2+}, Na^+) and an electron rich aromatic complex.[11,18] Last but not least there are hydrogen bond interactions (Figure 3D), which are continuously explored in different scientific fields, as they play an important role in the dynamics, structural and functional properties of various biological and inorganic complex systems.[19]

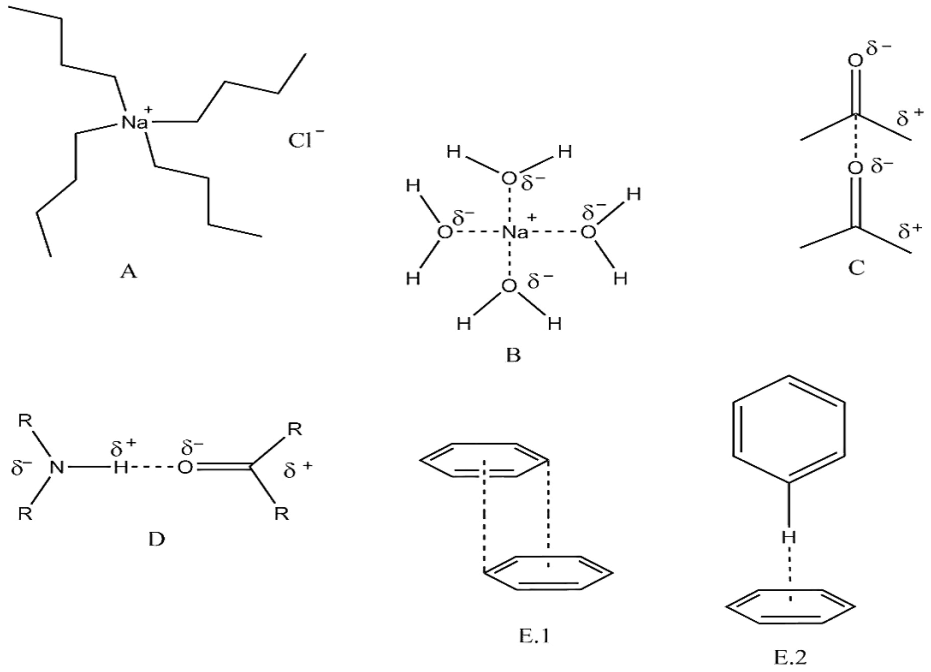

Figure 3: Illustrating the different types of non-covalent interactions: ion-ion (A), ion-dipole (B), dipole-dipole (C), hydrogen bonding (D), π-π face to face (E.1) and π-π edge to face (E.2).[19]

Hydrogen bond interactions are described by IUPAC task group[20] as interactions which occur between one or more atoms, from the same or different molecular structures, which show evidence of hydrogen bond formation.[20] Hydrogen bonds have different structural properties which are influenced by the nature of the functional groups (hydrogen bond acceptor and hydrogen bond donor) which are part of the binding mode.

HBA are units with electron-withdrawing properties (anions), which interact with a positively charged hydrogen atom, whereas HBD are units with a positively charged hydrogen attached to an electron withdrawing atom (O or N).[19] One of the most commonly observed HBA groups observed for neutral molecules are the oxygen, the nitrogen or fluorine atoms.[21] A standard example is that of hydrogen bonding observed in water molecules, where the partially positive charge of the hydrogen in a single molecule is attracted to the electronegative charge of the oxygen atom of a neighbouring molecule (Figure 4).[22]

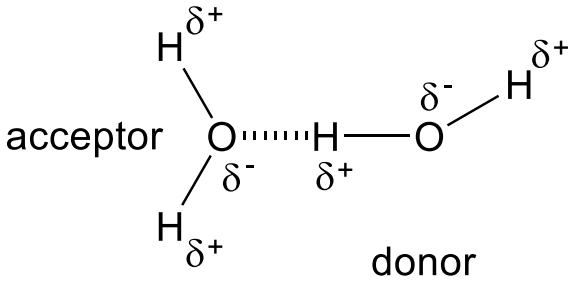

Figure 4: Hydrogen bonding observed in water molecules.[23]

The hydrogen bond strength is influenced by the nature of the HBD and the structural geometry of the interactions.[19] The average strength of the hydrogen bond interaction is known to range between 2-170 kJ mol^{-1},[24] with strong covalent interactions being 60-120 kJ mol^{-1}, moderate strength of 16-60 kJ mol^{-1} being mainly electrostatics and weak electrostatic having bond strength of < 12 kJ mol^{-1}.[11] The bond angle of these hydrogen bonds range between 90-180°, with the optimal hydrogen bond angle of 175-180° leading to the strongest bonds, 130-180° being moderate, 90-150° being weak and an average of bond angles ranging between 1.2-4.0 Å (strong to weak).[11]

The two types of hydrogen bond geometries are primary, which show the direct interactions occurring between the HBA and HBD moieties (linear, bent, donating bifurcated, accepting bifurcated, trifurcated and three-centre bifurcated) (Figure 5) and secondary, showing the interactions (attraction or repulsion) occurring between the neighbouring groups (Figure 6).[19]

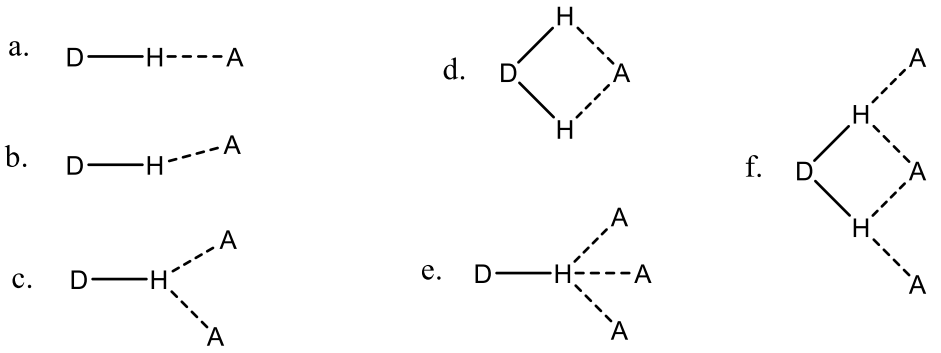

Figure 5: Different types of hydrogen bond geometries; linear (a), bent (b), donating bifurcated (c), accepting bifurcated (d), trifurcated (e), three-centre bifurcated (f).[19]

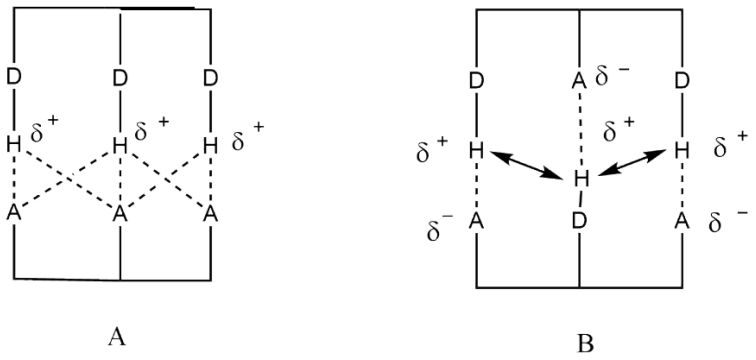

A B

Figure 6: Secondary hydrogen bond interactions; attraction occurring between neighbouring molecules (A) and repulsion occurring between hydrogen bond donor and acceptor units (B).[19]

In terms of strength, strong hydrogen bond interactions are known to be similar to covalent interactions, whilst weak hydrogen bonds resemble the weaker van der Waals interactions.[24]

However, the directionality properties of the hydrogen bonds favouring linear or close to linear geometries,[24] aid in distinguishing between these interactions, also showed by studies carried out by Gautam R. Desiraju.[25] The hydrogen bond directionality is affected by the charge transfer from the HBA to the HBD, as well as the polarity of the HBD of a molecular complex, which was also reported in studies carried out by Dr.Thomas Steiner, who observed that as the polarity of the molecular species he studied decreased, the directionality of the hydrogen bond increased.[26] Intermolecular hydrogen bonding plays an important role in the molecular complexation, self-association and self-assembly processes occurring between complex molecular species.[27] There are many theoretical and experimental studies carried out that show how significant these interactions can be when used in controlling and predicting these events, as well as used to design novel supramolecular complexes.

2.2 Complex formation

Complex formation using non-covalent interactions goes back to the mid-1960 early 1970, where supramolecular chemistry had already reached a series of breaking discoveries with the development of macrocyclic ligands for metal cations by the groups of Busch, Jäger, Curtis, and Pedersen (Figure 7).[28,11] Three of these systems used the Schiff base reaction, in which an aldehyde with an anime is used in order to produce an imine.[11]

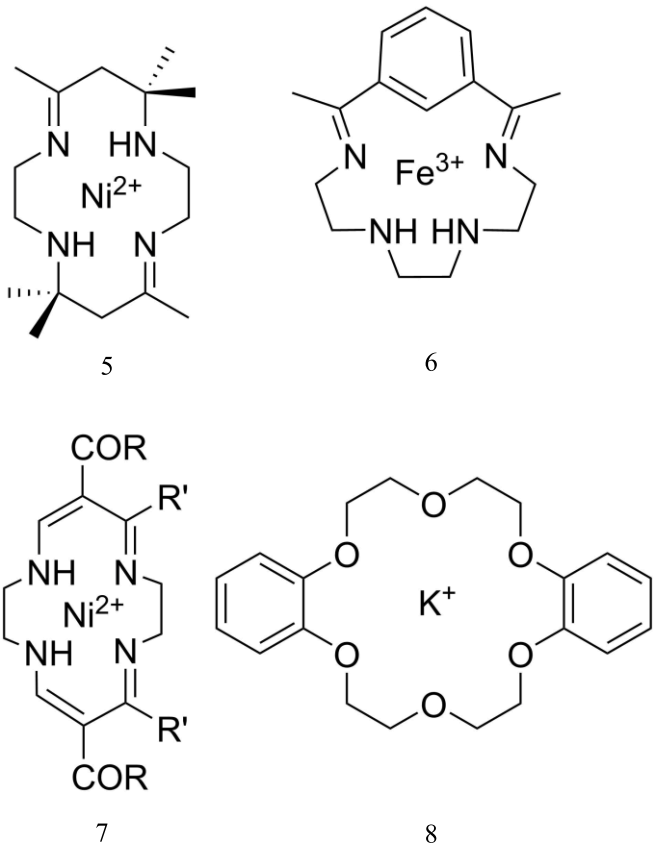

Figure 7: Four major systems of macrocyclic ligands for metal cations: Curtis 1961 (5), Busch 1964 (6), Jäger 1964 (7) and Pedersen 1967 (8).[11]

Whilst a large majority of innovation in this field has been recent, the root of the existence of intermolecular forces were first proposed in 1873 by the theoretical physicist Johannes Van der Waals.[29] Following this was another success by Nobel laureate Herman Emil Fisher who several years later introduced the "lock and key"[30] principle while looking at enzyme-substrate interactions.[31] This principle is also known as the host-guest example where intermolecular interactions hold together two or more molecular species thus forming more complex molecular structures.[31] In an example, occurring in biological systems, the enzyme would play the role of the host (larger molecule), whilst the substrate would be the guest (smaller molecule).[19]

This example along with other such as receptor-ligand,[32] dendrimers in drug-delivery,[33] provide the fundamental principles of selective interactions,[34] the way the host binds selectively to the guest, as well as molecular recognition[35] used in what we know today as host-guest chemistry. Along with that host-guest chemistry has provided the ability to further understand how drugs[36] should be designed, the way complex structures adapt to certain environments and ways in order to mimic biological systems.[37] A few years later in 1920, Wendell Latimer and Worth Rodebush were able to explore and understand more about non-covalent bonds and later presented the concept of "hydrogen bonding" in their work.[38] This concept was later used as a stepping stone in understanding the way a lot of complex biological processes worked.[39] An example of such a process is the way the DNA double-helix forms, as a result of two independent stands.[40] The double-helix is a ladder which is being held and stabilised by non-covalent hydrogen bonds which occur between the nucleotides and the four main nucleobases (Figure 8).[41]

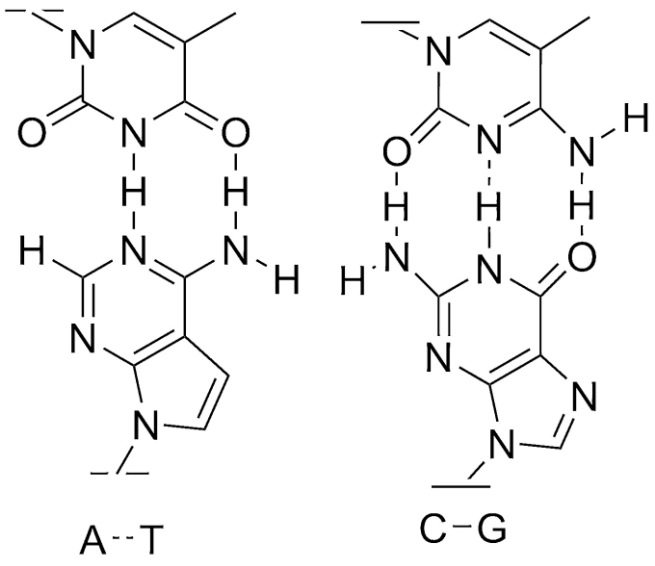

Figure 8: Hydrogen bonding between the four main nucleobases.[41]

The examples describing the host-guest interactions, enzyme-substrate and double-helix formation show selectivity. In the host-guest interactions, the host selectively chooses to bind to a specific guest,[42] similar to the enzyme binding to one specific substrate.[43] The same can be seen in the double-helix formation as well, where an adenine nucleobase will only choose to pair up with a thymine nucleobase (cytosine nucleobase will only pair up with a guanine nucleobase).[44] As a result of this, chemists began to realise that these non-covalent interactions can be further applied to systems in synthetic chemistry. This was established in 1960 when chemist Charles J.Pedersen made a breakthrough discovery by synthesising the crown ethers.[5] Later Donald J. Cram and Jean-Marie Lehn carried on the research by using the fundamentals which Pedersen had provided. Thus a new group of compounds was developed, showing selectivity which could allow for them to be used as building blocks for the design of more complex species.[45] The group included the crown ethers[46] by Pedersen, the cryptate[47] by Lehn and the spherand[47] by Cram (Figure 9).

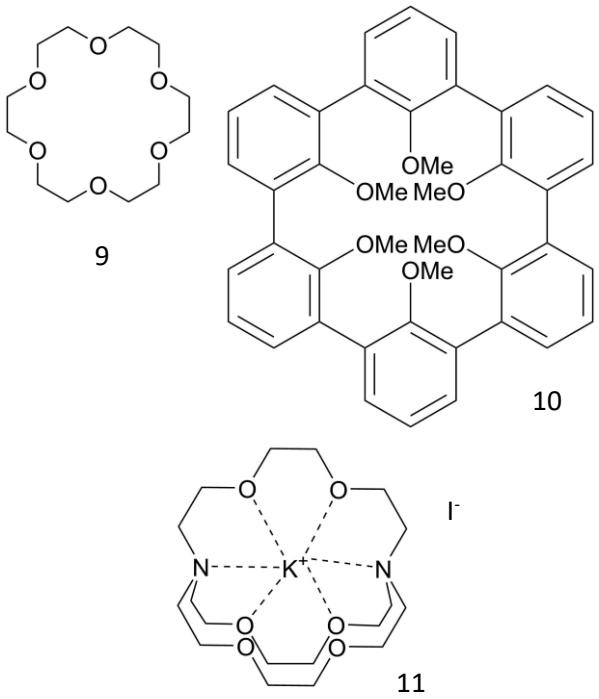

Figure 9: Difference in the binding constant shown between 18-crown-6 ether (9),[46] spherand (10)[46] and cryptate structure (11).[11]

As a result, supramolecular chemistry became one of the most challenging and sophisticated fields of research which has continued developing and growing to this day. Some of the main concepts which are continuously being explored in this field are self-assembly by non-covalent interactions,[48] molecular recognition,[49] molecular building blocks which are mechanically engaged,[50] molecular machinery[51] and imprinting.[52] The process of self-assembly using non-covalent interactions is one of the most complicated and broad concepts which has gathered a lot of attention from many researchers in recent years. It is one of the main processes used in determining the way complex structures are constructed, how they function in different solvent environments. These include cell membranes,[53] phospholipids,[54] micelles[55] and vesicles.[56] For example the biological cell membrane is made of a lipid layer (from phospholipids) and proteins with different functionalities, such as integral and peripheral.[57] Another example is the lipid bilayer which is produced as a result of the self-assembly of amphiphiles in a water environment.[58] For years the scientific community has studied these supramolecular principles in order to use them for the design of new amphiphilic molecules. An example of this is by Yuping Huang and co-workers, who by synthesising hydrophilic polyethylene glycol monomethyl ether (MPEG) substitutions and hydrophobic octanoyl, were able to obtain a novel biopolymeric amphiphile. The results from the experiments carried had shown that the new chitosan-based amphiphile had good solubility in non-polar solvents such as ethanol, $CHCl_3$ and aqueous solutions.[59] Along with they reported the ability of the amphiphile to self-assemble in an exact same way at the different concentrations they were observed, thus forming the same self-assembled structures, spherically shaped with a hydrodynamic diameter of 24.4 nm. Along with that the critical aggregation concentration (CAC) was also determined to be 0.0066 mg/mL and the amphiphile also was reported to have a very small cytotoxicity against HepG2 cells (cancer cell) at concentrations ranging between 0.1 μ*g*/mL and 0.1 mg/mL.[59] All of the data obtained had indicated that the amphiphile could be potentially used in different biological applications such as drug/gene delivery[60] or encapsulating the agent for food application.[61]

Another study carried out by Young Park and co-workers, in which hydrogen bond interactions were used in the production of a series supramolecular gel with chirality transcription and strong fluorescent properties (Figure 10).[62] From the results obtained from the experiments it was determined that there was a change in the absorption wavelength of the gels before and after the gelation process as the solution had a weak fluorescence with an emission of 430 nm, whereas after it was gelated the aggregate exhibited a more intense emission of 514 nm.[62] It was also determined that the intensity after gelation was up to 240 times higher. This was reported to be as a result of the hydrogen bond interactions which led to a change in the structure formation, resulting in a complex assembly having a J-type aggregation (a dye with a longer absorption wavelength) and planar structure.[62] In conclusion, the gels were determined to have AIEM properties, as a result of which they were found to have stronger fluorescence during the self-assembly processes.[62] It was also reported that the self-assembly processes occurring could be observed during the time in which they were taking place by fluorescence turn on, as a result of the AIEM.[62]

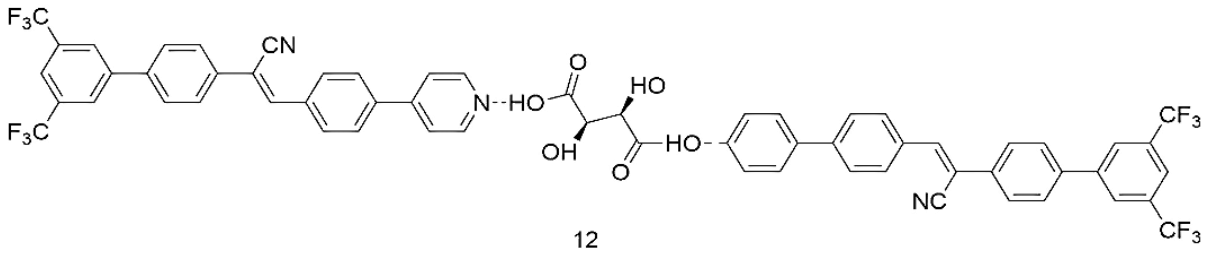

12

Figure 10: Complex formation of the organogel (using a non-fluorescent and achiral monomer and chiral L-tartaric acid) using hydrogen bonding (12).[62]

2.3 Anions

Anions are atoms that carry a negative charge which play an important role in a lot of biological and chemical processes. They are the ones that carry the genetic information in our bodies, like DNA, co-factors and enzymes.[63] For example, the presence of phosphate anions in the body stimulates the production of energy, with the inorganic phosphate being in the form of ATP and ADP.[63] Cl^- can be found in the extracellular fluid compartment and plays an important role in maintaining the osmoaility and electrochemical function across the bodies bilayers.[63,64] Other anions such as nitrates, sulphates, phosphates are found to affect different processes in nature.[63] For example, phosphate and nitrate anions are present in different water sources, affecting their environment and living conditions. The intermolecular interactions between the anionic species play an important role in complex formation. Examples include anionic receptors, anions used as sensors, anions used as transporters in various biological systems, etc.[65] When exploring the formation of an anionic receptor (host-guest chemistry) there are different anionic characteristics and properties which must be considered. The radius between an anion and a cation are very different, as anions are known to have a much larger radius compared to a cation, thus resulting in them having a lower charge-to-radius ratio (e.g K^+ having 1.52 Å, compared to Cl^- having 1.67 Å).[66] Along with that they also show sensitivity towards pH, meaning that they could become protonated at a lower pH environment, which would result in the loss of their negative charge.[66] There are different types of anionic species depending on their geometrical shape – spherical (Cl^-, I^-), linear (OH^-, CN^-), trigonal planar (NO_3^-), tetrahedral (SO_4^{2-}, MnO_4^-), octahedral ($[Fe(CN)_6]^{4-}$) and complex shapes such as DNA (double helix) or RNA.[66] An important factor which has an effect over the strength of the binding and the selectivity of the interactions between the anionic species is the solvent environement.[66]

Receptors which have a charge can bind solvated anions strongly through non-covalent interactions in polar solvents.[66] The type of interactions occurring between the anionic species aids in categorising the different types of anionic species which can be designed. The most popular HBD functional units used in the structural formation are ureas,[67] thioureas[67] and amides.[63,67] A lot of studies of anion recognition between anionic species. In a study carried out by Shang and co-workers have been reported in the anionic recognition functions of a series of hydrazone derivative receptors (anthracene based – Figure 11).[68] The anions used in the study were Cl^-,F^-,Br^-,AcO^-,$H_2PO_4^-$ and I^-. A series of experiments were carried out in the solution phase, including fluorescence and ^1H NMR titration studies.[68] From the results, it was determined that the receptor 13 had a lower binding ability, as a result of weak interactions with some of the anions, compared to receptor 14 and 15 which were established to have a significantly high binding capability for acetate (AcO^-).[68] This was determined to occur as a result of the increase in the intensity of the absorption values from 450 nm (decrease) to 610 nm (increase) for receptor 14 and from 430 nm (decrease) to 550 nm (increase) for receptor 15, with the addition of the anion (increase in concentration).[68] The final binding trend observed for both 14 and 15 was determined to be the following: I^-, Cl^- , $Br^- < H_2PO_4^- < F^- < AcO^-$, which was established to be as a result of the pH of the anion, as well as the interactions between the host and guest.[68] Along with that, it was reported that hydrogen bond interactions play an important role in the binding between receptor 14 and F^-, where after the NH has been deprotonated the addition of F^- leads to the formation of hydrogen bonds with the closest CH in Schiff base.[68] It was also reported that due to the presence of the NO_2 group and the hydrogen bond interactions 14 and 15 were established to have colour changing properties when interacting with F^- and AcO^-, therefore showing their potential ability to act as colorimetric sensors.[68]

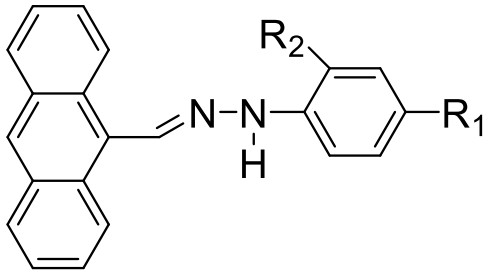

13. $R_1 = R_2 = H$

14. $R_1 = NO_2$ $R_2 = H$

15. $R_1 = R_2 = NO_2$

Figure 11: Structures of the anthracene based receptors (hydrazone derivatives).[68]

An example of anion interactions in biological applications can be observed in a study carried out by Gale and co-workers report the design of a group of thiourea and urea based anion compounds which have a hight transmembrane transport activity (Figure 12).[69] The molecules are fluorinated and nonfluorinated. A series of experiments were carried out in DMSO-d_6 + 0.5% H_2O which showed the ability of the compounds to bind to anions, thus obtaining the following trend $NO_3^- < HCO_3^- < Cl^- < H_2PO_4^- < SO_4^{2-}$, also some of them were determined to deprotonate ($H_2PO_4^-$ and HCO_3^-).[69] Also, the binding constants for the urea compounds were determined to be higher ranging between 152-882 M^{-1} (mainly observed for the TBA binding with Ka >10^4 M^{-1}), compared to that of the thioureas ranging between 128-256 M^{-1}, apart from one compound (Figure 12 – thiourea based compound 25) which could not be fitted to the 1:1 binding model.[69]A series of solid state, transport and structure activity relationship studies were also carried out for all of the compounds.

From the final results, it was concluded that this new series of compounds can be used in transporting chloride through the lipid layer, as a result of a series of chloride processes including chloride/nitrate, bicarbonate and sulphate.[69] It was also established that the fluorinated compounds have a higher transport activity (transport clog of *P* = 8), due to the increase in their lipophilicity which is increased by the higher amount of fluorine.[69] Along with that one of the receptors (containing a urea functional group) was determined to be able to transport chloride at a really low ratio of 1:250000. It was concluded that the fluorinated receptors had an activity against human cancer cells, which was suggested to be as a result of the changes of the pH of the cells, which was triggered by the ability of the transporters to carry ions.[69]

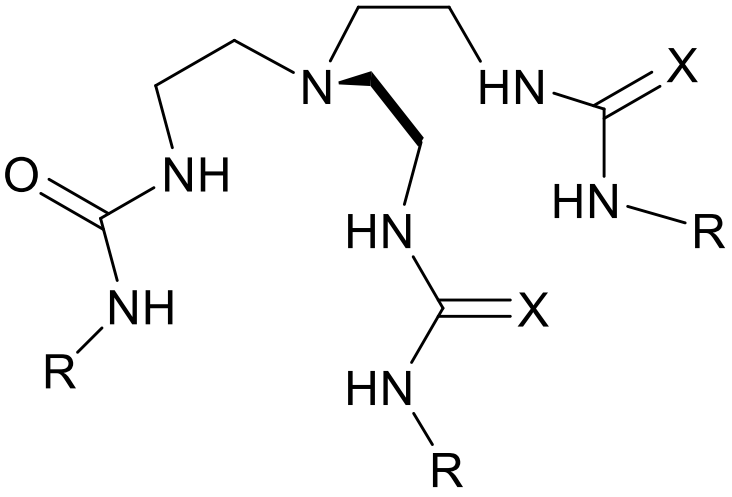

16. X = O, R = Ph
17.X = O, R = p-C_6H_4F
18. X = O, R = C_6F_5
19. X = O, R = p-$C_6H_4(CF_3)$
20. X = O, R =

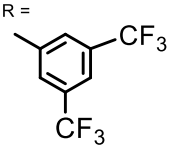

21. X = S, R = Ph
22. X = S, R = p-C_6H_4F
23. X = S, R = C_6F_5
24. X = S, R = p-$C_6H_4(CF_3)$
25. X = S, R =

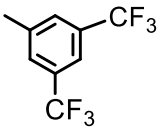

Figure 12: Structures of the urea (16 -20) and thiourea (21 - 25) based compounds.[69]

2.4 Amphiphile

An amphiphile is a molecule which has both hydrophobic (non-polar) and hydrophilic (polar) units. It has been determined from the studies reported in the literature that solvent environments play an important role in the non-covalent interactions occurring in solution. The nature of the solvent (polar/non-polar) and conditions (temperature, solubility) affects the stability,[70] interactions and strength of amphiphilic molecules which results in the formation of various structural species with a distinctive shape, functionalities and chemical properties such as micelles, nanotubes, vesicles, aggregate assemblies and others.[71] Micelles are aggregates formed by amphiphilic molecules in polar solvent environments such as water.[72] There are different types of structures which can be formed – direct and reverse micelles, as well as the lipid bilayer (biomolecular sheets). Direct micelles are formed in a way which causes their hydrophilic head component to interact with the aqueous environment, while the hydrophobic unit interacts with solvent (non-polar) or air (Figure 13).[71] The reverse micelles are formed in a reverse way with the head group facing the inner water phase, whereas the tail radiates away, thus interacting with the solvent environment (Figure 14). The lipid bilayer is an important part of the structure of the cell membrane, which is formed for the assembly of lipid molecules (non-polar solvents).[73] The bilayer is made of phospholipids which contain hydrophobic tails and a hydrophilic polar head (Figure 15). The tails are fatty acids which are different in length (containing between 14 and 24 carbon atoms).[73] The saturation of those tails is an important characteristic which affects the fluidity of the membrane.[73] The formation of the micelles depends on the interactions (repelling and attractive) occurring between the hydrophobic and the hydrophilic groups of the amphiphilic molecule and the solvent environment.[74] Micelles are formed at concentrations above and below the CMC of the surfactants. A low CMC value indicates stable micelles.

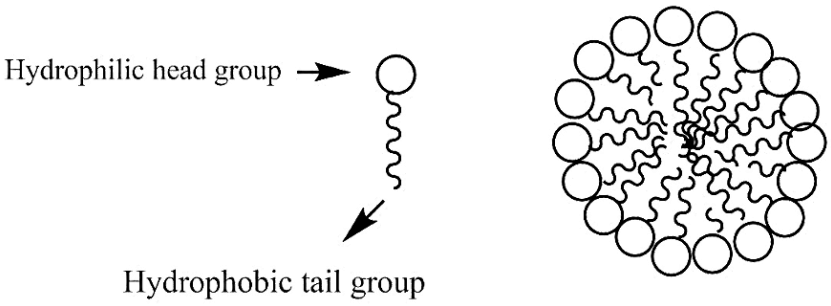

Figure 13: Direct micelle structure.[71]

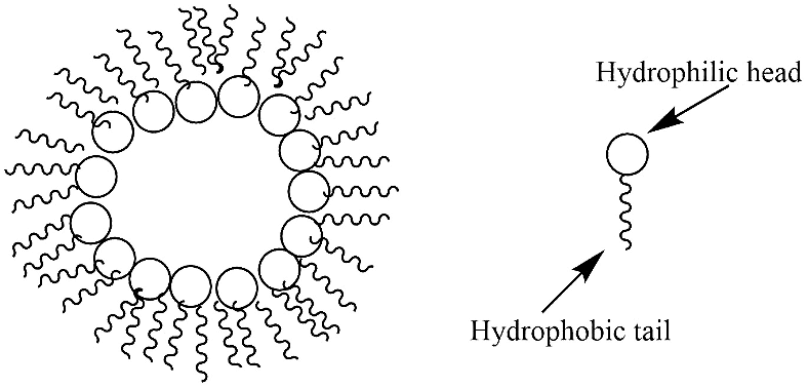

Figure 14: Reverse micelle structure.[71]

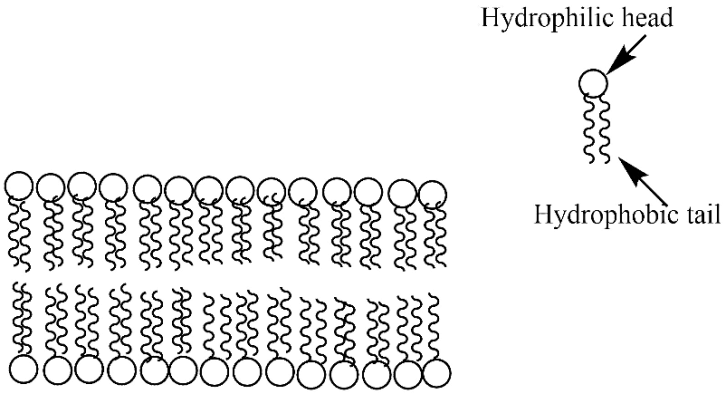

Figure 15: Structure of the lipid bilayer.[71]

Micelles have different shapes but the most commonly encountered are spherical, bilayer and cylindrical.[74] Their shape and size depend on the structure of the amphiphilic molecule, as well as the environmental conditions of the solvent such as temperature, concentration, pH, solubility.[71] Micellar systems play an important role in pharmaceuticals due to their ability to increase the solubility and stability of substances and compounds that are poorly soluble in water environments. This occurs as a result of the nature of the micelles, or more specifically the fact that they have a hydrophobic center which results in the decrease of the concentration of the water from the surface of the micelle towards the core.[75] Along with that micelles also play an important role in drug delivery/target systems or used as model systems in biological membranes. An example is a study carried out by Feng and co-workers, in which they reported the ability to enhance the solubility of drugs used in cancer treatments. RUB a diterpene glycoside was used in order to increase the drug solubility.[76] The studies carried out showed that that RUB could form micelles through self-assembly. The size of the micelles was reported to be horizontal 25 nm and vertical 1.2 nm (ellipsoidal form), whereas the CMC was determined to be 0.18 mM (blank RUB micelles in deionised H_2O).[76] The insoluble drugs used in the experiments were RES and CUR. After loading both anti-cancer drugs (RES and CUR) with RUB, thus forming CUR/RUB + RES micelles, an increase in the solubility of CUR (60 fold) and RES (33 fold) was observed. This, therefore, resulted in establishing the ability of RUB in being an effective carrier of insoluble drugs. Along with that, it was reported that after loading the RES and CUR onto RUB (CUR/RUB + RES) the micelles formed were more toxic and effective against MCF-7 cells, compared to the micelles formed by individual combinations of only RES + RUB, as well as RUB + CUR. It was concluded that RUB-based micelles can be used in increasing the effectiveness of insoluble drugs and enhancing their effect against cancer cells.[76] Depending on the nature of the head group, the amphiphilic molecules can be can be salts, zwitterionic (ionic) or non-ionic.[77] Anionic surfactants are one of the most encountered amphiphiles, with their hydrophilic head groups being negatively charged (Figure 16).

Examples include carboxylic acid salts, alkylbenzene sulphonates, phosphoric acid esters, sulphonic acids (sulphonates, carboxylates, phosphate and sulphate functional groups).[78] The different types of counter cations observed in anionic surfactants are sodium, potassium or quaternary ammonium ions.[79] Cationic surfactants have positively charged hydrophilic head groups and the most common examples are those of amine salts and ammonium ions (Figure 16).[79] Non-ionic surfactants are neutral and the most commonly encountered ones are ethoxylates (Figure 16).[80] Lastly, there are zwitterionic surfactants which have positively and negatively charged groups (Figure 16).[80]

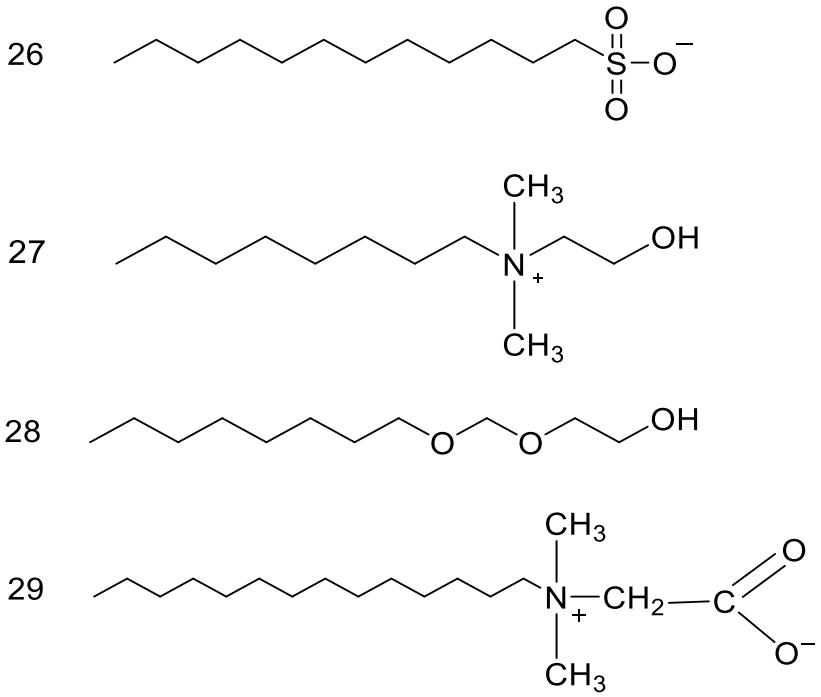

Figure 16: Different types of surfactants; anionic (26), cationic (27), non-ionic (28) and zwitterionic (29).[77]

Amphiphilic molecules containing a hydrophilic and hydrophobic component represent building blocks which can be used in order to create more complex structural species, as a result of the different interactions, such as hydrogen bonding or host-guest interactions which could occur in a solution.[81] This has been highlighted and reported in studies carried out by Faustino and co-workers,[82] in which they explore the properties of a series of anionic urea based amphiphiles in the solution state. Monomeric and dimeric species of anion urea amphiphiles derived from amino acids containing sulphur were synthesized (Figure 17).[82] The results from the analysis showed that the dimeric urea surfactants had a lower CMC ranging between 0.78 – 0.82 x 10^2 mol dm^{-3}, compared to the monomeric cysteine counterpart species (ranging between 3.37 – 8.42 x 10^2 mol dm^{-3}) which were determined to be more efficient in lowering the surface tension, as a result of the individual sulfhydryl group, more specifically compound 30 which had the lowest surface tension of 23.10 mN/m^{-1}. Hydrogen bonding was observed for the dimeric species, due to the presence of the urea unit.[82] The studies also showed that the hydrophobic interactions were resulting in the formation of micelles, rather than the hydrogen bonding which was established to play the main role in the absorption process. The amphiphiles were also tested against bacteria, however, none of them showed any antimicrobial activity which was suggested to be as a result of the short alkyl chains. No antimicrobial activity was also observed for the dimeric species which was suggested be as a result of them having an anionic polar group, also because the arginine diglycerides are known to be cationic.[82]

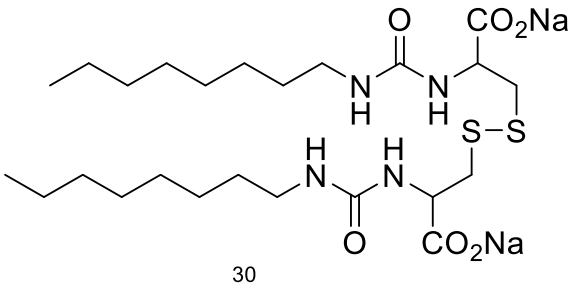

30

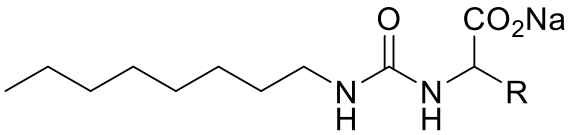

31. R = CH_2SH 32. R = $CH_2CH_2SCH_3$ 33. R = CH_2SO_3Na

Figure 17: Dimeric (30) and monomeric (31,32,33) urea species obtained from amino acids containing sulphur.[82]

3. Introduction to the amphiphilic compounds

Studies carried out by Hiscock and co-workers[83] report the different binding modes and self-association processes of a new series of amphiphiles designed by the model shown in Figure 18 using a urea HBD/HBA group, sulphonate and carboxylate anionic unit with a TBA counter cation and a hydrophobic component (aromatic benzene). This new structural model of the compound was unique in their studies. The new molecules were found to be "frustrated", as a result of the various binding modes they could attain simultaneously, however not limited to a urea-urea complex which could be both *syn*-stacking and *anti*-stacking;[83] (Figure 19) and the second one being a urea-anion dimer binding and urea-anion tape binding (Figure 19).

From the final results obtained from all experiments, it was established that the binding modes were affected by the molecular structure of the amphiphile and the solvent systems in which it had been observed.[83] The study by Hiscock and co-workers[84] was later expanded to a bigger group of novel amphiphiles which were designed with the same general structure shown in Figure 18. The HBD/HBA groups used for these new amphiphiles were expanded and included functional groups such as thiourea,[85] amide[86] or urea[87] (X) an anionic component from the previously mentioned sulphonate, carboxylate etc. (hydrophilic group) (Y) and a counter cation (TBA, TMA, TEA, TPA, etc.) (Z). The self-association processes of these were studied in all three states – gas, solid and solution. By presenting a series of anionic guest species[84] and altering the cationic units they were able to control the self-assembly processes, binding modes and structural species occurring in different solvent environments. It was established that the self-association processes which occur as a result of hydrogen bond interactions can be adapted due to the accumulation of different HBD and HBA units. Along with that it was determined that the coordination properties of the hydrogen bond, including angle and length were affected, as a result of the modified acidity of the HBD (thiourea/urea sulphonate).[83] Dimeric and large aggregate species[84] were also reportedly observed in different solvent systems, thus showing the ability of these molecules to self-assemble in solution, as a result of hydrogen bonding interactions.

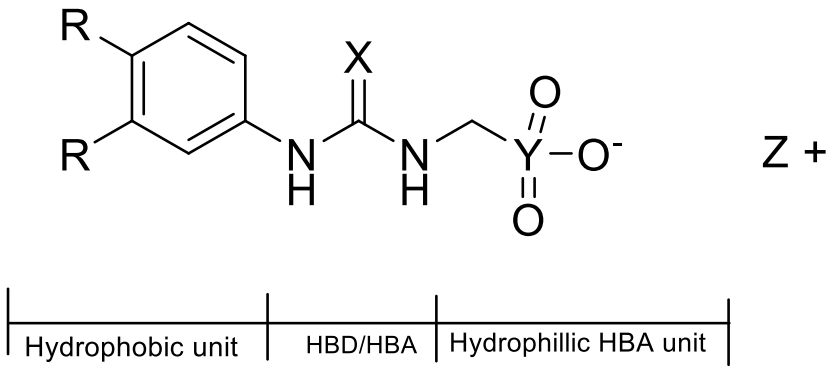

Figure 18: The structural components required to build an amphiphilic molecule.[83]

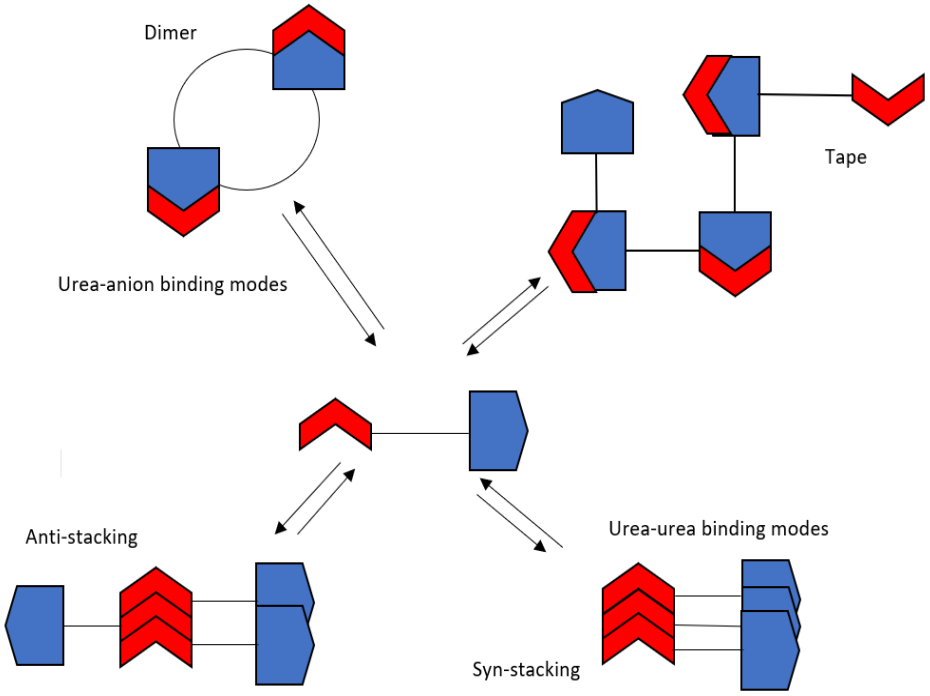

Figure 19: Binding modes of anionic molecules, as a result of hydrogen boning.[83]

The compounds presented in this thesis were synthesised (Figure 20) and were designed based on the amphiphilic model reported in the Hiscock studies (Figure 18).

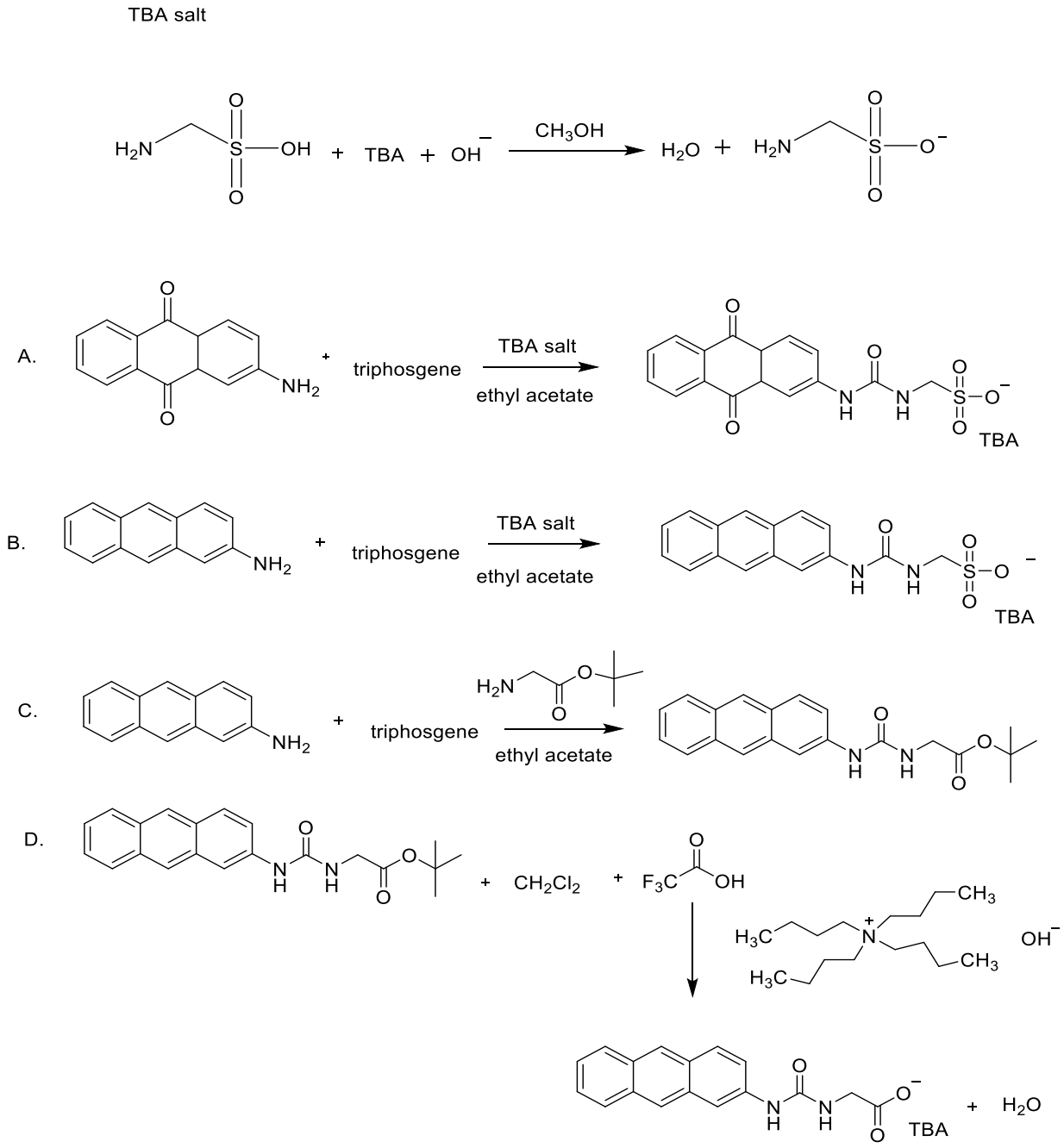

Figure 20: Synthesis scheme for compounds **1 – 4**; A = **1**, B = **2**, C = **3**, D = **4**.

Compounds **1** and **2** contain an anionic sulphonate group, while compound **3** and **4** have an anionic carboxylate group (Figure 20). The aromatic substituent of the amphiphiles **1**,**2** and **4** is hydrophobic in nature, whilst their anionic substituent is hydrophilic (Figure 21).

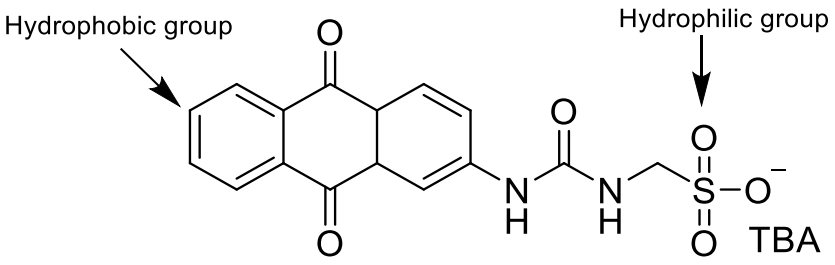

Figure 21: Showing both the hydrophilic and hydrophobic components of compound **1** with TBA = Tetrabutylammonium.

Compounds **2**, **3** and **4** are anthracene based, while compound **1** is anthraquinone based. An attempt to synthesise a carboxylate anthraquinone based compound was carried out. Although the compound was synthesised it could not be purified due to its unstable and reactive nature, thus resulting in the inability to obtain the desired final product at a purity level required for further investigation. Compound **2** (Figure 20) has been synthesised and characterised before in line with previously published methods.[2] Compound **1** (0.41 g, 0.68 mM, Yield: 23%) was synthesised by similar methods to those of compound **2**. Compound **3** (0.55 g, 1.57 mM, Yield: 61 %) was synthesised by a reaction of 2-aminoantharcene, triphosgene and tert-butyl-aminoacetate. After that **3** was deprotected using TFA and TBA hydroxide was added in order to obtain compound **4** (0.78 g, 1.46 mM, Yield: 56%). Compound **1**, **4** and a series of mixture combinations (compound **1** and **2**, compound **1** and **4**, compound **2** and **4)** were fully characterised and their physical properties were observed and recorded. All of the data obtained from each experiment will be discussed, interpreted and compared in order to establish the possibility of being able to predict the ways these amphiphiles self-associate, as well provide evidence for the antimicrobial mode of action.

4. Result and discussion

4.1 Single crystal x-ray diffraction:

Single crystal x-ray diffraction was developed by Max von Laue in 1912, when he established that crystalline like substances can be used as three-dimensional diffraction gratings for x-ray wavelengths.[88] It is a non-destructive technique and it can be used in order to obtain a three dimensional structure of a crystal,[88] explore their structure-property relationships [89] and observe both the covalent and non-covalent interactions occurring in the solid state.[89, 90] When looking at the hydrogen bonding, for this series of compounds, the urea substituents and the anionic groups would play an important role when exploring processes such as dimerisation,[91] stability [92] and selectivity.[93] The crystal structures for compound **1** and a mixture of compound **1** and **2** were obtained from concentrated solutions in DMSO-d_6. A dimer of compound **1** was observed along with the structure obtained for the mix of **1** and **2.** Attempts to obtain a crystal structure for **3** and **4** individually, as well as for mix of **1** and **4**, **2** and **4** were carried out using a mixture of different solvent systems, however, they were unsuccessful. Compounds **3** and **4** were only isolated as amorphous solid after evaporation of the solvent. The experiment was carried out by Dr. Jennifer Hiscock, while the data was processed by both Dr.Jennifer Hiscock and Dr.Helena Shepherd (Senior Lecturers in Chemistry – School of Physical Sciences, University of Kent, Canterbury, Kent).

4.1.1 Result and discussion:

A single crystal x-ray structure was obtained for compound **1** in a solution of DMSO-d_6. The structure shown in Figure 22, shows a symmetrical urea-sulphonate dimer species which was formed by the anionic monomer and is being held together by only four intermolecular hydrogen bonds.

The urea NHs act as the HBD units in this structure, whilst the sulphonate oxygen atoms from each individual monomeric species act as the HBA units. Disorder within the TBA counter cations has meant that the carbons of three of the eight butyl arms have been modeled isotopically without the presence of the associated hydrogen atoms. This provides the most accurate model based on the limitations placed on these data by the single crystal samples obtained.

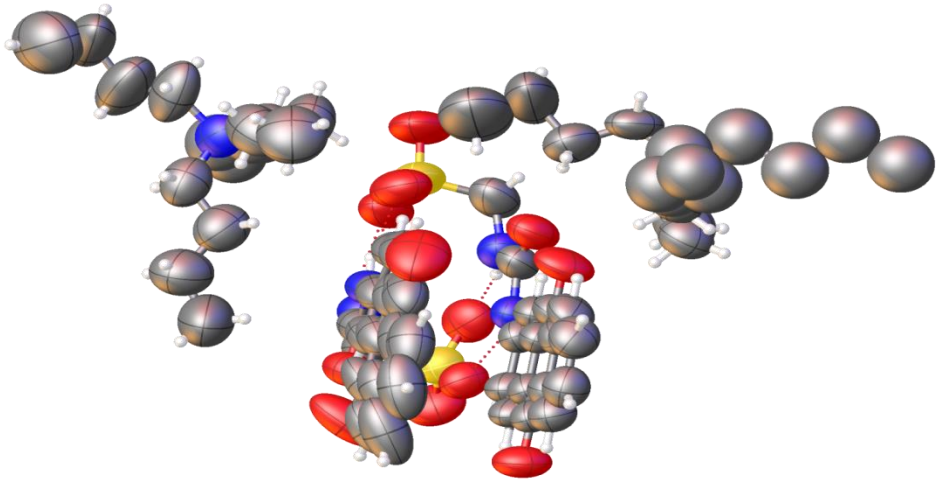

Figure 22: Single crystal x-ray structure of compound **1**; showing a dimer species formed through the urea-sulphonate substituent; White = Hydrogen, Blue = Nitrogen, Grey = carbon, Yellow = Sulphur, Red = Oxygen. ; The TBA counter cation has been omitted for clarity. CCDC 1866274, $C_{64}H_{64}N_6O_{12}S_2$ (M =1173.33): triclinic, space group P -1, a = 11.9182(9) Å, b = 12.8979(8) Å, c = 23.0180(13) Å, α = 84.931(5)°, β = 84.247(6)°, γ = 75.288(6)°, V = 3397.8(4) Å^3, Z = 2, T = 293(1) K, CuK\α = 1.5418 Å, Dcalc = 1.147 g/cm^3, 23306 reflections measured (7.102 ≤ 2Θ ≤ 133.200), 12023 unique (R_{int} = 0.0256, R_{sigma} = 0.0346) which were used in all calculations. The final R_1 was 0.1495 (I > 2σ(I)) and wR_2 was 0.4690 (all data).

Table 1: Hydrogen bond distances and angles observed for hydrogen bonded complex formation, calculated from single crystal x-ray structure of compound **1**.

Compound	Hydrogen bond donor	Hydrogen atom	Hydrogen bond acceptor	Hydrogen bond length (D•••A) (Å)	Hydrogen bond angle (D-H•••A) (°)
1	N1	H1	O7	2.957(10)	171.3(3)
1	N2	H2	O9	2.862(7)	167.0(3)
1	N3	H3	O2	2.893(8)	165.1(3)
1	N4	H4	O3	2.868(9)	174.5(2)

The hydrogen bond lengths from donor to acceptor of compound **1** shown in Table 1 range from 2.957 – 2.868 **Å** and hydrogen bond angles ranging from 171.3 – 174.5**°**.

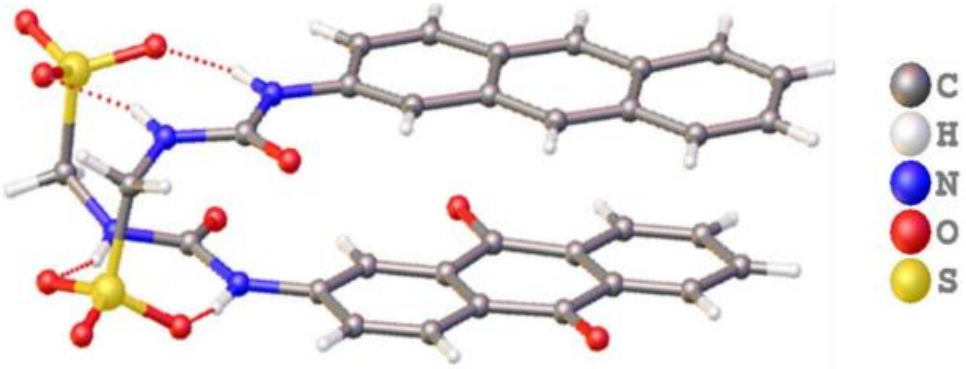

Figure 23: A single crystal x-ray structure of a solution containing compound **2,** showing the formation of an unsymmetrical dimeric species reported by Hiscock and co-workers.[2] Compound **2** has undergone partial oxidation into the anthraquinone.

A crystal structure obtained from a solution of **2** only, has been reported by Hiscock and co-workers.[2] However, the structure in Figure 23 was obtained due to an oxidation process that occurred during the crystallisation time. It is known that anthracene ,when exposed to air [94] for a period of time, can oxidise [95] and form anthraquinone.[94] The results shown by the Hiscock group showed this to be the case in this instance, as part of the anthracene had oxidised at some point into the anthraquinone and the structure shown in Figure 23 was observed. It showed the formation of a dimer species being held together by four intermolecular hydrogen bonds via the sulfphonate – urea substituents.[2] A similar crystal structure using 1:1 mix of compound **1** and **2** in DMSO–d_6 has been obtained in these studies (Figure 24). After making a 55.56 mM solution, after 30 min at room temperature, a crystal formation was observed. Only a single crystal was used in this study, the rest of the bulk sample was used in an x-ray powder diffraction study.

The crystal obtained was determined to be very disordered and contained an unsymmetrical dimer for compound **1** and **2** (mix) which had 85% occupancy, as well as a symmetric dimer of compound **1** which had 15% occupancy. The dimer for **1** and **2** was held together by four hydrogen bonds, similar to the hydrogen bonding mode previously seen in compound **1**. This structure observed for the mix **1** and **2** in this sample was found to be similar to the unsymmetrical dimer reported by Hiscock and co-workers.[2]

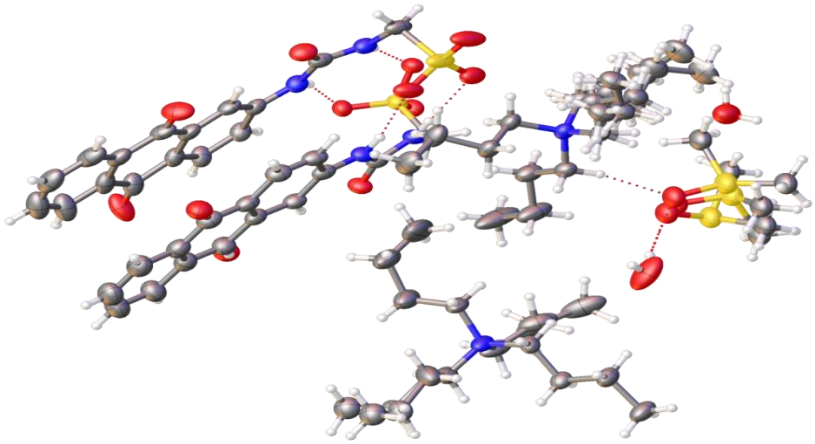

Figure 24: A single crystal x-ray structure of compound **1** and **2** (mix 1:1) and a dimer formation of compound **1;** White = Hydrogen, Blue = Nitrogen, Grey = carbon, Yellow = Sulphur, Red = Oxygen; The TBA counter cation has been omitted for clarity. CCDC 1866275, $C_{66}H_{105.09}N_2O_{13.31}S_3$ (M =1395.66): triclinic, space group P -1, a = 11.4872(10) Å, b = 12.4679(2) Å, c = 25.0105(13) Å, α = 95.236(5)°, β = 90.694(6)°, γ = 105.370(7)°, V = 3437.1(4) $Å^3$, Z = 2, T = 100(1) K, CuK\α = 1.5418 Å, Dcalc = 1.248 g/cm^3, 22986 reflections measured (7.388 ≤ 2Θ ≤ 133.192), 12134 unique (R_{int} = 0.0784, R_{sigma} = 0.0808) which were used in all calculations. The final R_1 was 0.0981 (I > 2σ(I)) and wR_2 was 0.2846 (all data).

Table 2: Hydrogen bond distances and angles observed for hydrogen bonded complex formation, calculated from single crystal x-ray structure of compound **1** and **2** (mix 1:1).

Compound	Hydrogen bond donor	Hydrogen atom	Hydrogen bond acceptor	Hydrogen bond length (D•••A) (Å)	Hydrogen bond angle (D-H•••A) (°)
1 and **2**	N00G	H00G	O004	2.863(4)	165.5(1)
1 and **2**	N9	H9	O003	2.873(4)	162.8(1)
1 and **2**	N10	H10	O00D	3.003(4)	163.6(2)
1 and **2**	N11	H11	O1AA	2.868(9)	173.0(3)

The hydrogen bond lengths from donor to acceptor of compound **1** and **2** shown in Table 2 range from 2.863 – 2.868 **Å** and hydrogen bond angles ranging from 165.5 – 173.0**°**. From the data presented the presence of dimer formation was established for compound **1**, as well as mix of **1** and **2.** The dimer species were determined to be more stabilised as a result of the urea NH hydrogen bond donating groups and the sulphonate-oxygen atoms being HBA. In the mix containing the **1** and **2** dimer species the selectivity was recognised to play an important role – the compounds are selectively picking each other out and the complex is being held together and is being stabilised due to the electron poor (anthraquinone) and electron rich (anthracene) components from each individual monomeric species.

4.2 X-ray powder diffraction:

X-ray powder diffraction is a non-destructive analytical technique used in characterising crystalline solid materials.[96] The data obtained is from a powder form of the main material, rather than an individual crystal structure.[97] The results are received as a sequence of Gaussian functions, allowing a comparison between the main powder pattern, from a main structure, and the experimental, as well as minimising the differences and errors between both patterns.[98] The powder patterns obtained are like a fingerprint and can be used to determine the presence of different crystal phases. In cases where a mixture of crystal phases is being analysed, the final data can also provide information about the proportion of different materials/compounds present.[99] For this experiment, the remaining bulk of the sample containing compound **1** and **2** mix (Figure 25) from which one crystal was used in the single crystal x-ray diffraction studies was observed. This was carried out in order to differentiate the presence and the proportion for each crystal phase in the sample bulk. The experiment and data processing were carried out and written with the help of Dr. Paul Saines (School of Physical sciences, University of Kent, Canterbury, Kent).

4.2.1 Result and discussion

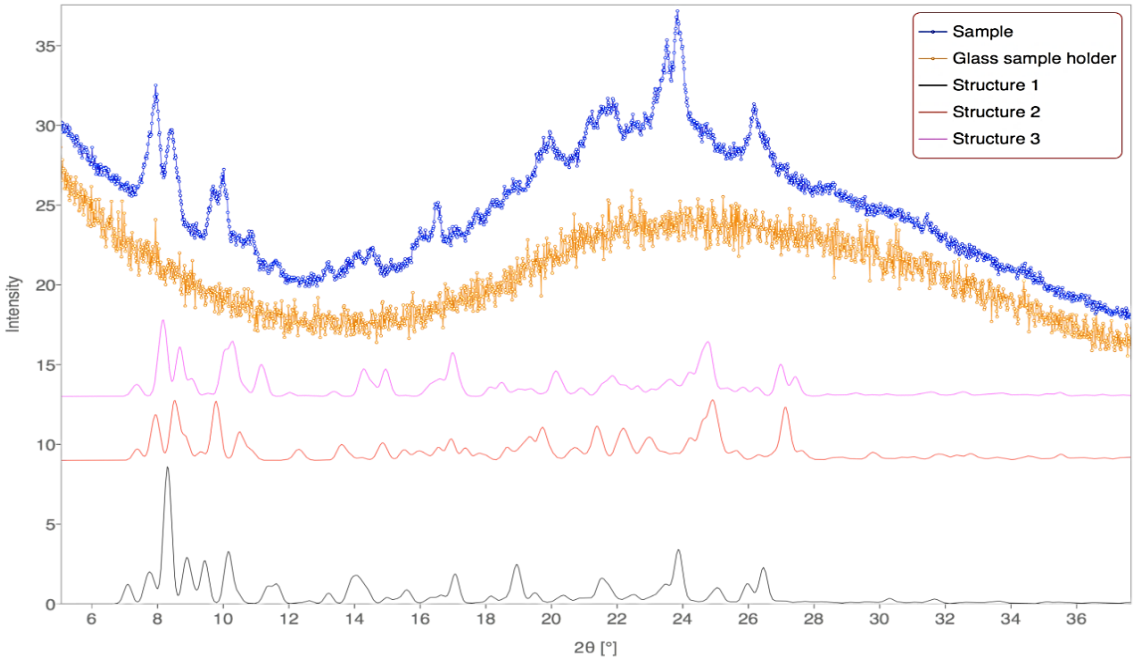

Figure 25: Showing comparison data between the x-ray powder diffraction pattern (in blue), the glass plate sample holder (orange) and the patterns observed for structure 1 (compound **1** – grey, CCDC 1866274, Figure 22), structure 2 (compound **2** – red, CCDC 1866275, Figure 23)[2] and structure 3 (compound **1** and **2** mix – pink, CCDC 1562758, Figure 24).

From Figure 25, the diffraction pattern of the symmetrical dimer can be seen (compound **1** – grey, CCDC 1866274, Figure 22), the hydrated asymmetrical dimer (compound **2** – red, CCDC 1866275, Figure 23)[2] and anhydrous asymmetrical dimer (mix of **1** and **2** – pink, CCDC 1562758, Figure 24). The diffraction nature of the main sample results in a diffraction pattern with a slight signal ratio, similar to the diffraction pattern observed from the glass holder (Figure 25 – orange). By comparing the result from the graph, it was established that the main sample diffraction pattern (in blue) shares similarities with anhydrous asymmetrical dimer (mix of **1** and **2** – in pink) with the majority of the peaks being observed and the peak splitting being consistent, thus resulting in it being the leading phase in the solid state.

Differences observed between the symmetrical dimer (compound **1** - grey) and the experimentally observed diffraction pattern (in blue) suggest that the phase is not present. On the other hand, when looking at the hydrated asymmetrical dimer (compound **2**- red) some similarities can be seen when comparing it to the calculated diffraction pattern (blue), suggesting that a small amount of this phase is present. Nevertheless, when the quality of the data and the similarities of the powder diffraction patterns of both symmetrical dimer (compound **1**) and hydrated asymmetrical dimer (compound **2**) are considered, this prevented the ability to determine that the sample is entirely anhydrous. However, if structure 1 (compound **1**) was to be present, it would most likely be only a small part of the phase, due to the fact that the diffraction peaks from this structure cannot be observed.

From the data presented it was established the inability to identify the sample as being entirely anhydrous, due to the lack of presence of structure 1 (compound **1**). This is not surprising given the fact that the crystal, used in the single crystal x-ray diffraction, was obtained from this sample. Along with that, the proportion of each individual compound present in this phase could not be determined.

4.3 ESI – MS

Electrospray ionisation mass spectrometry is known to be one of the most significant analytical techniques used in various scientific fields – chemistry, biology, physics, from which both quantitative (ex. concentration) and qualitative (structure)[100] information about analyte molecules can be obtained.[101] Firstly the molecules have to be converted into ionic species.[101] In order to achieve this , the sample is injected into the ionisation source of the instrument in order to ionise the sample.[101] The ions are sorted based on their mass to charge ratio (*m/z*), which also used to identify the main molecule, as well as any other formed species.[102]

The technique can be used in order to observe non-covalent interactions, such as hydrogen bonding in big and small molecules,as well as complex biological structures.[103] ESI – MS is considered a very significant technique when it comes to observing hydrogen bonding interactions in the gas phase.[104]

Compounds **1-4** were analysed using this technique in order to determine if there is any evidence of self-association processes occurring or possible dimer formation.

4.3.1 Result and discussion

The results which were obtained from the ESI-MS studies, as expected, show anionic monomer species $[M]^-$ for amphiphiles **1, 2** and **4**, whilst compound **3** required ionisation as the compound was not an anionic species, thus being able to have an anionic monomer $[M-H]^-$ state shown in Table 3.

Table 3: An overview of theoretical and actual data collected using high-resolution mass spectrometry (ESI negative) for individual compounds **1-4**.

Compound	Theoretical (*m/z)*		Actual (*m/z)*	
	$[M]^-$	$[M-H]^-$	$[M]^-$	$[M-H]^-$
1	359.0343	N/A	359.0339	N/A
2	329.0602	N/A	329.0685	N/A
3	N/A	349.1557	N/A	349.1628
4	293.0932	N/A	293.0932	N/A

Along with that, the presence of dimer species $[2M+H]^-$ was established for amphiphiles **1**, **2** and **4** shown in Table 4.

Table 4: An overview of theoretical and actual data collected using high-resolution mass spectrometry (ESI negative) for individual compounds **1-4**.

[a] Ion not observed.

Compound	Theoretical (*m/z)*				Actual (*m/z)*			
	$[2M+H]^-$	$[2M-H]^-$	$[2M+Na]^-$	$[2M+K]^-$	$[2M+H]^-$	$[2M-H]^-$	$[2M+Na]^-$	$[2M+K]^-$
1	719.0759	N/A	741.0578	[a]	719.0765	N/A	741.0586	[a]
2	[a]	N/A	681.1096	[a]	[a]	N/A	681.1249	[a]
3	N/A	[a]	N/A	N/A	N/A	[a]	N/A	N/A
4	587.1937	N/A	609.1756	[a]	587.1877	N/A	609.1683	[a]

There were no dimer species present for compound **3**, due to the fact the compound does not have an anion substituent to allow dimerization to occur. With some of the compound samples, more than one dimeric species was observed. Taking compound **1** (Figure 26) as an example, showing m/z peak which corresponds to the anionic monomer $[M]^-$ actual value from the mass spec to be 359.0339 (red). A symmetrical dimer species is observed $[2M+H^+]^-$ which is x(359.0343) + 1.0073 = 719.0759 (theoretical value), while the actual from the mass spec is 719.0765 (blue) (Figure 26). Another symmetrical dimer species is present for compound **1** $[2M+Na]^-$ which is 2x(359.0343) + 22.9892 = 741.0578 (theoretical) and the actual value from the mass spec is 741.0586 (yellow) (Figure 27).

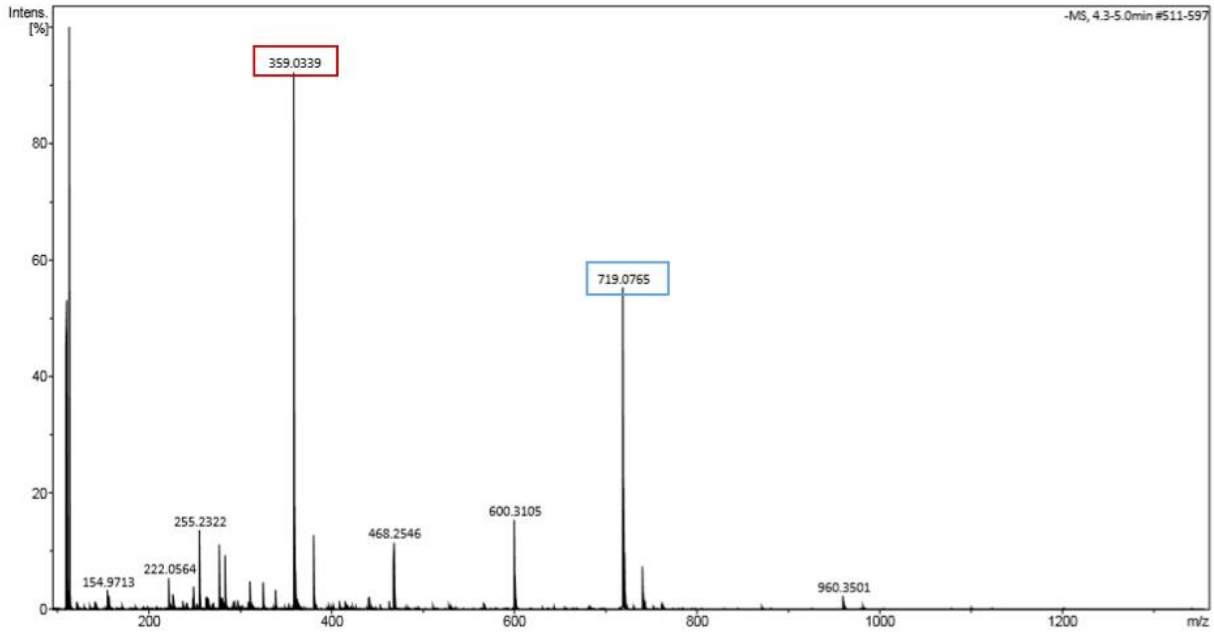

Figure 26: Electrospray mass spectrometry spectra of compound **1** showing both the monomeric (red) and dimer species (blue).

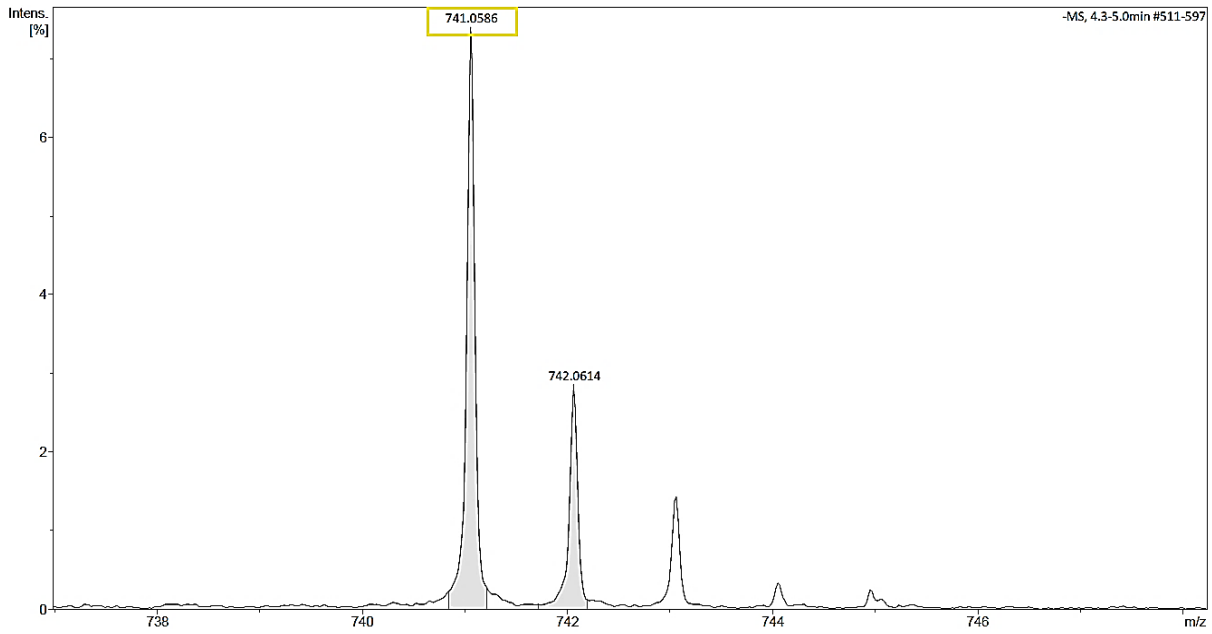

Figure 27: Electrospray mass spectrometry spectra of compound **1** showing both the second dimer species (yellow).

Mixtures of 1:1 of **1**, **2** and **4** were also observed. The one containing **1** and **2** identified the presence of anionic monomer $[M_a]^-$ for **1** at 359.0469 (Figure 28) and a monomer $[M_b]^-$ for **2** at 329.0696 (Figure 28). Along with that, the presence of several unsymmetrical dimer species was determined. One of them is $[M_a+M_b+H]^-$ which is (359.0343 + 329.0602 + 1.0073) = 689.1018 (theoretical) and actual from mass spec at 689.1358 (Figure 28). Second one is $[M_a+M_b+Na]^-$ which is (359.0343 + 329.0602 + 22.9892) = 711.0837 (theoretical) and actual is at 711.1001 (can be seen in appendix Figures S31 and S32). The symmetrical dimer species observed for **1** were $[M_a+M_a+Na]^-$ at 741.0737 (Figure 29) and $[M_b+M_b+Na]^-$ at 719.1045. As for **2**, the presence of a single symmetrical dimer was observed being $[2M_b+Na]^-$ at 681.1333 (Figure 29). This shows that these amphiphiles can form homogeneous dimers, as well as heterogeneous dimers – Table 5. Similar results were observed for the remaining mix of **1** and **4**, **2** and **4.** All remaining ESI-MS -ve spectra and table results can be found in the appendix – Figures S27 – S39 and table S1.

Table 5: An overview of species observed by high resolution mass spectrometry for mixtures containing **1** and **2** in a 1:1 ratio. M_a and M_b represent the anionic component of that amphiphilic salts contained within the mixtures analysed.

Molecular complex	**1** (M_a) + **2** (M_b)	
	Theoretical *(m/z)*	Actual *(m/z)*
$[M_a]^-$	359.0343	359.0469
$[M_b]^-$	329.0602	329.0696
$[M_a+M_b+H]^-$	689.1018	689.1358
$[M_a+M_b+Na]^-$	711.0837	711.1001
$[M_a+M_b+K]^-$	[a]	[a]
$[M_a+M_a+H]^-$	719.0759	719.1045
$[M_a+M_a+Na]^-$	741.0578	741.0737
$[M_a+M_a+K]^-$	[a]	[a]
$[M_b+M_b+H]^-$	[a]	[a]
$[M_b+M_b+Na]^-$	681.1096	681.1333
$[M_b+M_b+K]^-$	[a]	[a]

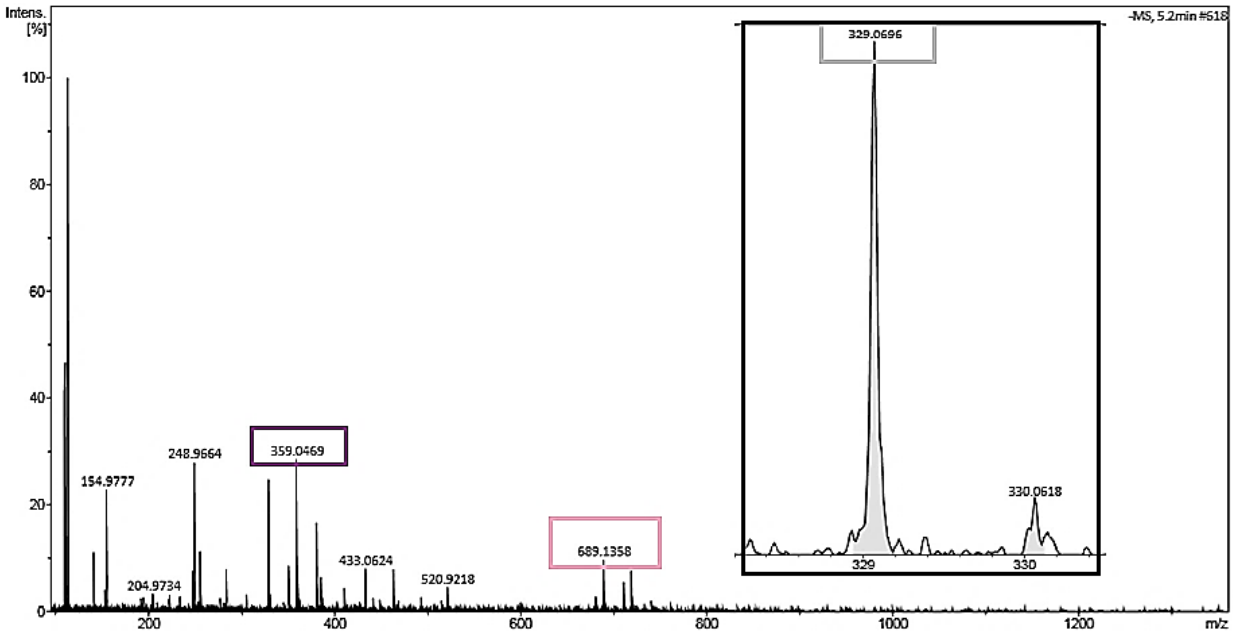

Figure 28: Electrospray mass spectrometry spectra of mix of compound **1** and **2** showing the anionic monomer species of **1** (purple), anionic monomer species of **2** (grey) and the unsymmetrical dimer $[M_a+M_b+H]^-$ of **1** and **2** (pink).

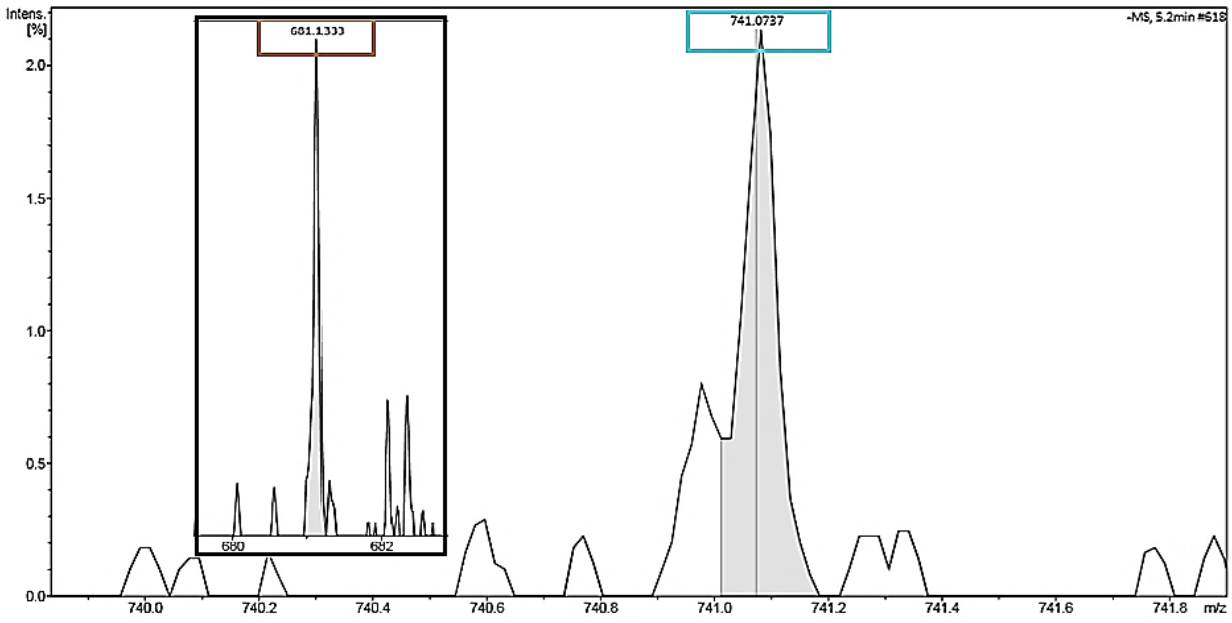

Figure 29: Electrospray mass spectrometry spectra of mix of compound **1** and **2** showing the symmetrical dimers $[M_a+M_a+Na]^-$ for **1** (turquoise) and $[M_b+M_b+Na]^-$ for **2** (brown).

This study confirmed the presence of dimer species in the gas phase, as a result of the non-covalent interactions occurring between the molecules. Unsymmetrical and symmetrical dimer formations were observed. Nevertheless, the stability of these structures cannot be determined in the gas phase, which is why these amphiphiles were also explored in the solution phase.

4.4 Solution phase

In the gas and solid phase, intermolecular binding modes and dimerization species occur in the absence of solvent-solute interactions. That ,however, is not the case in the solution phase, where solvent-solute interactions play an important role in the self-association processes, resulting in aggregate and micelle formation.[2,105] Inverse or reverse aggregates or micelles are also known to form depending on the polarity of the solvent.[106] Example of solvents that contain hydrogen bond acceptor donor group are DMSO and water,[107] where the interactions occur between the protons of the water and the oxygen atom of the DMSO.[108] It is suggested that the self-assembly interactions of these amphiphiles, as well as the nature of aggregates being formed, could be greatly affected by the solvent solutions in which they are observed, as a result of their structural properties (HBA/HBD moieties and electron rich/electron poor components). In order to explore this hypothesis compounds **1**, **2**, **4** and mixtures of **1** and **2**, **1** and **4**, **2** and **4** were looked at in the following solvent solutions, chosen as a result of solubility and comparability – DMSO and EtOH: H_2O (1: 19). A series of experiments were carried out for each solvent system in order to explore the formation of complex aggregate structures, as well as the dimerisaiton processes and structural stability in the solution state.

4.4.1 Dynamic light scattering (DLS) studies

Dynamic light scattering is a well known non–destructive indirect technique used in chemical and biological testing for determining the state of motion of particles, as well as their size.[109] As light beam hits the solution being measured, the Brownian motion of those aggregates in solution causes a change in the intensity of light detected. By measuring the particle motion, the size of the particles can be calculated using the Stokes-Einstein equation (Equation 1).[110]

Equation 1: Stokes-Einstein equation that can be used to determine the hydrodynamic diameter. [110]

$$d\,(\mathrm{H}) = \frac{kT}{3\pi\eta \mathrm{D}}$$

where:

the d (H) – Hydrodynamic diameter

D – Translational diffusion coefficient

k – Boltzmann's constant

T – Temperature

η – Viscosity

The light being scattered during this experiment is affected by the size of the particles.[111] Smaller particles are known to scatter light very weakly, resulting in a signal that by number is proportionally weaker than larger particles.[111] Smaller particles travel faster in solution, compared to bigger ones which are slower. Like any other technique certain limitations of this technique exist, which need to be considered when interpreting the final results.

Some of these for DLS are as follows: hydrodynamic instabilities due to gradients; the limited particle size depends on the viscosity and density; due to the broad distribution a long period of time in order to make the measurements is needed; measuring the hydrodynamic radius of a particle rather than the area diameter.[112] The number of particles cannot be calculated, compared to the signal intensity. The measurement of the diameter of the particle is made by assuming that it has a spherical structure (Figure 30).[113]

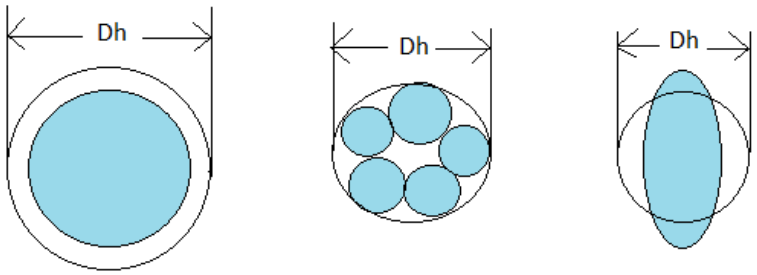

Figure 30: Showing the hydrodynamic diameter (D_h) which is measured by DLS providing the diameter of the sphere diffusing the same way as the particle.[114]

In this study, the average intensity particle size distribution for each of the amphiphiles and mixtures is presented. Intensity was used as there was not sufficient information to calculate number distribution. The self-association processes of compounds **1, 2, 4** and mixtures of **1** and **2**, **1** and **4**, **2** and **4** were observed in both DMSO and EtOH: H_2O (1: 19) solution. Comparable data for compound **2** has been reported by Hiscock and co-workers.[2] All samples underwent a serial dilution process starting from the most concentrated sample. The compounds were observed at concentrations of 55.56 mM and 5.56 mM in DMSO and at concentrations of 5.56 mM and 0.56 mM in EtOH: H_2O (1: 19), as a result of the solubility issues which were encountered, due to the polarity of water. All samples in DMSO were heated to 40° (5 repeats) in order to make sure they had reached thermodynamic stability. After that, each sample was cooled down to 25° (10 repeats).

4.4.1.1 Result and discussion

The data obtained from the analysis was initially presented as correlation curve graphs which helped in observing and establishing the validity of the data. The appearance of the correlation curve aids in determining the stability of the compound and the processes occurring in solution. A smooth reproducible correlation curve, showing the size distribution for all runs measured indicates the reliability of the data. Correlation graphs for compounds **1**, **2**, **4** and mixtures **1** and **2**, **1** and **4**, **2** and **4** were all presented showing the difference in the stability, which in most cases was influenced by the concentration of the sample and compound present. Figures 31–34 illustrate an example of the DLS correlation graphs of compound **1**, showing also the two-stage annealing process carried out at each concentration.

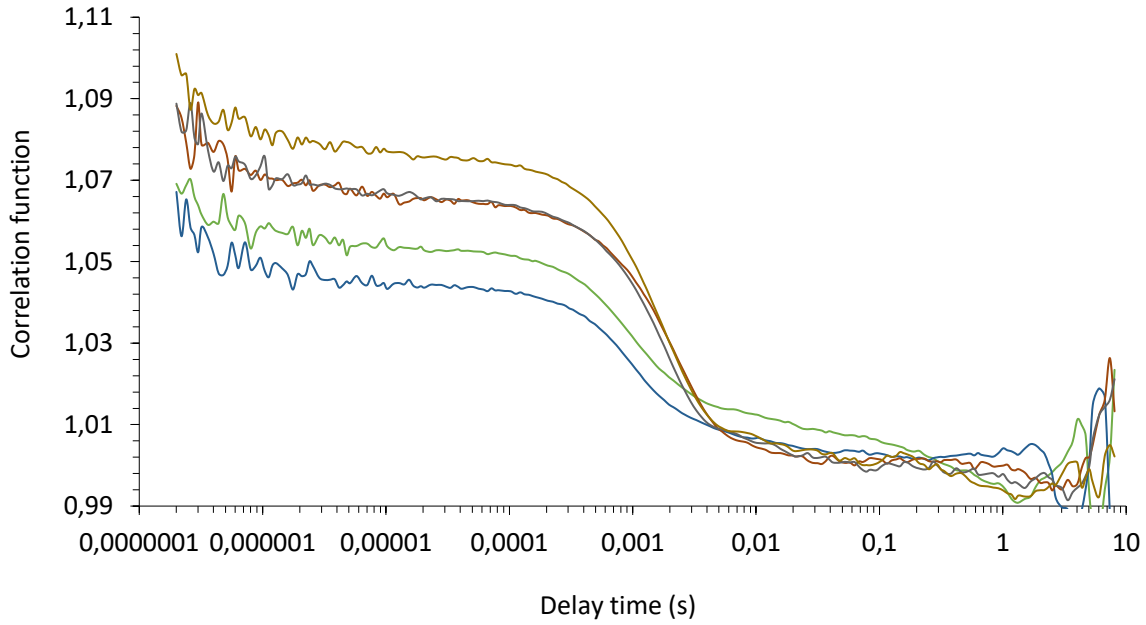

Figure 31: Correlation function data for 5 DLS runs heated up to 40 °C of compound **1** (55.56 mM) in a DMSO solution.

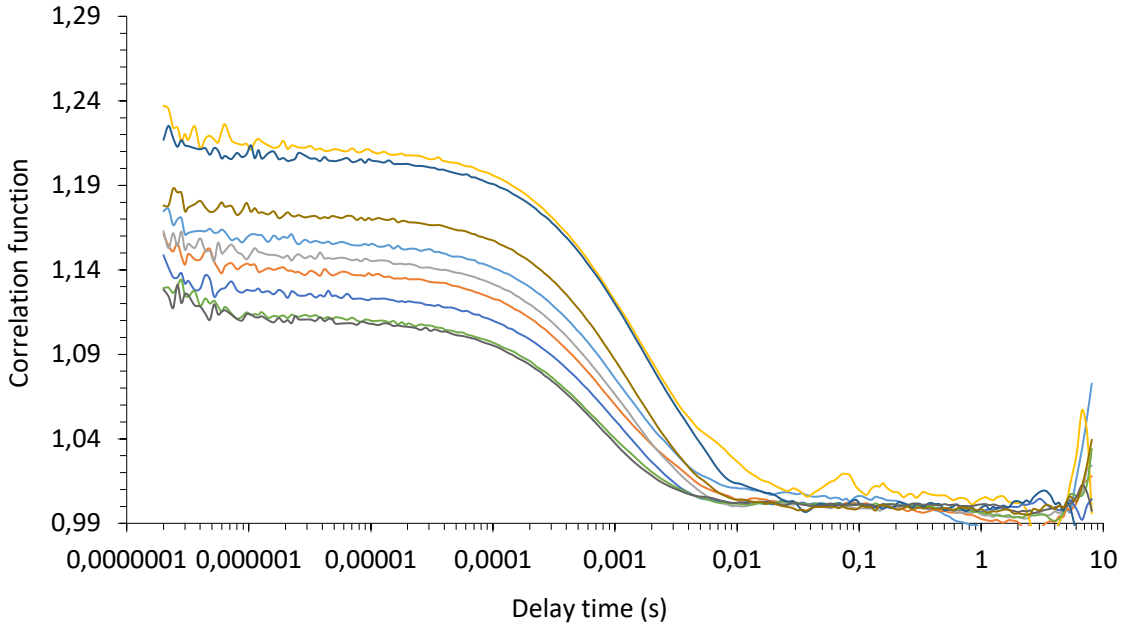

Figure 32: Correlation function data for 10 DLS runs cooled down to 25 °C of compound **1** (55.56 mM) in a DMSO solution.

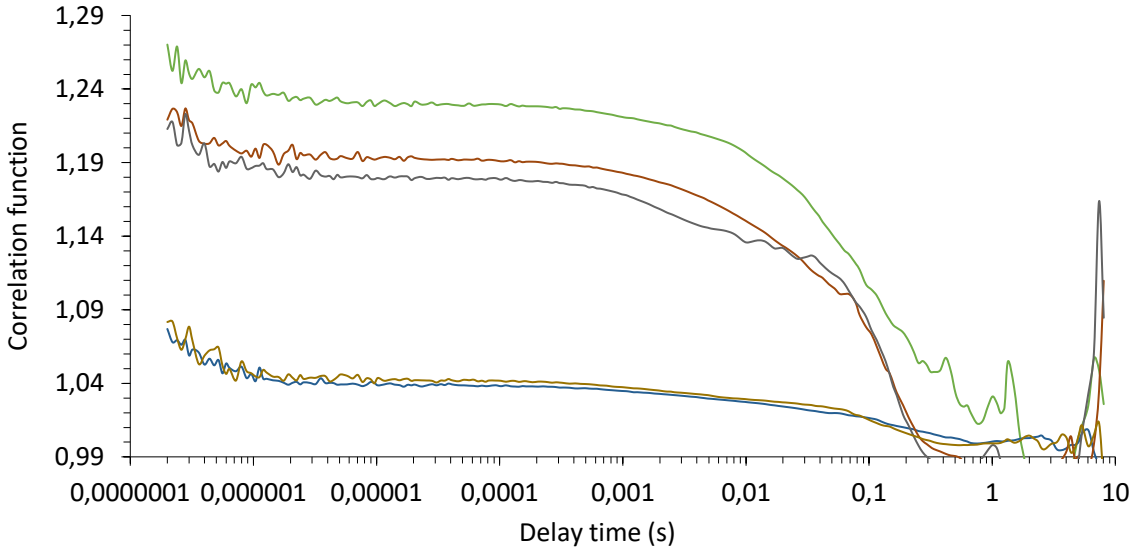

Figure 33: Correlation function data for 5 DLS runs heated up to 40 °C of compound **1** (5.56 mM) in a DMSO solution.

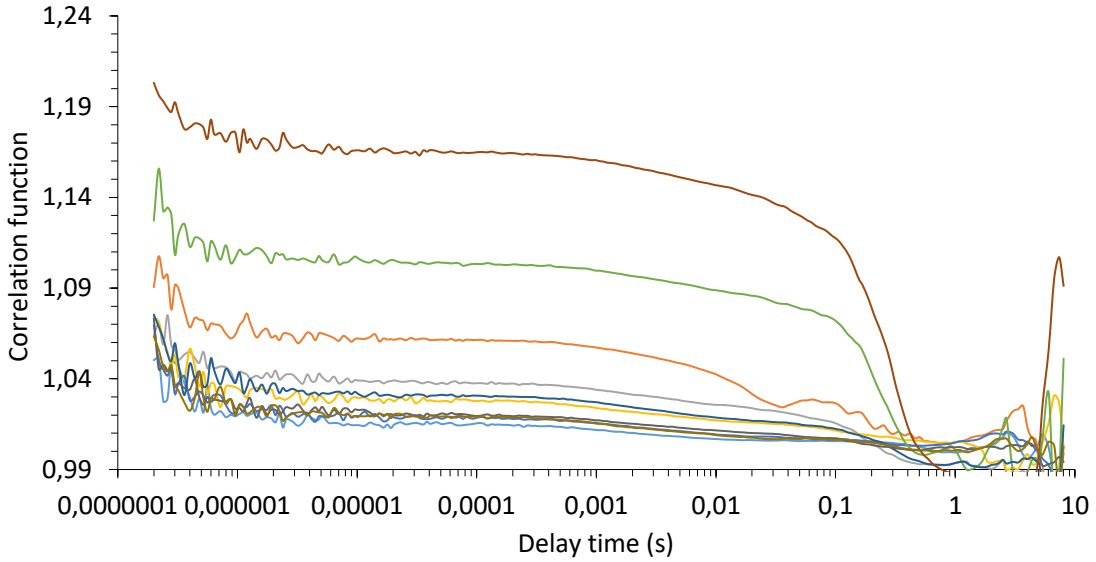

Figure 34: Correlation function data for 10 DLS runs cooled down to 25 °C of compound **1** (5.56 mM) in a DMSO solution.

From the results shown in Figures 31-34, it can be determined that the data for compound **1** is not reliable despite the annealing process. This, therefore, shows that there is little evidence of stable aggregate structures forming for that compound. As a result, the calculated peak maxima values cannot be used. Similar results were observed for compound **2** and mix of **1** and **2** (1:1) at both 55.56 mM and 5.56 mM concentrations. The correlation graphs of compound **4** (Figure 35) and the mixtures containing that compound **1** and **4** (Figure 36), **2** and **4** (Figure 37) showed smoother reproducible correlation curves, meaning that the data is more reliable than that of **1**,**2**, **1** and **2**. This also suggests the presence of bigger aggregate self-associated structures. On the other hand, the results from the calibration graphs for mixtures of **1** and **4** (Figure 36), **2** and **4** (Figure 37) show that the data is not as reliable as the one for compound **4** on its own (Figure 35). This ,however, would be due to the fact that one of the mixtures contains compound **1**, while the other mix contains **2**, both of which showed that they the data for them is not reliable when observed individually or together.

Compound **4**, mix of **1** and **4**, **2** and **4** also shows reliable data at higher concentration (55.56 mM), compared to when they are observed at a lower concentration (5.56 mM) which can be observed from the correlation function graphs in Figure 38–40. All additional graphs can be found in appendix Figures S61 – S74.

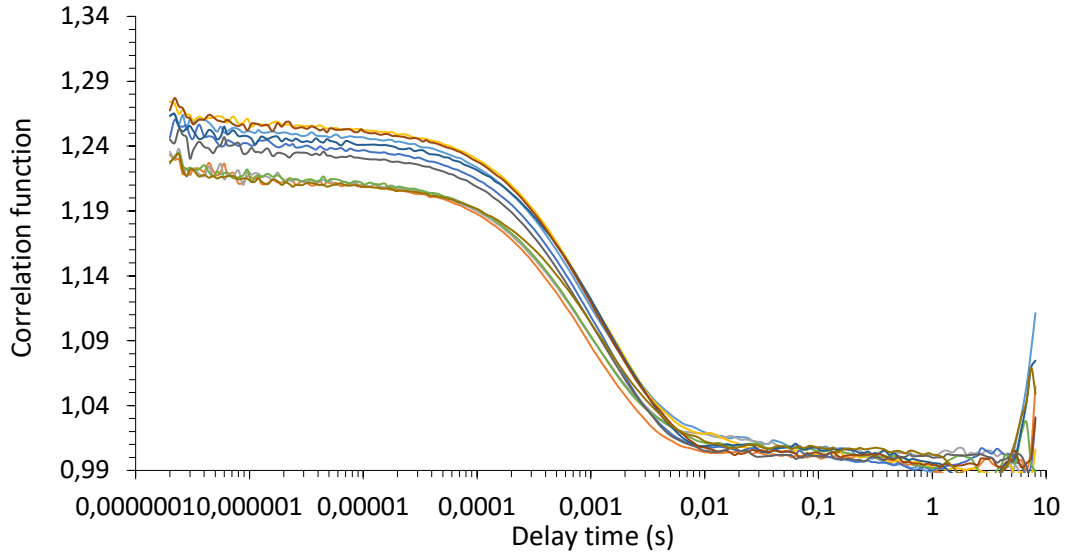

Figure 35: Correlation function data for 10 DLS runs cooled down to 25 °C of compound **4** (55.56 mM) in a DMSO solution.

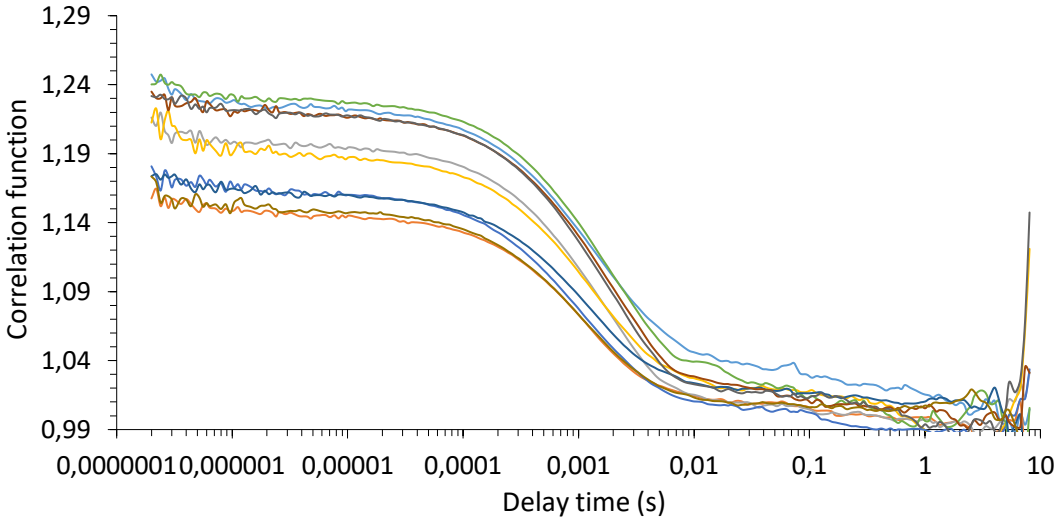

Figure 36: Correlation function data for 10 DLS runs of compounds **1** and **4** in a 1:1 mix (total concentration 55.56 mM) cooled down to 25 °C of in a DMSO solution.

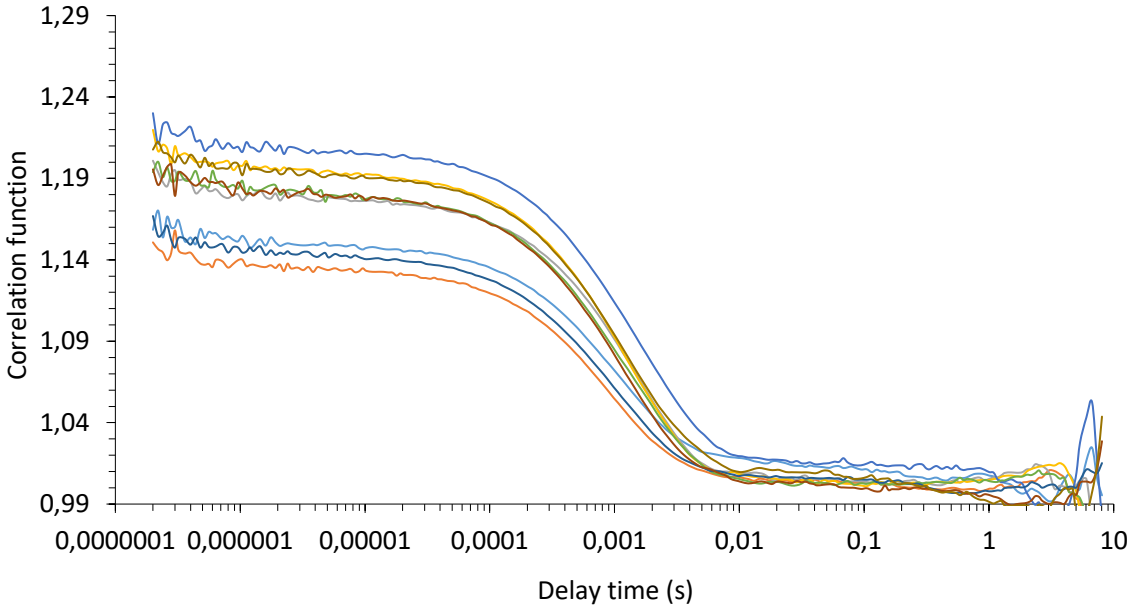

Figure 37: Correlation function data for 10 DLS runs of compounds **2** and **4** in a 1:1 mix (total concentration 55.56 mM) cooled down to 25 °C of in a DMSO solution.

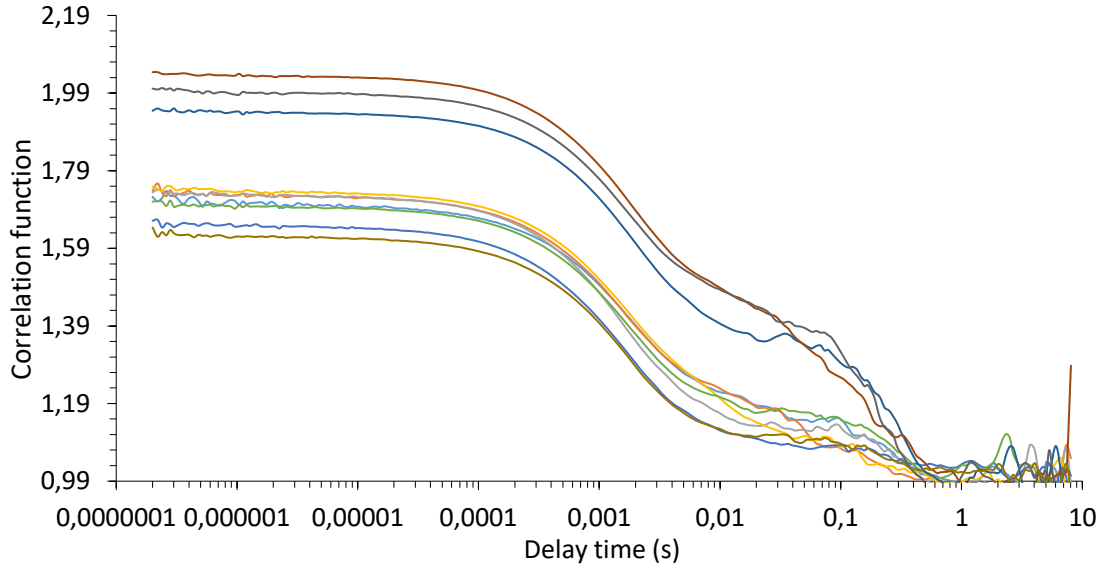

Figure 38: Correlation function data for 10 DLS runs cooled down to 25 °C of compound **4** (5.56 mM) in a DMSO solution.

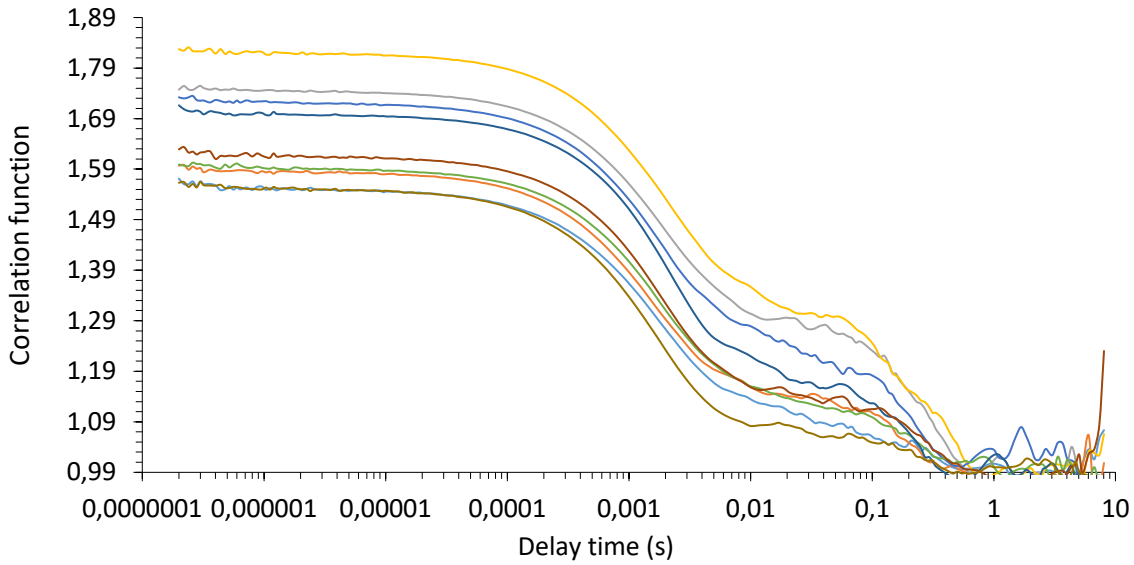

Figure 39: Correlation function data for 10 DLS runs of compounds **1** and **4** in a 1:1 mix (total concentration 5.56 mM) cooled down to 25 °C of in a DMSO solution.

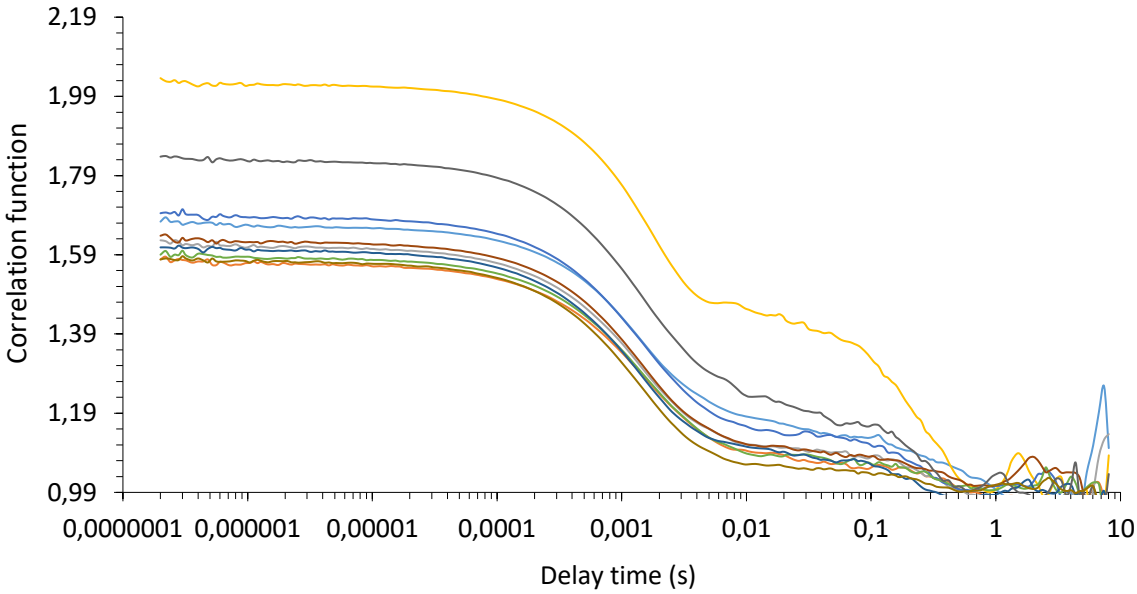

Figure 40: Correlation function data for 10 DLS runs of compounds **2** and **4** in a 1:1 mix (total concentration 5.56 mM) cooled down to 25 °C of in a DMSO solution.

The DLS data for the average intensity size distribution for compound **4**, mix of **1** and **4**, **2** and **4** showed particles with a hydrodynamic diameter ranging between 400 – 500 nm, with the peak maxima for compound **4** being 436 nm (Figure 41), mix of **1** and **4** being 496 nm (Figure 42), mix of **2** and **4** being 404 nm (Figure 43) at the higher concentration showing a reliable set of data. From the results in Table 6, the average polydispersity index which is used in measuring the distribution of the self-associated structures in solution can be observed to be 27% for compound **4**, 26% for mix of **1** and **4**, 27% for mix of **2** and **4**. From the results, the difference in the size and the error occurring at 5.56 mM can be observed, which shows that as the concentration of the sample decreases the hydrogen bond network of the structures destabilise, thus results in increasing their size significantly. This shows that the data obtained at 5.56 mM is unreliable. The rest of the size distribution graphs for the DLS studies in DMSO can be found in the appendix Figures S40 – S60.

Table 6: Showing the average intensity particle size distribution values for compounds **4** and mixtures **1** and **4**, **2** and **4** calculated using 10 DLS runs in DMSO at concentrations of 55.56 mM and 5.56 mM at 25 °C. The samples were initially heated up to 40 °C and then cooled down to 25 °C. Samples were prepared in series, with an aliquot of the most concentrated solution undergoing serial dilution.

* - data obtained determined to be unreliable

	DMSO		
Amphiphile	Concentration (mM)	Peak maxima (nm)	Polydispersity (%)
4	55.56	436 (± 23.15)	27 (± 0.91)
	5.56*	1688 (± 1405.66)*	31 (± 3.52)*
1 and **4**	55.56	496 (± 21.39)	26 (± 1.06)
	5.56*	1678 (± 1462.82)*	29 (± 2.51)*
2 and **4**	55.56	404 (± 23.04)	27 (± 0.72)
	5.56*	1471 (± 1280.51)*	33 (± 6.28)*

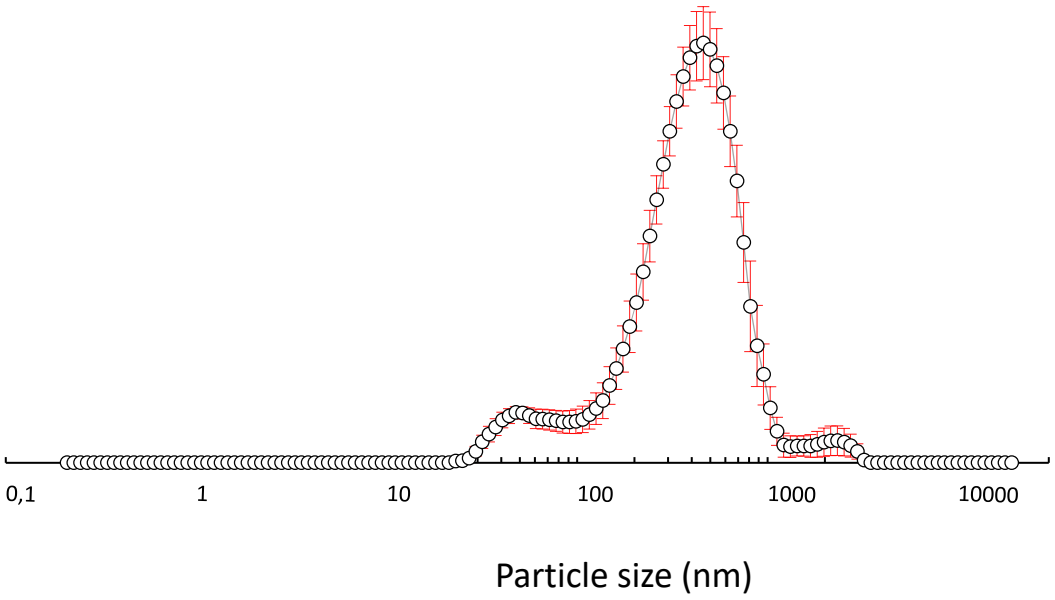

Figure 41: Particle size distribution for 10 DLS runs cooled down to 25 °C of compound **4** (55.56 mM) in a DMSO solution.

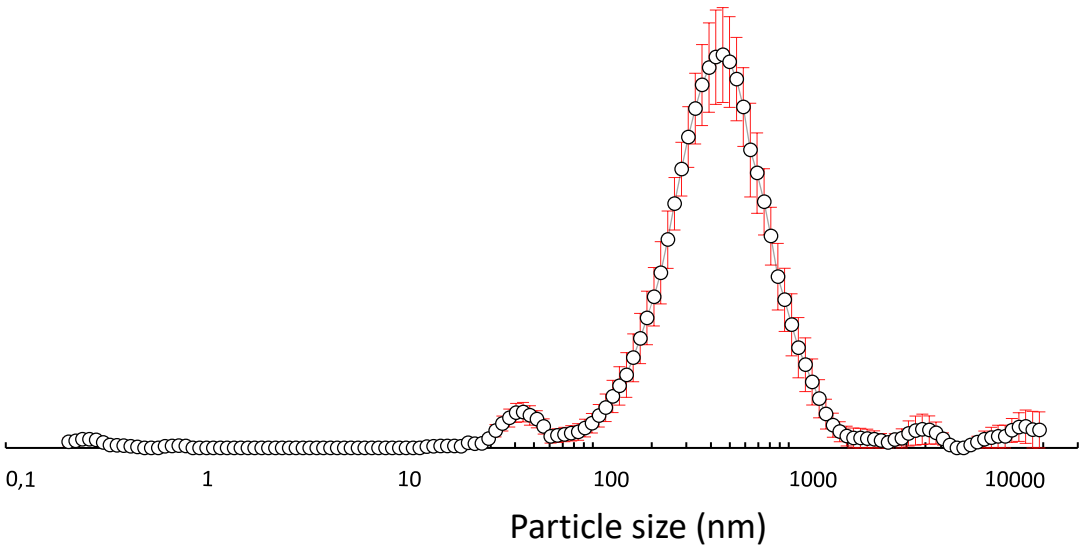

Figure 42: Particle size distribution for 10 DLS runs of compounds **1** and **4** in a 1:1 mix (total concentration 55.56 mM) cooled down to 25 °C of in a DMSO solution.

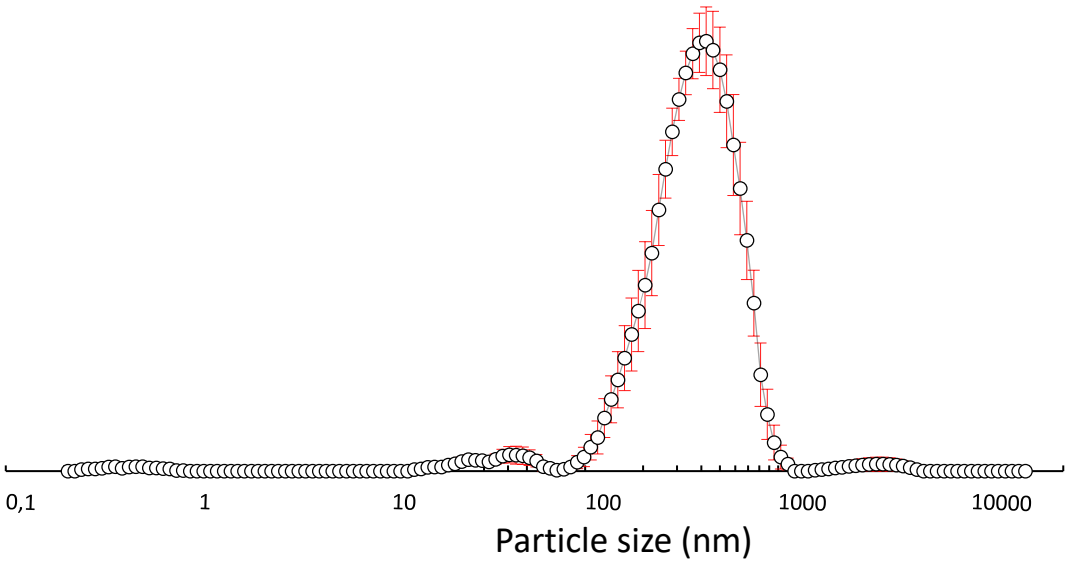

Figure 43: Particle size distribution for 10 DLS runs of compounds **2** and **4** in a 1:1 mix (total concentration 55.56 mM) cooled down to 25 °C of in a DMSO solution.

Moving into the EtOH: H_2O (1:19) solvent environment. The hydrodynamic diameter of the aggregates for all amphiphiles and mix of **1** and **4, 2** and **4** observed in Table 7 ranges between 100 – 350 nm, apart from mix **1** and **2** at 5.56 mM which could not be analysed due to solubility barrier. From the data presented in Table 7, a comparison can be made between the concentrations and the particle size. The size of the aggregates can be observed at both concentration of 5.56 mM and 0.56 mM for compounds **1** (142 and 124 nm, with a polydispersity being 27–18%), **2** (209 and 198 nm, with polydispersity being 22-16%) and mix **1** and **4** (288 and 275 nm, with polydispersity being 24-25%) does not change intensively, which would indicate that the structures remain stable. The opposite, however, can be seen occurring for compound **4** (217 nm and 324 nm, with polydispersity being 23-27%) and mix 1:1 containing **2** and **4** (155 and 193 nm, with polydispersity being 22-27%) where the average size of the structures increases as the concentration decreases to 0.56 mM. This would indicate an alteration in the size of the species being formed.

This is hypothesised to be due to reduced aggregate stability with regards to the concentration (Table 7), as the structures become more diffuse and dynamic in nature. This lack of stability could be attributed due to the mixture of only anthracene + anthracene based amphiphiles which would explain the results obtained for mix containing compound **2** and **4**. This can be compared to the mixture containing compound **1** and **4**, where the mixture is composed of electron poor (anthraquinone) and electron rich (anthracene) based amphiphiles. This suggests that an increase in the stability of the self-associated structures can be obtained as a result of the pairing of electron rich and electron poor systems. This is not possible when there is only anthracene + anthracene pairing. When looking at the stable structure formation for individual compounds, more specifically compound **2** and **4,** a significant difference can be seen, showing that the sulphonate binding mode for compound **2**, when observed individually is more stable, compared to compound **4** where less stable structure formation is observed. The same is established when they are observed in a mixture together, which would suggest that the main reason for stable structure formation would be the presence of both an electron rich and electron poor system combined with the presence of the sulfonate moiety. These results were compared to complementary microscopy studies in this solvent environment in order to directly visualise the aggregates being formed. The particle size distribution and correlation function graphs for the compounds in EtOH: H_2O (1:19) can be observed in the appendix Figures S75 – S98.

Table 7: Summary of average intensity particle size distribution data in EtOH: H_2O (1:19) solutions of **1**, **2**, **4** and associated 1:1 mixture. Error = standard error of the mean.

Compound	Concentration (mM)	Peak maxima (nm)	Polydispersity (%)
1	5.56	142 (± 1.49)	27 (± 0.67)
	0.56	124 (± 1.54)	18 (± 1.21)
2	5.56	209 (± 2.90)	22 (± 0.44)
	0.56	198 (± 3.83)	16 (± 2.52)
4	5.56	217 (± 2.74)	23 (± 0.39)
	0.56	324 (± 14.23)	27 (± 0.50)
1 + **2**	5.56	[a]	[a]
	0.56	224 (± 7.87)	26 (± 1.16)
1 + **4**	5.56	288 (± 4.69)	24 (± 0.52)
	0.56	275 (± 7.48)	25 (± 0.99)
2 + **4**	5.56	155 (± 2.13)	22 (± 0.73)
	0.56	193 (± 2.73)	27 (± 0.65)

4.4.2 ^{1}H NMR studies

A series of ^{1}H NMR studies were carried out in order to explore the molecular binding characteristics of our novel molecules: DOSY,[115] quantitative ^{1}H NMR studies (DCM spiking and 5% EtOH: D_2O),[116] dilution studies[117] and titration studies. The results obtained from the DLS experiment in DMSO play an important role alongside the data obtained from the NMR studies in observing the structures being formed in the solution state.

From the DLS studies, it was established that there was little evidence for the formation of stable large aggregate structures for **1**, **2** and mix of **1** and **2** in DMSO, as the data was established to be unreliable. On the other hand, the DLS results for compound **4**, mix of **1** and **4,** mix of **2** and **4** showed the formation of these self-associated large aggregate structures in DMSO with a hydrodynamic diameter ranging between 400 - 500 nm. The DOSY study was carried out at a comparable concentration to the DLS studies (55.56 mM) in order to determine the size of the structures being formed in solution. An important factor which must be taken into account is that the size of these structures, similar to the DLS, could potentially be bigger and may not be able to be observed fully by NMR spectrum.[118] Which is why a series of quantitative ^{1}H NMR studies (DCM doping studies) were carried out alongside the DOSY experiments in order to determine the amount of compound present in the solution which can be observed by the NMR spectrum. Compounds **1**, **2** and mix of **1** and **2** (55.56 mM of **1** and 55.56 mM of **2**) were observed at a concentration of 111.12 mM (0.500 mL) in a DMSO-d_6 solution. Due to solubility problems compound **4**, mix of **1** and **4** (27.78 mM of **1** and 27.78 mM of **4**), mix of **2** and **4** (27.78 mM of **2** and 27.78 mM of **4**), were all observed at a concentration of 55.56 mM (0.500 mL) in DMSO-d_6. Each of the samples was doped with 5 µL of DCM. The compounds were weighted out in the NMR tubes in order to ensure the accuracy of the experiment. A second study similar to the DCM doping one was carried out for all amphiphiles and mixtures in 5% EtOH: D_2O at a concentration of 5.56 mM (**1**, **2** and **4**) and 1:1 for all mix (2.78 mM of one compound and 2.78 mM of the other)**.** Each of the samples was spiked with 25 µL of EtOH. The solvent system used was comparable to the one used in the microscopy and DLS studies. Because H_2O cannot be used in NMR studies, D_2O was used instead. Along with that a series of dilution and titration studies were carried out in order to explore the molecular self-association interactions of the individual amphiphiles.

4.4.2.1 Result and discussion

From the data for compound **1** – DMC spiking in DMSO-d_6 (Figure 44) by comparing the peak integrations of the sulphonate-urea CH_2 and the aromatic CH with that of the DCM signal (Figure 44) it was established that there was no loss of compound from the solution. Because the NMR spectrum is able to observe the entire compound, it is suggested that there are no extended aggregate structures being formed, thus the entire compound remains in the solvent state. This was also confirmed by the DLS data (at a comparable concentration of 55.56 mM, where it was established that large aggregate structures cannot be observed. Similar results were observed for both compound **2** and mix of **1** and **2**, which showed no apparent loss of compound, confirming that extended aggregates are not present. The graphs can be found in the appendix Figures S99 and S100.

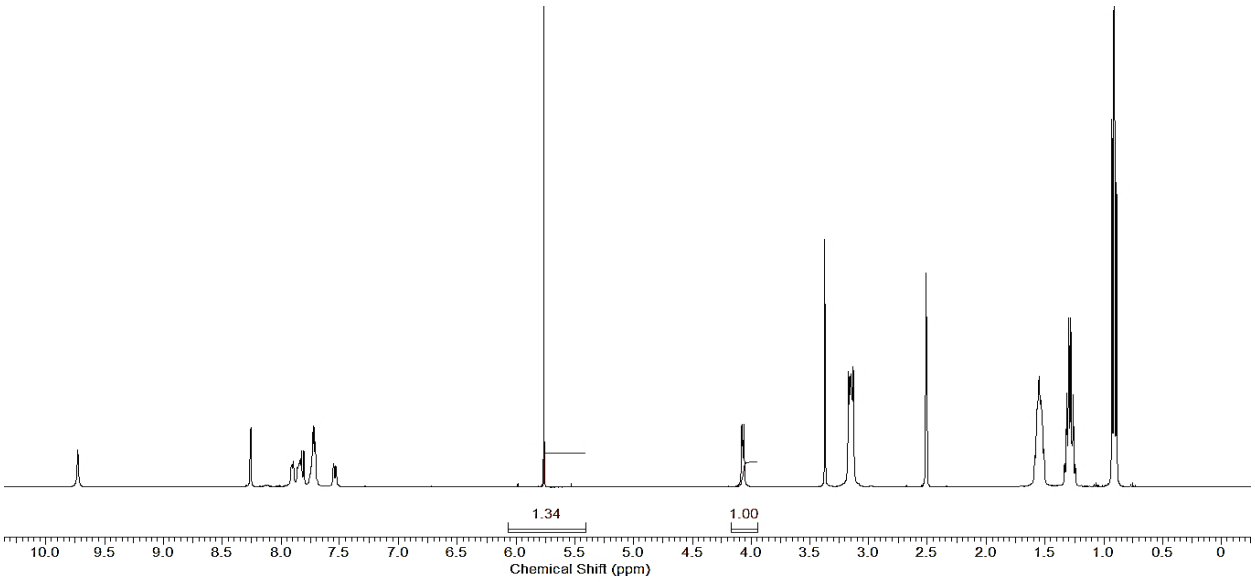

Figure 44: A ^{1}H NMR spectrum of compound **1** (33.50 mg, 0.055 mM) in a solution of DMSO-d_6 (0.495 mL) and dichloromethane (5 µl, 0.078 mM) with a delay (d_1 = 60 s). No apparent loss of compound observed.

On the other hand, this was not the case for compound **4** and the mixtures of **1** and **4**, **2** and **4**, analysed using the same conditions, where an apparent loss of compound was observed. For compound **4** there was a 15% sample reduction at a concentration of 55.56 mM, calculated upon integration comparison (Figure 45). The loss of compound indicates the formation of large aggregate structures. It also suggested that they cannot be fully detected and observed by the NMR spectrum, due to the fact that these structures are formed tumble too slowly because of their size so they appear solid, while the remaining compound remains in the solution state. For compound **4** it was determined that only 15% of the amphiphile is part of these extended aggregate self-assembly species, while the remaining 85% of the compound remains in the solution state and is visible by the NMR spectrum. The same results were established for both mixtures containing compound **4**. With a 56% total loss of compound (of equal ratio in the solution), calculated upon integration comparison observed for **1** and **4** (Figure 46) and 50% compound loss calculated for **2** with **4** (Figure 47). This suggested the formation of extended solid-state aggregate structures, consisting of both compounds in equal amounts, being formed, thus not visible by the NMR spectrum. The remaining equal amount of compound, for both mix, remains in the solution state and can be observed by the NMR spectrum.

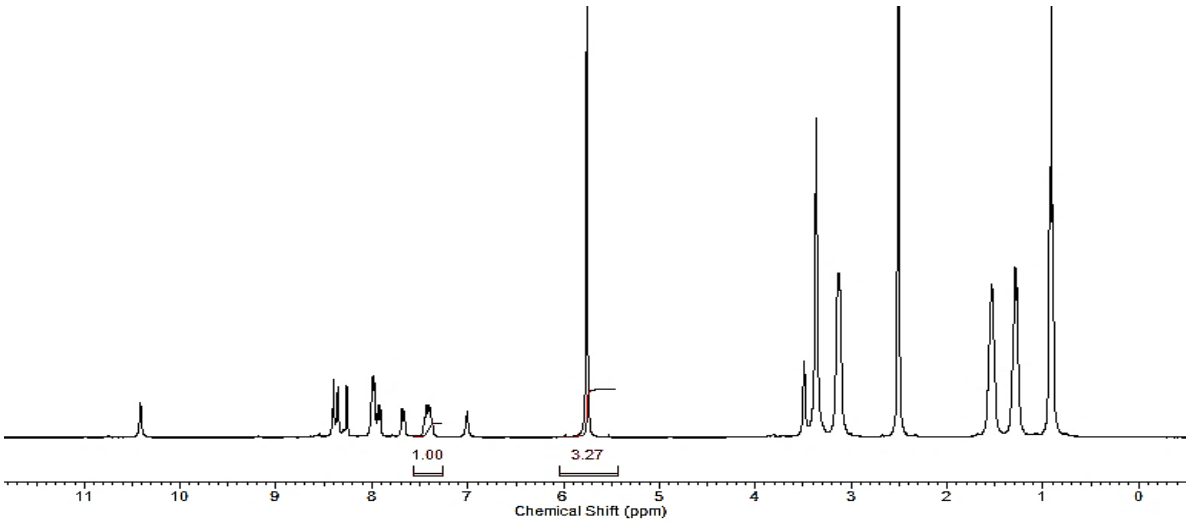

Figure 45: A ^{1}H NMR spectrum of compound **4** (14.98 mg, 0.028 mM) in a solution of DMSO-d_6 (0.495 mL) and dichloromethane (5 µl, 0.078 mM) at with a delay (d_1 = 60 s). The experiment was carried out at a lower concentration due to solubility problems. A 15% reduction of compound was observed upon integration comparison.

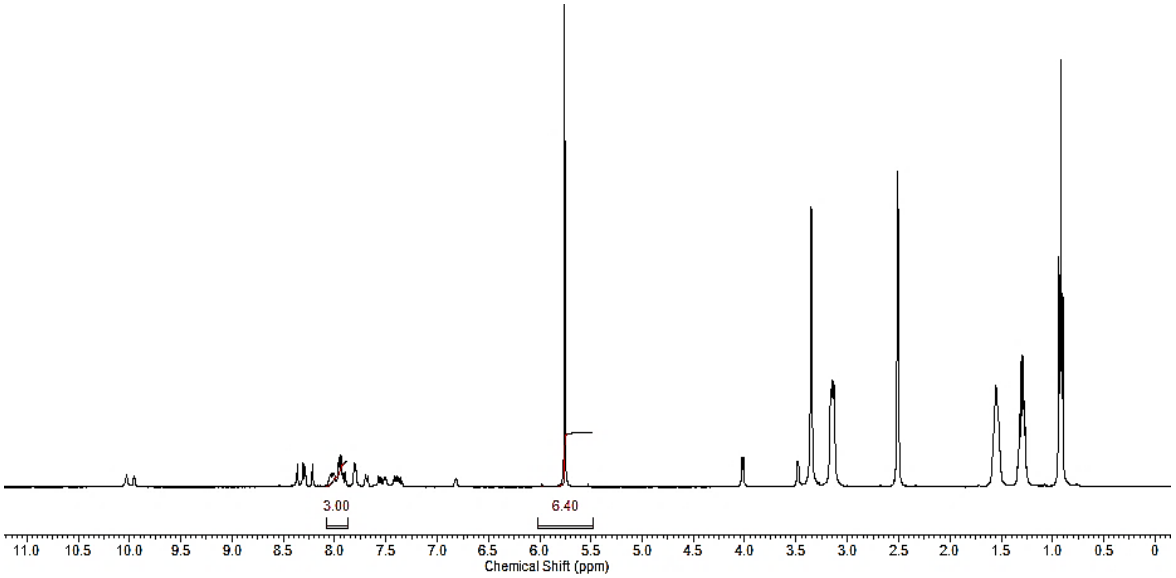

Figure 46: A ^{1}H NMR spectrum of compound **1** (8.40 mg, 0.014 mM) and **4** (7.54 mg, 0.014 mM) (both together 15.94 mg, 0.028 mM) in a solution of DMSO-d_6 (0.495 mL) and dichloromethane (5 µL, 0.078 mM) solution with an extended delay (d_1 = 60 s). The experiment was carried out at a lower concentration due to solubility. A 56% reduction of compound was observed upon comparative integration.

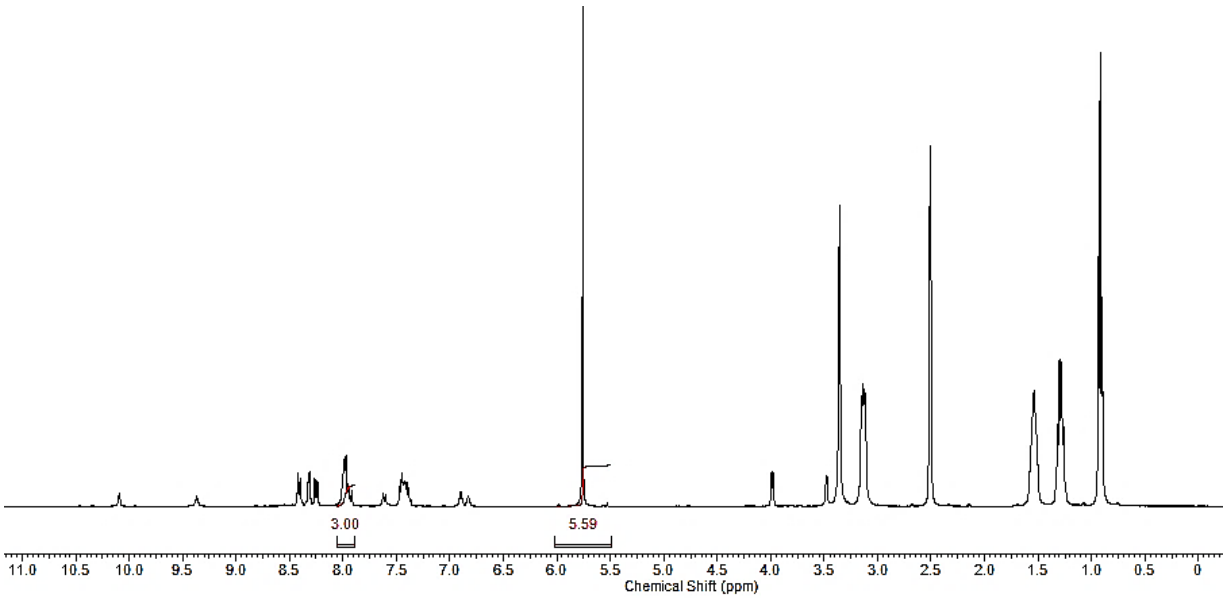

Figure 47: A ^{1}H NMR spectrum of compound **2** (7.95 mg, 0.014 mM) and **4** (7.40 mg, 0.014 mM) (both together 15.35 mg, 0.028 mM) in a solution of DMSO-d_6 (0.495 mL) and dichloromethane (5 µL, 0.078 mM) solution with an extended delay (d_1 = 60 s). The experiment was carried out at a lower concentration due to solubility. A 50% reduction of compound observed upon comparative integration.

From the results obtained from the EtOH: D_2O solvent environment, upon peak integration of the EtOH signal and the main molecule, it was established that there was an apparent loss of compound at a total concentration of 5.56 mM observed for all individual amphiphiles and mixture combinations. For individual compounds **1**, **2** and **4**, a 34%, 77% and 92% loss of compound was observed upon integration comparison respectively (Figure 48 – 50). This shows that in the cases for compound **2** and **4** more than half of the amphiphile is used in the formation of these extended molecular species, with only 23% and 8% of the amphiphile being visible via the NMR spectrum. As for the mixtures at 5.56 mM and 1:1 (equal ratio in the solution) the following loss of sample was observed – for **1** and **2** a 95%, for **1** and **4** a 65%, for **2** and **4** a 94% respectively (Figure 51 – 53). An apparent compound reduction can be seen for the mixtures. This suggests that greater quantities of these molecules are incorporated into the extended molecular structures, due to symbiotic processes occurring between the individual amphiphilic salts in the mixtures, thus the remaining 5%, 35% and 6% compound remains in the solution state and can be seen by the NMR technique.

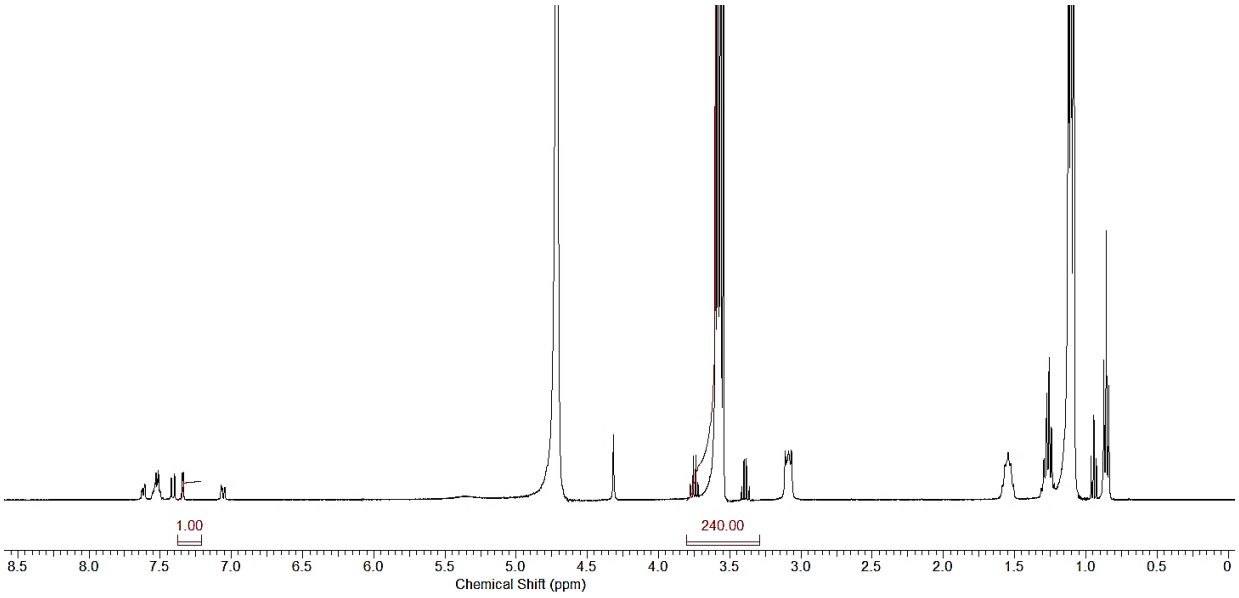

Figure 48: A ^1H NMR spectrum of compound **1** (1.65 mg, 0.0027 mM) in a solution of ethanol (25 µl, 0.43 mM) and D_2O (0.475 mL). A 34% reduction of compound was observed upon integration comparison.

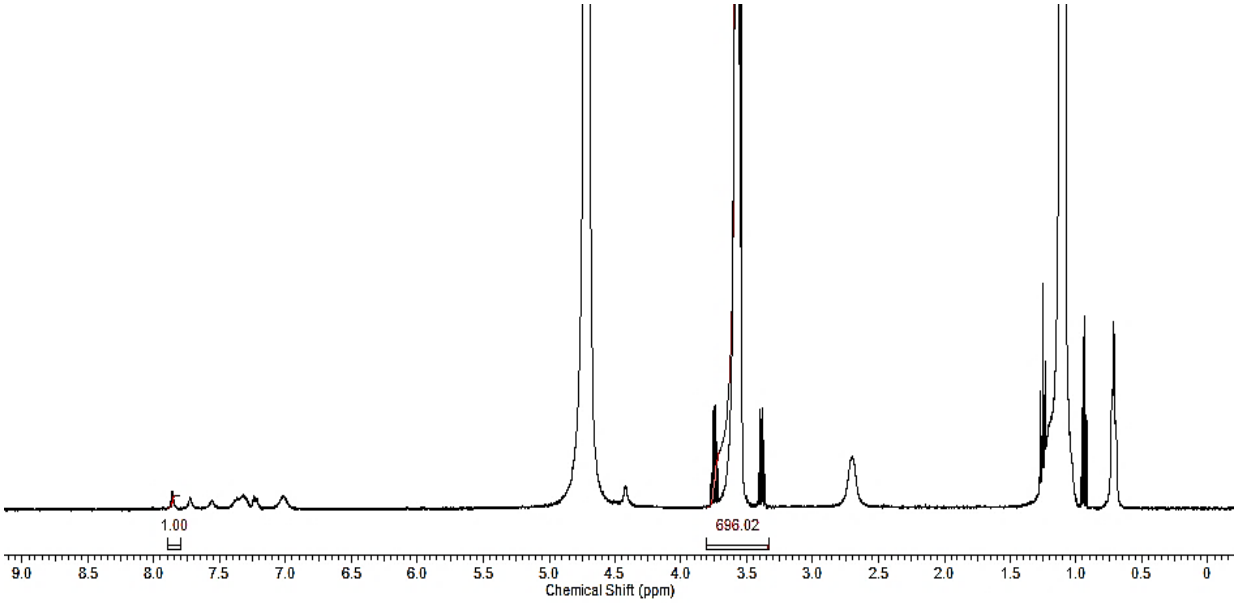

Figure 49: A ^{1}H NMR spectrum of compound **2** (1.57 mg, 0.0027 mM) in a solution of ethanol (25 µl, 0.43 mM) and D_2O (0.475 mL). A 77% reduction of compound was observed upon integration comparison.

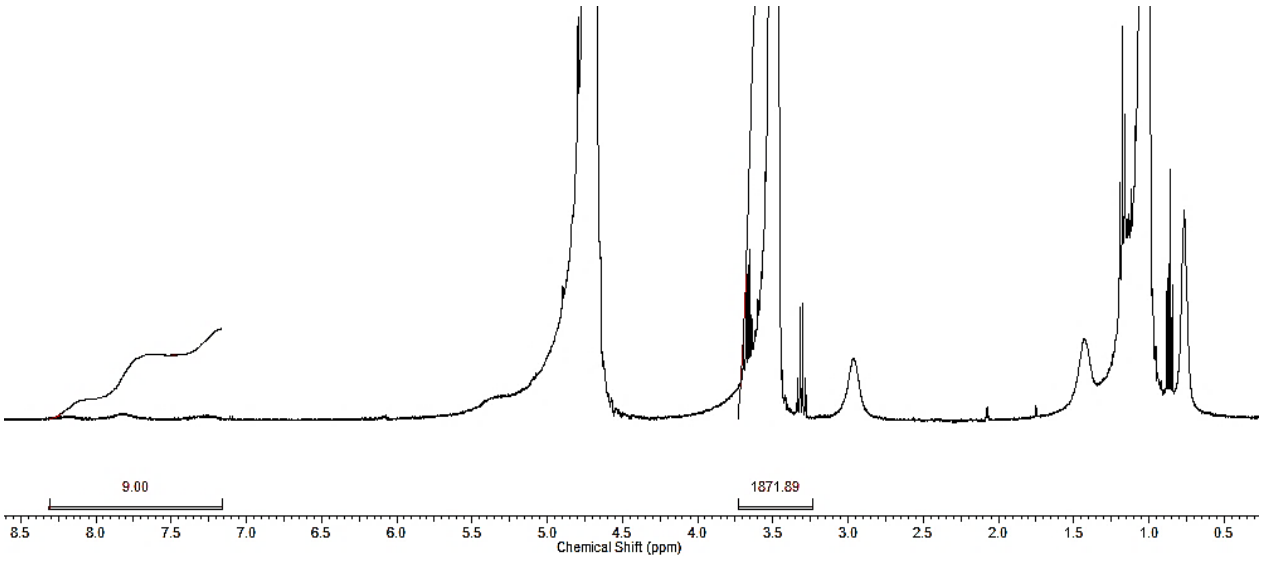

Figure 50: A ^{1}H NMR spectrum of compound **4** (1.51 mg, 0.0028 mM) in a solution of ethanol (25 µl, 0.43 mM) and D_2O (0.475 mL). A 92% reduction of compound was observed upon integration comparison.

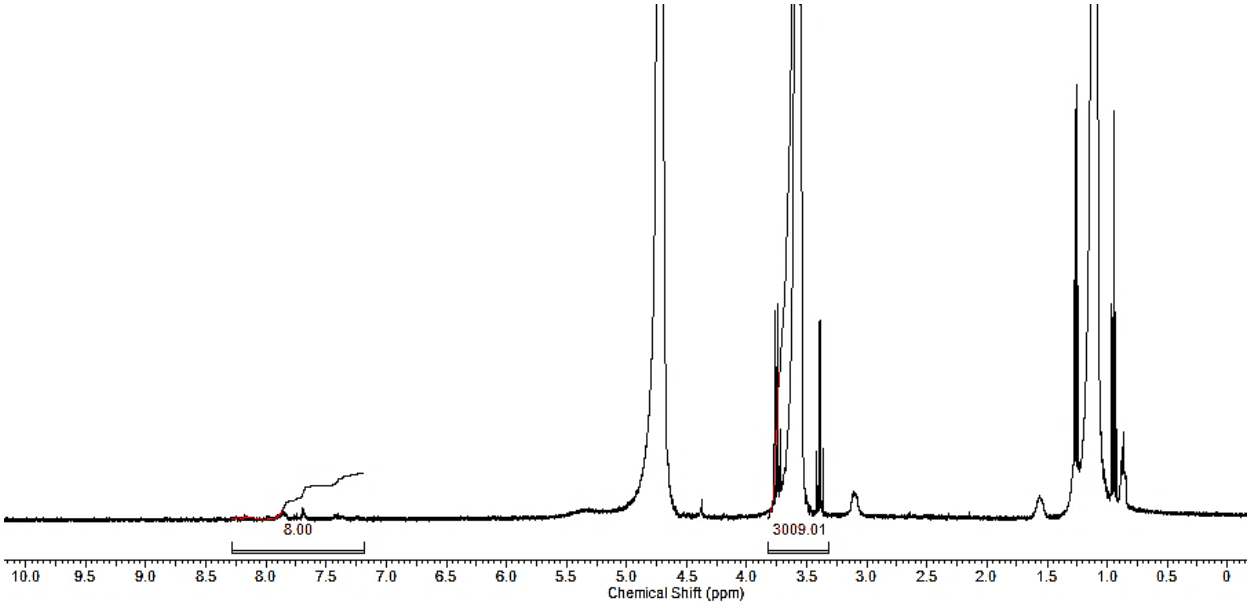

Figure 51: A ^{1}H NMR spectrum of compound **1 and 2** (mix) with compound **1** (0.89 mg, 0.0015 mM) and compound **2** (0.78 mg, 0.0014 mM) (both together 1.68 mg, 0.0029 mM) in solution of ethanol (25 µl, 0.43 mM) and D_2O (0.475 mL). A 95% reduction of compound was observed upon integration comparison.

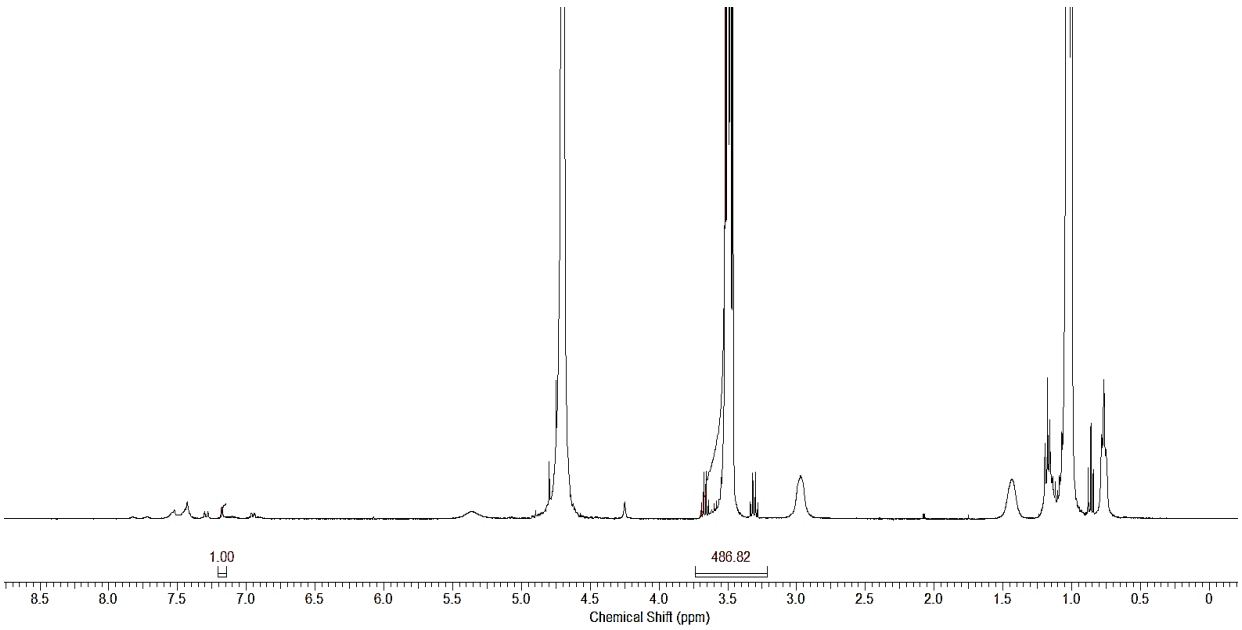

Figure 52: A ^{1}H NMR spectrum of compound **1 and 4** (mix) with compound **1** (0.84 mg, 0.0014 mM) and compound **4** (0.74 mg, 0.0014 mM) (both together 1.58 mg, 0.0028 mM) in a solution of ethanol (25 µl, 0.43 mM) and D_2O (0.475 mL). A 68% reduction of compound was observed upon integration comparison.

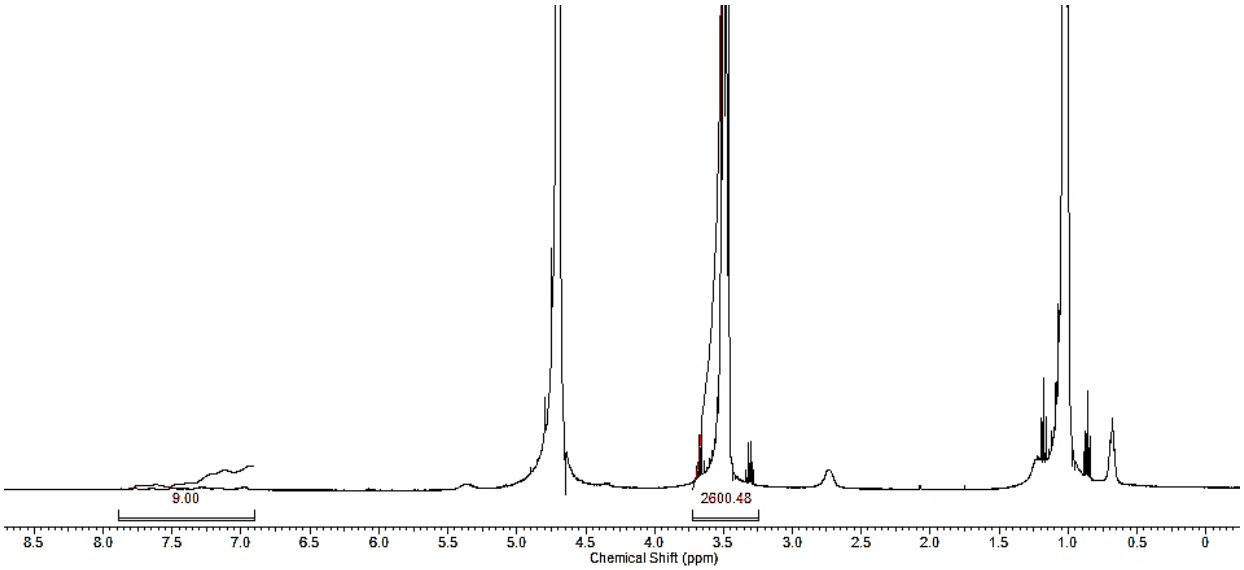

Figure 53: A ^{1}H NMR spectrum of compound **2 and 4** (mix) with compound **2** (0.75 mg, 0.0013 mM) and compound **4** (0.72 mg, 0.0013 mM) (both together 1.47 mg, 0.0026 mM) in a solution of ethanol (25 µl, 0.43 mM) and D_2O (0.475 mL). A 94% reduction of compound was observed upon integration comparison.

The ^{1}H DOSY studies were carried out in order to explore the size of the structures being formed mainly for compounds **1**, **2** and mix 1:1 of **1** and **2**. This experiment was not concluded for compound **4**, mix of **1** and **4**, **2** and **4**, due to the inability to observe the entire mass of the compound by NMR spectrum, also confirming that the aggregate species being formed are too big and cannot be measured via this study. This was supported by results obtained in the quantitative ^{1}H NMR studies. The ^{1}H DOSY experiments carried out for **1**,**2** and mix of **1** and **2**, show that the TBA cation does not move at the same speed as the sulphonate-urea anion, meaning that they both have different diffusion constants. This proves that these two species do not coordinate strongly in a DMSO solution.[2] The diffusion constant calculated in the experiment was used to determine the hydrodynamic diameter of the anion structure by the Stokes-Einstein equation (Equation 1 – DLS studies).[2,119] The hydrodynamic diameter calculated for the sulphonate-urea anion of compound **1** was determined to be 1.39 nm at a concentration of 55.56 mM (Figure 54).

The hydrodynamic diameter of compound **2** was 1.26 nm, whereas for the mix of **1** (1.41 nm) and **2** (1.31 nm) at the same concentration, suggesting that the anionic substituent of these amphiphiles exist in the form of monomers or dimers in the solutions. This confirms that there are no large aggregate structures being formed in the solution state, which was also determined by the quantitative ^{1}H NMR (DCM doping) studies and the DLS studies carried out for this group of amphiphiles **1**, **2**, mix of **1** and **2**. To summarise, quantitative ^{1}H NMR studies were performed in order to confirm that all of the compound dissolved into the solution was visible using this technique, as large aggregates may tumble too slowly within the solution to be observed by this method. After confirming that the compound is fully visible in DMSO-d_6 via the quantitative NMR experiments the size of the structures was then determined through the DOSY studies in DMSO-d_6. However, this is not the case for EtOH: H_2O (1:19), as the total concentration of compound was not fully visible in that solvent environment, due to the size of those aggreges produced being too large to be observed using this technique. As a result, the DLS studies were also carried out in order to determine the size of those larger nanostructures present in solution. The different solutions were used in order to stabilise the different nanostructures. The different self-associated structures are supported by different solvents – in DMSO-d_6 there are dimers and monomers, which were observed by NMR spectrum and their size was determined using the DOSY technique, whilst in EtOH: H_2O (1:19) the bigger self-associated structures were observed by the DLS studies and visualised via Fluorescence microscopy. This is why the size for the structures carried out in DMSO-d_6 (for the ^{1}H NMR studies and DOSY studies) are so different from those observed in EtOH: H_2O (1:19) solution in the DLS studies. This is due to the fact that the different structures are studied in two different solvent environments. The remaining DOSY graphs can be found in the appendix Figures S101 and S102.

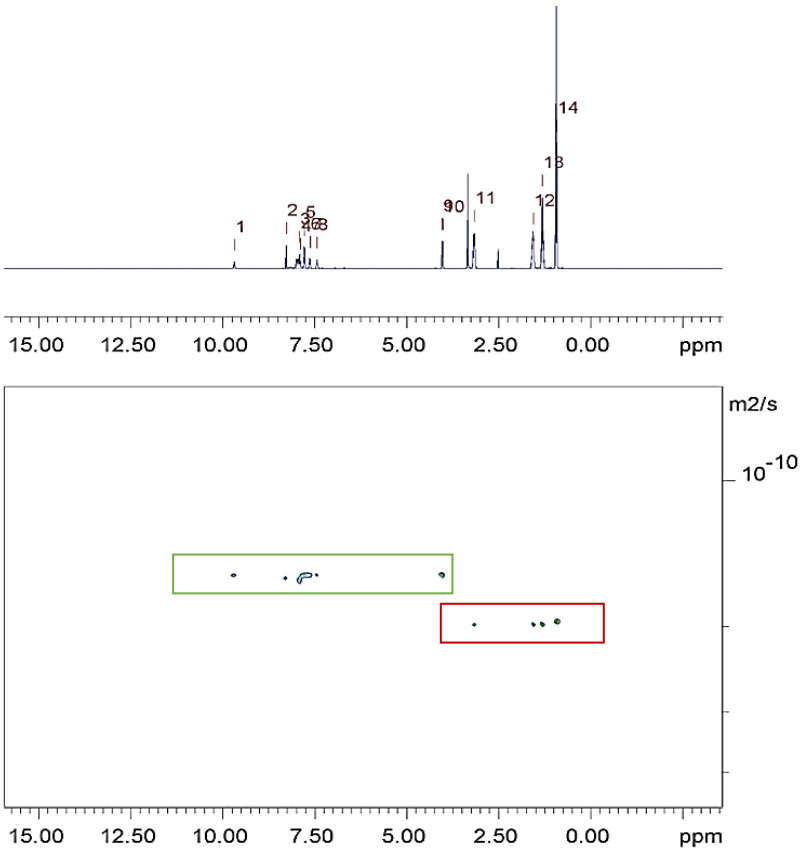

Peak name	F2 [ppm]	Io	error	D [m2/s]	error
1	9.677	6.03e+06	9183	1.58e-10	5.268e-13
2	8.262	2.12e+07	9186	1.58e-10	1.501e-13
3	7.913	1.25e+07	9241	1.61e-10	2.619e-13
4	7.891	1.32e+07	9185	1.58e-10	2.404e-13
5	7.774	1.90e+07	9175	1.57e-10	1.660e-13
6	7.633	9.51e+06	9172	1.57e-10	3.320e-13
7	7.611	8.33e+06	9174	1.57e-10	3.796e-13
8	7.432	7.86e+06	9172	1.57e-10	4.019e-13
9	4.032	2.47e+07	9149	1.56e-10	1.266e-13
10	4.017	2.49e+07	9153	1.56e-10	1.256e-13
11	3.160	3.11e+07	9829	1.99e-10	1.362e-13
12	1.563	3.37e+07	9822	1.99e-10	1.254e-13
13	1.313	6.38e+07	9793	1.97e-10	6.547e-14
14	0.927	2.74e+08	9775	1.96e-10	1.515e-14

Figure 54 – Showing ^{1}H DOSY of compound **1** (16.76 mg, 0.028 mM) at a concentration of 55.56 mM (stock) in DMSO-d_6 (0.500 mL) conducted at 298K and a table representing the values for the diffusion constant for each peak used for calculating the hydrodynamic diameter (d_H = 1.39 nm) of the sulphonate – anion (green). This does not include the TBA counter cation peaks (red). Peaks 1-10 correspond to the anionic component of **1** while peaks 11-14 correspond to the cationic component of **1**.

4.4.3 ^{1}H NMR association studies

A series of dilution and titration studies were carried out in order to explore the strength of the molecular self-association interactions of this new series of amphiphiles. The dilution studies were conducted for amphiphiles **1** and **4**. Titration studies, however, were only carried out for compound **1** and **2**, with compound **1** being the host and **2** being the guest for the first set of experiments and their positions were switched around for the second set, with **2** being the host and **1** the guest. Results for compound **2** for the dilutions studies have been previously reported by Hiscock and co-workers[93] showing that as the concentration increases, a change in the chemical shift is observed, thus making the hydrogen bonds stronger which results in the formation of dimer species.[2] The samples underwent serial dilutions starting from the most concentrated sample. For the dilution studies, compound **1** was studied at a concentration of 111.12 mM, while compound **4** was studied at 55.56 mM due to solubility barrier. The solvent used for this study was DMSO-d_6 + 0.5 % H_2O solution. This solvent system allowed the binding mechanism of the HBD urea NH groups to be studied. The titration studies were carried out at a concentration of 111.12 mM (for both sets of experiments) in DMSO-d_6 + 0.5 % H_2O solution. The sample preparation method can be found in the experimental techniques (section 8).

4.4.3.1 Result and discussion

The results of the dilution studies carried out for compound **1** (Figure 55) and compound **4** (Figure 56), showed that as the concentration increases a downfield change in the chemical shift for both urea NH groups (from both compounds) is apparent, suggesting the formation of self-associative hydrogen-bonded complexes.

The increase in concentration would also imply more stable hydrogen bond interactions between the structures being formed. The results for compound **1**, demonstrate that the NH (orange) closest to the sulphonate-urea shows a bigger change in chemical shift, compared to the NH closest to the aromatic ring system (blue) (Figure 55). As for compound **4,** a greater change in the chemical shift for resonances corresponding to both urea NH groups can be seen (Figure 56). One of the NHs (orange) for compound **1** could not be fitted to a binding isotherm due to peak overlapping, which prevented us from obtaining a full set of points.

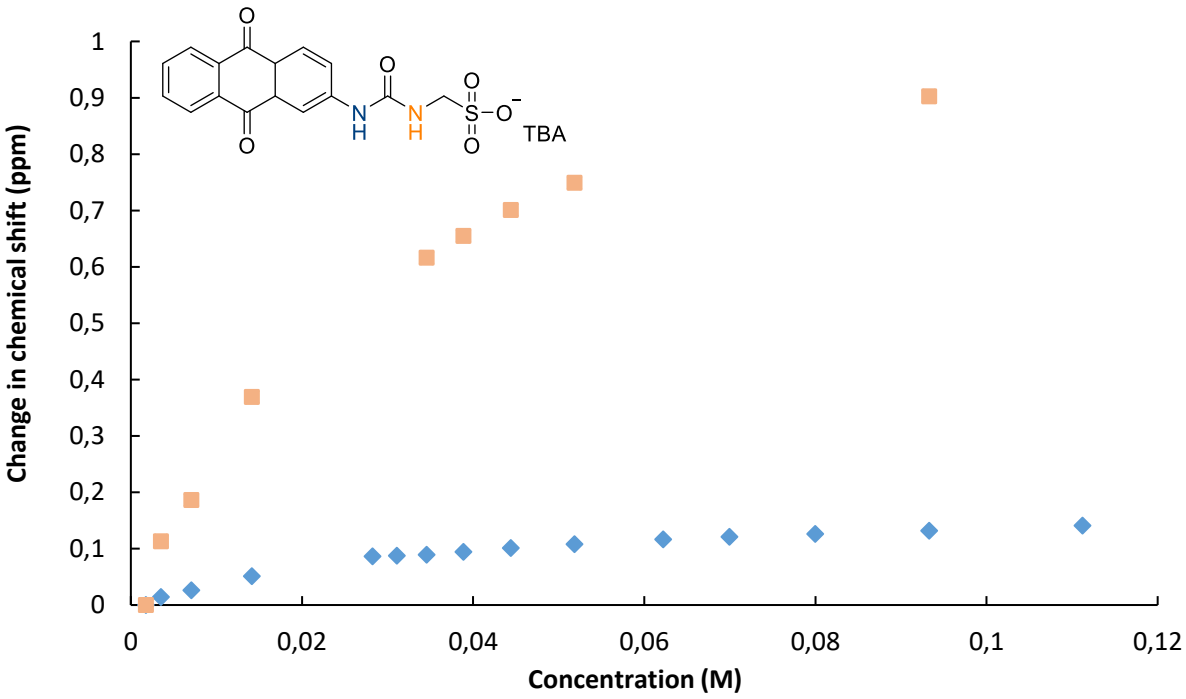

Figure 55: Graph showing the ^{1}H NMR down-field change in chemical shift of urea NH resonances with increasing concentration of compound **1** in DMSO- d_6/ 0.5% H_2O mixture (298 K). Peak overlapping during the experiment prevented the fitting of NH (orange) to a binding isotherm.

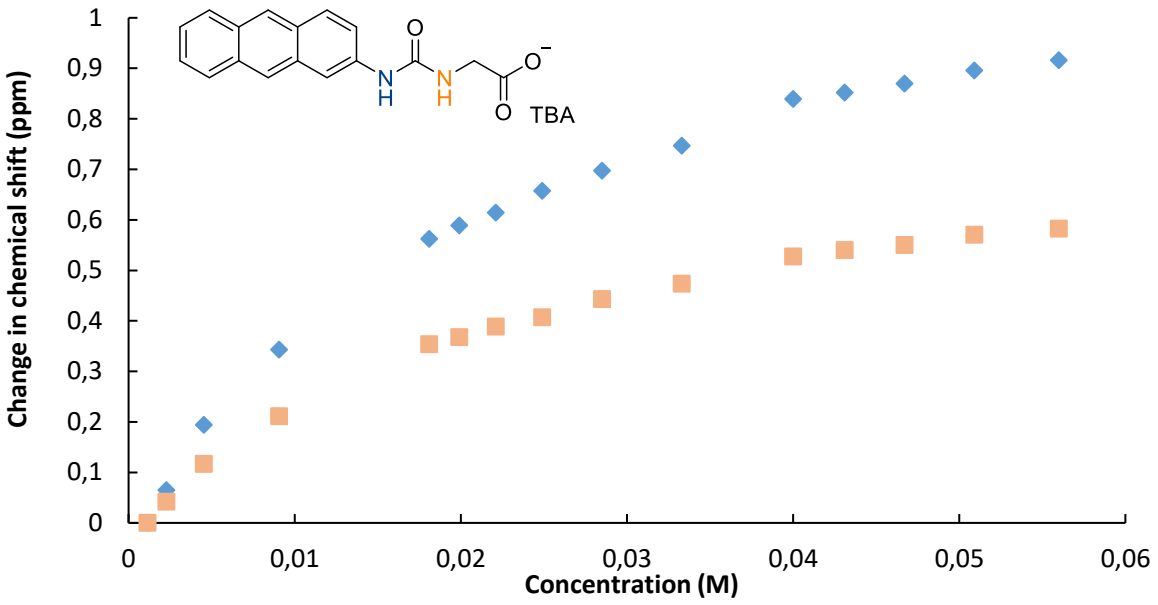

Figure 56: Graph illustrating the ^{1}H NMR down-field change in chemical shift of urea NH resonances with increasing concentration of compound **4** in DMSO-d_6/ 0.5% H_2O mixture (298 K).

In order to determine the binding strength of self-assembly systems, further analysis is usually carried out by obtaining measurements which are affected by both temperature and concentration.[118,120] Meijer and co-workers are known to have explored both methods with the intention of determining and presenting quantitative information about both cooperative and isodesmic[121] self-assembly systems.[122] Based on the aggregate formation mechanism there are two main systems - multicomponent (heterogeneous)[123] and single component (homogeneous).[123] For this study the single component (homogeneous) aggregate formations will be studied. The following can be considered when looking at the general linear aggregation system: equal K model where the initial association constant (K_e) is the same as the as the rest of the association constants and the CoEK model, where the initial association constant (K_2) is different from the subsequent association constants (k3, k4, k5….ki)[124] (Figure 57).

$$\overset{k_2}{\longleftrightarrow} \quad \overset{k_3}{\longleftrightarrow} \quad \overset{k_4}{\longleftrightarrow} \quad \overset{k_5}{\longleftrightarrow} \quad \overset{k_i}{}$$

1. $A + A \quad A_2 + A \quad A_3 + A \quad A_4 + A \quad \ldots\ldots A_i$

2. $K_E = K_2 = K_3 = K_4 = \ldots\ldots K_i$

3. $K_E = K_2/_p = K_3 = K_4 \ldots\ldots\ldots K_i$

4. $p < 1$: Positive cooperativity

$p = 1$: Non-cooperative

$p > 1$: Negative cooperativity

Figure 57: Showing the one-component general linear aggregation system (1), equal K/dimerisation model (2), the CoEK model (3) , and *p* which is the induced difference in free energy (4).[124,88]

Both the equal K/dimerisation model and the CoEK model were used to fit the data provided by the ^{1}H NMR dilution study. The data for compound **1** was plotted using Bindfit v0.5.,[125] software developed by Meijer, which was used for determining the binding constants of our amphiphiles. Results for compound **2** have been previously reported by Hiscock and co-workers.[2] The data for both the equal K/dimerisation model and the CoEK model for compound **1** can be found in Figure 58. The calculated equal K/dimerisation model was determined to be $K_{dim} = 16.84\ M^{-1}$, the CoeK model was calculated to be $K_{dim} = 21.45\ M^{-1}$. The equal K model showed a lower error of ± 1.6117%, compared to that of the CoeK model of ± 1.7665%, thus confirming the presence of complex dimeric species in the solution state supported by the data obtained from the ^{1}H NMR DOSY experiment, as well as the results obtained from the high-resolution mass spectrometry and the single crystal x-ray studies.

From both models, the dimerisation/equal K model was determined to give the best fit for the data presented for compound **1**. Comparing the equal K model for compound **1** (K_{dim} = 16.84 M^{-1} ± 1.6117%) to the already reported value of compound **2** (K_{dim} = 1.5 M^{-1}± 0.2%) by Hiscock and co-workers[2] a significant difference between both values can be seen. A high K_{dim} would indicate a more stable hydrogen bonding network, which can be seen for compound **1.** However, despite the complexes formed being somewhat weak**,** the ones by **1** were determined to be more fitting compared to those for **2**. This could be due to the electron poor nature of the anthraquinone, thus having stronger electron withdrawing properties compared to the anthracene, which would increase the amount of self-association processes occurring in the solution, leading to more stable and stronger complex formation.

1. Equal K/dimerization model

K_e = 33.68 M^{-1} ± 3.2234% K_{dim} = 16.84 M^{-1} ± 1.6117%

http://app.supramolecular.org/bindfit/view/744e6c77-6407-49f5-9bc7-b4046934f1b6

2. CoEK model

K_e = 42.90 M^{-1} ± 3.5330% K_{dim} = 21.45 M^{-1} ± 1.7665% ρ = 0.69 ± 15.3365%

http://app.supramolecular.org/bindfit/view/04f112af-9bd0-4280-a7d5-446f68d4fa57

Figure 58: Self-association constant calculations of compound 1 using the change in chemical shift of a single urea NH (blue – shown in Figure 55)

Although the same dilution experiment was performed with compound **4** (Figure 56), the data was not fitted to the self-association binding model due to the fact that this model can only calculate a self-association process involving one component self-association systems, rather than complex ones.

This is not the case with compound **4**, as it was shown from previous studies the formation of large aggregate structures which are not visible by NMR spectrum. This is also why this amphiphile was not used for any titration studies.

A series of ^{1}H NMR titration studies, however, were carried out with both compound **1** and **2.** For the first study compound **1** was the host and **2** being the guest (Figure 59). For the second experiment, they were switched around – **2** being the host and **1** the guest (Figure 60). The guest was added to the host through a series of additions of 2 x 10 µL, 5 x 8 µL, 4 x 10 µL, 5 x 50 µL. From the data observed for compound **1** (host) (Figure 59) and compound **2** (host) (Figure 60) a downfield change in the chemical shift of the urea-NH, corresponding to the host compound can be observed upon adding the guest to each host. The change in the chemical shift indicates the formation of heterogeneous (multicomponent) species in each of the solutions. As mentioned before this model can only assume the formation of one self-association process. In this case for compound **1** and **2,** the presence of one component (homogeneous) and a multicomponent (heterogeneous) self-association process was determined, confirming the presence of monomeric and dimeric complex formation. As a result, the dimerisation constant was not calculated because there was more than one interaction process occurring in each solution.

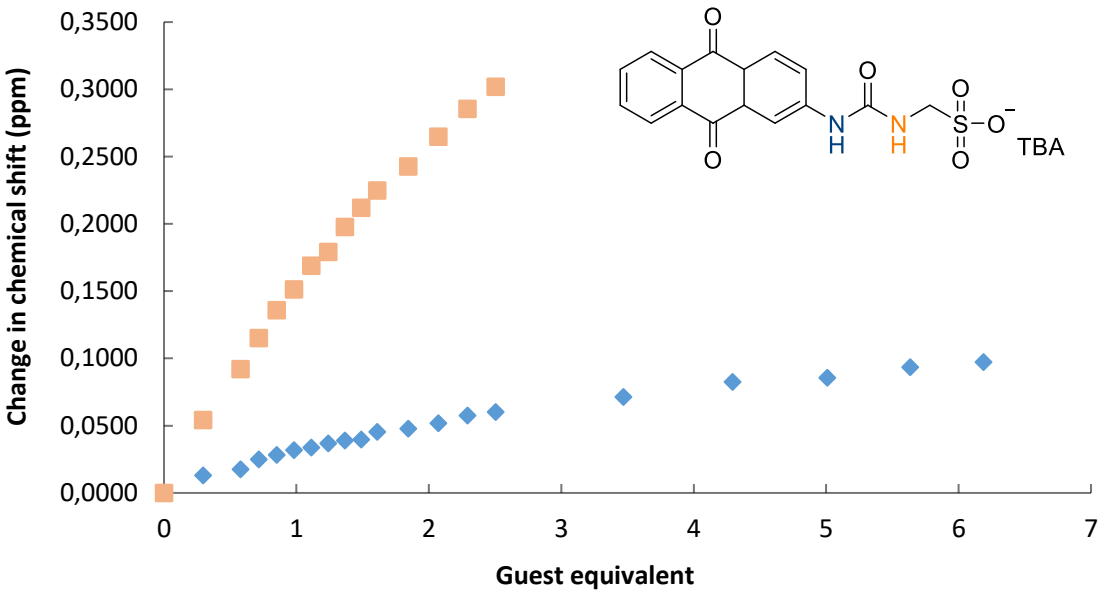

Figure 59: A graph showing the downfield ^{1}H NMR change in chemical shift for the NHs of compound **1** (host) with increasing the concentration of compound **2** (guest) in a DMSO-d_6/0.5% H_2O solution (298 K).

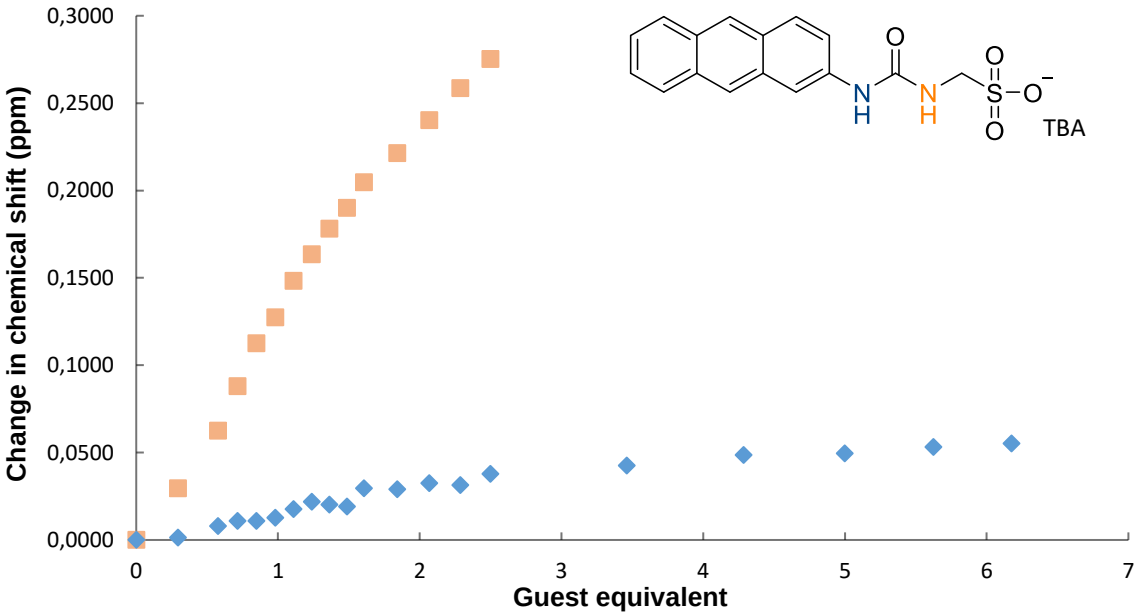

Figure 60: A graph showing the downfield ^{1}H NMR change in chemical shift for the NHs of compound **2** (host) with increasing the concentration of compound **1** (guest) in a DMSO-d_6/0.5% H_2O solution (298 K).

4.4.4 Zeta potential measurements and tensiometry studies

The CMC is the concentration at above which adding extra amphiphilic, results in the formation of bigger micelle structures.[126] Micelles ,however, can be present before the CMC value is determined. The CMC is calculated by measuring the surface tension of the molecular solution.[127] An important factor which must be considered when carrying out the studies is the aggregate stability. This can be affected by the solvent systems in which they are being observed and the aggregate formation. As a result, a series of zeta potential measurements were carried out. Both the surface tension and zeta potential measurements were carried out in the same solvent system in order for the results to be comparable – EtOH: H_2O (1: 19). Results of compound **2** for both studies have been previously reported by Hiscock and co-workers.[2] The samples in both studies underwent a serial dilution process starting from the most concentrated sample**.** For the tensiometry studies, the CMC was calculated using the methods reported by Costas and co-workers.[128]

4.4.4.1 Result and discussion

A series of comparative zeta potential studies were carried out in order to study and determine the stability of aggregates formed by these amphiphiles. From previous research carried out and results reported in the literature, it is known that a measurement which is more negative than -30 mV or more positive than +30 mV is considered stable.[129,130] A lower zeta potential ,however, means a lower aggregate stability and a tendency for the particles to flocculate (Figure 61).[130]

Incipient stability (± 10 mV to ± 30 mV)

Moderate stability (± 30 mV to ± 40 mV)

Good stability (± 40 mV to ± 60 mV)

Greatest stability (± 60 mV <)

Figure 61: Showing the stability of colloidal species depending on their zeta potential value.[131]

From the results reported in Table 8, the variation in the zeta potential measurements for each individual compounds and mixtures can be seen. At a higher concentration compound **4**, mix of **1** and **4**, mix of **2** and **4** are a little more stable with the values ranging between - 57 mV to - 65 mV, while at a lower concentration a destabilisation of the formed aggregate species can be observed, with values ranging between - 38 mV to - 48 mV. On the other hand, compound **1**, mix of **1** and **2** are more stable at a lower concentration with values of - 78 mV and - 83 mV respectively. Values for mix **1** and **2** at a concentration of 5.56 mM could not be obtained due to a solubility barrier. Compound **2** is stable at both tested concentrations. The zeta potential graphs for all compounds can be found in the appendix Figures S103 – S114.

Table 8: Zeta potential measurements for compounds **1**, **2**, **4** and mixtures of compound **1** and **2**, **1** and **4**, **2** and **4** calculated using 10 zeta potential runs in EtOH: H_2O (1: 19) at concentrations of 5.56 mM and 0.56 mM at 25 °C. Samples were prepared in series, with an aliquot of the most concentrated solution undergoing serial dilution. Compound **2** was analysed despite values for it being reported by Hiscock and co-workers.[2]

[a] Compound solubility prevented experiment.

Amphiphile	EtOH: H_2O 1: 19	
	Zeta potential (mV)	
	5.56 mM	0.56 mM
1	- 64	- 78
2	- 88	- 78
4	- 57	- 38
1 + **2**	[a]	- 83
1 + **4**	- 65	- 48
2 + **4**	- 60	- 41

From the data, it can be seen that the amphiphile molecules which, contain a sulphonate ion (**1**,**2**, mix of **1** and **2**) are shown to form more stable aggregate structures compared to compound **4**, **1** and **4**, **2** and **4**, which contain a carboxylate ion. It is suggested that this could be as a result of changing the geometry parameters of the anionic substituent or its hydrophilicity which could lead to changes in the strength and stability of the self-association binding modes. The surface tension was measured using the pendant drop method. Three sets of measurements were taken from an individual droplet at each concentration. The surface tension was plotted on a graph against the concentration allowing to calculate the CMC values for compounds **1**, **4**, mix of **1** and **2**, **1** and **4**, **2** and **4** (Table 9).

The results from the CMC show the following trend (lowest to highest): mix of **1** and **2** < mix of **2** and **4** < **4** < mix of **1** and **4** < **1**. The CMC was the point at which no further decrease in surface tension was observed. The CMC values can be affected by temperature and the compound structure (hydrophobic and hydrophilic group). In this case mix of compound **1** and **2** has the lowest CMC value of 1.09 mM (Figure 62). Compared to that individually, compound **1** (Figure 63) (anthraquinone) has the highest CMC value of 8.17 mM, while compound **2** (anthracene) has a reported CMC value of 2.52 mM by Hiscock and co-workers.[2] Compound **4** also has a low CMC value of 2.57 mM. This explains why mix **2** and **4** has the second lowest CMC value (2.17 mM), considering the low CMC for both compounds individually and the fact that they have anthracene-based structures. This also explains why mix **1** and **4** has the second highest CMC (5.12 mM), which can be mainly because of compound **1**, being anthraquinone-based having such a high CMC value. The results obtained show that by changing the molecular species the CMC value can be modified, as shown in mix **1** and **2** where the CMC value for each individual compound **1** (8.17 mM) and **2** (2.52 mM) is lower to that of 1.09 mM for the mix solution containing 1:1 of each.

This also suggests that having an electron rich (anthracene) and electron poor (anthraquinone) systems can result in a decrease of the CMC value. Furthermore, the surface tension measurements for this series of compounds create the following trend (lowest to highest): **2** and **4** < **1** and **4** < **1** and **2** < **4** < **1** which can be seen in Table 9. The rest of the tensiometry graphs can be observed in the appendix Figures S115 – S117.

Taking into account the solvent system in which the study was carried out in EtOH: H_2O (1: 19) , the surface tension of water is known to be 72.75 mN m^{-1} at a temperature of 21.5 °C.[132] Any addition of surfactants to the solution will lead to a decrease in the surface tension, due to the disruption of the hydrogen bond network.[133] This can be seen in the results for compound **1**,**4**,**1** and **2**, **1** and **4**, **2** and **4** whose surface tension measurements range between 46 - 53 mN m^{-1} (Table 9).

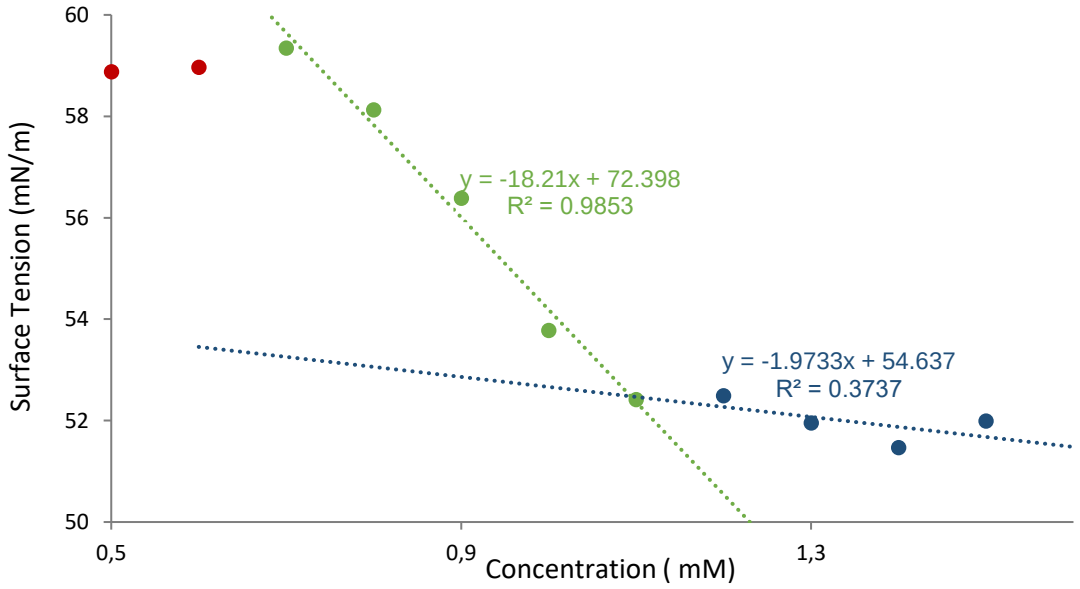

Figure 62: Calculation of CMC (**1.09 mM**) for compounds **1** and **2** (1:1 mix) in an EtOH: H_2O (1:19) mixture using surface tension measurements.

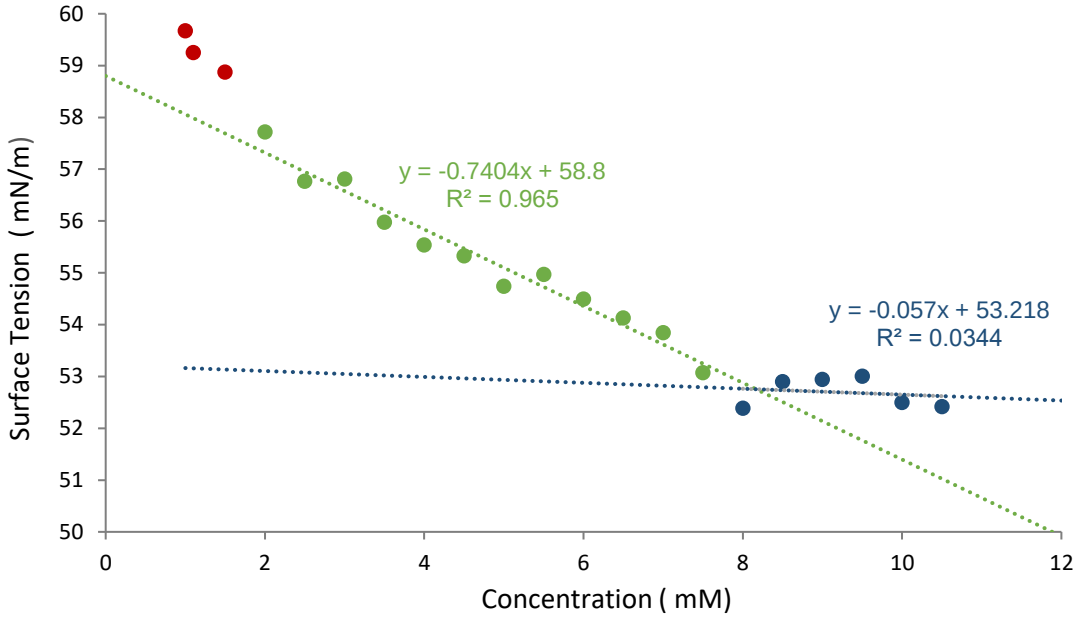

Figure 63: Calculation of CMC (**8.17 mM**) for compound **1** in an EtOH: H_2O (1:19) mixture using surface tension measurements.

Table 9: CMC and surface tension measurements for compounds **1**, **2**, **4** and mixtures of compound **1** and **2**, **1** and **4**, **2** and **4** in EtOH: H_2O (1: 19). Compound **2** was analysed despite values for it being reported by Hiscock and co-workers.[2]

a – previously published values by Hiscock and co-workers.[2]

Amphiphile	CMC (mM)	Surface tension (mN m^{-1})
1	8.17	52.75
2	a	a
4	2.57	52.65
1 + **2**	1.09	52.49
1 + **4**	5.12	51.60
2 + **4**	2.17	45.74

4.4.5 Fluorometry studies and UV-Vis spectroscopy

Ultra-violet visible spectroscopy and fluorometry are two techniques which were used in order to aid the fluorescence microscopy and transmission studies, by gaining more information about the species being monitored. The studies allowed the determination of the most suitable filters to be used for the microscopy studies. Each of the individual compounds **1**, **4** and mixtures, were analysed using UV-Vis spectroscopy in order to determine their absorption wavelengths. Following the information from the UV-Vis, fluorescence studies were carried out for each individual amphiphile and mixtures in order to determine their excitation and emission wavelengths. Both studies were carried out in a solution of EtOH: H_2O (1: 19). Data for compound **2** for each of these studies have been previously reported by Hiscock and co-workers.[2]

4.4.5.1 Result and discussion

The data obtained from the UV-Vis spectroscopy studies showed that the absorption wavelengths of compounds **1**,**4** and mixtures of **1** and **2**, **1** and **4**, **2** and **4** range between 260 – 280 nm (Table 10).

Table 10: Showing the UV-Vis absorbance properties of compounds **1**, **4** and mixtures **1** and **2**, **1** and **4**, **2** and **4** in a solution of EtOH: H_2O (1: 19).

Amphiphile	Peak maxima (nm)
1	280
4	260
1 + **2**	262
1 + **4**	262
2 + **4**	260

These results were then used in the fluorometry studies in order to guide the determination of the excitation and emission wavelengths of each individual compound and the mixtures (Table 11). The data shows that the values for the excitation wavelengths range between 270 – 422 nm, while the emission wavelengths range between 438 – 476 nm. Compound **1** has a small Stoke shift of 54 nm (Figure 64). If the shift had been smaller than < 25 nm then this could result in measurement errors or self-quenching.[134,135] Compared to that compound **4** has a large Stoke shift of 186 nm (Figure 65). Fluorescent molecules that have a big Stoke shift are known to have low fluorescence emission intensity, which results in poor photostability.[136]

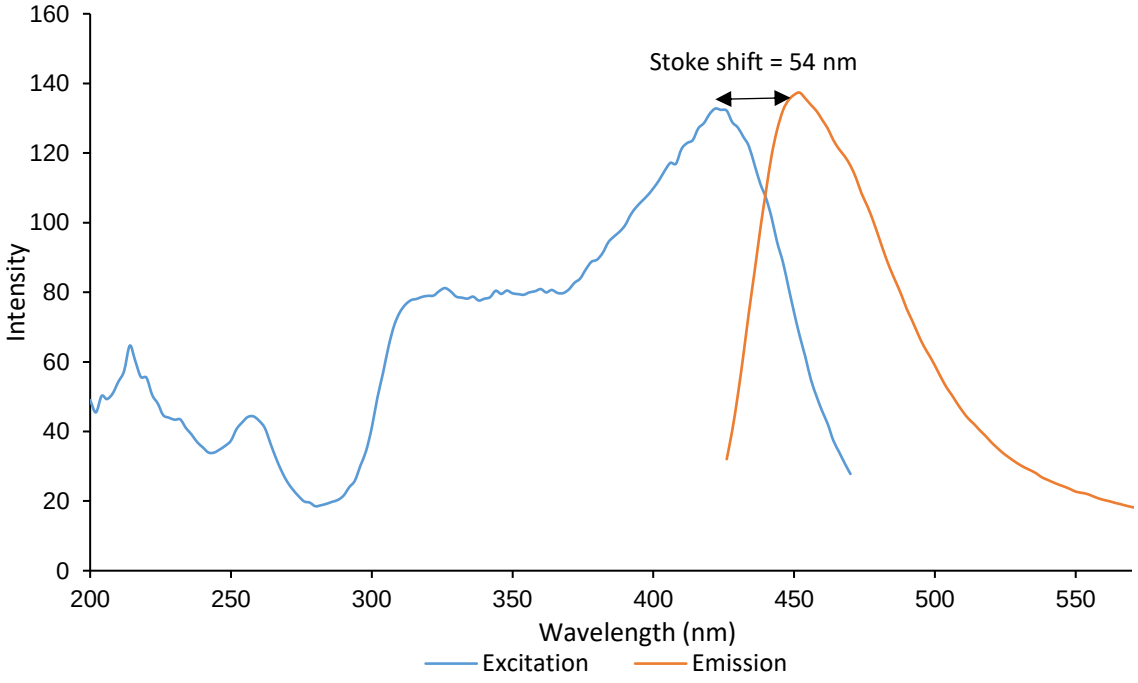

Figure 64: Fluorescence spectra of compound **1** at a concentration of 1 mM in EtOH: H_2O (1: 19) showing a Stoke shift of 54 nm.

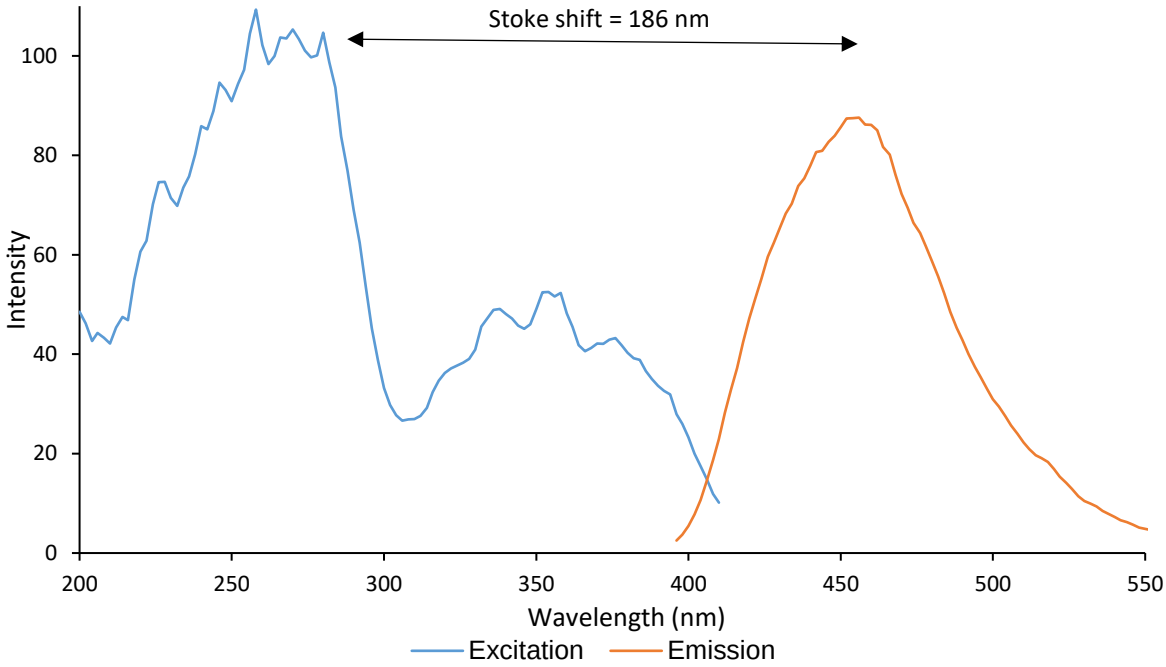

Figure 65: Fluorescence spectra of compound **4** at a concentration of 0.1 mM in EtOH: H_2O (1: 19) showing a Stoke shift of 186 nm.

By comparing the Stoke shifts of the mixtures from Table 11 it can be seen that the mix of **1** and **2** has the smallest Stoke shift of 82 nm, 1: 1 mix **2** and **4** has a shift of 98 nm, 1:1 mix of **1** and **4** has the greatest Stoke shift of 114 nm. As a result of its low shift, 1:1 mix of **1** and **2** (Figure 66) was observed via the microscopy studies. The greater the Stoke shift, the easier it would be to obtain the microscopy images, due to the fact that the background light cannot be imaged. The rest of the graphs for the UV-Vis and fluorometry studies can be found in the appendix Figures S118 – S124.

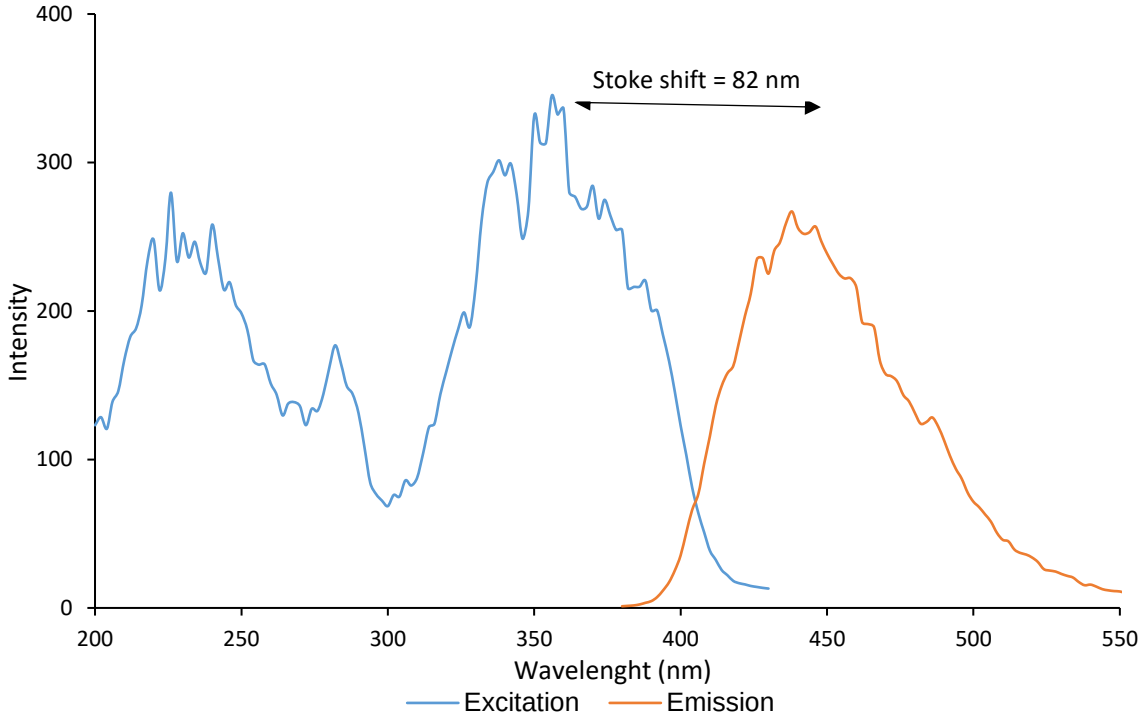

Figure 66: Fluorescence spectra of compound **1** (0.5 mM) and **2** (0.5 mM) in EtOH: H_2O (1: 19). showing a Stoke shift of 82 nm.

Table 11: Showing the fluorescence excitation and emission values of compounds **1**, **4** and mixtures **1** and **2**, **1** and **4**, **2** and **4** in a solution of EtOH: H_2O (1: 19).

Amphiphile	$\lambda_{Ex\ (nm)}$	$\lambda_{Em\ (nm)}$	$\Delta\lambda_{ST}$
1	422	476	54
4	270	456	186
1 + **2**	356	438	82
1 + **4**	356	470	114
2 + **4**	356	454	98

4.4.6 Fluorescence microscopy and transmission studies

Fluorescence microscopy is an important scientific technique used for visualising fluorescent images. This technique has developed greatly throughout the years and can be used for studying intermolecular non-covalent interactions in both chemical and biological studies such as molecular cell biology,[137] protein structure formation[138] and fluorescent molecules.[139] Compounds **1**,**2**, **4** and mixtures **1** and **2**, **1** and **4**, **2** and **4** are fluorescent based amphiphiles which were confirmed by the fluorometry studies. Compounds **1**,**2**, **4** and mix of **1** and **2** were visualised using both fluorescent and transmission microscopy, which identified the structures formed using these amphiphiles, provided the ability to directly visualise these structures in the solution state. The results obtained are directly comparable to the data from the DLS and NMR studies carried out in the solution phase, thus achieving both quantitative and qualitative information about the molecules. The solvent system used in this study was EtOH: H_2O (1: 19). All molecules were observed at concentrations of 1 mM and 0.56 mM which are directly comparable to the DLS studies carried out at the same concentration of 0.56 mM. A limitation of this technique includes unconscious bias, thus presuming that everything being observed through the microscope is part of the bulk sample. In order to avoid this, the transmitted images were overlaid with the comparable fluorescence microscopy image, in order to determine which structures observed contain those fluorescent amphiphiles **1**, **2**, **4** and 1:1 mix of **1** and **2**. Each sample was pipetted (10 µl) on to an agarose pad and a coverslip was added on top reducing the movement of structures formed in the solution, as well as solvent evaporation. This was carried out by methods reported by Levin.[140] The filters used in the study were chosen by considering the excitation and emission wavelengths of the amphiphiles, thus the following filters were used: GFP (excitation – 480 nm and emission – 510 nm) and DAPI (excitation – 350 nm and emission – 450 nm). Some of the compounds could be visualised using both filters, while others only one. The data was interpreted with the help of Tara Eastwood (Dan Mulvihill group, School of Biosciences, University of Kent) and Dr. Dan Mulvihill.

4.4.6.1 Result and discussion

The microscopy images of compound **1** (Figure 67) show the formation of spherical shaped structures with diameters ranging between 80 – 120 nm observed from both concentrations (1 mM and 0.56 mM) (Table 12). The overlaid image in Figure 68 confirms that the structure is part of the main sample.

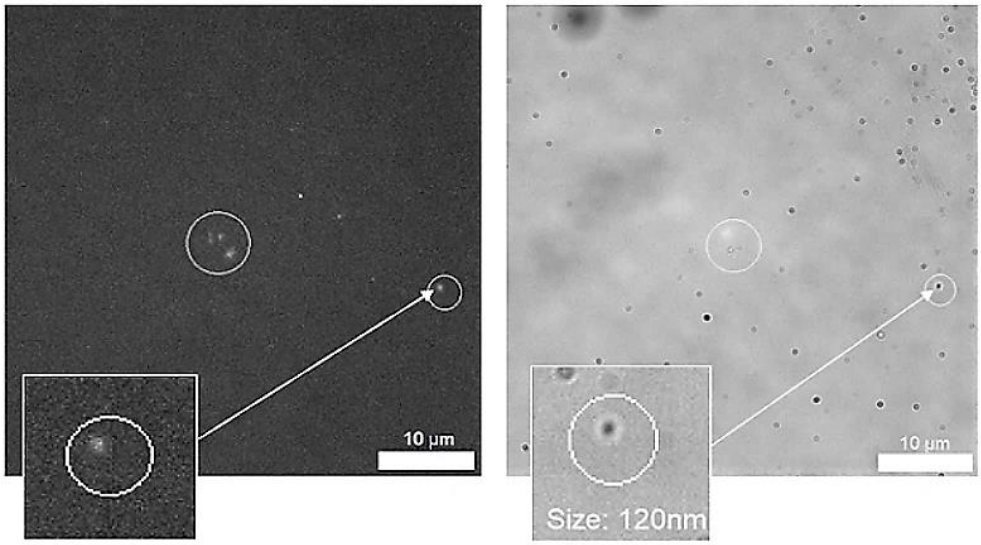

Figure 67: Left: a DAPI filtered fluorescence microscopy image of compound **1** (1 mM) in an EtOH: H_2O (1: 19) solution. Right: an analogous transmitted light microscopy image. Evidence of aggregated spherical structures is circled for clarity. Photobleaching during the imaging process resulted in loss of fluorescence emission intensity, as a result, some aggregates could not be captured in the fluorescence microscopy image. Only clearly visible spherical structures which appeared in both images were measured. Shape variation can be due to individual aggregation and or moving structures.

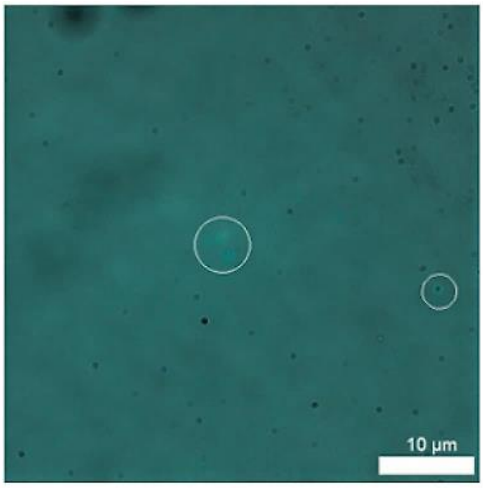

Figure 68: An overlaid image of those shown in Figure 67 (left and right) image. Clear evidence of aggregated spherical structures of compound **1** are circled for clarity.

The same spherical structures can be observed in compound **2** (Figure 69) with diameters between 100 – 130 nm from both concentrations (Table 12). An overlaid image for these structures can be seen in Figure 70.

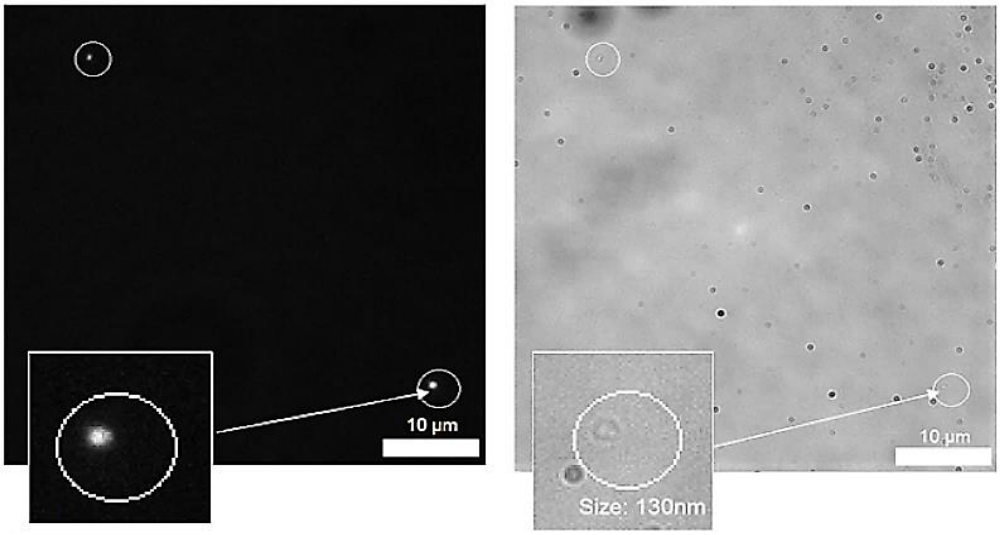

Figure 69: Left: a CFP filtered fluorescence microscopy image of compound **2** (1 mM) in an EtOH: H_2O (1: 19) solution. Right: an analogous transmitted light microscopy image. Evidence of aggregated spherical structures are circled for clarity. Photobleaching during the imaging process resulted in loss of fluorescence emission intensity. As a result, some aggregates could not be captured in the fluorescence microscopy image. Only clearly visible spherical structures which appeared in both images were measured. Shape variation can be due to individual aggregation and or moving structures.

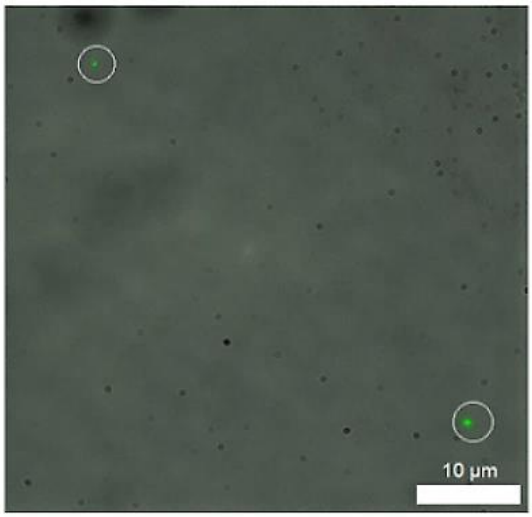

Figure 70: An overlaid image of those shown in Figure 69 (left and right) image. Clear evidence of aggregated spherical structures of compound **2** are circled for clarity.

From the images obtained from compound **4** (Figure 71)**,** the formation of both spherical and irregular shaped aggregates can be observed. The diameters of the spherical structures ranged between 90 – 210 nm (Table 12). The overlaid image can be seen in Figure 72.

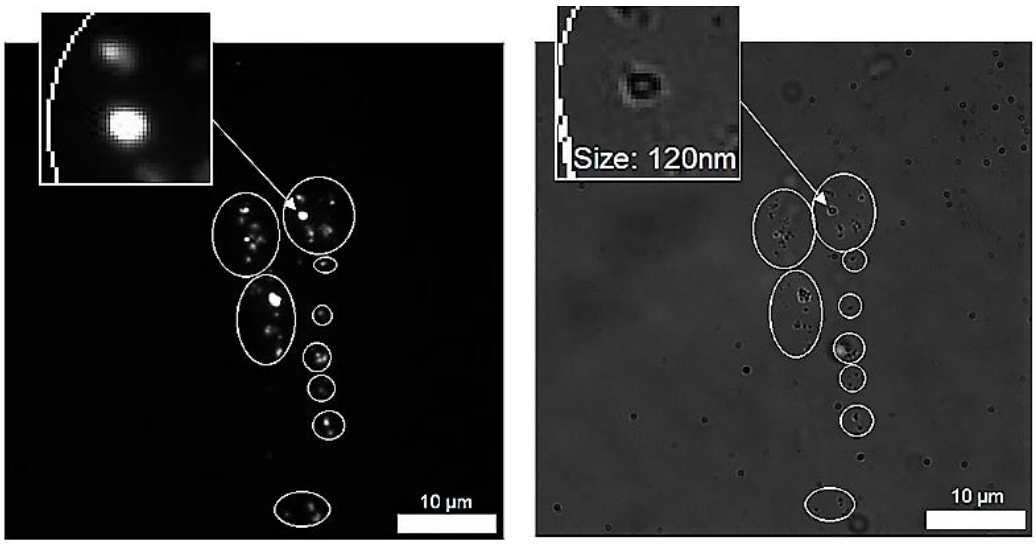

Figure 71: Left: a DAPI filtered fluorescence microscopy image of compound **4** (1 mM) in an EtOH: H_2O (1: 19) solution. Right: an analogous transmitted light microscopy image. Evidence of aggregated spherical structures are circled for clarity. Photobleaching during the imaging process resulted in loss of fluorescence emission intensity, as a result, some aggregates could not be captured in the fluorescence microscopy image. Only clearly visible spherical structures which appeared in both images were measured. Shape variation can be due to individual aggregation and or moving structures.

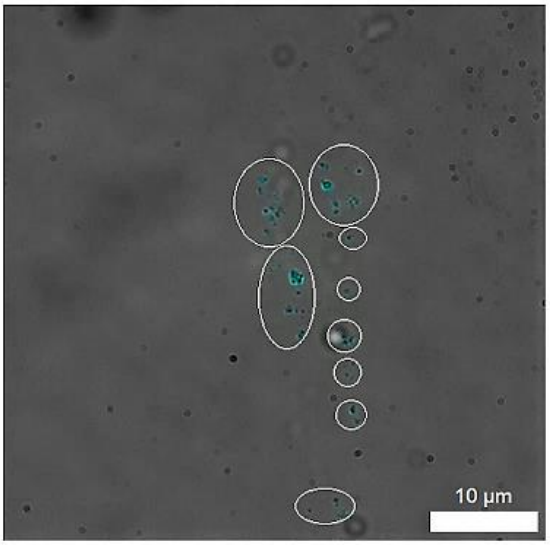

Figure 72: An overlaid image of those shown in Figure 71 (left and right) image. Clear evidence of aggregated spherical structures of compound **4** are circled for clarity.

The formation of these spherical aggregates from each individual compound can be observed. Furthermore, the presence of these structures (Figure 73) was also seen in the mixture solution containing both compound **1** and **2** with varying diameters between 100 – 170 nm from both concentrations (Table 12). The overlaid image can be seen in Figure 74. Carrying out this study enabled direct visualisation these structures formed through aggregation processes at room temperature in their native solvent environment. From the results (Table 12) the presence of both spherical and irregular shaped aggregates (containing multiple spherical ones) for all molecules were identified. The spherical shaped structures were observed for all molecules at both concentrations. The measurements of clearly visible individual spherical from each compound were measured and an average size was calculated (Table 12). Compound **1** has structures with diameters ranging from 80 – 120 nm, with an average size of 100 nm. In compound **2** the diameters vary between 100 – 130 nm, with an average diameter of 117 nm. For compound **4**, formations with diameters between 100 – 210 nm and an average diameter of 102 nm were observed. And finally, with the mix of both **1** and **2,** structures with diameters between 100 – 170 nm, with an average of 133 nm were seen. Only clearly spherical particles were measured and were used to calculate the average size in each individual compound. By knowing the average size of these structures, the results are compared to the data obtained from the DLS studies carried out in the same solvent environment and concentration. From the results shown in Table 12 and Table 13, the similarities in terms of the sizes measured can be observed. For compound **1** individual particles are seen with a size of 120 nm which is similar to the size observed in the DLS for 124 nm. For compound **2** particles with a size of 130 nm are observed, which is slightly lower than the size measured by the DLS of 198 nm. The results for compound **4** established the presence of structures with size up to 210 nm which is lower compared to the ones measured via DLS with 324 nm. Finally, for the mix of **1** and **2,** sizes of 170 nm were established which is slightly low compared to the ones determined by the DLS studies of 224 nm.

The reason why the sizes measured via the microscopy studies are so different compared to the DLS is due to the hydrodynamic solvent sphere surrounding the aggregates, which is included by the DLS instrument when carrying out the measurements. Full range of images can be found in the appendix Figures S125 – S158.

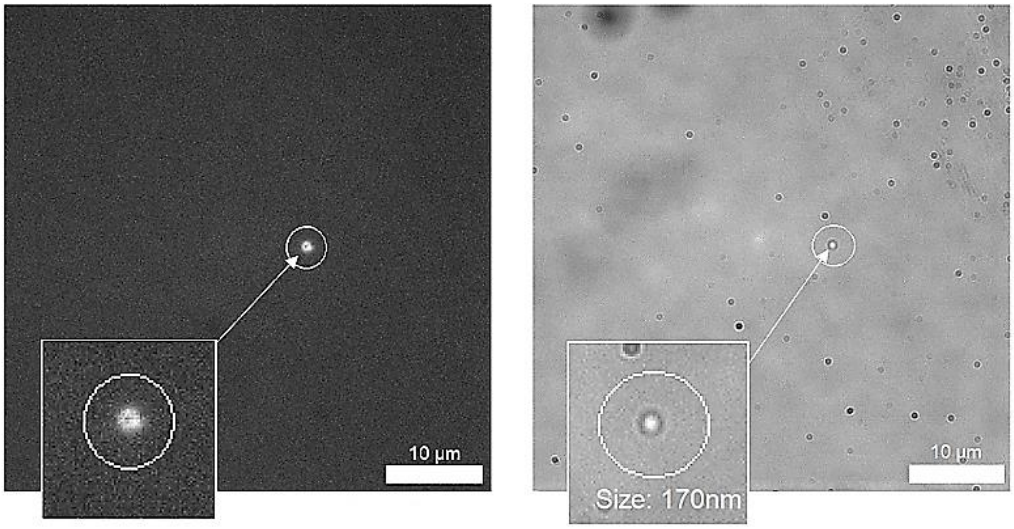

Figure 73: Left: a DAPI filtered fluorescence microscopy image of compound **1** and **2** (1:1 mix) (total concentration 0.56 mM) in an EtOH: H_2O (1: 19) solution. Right: an analogous transmitted light microscopy image. Evidence of aggregated spherical structures are circled for clarity. Photobleaching during the imaging process resulted in loss of fluorescence emission intensity, as a result, some aggregates could not be captured in the fluorescence microscopy image. Only clearly visible spherical structures which appeared in both images were measured. Shape variation can be due to individual aggregation and or moving structures.

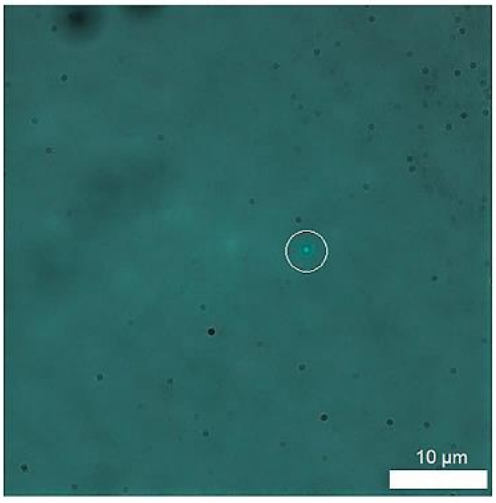

Figure 74: An overlaid image of those shown in Figure 73 (left and right) image. Clear evidence of aggregated spherical structures of compound **1** and **2** (1:1 mix) (total concentration 0.56 mM) are circled for clarity.

Table 12: Individual and average size of clearly visible single spherical structures observed for compounds **1**, **2**, **4** and mix of **1** and **2**, **1** and **4**, **2** and **4.**

[a] compounds supplied in a 1:1 ratio. [b] Total molecular concentration.

Compound	Aggregate diameter (nm)		Average size (nm) and error %
	1 mM[b]	0.56 mM[b]	
1	90, 110, 120	80	100 (± 9.1287)
2	130	100, 120	117 (± 8.8191)
5	90, 90, 90, 90, 100, 120	80, 80, 90, 90, 90, 210	102 (± 10.2863)
1 + 2[a]	100, 130	170	133 (± 20.2758)

Table 13: Average size of clearly visible single spherical structures (microscopy) and average peak maxima size of the structures analysed in the DLS studies.

Amphiphile	Average size (nm) and error % (microscopy)	Average size (nm) and error % at 0.56 mM (DLS)
1	100 (± 9.1287)	124(± 1.5359)
2	117 (± 8.8191)	198 (± 3.8297)
4	102 (± 10.2863)	324 (±14.2343)
1 + 2	133 (± 20.2758)	224 (± 7.8719)

5. Amphiphiles as novel antibiotics

5.1 Introduction

The increase in bacterial resistance over the years is one of the greatest problems to global health, leading to countless research studies being carried out towards the development of novel antimicrobial agents.[141] Both Gram +ve and Gram -ve bacteria have revealed signs of multiresistant patterns towards various antibiotics used in medical practice. As a result, antibiotics are shown to have little effect on a disease or an infection, with worst cases leading to no effect at all.[142] There are various resistant bacteria which are categorized based on their structural morphology, shape, cell wall, etc. Two of the most common bacteria ones encountered in clinical practice are Gram +ve Methicillin-resistant *Staphylococcus aureus* (MRSA USA300)[143] and Gram -ve Escherichia coli (*E.coli*).[144] The main difference between Gram +ve and Gram -ve bacteria is the cell wall structure, which can have an influence over the activity of an antibiotic. Gram +ve bacteria have a thicker layered homogeneous cell wall with values ranging between 15 – 20 nm, with some being as thick as 80 nm, whereas Gram -ve bacteria have a much thinner heterogeneous cell wall with values ranging between 7.5 – 12 nm (Figure 75).[145] However along with that, Gram -ve bacteria also have an extra outer membrane with additional porins, making their membrane wall harder to be treated by antimicrobial agents (Figure 75).[145]

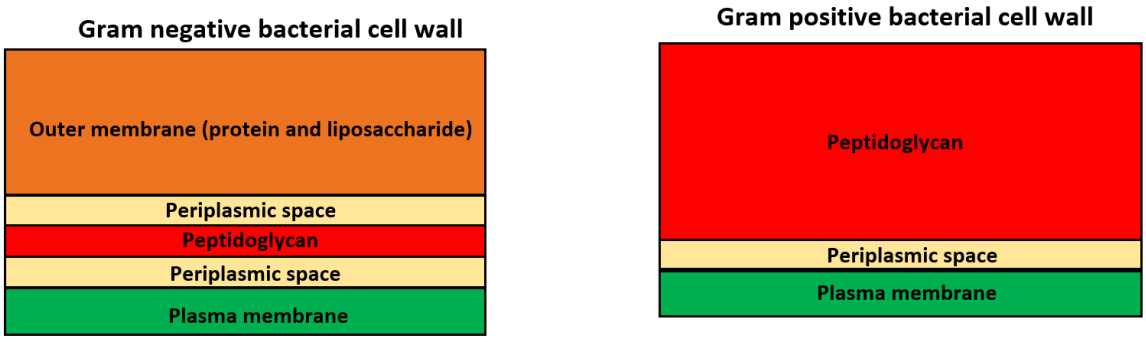

Figure 75: Cell wall structure of both Gram +ve and Gram -ve bacteria.

Bacterial cells can be grown in a laboratory environment under controlled conditions and can be used in screening testing to determine whether they are susceptible towards novel compounds.[146] Depending on the conditions they can grow quickly, however that also depends on the bacteria being observed.[147, 148]

When bacteria begin to grow they follow a particular growth pattern which is depicted as a growth curve.[147] The growth curve presents four different phases through which the bacterial growth over time is observed – lag phase, exponential phase, stationary phase, and death phase.[146] The first phase is the lag phase where bacteria must adjust to their new environment. If the bacteria are grown in similar conditions then they will have a smaller lag phase.[146] If the cells are grown in a less favorable environment, the time taken to adjust to that environment will increase, resulting in an elongated lag phase.[148] The next phase is the exponential phase, also known as the log phase in which the amount of each individual cell doubles.[148] After that the cells go into stationary phase (third phase), where some new cells will continue to grow, however, an equivalent amount of cells will begin to die, resulting in a plateau of live cells.[146,148] This is due to the absence of essential nutrients which are required for the bacteria to keep growing.[148] The final fourth phase is the death phase, where the number of viable cells begin to decrease. This does not mean that all cells die at the same time, some could die immediately while others may be resistant and carry on growing.[148,149] An example of a cell growth curve can be seen in Figure 76.

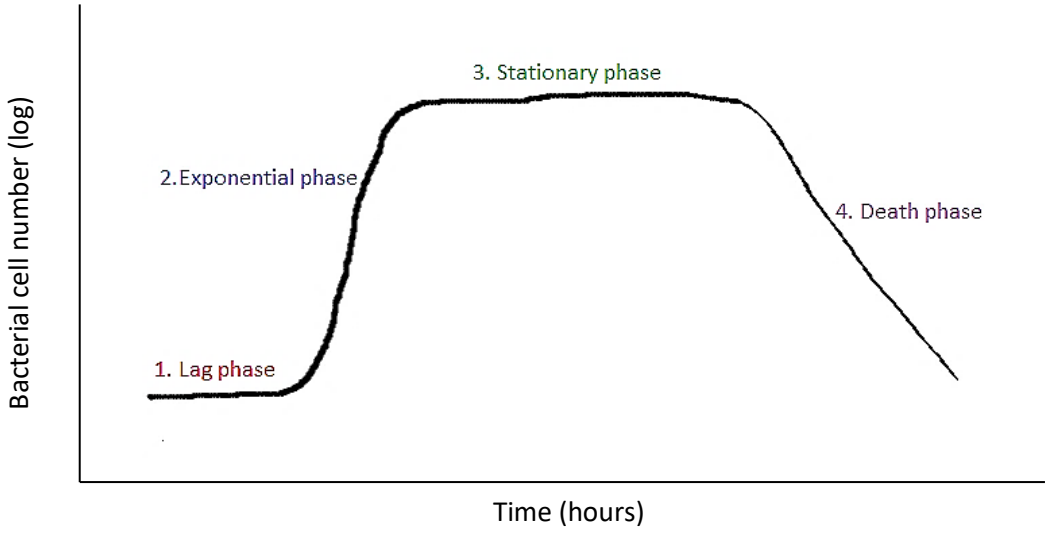

Figure 76: Bacterial growth curve showing the four growth stages – lag phase, exponential (log phase), stationary and death phase.[149]

The hydrophilic and hydrophobic units of the amphiphile play an important role in their activity towards bacteria. The mode of action depends on the functional group of the hydrophilic component and the formation of micelles which can disrupt the cell wall. Anionic and cationic surfactants are known to be more effective at solubilising and disrupting the cell membrane, compared to non-ionic.[150] This occurs as a result of the acidity of the molecule, which in the case for anionic compounds shows an increase in their activity against bacteria, as the pH decreases.[150] The opposite is observed for cationic compounds, showing that an increase in the acidity leads to a decrease in the activity against bacterial cells. An important fact which must be considered when designing new molecules is that anionic species are negatively charged, thus require a positively charged cation which can be TBA, TMA, TPA and other. In recent years, the research and interest toward anionic based amphiphiles which can be used in biological processes has increased significantly. A study carried out by Nabel and co-workers has reported the activity of a series of synthesized anionic gemini surfactants against Gram +ve Gram -ve bacteria and fungi.[151]

It was presented in the study that the gemini surfactants were obtained by linking two monomeric surfactants using a spacer. Along with that, it was reported that the anionic gemini surfactants contained phosphates head groups and different hydrocarbon chain lengths (C8A, C12A, C16A and C18A).[151] It was determined that the CMC value of the surfactants decreases as the length of the alkyl hydrocarbon chain increases (chain length C8A to C18A). It was established to lead to a high hydrophobicity of the surfactants, as a result in the increase of the methylene groups (-CH_2-) in the hydrophobic chains.[151] The results from the study also showed that the interfacial tension values of the surfactants had a range between 11 - 14 mN/m.[151] It was determined that the decrease of the interfacial tension was due to the increase of the alkyl hydrocarbon chain length (with C8A being 14 mN/m and C18A being 11 mN/m).[151] This was determined to have an effect over the inhibitory ability of the anionic surfactants. The surfactants were also tested against bacteria (both Gram +ve and Gram -ve), as well as fungi. It was reported that the synthesised surfactants had a very good antimicrobial activity against both Gram -ve and Gram +ve bacteria, with examples of inhibitory values against *E.coli* which ranged from 15 – 32 mm/mg, as well as against *B.pumilus* which ranged from 13 – 34 mm/mg.[151] It was concluded that the antimicrobial action of the anionic surfactants is affected by the length of the alkyl hydrophobic chains, thus by increasing the length of the chains, the surfactants had become more effective and their antimicrobial activity increased.[151]

5.2 MIC_{50} studies

There are various screening methods used for observing the antibacterial activity of new compounds. Two of the most commonly used are the disk diffusion test[152] and broth dilution test.[153]

The both dilution test was chosen for these studies, which can be used to calculate the minimal inhibitory concentration (MIC) of the compound being analysed.[153] MIC represents the minimal concentration at which an antimicrobial agent inhibits the growth of bacterial cells.[154] Both the cells and the potential antibiotic undergo a dilution process and are then pipetted into a plastic microdilution plate, each containing 96 wells which allows the analysis of several different compounds at the corresponding concentrations. Some of the advantages this screening method include reproducibility, the ability to analyse several different compounds at the same time, microplate preparation, as well as being able to calculate the MIC.[148,155]

For this study, the MIC_{50} value for each amphiphile and mixtures was established. The MIC_{50} represents the minimal concentration at which only 50% of the test population is inhibited.[156] The series of MIC_{50} studies were carried out in order to observe the susceptibility of this new series of amphiphiles towards both +ve Methicillin-resistant Staphylococcus aureus (MRSA USA300)[157] and –ve Escherichia coli (E.*coli)* bacteria in the log phase.[158] A detailed explanation of the preparation and calculating method for the MIC_{50} can be found in the experimental techniques (section 8). The ratio of amphiphile solution to cell suspension culture used in the wells for *S.aureus* was 1:2, while the ratio for *E.coli* was 1:6. Initial screening established that due to slow cell growth they could not be run at lower volume than 140 µL (+ 60 µL of the compound, resulting in a total volume of 200 µL), unlike the *S.aureus* which was ran at 90 µL (+ 90 µL of the compound, resulting in a total volume of 180 µL). The studies for compounds **1**,**2**,**4**, 1:1 mix of **1** and **2**, **1** and **4**, **2** and **4** were carried out in 5% EtOH:H_2O (1: 19). The samples underwent a series of dilutions starting from the most concentrated sample. Growth curves were plotted using an average of the six comparative absorbance readings, taken on two separable days, using Microsoft Excel. I assisted in carrying out the studies; however, the main experiments were conducted with the help of Nyasha Allen (School of Biosciences, University of Kent).

5.2.1 Result and discussion

The MIC_{50} was calculated for each of each of the individual compounds **1**, **2**, **4** and the series of mixtures of **1** and **2**, **1** and **4**, **2** and **4.** The 0 mM value in the graphs corresponds to the control sample of EtOH: H_2O and the bacterial cells.

The average growth curve graphs showing the activity of each compound **1**, **2**, and **4** against the bacterial growth (*S.aureus*) can be observed in Figures 77-79. From those, the activity for each compound at the corresponding concentration can be seen. Compound **1** (Figure 77) and **2** (Figure 78), for example, both show an increase in activity against the bacterial cells at higher concentrations, resulting in cell death. In between them, however, **2** has a bigger effect over cell death at those high concentrations compared to **1.** Also, on compound **1**, slight aggregation can be observed at 1.5000 mM which could be due to the cells getting agitated or the compound dropping out of solution. Compound **4** shows some activity, however, does not entirely kill the cells, as it can be seen from the graph in Figure 79 that they continue to grow after some time (observed at the highest concentration of 1.0000 mM and 0.8750 mM). The lower concentrations for all compounds **1**, **2** and **4** compounds have no effect over the bacterial growth, as observed from the graphs.

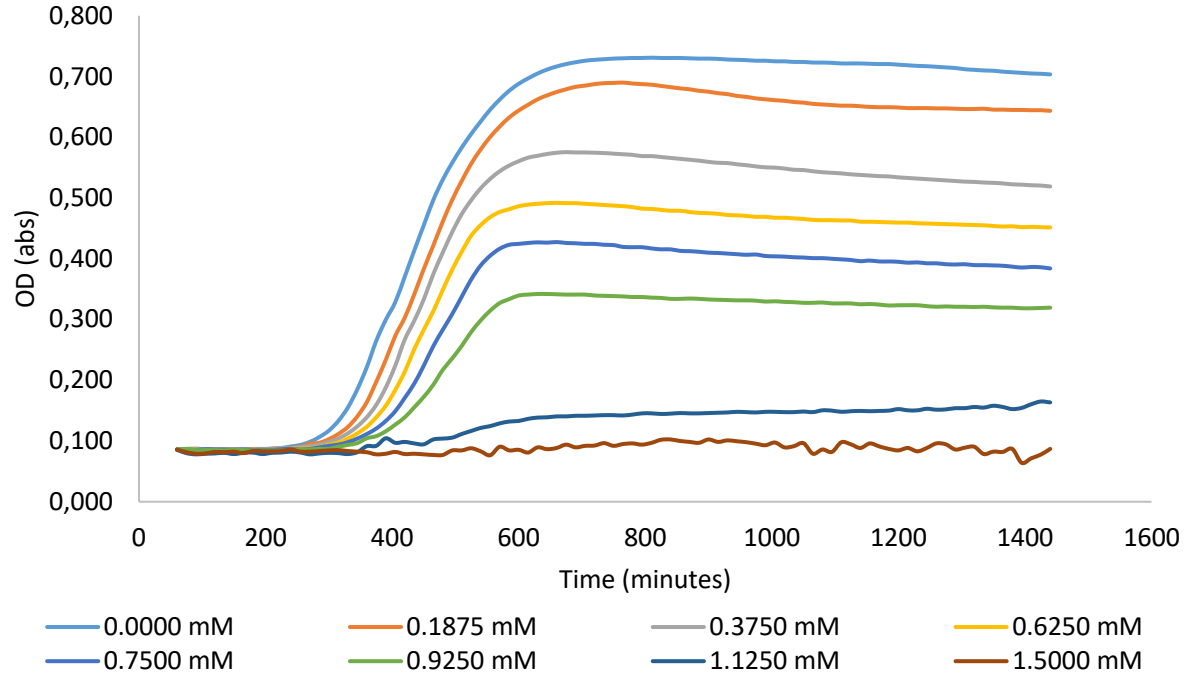

Figure 77: Average growth curves obtained for MRSA USA300 in the presence of compound **1** at eight different concentrations. Optical density (OD) relates to the number of cells present.

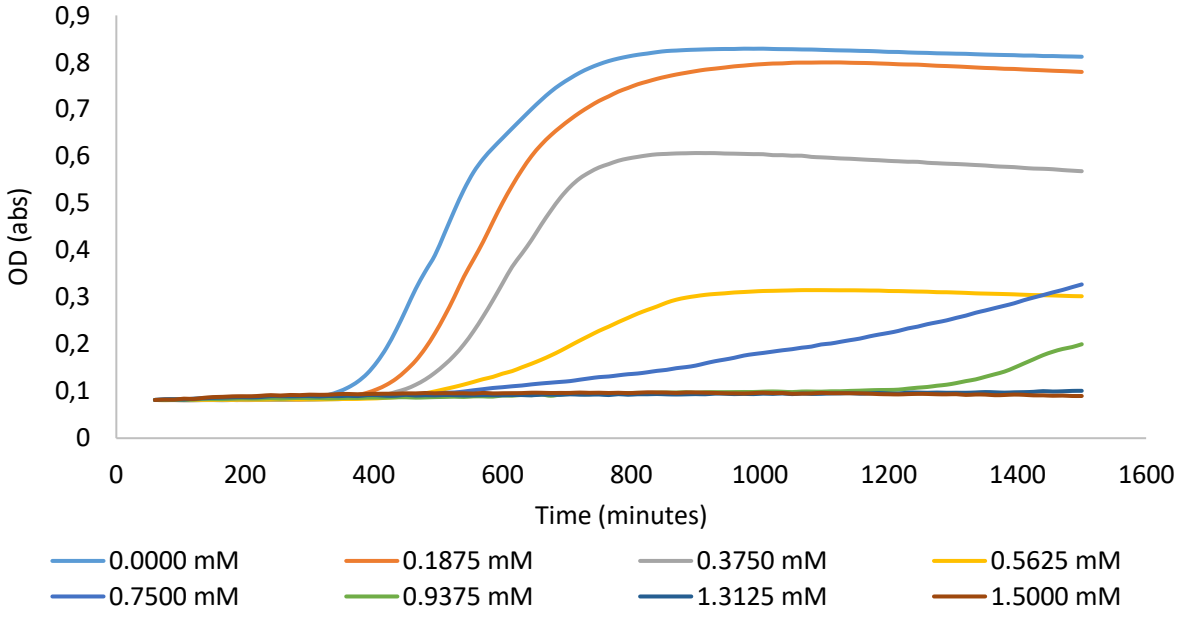

Figure 78: Average growth curves obtained for MRSA USA300 in the presence of compound **2** at eight different concentrations. Optical density (OD) relates to the number of cells present.

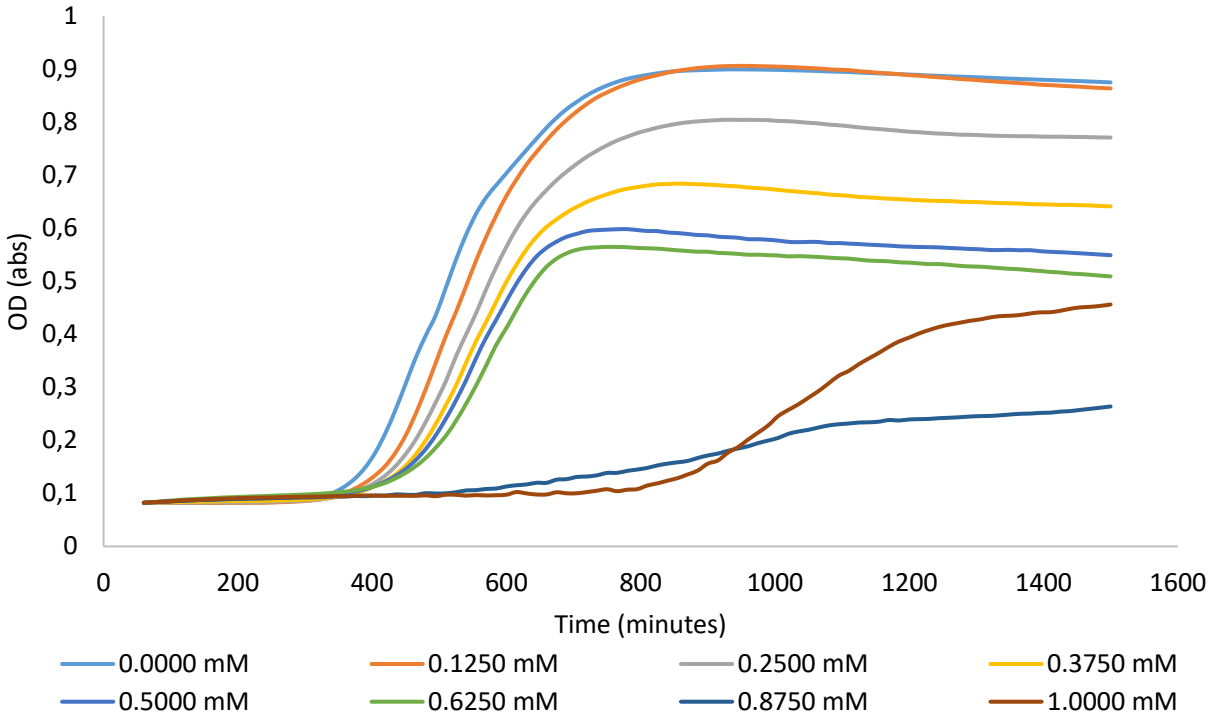

Figure 79: Average growth curves obtained for MRSA USA300 in the presence of compound **4** at eight different concentrations. Optical density (OD) relates to the number of cells present.

The same can be observed in all the 1:1 mixtures including these compounds – **1** and **2**, **1** and **4**, **2** and **4** shown in Figures 80 – 82. The mixtures kill the bacteria at lower concentrations, compared to the concentrations observed for the compounds when they are by themselves.

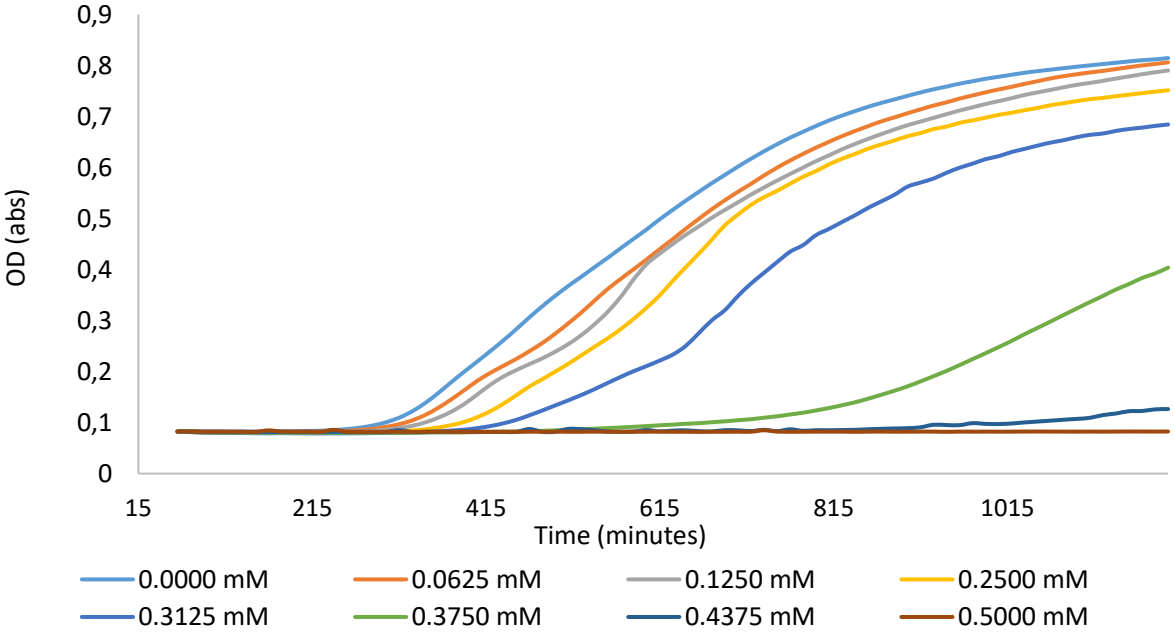

Figure 80: Average growth curves obtained for MRSA USA300 in the presence of compounds **1** and **2** (1:1 mixture) at eight different concentrations. Optical density (OD) relates to the number of cells present.

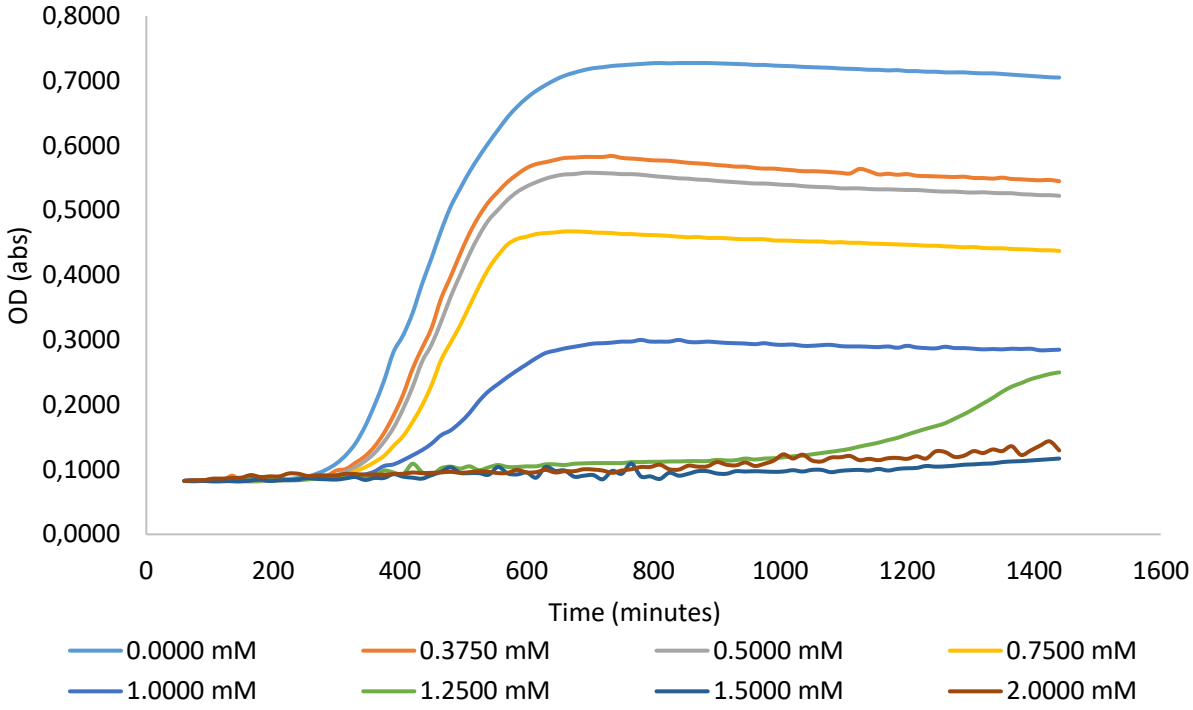

Figure 81: Average growth curves obtained for MRSA USA300 in the presence of compounds **1** and **4** (1:1 mixture) at eight different concentrations. Optical density (OD) relates to the number of cells present.

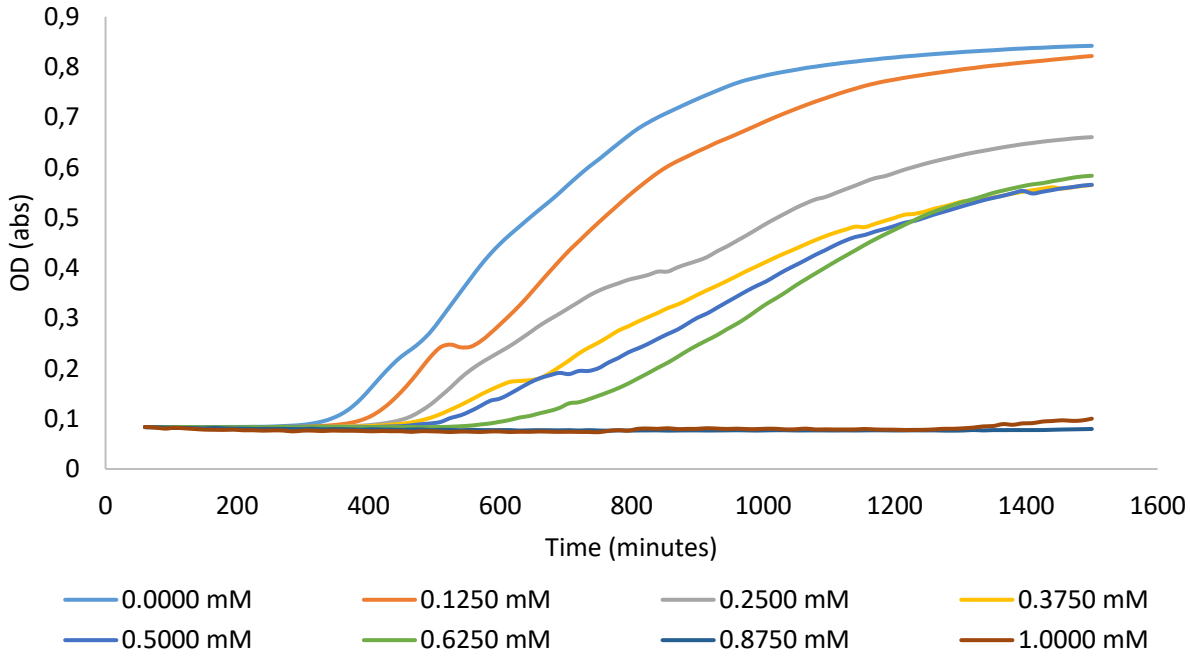

Figure 82: Average growth curves obtained for MRSA USA300 in the presence of compounds **2** and **4** (1:1 mixture) at eight different concentrations. Optical density (OD) relates to the number of cells present.

A summary of the calculated MIC_{50} results from all individual amphiphiles and 1:1 mixtures can be observed in Table 14 and a graphical representation with a comparable concentration of 0.3750 mM can be seen in Figure 83. By comparing the MIC_{50} values for single compounds **1**, **2** and **4** it can be established that compound **2** has the lowest MIC_{50} value of 0.4638 mM compared to that of compound **4** (0.6068 mM) and compound **1** (0.7146 mM). A low MIC_{50} would mean a more effective antimicrobial agent. This gives the following trend **2** > **4** > **1** indicating that **2** (being an anthracene-based and having a sulphonate anion) has a higher antimicrobial activity and is considered a more effective antimicrobial compared to **4** (anthracene-based and having a carboxylate anion) and **1** (being anthraquinone based and having a sulphonate anion). This shows that by swapping an electron poor system for an electron rich one, both having a sulphonate anion, the activity of the potential antibiotic towards the bacteria increases.The results for the mixtures on the other hand, showed that by having both the anthraquinone (electron poor) and anthracene (electron rich) based compounds (**1** and **2**) with sulphonate anions there is an even bigger decrease in the MIC_{50} (0.3352 mM) when compared to the compounds alone, meaning that these self-association complexes have a higher antimicrobial activity when they are together compared to when they are observed individually. Adding a mixture of two anthracene-based amphiphiles to the microbial culture also showed an increase in the antimicrobial activity. This is observed for 1:1 mix of compound **2** and **4** which gave an MIC_{50} value of 0.3169 mM. This combination has the same electron rich system, however, it also has two different anions – sulphonate and carboxylate. Compared to the final one with **1** and **4** with an MIC_{50} value of 0.7505 mM where no apparent decrease of the MIC_{50} was observed, making it less effective compared to **1** and **2**, **2** and **4** as shown in Table 14. The final results show the following trend (lowest MIC_{50} with the highest antimicrobial effect to highest MIC_{50}, lowest effect): **2** and **4** = **1** and **2** < **2** < **4** < **1** < **1** and **4**. From this trend, it can be established that the mixtures which have the highest antimicrobial effect are **2** and **4**, along with **1** and **2.**

The least effect can be seen with mix of **1** and **4.** This also shows that these compounds work better as antimicrobials when they are together, compared to when they are observed individually. Along with that, the significance in the presence of both anthraquinone (electron poor) and anthracene (electron rich) based systems was established, in the case of 1:1 mix of **1** and **2**. This also suggested that the effect of these antimicrobial amphiphiles depends on the supramolecular self-association processes which occur on the surface of the bacterial cell wall. These processes create self-associated complex structures which disrupt the cellular membrane, thus preventing the bacterial cells from growing. From this, it is proposed that presence of both electron poor and electron rich systems, along with ionic interactions and hydrogen bonding is essential in order to stabilise the structures being formed, which then leads to an increase in their antimicrobial efficacy. The graphs used in calculating the MIC_{50} can be observed in the appendix Figures S159 – S164.

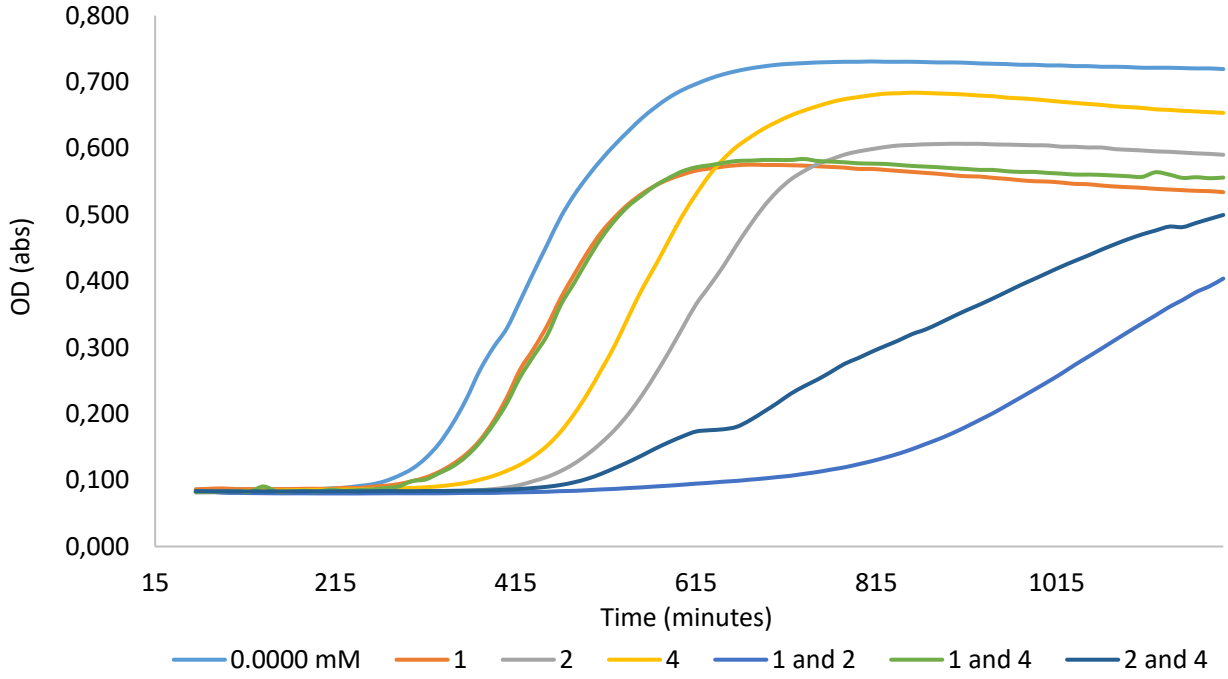

Figure 83: Growth curve for clinical isolates of MRSA in the presence and absence of **1**, **2**, **4** and 1:1 mixtures of those three amphiphiles at a total molar concentration = 0.3750 mM. Optical density (OD) relates to the number of cells present.

Table 14: MIC_{50} values calculated for compounds **1**, **2**, **4** and their 1:1 mixtures against MRSA UAS300.

Compound	MIC_{50}	
	mM	μg/mL
1	0.7146	431.1539
2	0.4638	264.9921
4	0.6068	324.8200
1 and **2**	0.3352	397.2835
1 and **4**	0.7505	854.5568
2 and **4**	0.3169	350.6974

A series of experiments were carried out against–ve Escherichia coli (E.*coli).*The results, however, showed no antimicrobial activity against this type of bacteria for all amphiphiles **1**, **2**, **4** and 1:1 mixtures of **1** and **2**, **1** and **4**, **2** and **4**, thus the MIC_{50} could not be calculated. An example of the growth curve for compound **1** against *E.coli* is shown in Figure 84. A limitation to this experiment, however, was the fact that each compound was repeated only once, while for MRSA each compound was repeated six times in order to make sure the results were consistent and accurate. Therefore, this experiment needs to be carried out several more times in order to fully explore the effect of this series of amphiphiles against Gram -ve *E. coli*. The rest of the growth curve graphs can be found in the appendix Figures S165 – S169.

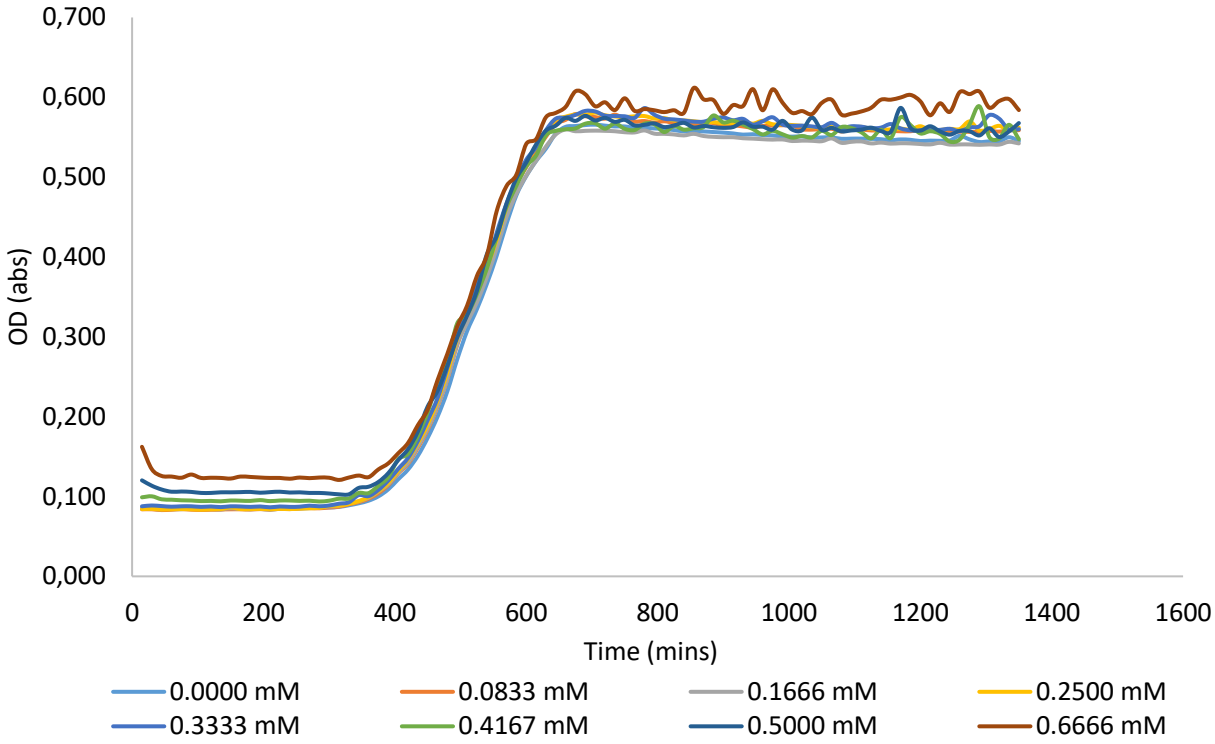

Figure 84: Average growth curves obtained for *E.coli* in the presence of compounds **1** at eight different concentrations. Optical density (OD) relates to the number of cells present.

6. Conclusion

In conclusion, a new group of electron rich (anthracene) and electron poor (anthraquinone) based amphiphiles were synthesised and their self-association properties were studied. These compounds were observed individually **1** and **4**, as well as part of a mixture **1** and **2**, **1** and **4**, **2** and **4**. As mentioned before, results for **2** for some of the studies have been reported by Hiscock and co-workers. It has been determined that the self-association properties of this series of new amphiphiles depend on the solvent systems in which they are observed, as well as their physical components. Studies in the solid state by solid crystal x-ray diffraction showed the presence of symmetrical dimer formation through the intermolecular binding of four hydrogen bonds observed for compound **1** and **2** individually, as well as an unsymmetrical hydrogen dimer formed in a solution of 1:1 mix containing both **1** and **2**, due to the favourable presence of both an electron rich and electron poor system. This also presumed to affect the selectivity and stability of these dimer complexes. These unsymmetrical and symmetrical dimeric species were also observed in the gas phase using ESI – MS, with both being present in all the 1:1 mixtures while only symmetrical were observed in the individual amphiphiles **1**, **2** and **4**. The quantitative ^{1}H NMR studies for compound **1**, **2** and mix of **1** and **2** showed that the entire compound mass is visible by NMR spectrum, ^{1}H NMR spectrum DOSY studies which confirmed the size of the structures formed not being bigger than 1.41 nm. Followed by the ^{1}H NMR dilution studies which showed the formation of stable hydrogen bonded systems due to the change in the chemical shift observed for compound **1**. For those solutions containing compound **4**, including mix of **1** and **4**, **2** and **4**, the formation of extended large aggregate structures was determined and supported through the results obtained in the quantitative ^{1}H NMR spectrum studies, which showed an apparent loss of compound which could not be observed via the NMR spectrum.

The DLS data showed structures with a diameter ranging between 400 – 500 nm in these instances. Results from the solution state obtained through DLS and quantitative ^{1}H NMR spectrum studies (apparent loss of compound, which could not be seen by the NMR spectrum) in an EtOH: H_2O (1:19) solution showed the presence of extended self-association spherical structures observed for all amphiphiles and 1:1 mixtures. The fluorescence of the amphiphiles **1**, **2**, **4** and mix of **1** and **2** allowed them to be directly observed through fluorescence microscopy. The zeta potential measurements showed that the amphiphiles containing sulphonate ion (**1**, **2**, mix of **1** and **2**) formed more stable structures compared to those containing a carboxylate ion (**4**, **1** and **4**, **2** and **4**). Along with that, the CMC and surface tension studies showed that the formed structures can be stabilised through the presence of both electron poor and electron rich systems (mix of **1** and **2**) which results in a decrease of the CMC, compared to when they are observed individually. The same trend was observed in the antimicrobial studies carried out against Gram +ve Methicillin-resistant *Staphylococcus aureus* (MRSA USA300). From the calculated MIC_{50} values it was determined that the presence of both electron poor and electron rich systems (mix of **1** and **2**) is essential in order to achieve greater antimicrobial efficacy against Gram +ve *MRSA*, thus proving that they work better as antimicrobials when they are together, rather than when they are used individually. It was also determined that further studies need to be carried out in order to fully explore the activity of these amphiphiles against Gram -ve *E.coli*. To conclude, through a series of chemical techniques the self-association properties of this new group of amphiphiles were explored, along with their antimicrobial activity against Gram +ve MRSA USA300, which from the results obtained show their potential of being novel antibiotics.

7. Future work

Initial studies carried out for this series of amphiphiles discussed was aimed at exploring their self-association properties and potential antimicrobial activity against Gram +ve *S.aureus*, as well preliminary studies carried out against Gram -ve *E.coli*.

Future work which can be carried out with these amphiphiles is the following:

- Further testing these amphiphiles and mixtures against Gram -ve *E.coli*, in order to establish whether they have any potential antimicrobial activity against this type of bacteria.
- Further clinical testing of these amphiphiles against pombe cells (imitating human cells) in order to determine whether they are deemed safe and can be used against human cells for further testing
- Substitution of the urea functional group with a thiourea and exploring whether this modification would have any effect over the self-association properties and stability of the amphiphiles

8. Experimental techniques

General remarks: Positive pressure of nitrogen and oven dried glassware were used for all reactions. All solvents and starting materials were purchased from known chemical suppliers or available stores and used without any further purification unless specifically stipulated. The NMR spectra were obtained using a Burker AV2 400 MHz or AVNEO 400 MHz spectrometer. The data was processed using ACD Labs or Topspin software. NMR Chemical shift values are reported in parts per million (ppm) and calibrated to the center of the residual solvent peak set. Tensiometry measurements were undertaken using the Biolin Scientific Theta Attension optical tensiometer. The data was processed using Biolin OneAttension software. A Hamilton (309) syringe was used for the measurements. The melting point for each compound was measured using Stuart SMP10 melting point apparatus. High-resolution mass spectrometry was performed using a Bruker microTOF-Q mass spectrometer and the spectra were recorded and processed using Bruker's Compass Data Analysis software. Infrared spectra were obtained using a Shimadzu IR-Affinity 1 model Infrared spectrometer. The data was analyzed in wavenumbers (cm^{-1}). Fluorescence emission and excitation spectra were obtained using Agilent Technology Cary Eclipse Fluorescence Spectrophotometer and processed using Eclipse ADL (Advanced Reads) software. The results were reported in nm. DLS and Zeta Potential studies were carried out using Anton Paar Litesizer™ 500 and processed using Kalliope™ Professional. Cellular growth curve measurements were obtained using Thermo Scientific Multiscan Go 1510-0318C plate reader and recorded using the SkanIt Software 4.0. Bulk solid-state phase purity was examined using X-ray powder diffraction carried out on a PANalytical Empyrean diffractometer (40.0 kV, 30.0 mA) operating in θ-2θ reflection geometry and equipped with monochromated Cu $K\alpha_1$, λ = 1.5406 Å, X-rays, and a X'Celerator 1D detector.

HRMS: Approximately 1mg of each compound or mixture of compounds was dissolved in 1 mL of methanol. This solution was further diluted 100-fold before undergoing analysis. 10 µL of each sample was then injected directly into a flow of 10 mM ammonium acetate in 95% water (flow rate = 0.02 mL/min).

X-ray powder diffraction: The sample was hand grinded in an agate mortar. The sample was then transferred onto a glass plate and was held there at room temperature. The data was collected in intervals of 0.017° over the course of 14hrs.

Single crystal x-ray studies: a suitable crystal of each amphiphile was selected and mounted on a Rigaku Oxford Diffraction Supernova diffractometer. Data were collected using Cu Kα radiation at 100 K or 293 K as necessary due to crystal instability at lower temperatures. Structures were solved with the ShelXT[159] or ShelXS structure solution programs via Direct Methods and refined with ShelXL[159] on Least Squares minimisation. Olex2[160] was used as an interface to all ShelX programs (CCDC 1866274-1866275).

DLS studies: All vials used for preparing the compound were clean and dry. All solvents used were filtered to remove any particulates that may interfere with the results obtained. Samples of differing concentrations were obtained through serial dilution of a concentrated solution. All samples underwent an annealing process, in which they were heated to 40 ^{o}C before being allowed to cool to 25 ^{o}C. A series of 5 runs were recorded at 40 ^{o}C to check for sample stability before a series of 10 runs were recorded at 25 ^{o}C.

Zeta potential studies: All vials used for preparing the compound were clean dry. All solvents used were filtered to remove any particulates that may interfere with the results obtained. All samples underwent an annealing process in which the various solutions were heated to approximately 40 °C before being allowed to cool to room temperature for 2 mins and then a series of 10 runs were carried out at 25 °C for each sample. Samples of differing concentrations were obtained through serial dilution of an initial stock solution.

Tensiometry studies: All the samples were prepared in a EtOH: H_2O (1:19) solution. All samples underwent an annealing process in which the various solutions were heated to approximately 40 °C before being allowed to cool to room temperature. All samples were prepared through a serial dilution of the most concentrated sample. Three surface tension measurements were obtained for each sample at a given concentration, using the pendant drop method. The average values were then used to calculate the CMC.

Fluorometry studies: All samples were prepared at the highest solubility concentration and underwent a series of dilutions. Glass cuvettes were used for the analysis. The cuvettes were washed with the solvent used which was EtOH: H_2O (1:19). All solutions underwent an annealing process and were allowed to rest for approximately 2 minutes before undergoing analysis.

UV-Vis studies: All samples were prepared at the highest solubility concentration and underwent a series of dilutions. Glass cuvettes were used for the analysis. The cuvettes were washed with the solvent used which was EtOH: H_2O (1:19). A blank was run first before analysing the prepared samples. A spectrum was obtained with the absorption wavelengths for each solution. The values were written down at an equilibrium temperature of 298.15 K.

Titrations (self-association studies): Clean and oven dried vials were used for preparing the samples. The solvent used was dimethyl sulfoxide-d_6 (DMSO). A series of calculations were carried out in order to esteem the amount of host and guest: 0.01 x 1.5 mL = ……..x g/mol (MW) = host (mg) and 0.15 x 1.0 mL = ……..x g/mol (MW) = guest (mg). The host was dissolved in 1.5 mL of DMSO-d_6, from which 0.500 mL was added to an NMR tube. The guest was weighted out on the lid of the vial in which the host was dissolved and both were mixed together (solution used for the additions) Two sets of experiments were run. In the first the host was compound **1** and the guest was compound **2.** They were both switched the other way around for the second set of experiments. A Hamilton TLC syringe was used for the titrations. The set of spectra obtained was that of the host followed by additions of 2 x 10 µL solvent, 8 x 5 µL, 4 x 10 µL and 5 x 50 µL.

Dilution studies: Clean and oven dried vials were used for preparing the samples. The highest concentration which was used for compound **1** was 111.12 mM for 0.500 mL of solvent, whereas for compound **4** was 55.56 mM. The solvent used was DMSO-d_6. A separate 7.5 mL of DMSO: H_2O was made used for the additions. The dilution process was as followed: an initial proton spectrum was obtained of just the compound. Then a series of 4 x 100 µL, in a new vial 500 µL (solution) + 100 µL (solvent) was added (sixth dilution), followed by another series of 5 x 100 µL dilutions, the last four serial dilutions were the same as the sixth dilution. A good shake of the NMR tube was given after each addition, before running the sample.

Fluorescence microscopy and transmission studies: All samples were visualized using an Olympus XI71 microscope with a PlanApo 100x OTIRFM-SP 1.49 NA lens attached to a PIFOC z-axis focus drive (Physik Instrumente, Karlsruhe, Germany), which was placed onto a ASI motorised stage (ASI, Eugene, OR). The objective lens, the environmental chamber along with the sample holder sustained the required temperature.

The samples were illuminated using LED light sources (Cairn Research Ltd, Faversham, UK) using filters suitable for each sample (Chroma, Bellows Falls, VT). Metamorph software (Molecular Devices) software was used to control the settings and analze the images, visualised using Zyla 5.5 (Andor) CMOS camera. 10 µl of each of the appropriate sample was pipetted onto the centre of an agarose pad. Coverslip was used to cover the pipetted sample and was secured in place. Each of the agarose pads was labeled. Filters used in the studies: GFP excitation 480 nm and emission 510 nm, DAPI excitation 360 nm and emission 460 nm.

Self-association constant calculation: Self-association constants were determined using Bindfit v0.5 (http://app.supramolecular.org/bindfit/). All the data can be accessed online using the hyperlinks provided.

MIC^{50} studies:

- **Preparation of luria broth media (LB):** Yeast extract (5 g), tryptone (10 g) and sodium chloride (10 g) were dissolved in milli-q H_2O (1000 mL) then divided into 400 mL bottles and autoclaved.
- **Preparation of luria broth (LB) Agar plates:** Agar (6 g) was added to LB (400 mL) and autoclaved. Once cool, the LB agar was poured into sterile petri dishes under sterile conditions and allowed to set. LB plates were stored at 4 °C until use.
- **Preparation of bacterial plates:** Sterile LB agar plates were streaked using the desired bacteria (MRSA USA300) then incubated in the 25 °C incubator overnight.
- **Preparation of antimicrobial compounds for MIC_{50} studies:** Stock solutions of compounds **1**, **2** and **4** were prepared in a 1:19 EtOH:milli-q H_2O mixture the day of the experiment. Eight concentrations of each compound/mixture were then prepared from the stock solution in the same solvent mixture.

- **Preparation of inoculum:** A starter culture was produced through the innoculation of LB media (5 mL) with ≥ 4 single colonies of the desired bacteria under sterile conditions and incubated at 37 °C overnight. The following day, a subculture was made using LB (5 mL) and the starter culture (100 µL), then incubated at 37 °C until the culture had reached an optical density of 0.4 at 600 nm. Cellular density was then adjusted using sterile milli-q H_2O to equal a 0.5 McFarland Standard ($10^7 – 10^8$ cfu/mL), then a 1:10 dilution was carried out using sterile milli-q H_2O (900 µL) and the McFarland adjusted suspension (100 µL). A final dilution (1:100) was carried out on the 1:10 suspension (150 µL) using LB (14.85 mL) before use (10^5 cfu/mL).
- **Preparation of 96 well microplate:** The 1:100 suspension (90 µL) was pipetted into the desired wells under sterile conditions, then solutions containing **1**, **2**, **5** or 1:1 mixtures of **1**, **2** and **5** (90 µL) were added to the wells to equal a total volume of 180 µL for MRSA USA300, whereas for *E.coli* 140 µL of cells in each of the wells + 60 µL of compound, making the entire volume 200 µL. The plates were sealed using Parafilm, then incubated at 37 °C in a microplate reader for 18-25 hours. An absorbance reading was taken at 600 nm every 15 minutes. Each experiment was repeated three times on two different days giving six repetitions in total.
- **Calculation of MIC_{50}:** Growth curves were plotted using the average of the six comparative absorbance readings in Microsoft Excel. The MIC_{50} value was determined by plotting the average absorbance reading obtained at 900 minutes for each compound concentration in Origin. The resulting curve was [normalized] and fitted using the Boltzmann fit, and the equation from this fit was used to calculate the MIC_{50}.

9. Synthesis

TBA aminomethanesulphonate: TBA hydroxide (1N) in methanol (1.71 mL) was added to aminomethanesulfonic acid (0.19 g, 1.71 mM) at room temperature and taken to dryness. Assumed Yield 100 % (0.60 g, 1.71 mM).

Compound 1: A solution of 2-aminoanthraquinone (0.67 g, 3.01 mM) and triphosgene (0.45 g, 1.50 mM) in ethyl acetate (30 mL) was heated at reflux for four hours. TBA aminomethanesulphonate (1.06 g, 3.01 mM) in ethyl acetate (10 mL) was added to the reaction mixture, which then heated at reflux overnight. The resultant mixture was filtered and the solid isolated was dissolved in methanol (15 mL). Any remaining solid was removed by filtration and the filtrate taken to dryness and the resultant solid re-dissolved in chloroform (20 mL) and washed with water (1 x 10 mL). The organic layer was then taken to dryness to give the final product as an orange solid (0.41 g, 0.68 mM). Yield: 23%; mp: 145 °C; ^{1}H NMR (400 MHz, DMSO-d_6): δ:9.68 (s,1H,NH), 8.25 (d, J = 2.1 Hz, 1H), 7.97 – 7.86 (m, 3H), 7.76 – 7.73 (m, 2H), 7.59 (d, J = 8.5 Hz, 1H), 7.51 (br t, 1H, NH), 4.03 (d, J = 5.7 Hz, 2H), 3.17 – 3.13 (m, 8H), 1.59 – 1.51 (m, 8H), 1.34 – 1.25 (m, 8H), 0.92 (t, J = 7.3 Hz, 12H); ^{13}C{^{1}H} NMR (100 MHz, DMSO-d_6): δ:182.8 (C=O), 181.3 (C=O), 154.4 (C=O), 147.0 (ArC), 134.6 (ArCH), 134.2 (ArCH), 134.1 (ArC), 133.3 (ArC), 133.3 (ArC), 128.3 (ArCH), 126.8 (ArCH), 126.7 (ArCH), 126.1 (ArC), 122.8 (ArCH), 114.3 (ArCH), 58.0 (CH_2), 56.4 (CH_2), 23.5 (CH_2), 19.7 (CH_2), 13.9 (CH_3); IR (film): ν (cm^{-1}) = 3269 (NH stretch), 1670, 1209, 1177, 853; HRMS for the sulphonate-urea ion ($C_{16}H_{13}N_2O_6S$) (ESI^-): m/z: act: 359.0339 $[M]^-$ cal: 359.0343 $[M]^-$.

Compound 2: This compound was synthesised in line with previously published methods.[2] The proton spectrum matches previously reported data.[41] ^{1}H NMR (400 MHz, DMSO-d_6): δ:9.14 (s,1H,NH), 8.40 (s,1H), 8.29 (s,1H), 8.22 (s,1H), 7.99 – 7.93 (m,3H), 7.45 – 7.37 (m,3H), 6.88 (t, J = 5.9 Hz, 1H), 4.00 (d, J = 5.9 Hz, 2H), 3.14 – 3.10 (m, 8H), 1.57 – 1.49 (m, 8H), 1.33 – 1.23 (m, 8H), 0.92 (t, J = 7.3 Hz, 12H).

Compound 3: A solution of 2-aminoanthracene (0.50 g, 2.58 mM) and triphosgene (0.38 g, 1.29 mM) in ethyl acetate (35 mL) was heated at reflux for 4 hours. *Tert*-butyl 2-aminoacetate (0.34 mL, 2.58 mM) was then added to the reaction mixture. This mixer was then heated at reflux overnight. The resultant mixture was then filtered ant the final product obtained as a grey solid (0.55 g, 1.57 mM). Yield: 61.0%; mp: > 200 °C; ^{1}H NMR (400 MHz, DMSO-d_6): δ:9.09 (s,1H, NH), 8.44 (s, 1H), 8.34 (s, 1H), 8.22 (s,1H), 8.01 – 7.97 (m, 3H), 7.47 – 7.39 (m, 3H), 6.53 (t, J = 5.9 Hz, 1H), 3.83 (d, J = 5.9 Hz, 2H), 1.44 (s, 9H); ^{13}C{^{1}H} NMR (100 MHz, DMSO-d_6): δ:170.4 (C=O), 155.8 (C=O), 137.8 (ArC), 132.6 (ArC), 132.2 (ArC), 130.4 (ArC), 129.2 (ArCH), 128.5 (ArCH), 128.5 (ArC), 128.0 (ArCH), 126.2 (ArCH), 126.0 (ArCH), 125.0 (ArCH), 124.6 (ArCH), 121.3 (ArCH), 111.5 (ArCH), 81.1(C) , 42.5 (CH_2), 28.3 (CH_3); IR (film): ν (cm^{-1}) = 3308 (NH stretch), 1653, 1244, 1161, 889; HRMS ($C_{21}H_{22}N_2O_3$) (ESI^-): m/z: act: 349.1628 $[M]^-$ cal: 349.1557 $[M]^-$.

Compound 4: Compound **3** (0.90 g, 2.59 mM) was dissolved in dichloromethane (50 mL) and trifluoroacetic acid (8 mL) and stirred for 1 hour. The mixture was then washed with sodium hydroxide (50 mL, 6 M) and the resultant green solid (0.70 g) isolated by filtration and dissolved in methanol (20 mL). To this solution was added TBA hydroxide (1N) in methanol (2.32 mL). This solution was passed through a biotage SCX(II) column and the TBA:carboxylate ratio equilibrated through the further addition of TBA hydroxide (1N) in methanol, resulting in the isolation of the pure product as a yellow-green solid (0.78 g, 1.46 mM). Yield: 56%; mp: > 200 °C; ^{1}H NMR (400 MHz, DMSO-d_6): δ:9.88 (s, 1H, NH), 8.40 (s, 1H), 8.29 (s, 2H), 8.00 – 7.93 (m, 3H), 7.55 (d, J = 9.1 Hz, 1H), 7.45 – 7.37 (m, 2H), 6.98 (s, 1H, NH), 3.64 (d, J = 4.4 Hz, 2H), 3.15 – 3.11 (m, 8H), 1.57 – 1.50 (m, 8H), 1.33 – 1.24 (m, 8H), 0.92 (t, J = 7.2 Hz, 12H); ^{13}C{^{1}H} NMR (100 MHz, DMSO-d_6): δ:172.6 (CO), 155.8 (CO), 138.8 (ArC), 132.9 (ArC), 132.2 (ArC), 130.2 (ArC), 129.0 (ArCH), 128.5 (ArCH), 128.4 (ArC), 128.0 (ArCH), 126.2 (ArCH), 125.8 (ArCH), 124.7 (ArCH), 124.3 (ArCH), 121.7 (ArCH), 110.6 (ArCH), 58.0 (CH_2), 44.2 (CH_2), 23.5 (CH_2), 19.7 (CH_2), 14.0 (CH_3);IR (film): ν (cm^{-1}) = 3332.99 (NH stretch), 1684, 1225, 1163, 889; HRMS for the carboxylate-urea ion ($C_{17}H_{13}N_2O_3^-$) (ESI^-): m/z: act: 293.0932 $[M]^-$ cal: 293.0932 $[M]^-$.

10. References

1 T. R. Kelly and M. H. Kim, *J. Am. Chem. Soc.*, 1994, **116**, 7072–7080.
2 L. J. White, N. J. Wells, L. R. Blackholly, H. J. Shepherd, B. Wilson, G. P. Bustone, T. J. Runacres and J. R. Hiscock, *Chem. Sci.*, 2017, **8**, 7620–7630.
3 J.-M. Lehn, *Proc. Natl. Acad. Sci. U. S. A.*, 2002, **99**, 4763–8.
4 J.-M. Lehn, *Angew. Chemie Int. Ed. English*, 1988, **27**, 89–112.
5 C. J. Pedersen, *Angew. Chemie Int. Ed. English*, 1988, **27**, 1021–1027.
6 R. J. Gillespie and E. A. Robinson, *J. Comput. Chem.*, 2007, **28**, 87–97.
7 G. N. Lewis, *J. Am. Chem. Soc.*, 1916, **38**, 762–785.
8 Khan Academy, Ionic, covalent, and metallic bonds (video) | Khan Academy, https://www.khanacademy.org/science/biology/chemistry--of-life/chemical-bonds-and-reactions/v/ionic-covalent-and-metallic-bonds, (accessed 8 September 2018).
9 P. Hobza, R. Zahradník and K. Müller-Dethlefs, *Collect. Czechoslov. Chem. Commun.*, 2006, **71**, 443–531.
10 P. D. Beer, P. A. Gale and D. K. Smith, *Supramolecular chemistry*, Oxford University Press, 1999.
11 J. L. Atwood and J. W. Steed, *Supramolecular chemistry*, Wiley, 2013.
12 W. M. Latimer and W. H. Rodebush, *J. Am. Chem. Soc.*, 1920, **42**, 1419–1433.
13 J. N. Israelachvili, *Intermolecular and surface forces*, Academic Press, 2011.
14 and C. D. S. Mutasem Omar Sinnokrot, *J. Phys. Chem. A*, 2003, **107**, 8377–8379.
15 Eun Cheol Lee, Byung Hee Hong, Ju Young Lee, Jong Chan Kim, Dongwook Kim, Yukyung Kim, † and P. Tarakeshwar and K. S. Kim*, *J. Am. Chem. Soc*, 2005, **127**, 4530–4537.
16 B. L. Schottel, H. T. Chifotides and K. R. Dunbar, 2008, **37**, 1–236.
17 D. A. Dougherty, *Acc. Chem. Res.*, 2013, **46**, 885–893.
18 C. A. Hunter, K. R. Lawson, J. Perkins and C. J. Urch, *J. Chem. Soc*, 2001, 651–669.
19 J. W. Steed, D. R. Turner and K. J. Wallace, *Core concepts in supramolecular chemistry and nanochemistry*, John Wiley, 2007.
20 E. Arunan, G. R. Desiraju, R. A. Klein, J. Sadlej, S. Scheiner, I. Alkorta, D. C. Clary, R. H. Crabtree, J. J. Dannenberg, P. Hobza, H. G. Kjaergaard, A. C. Legon, B. Mennucci and D. J. Nesbitt, *Pure Appl. Chem*, 2011, **83**, 1619–1636.
21 K. Roy, S. Kar, R. N. Das, K. Roy, S. Kar and R. N. Das, *Underst. Basics QSAR Appl. Pharm. Sci. Risk Assess.*, 2015, 1–46.
22 H. F. Lodish, *Molecular cell biology*, W.H. Freeman, 2000.
23 Pat B. · Jackie Shlecter, What type of intermolecular force would water molecules have? London dispersion? Dipole dipole? Or hydrogen bonding? | Socratic, https://socratic.org/questions/what-type-of-intermolecular-force-would-water-molecules-have-london-dispersion-d, (accessed 2 October 2018).
24 P. Panini and D. Chopra, in *Lecture Notes in Chemistry*, 2015, pp. 37–67.
25 G. R. Desiraju, *Angew. Chemie - Int. Ed.*, 2011, **50**, 52–59.
26 T. Steiner, *Angew. Chem. Int. Ed.*, 2002, **41**, 48–76.
27 G. Yu, K. Jie and F. Huang, *Chem. Rev.*, 2015, **115**, 7240–7303.
28 R. M. Izatt, K. Pawlak, J. S. Bradshaw and R. L. Bruening, *Chem. Rev.*, 1991, **91**, 1721–2085.
29 H. Margenau, *Rev. Mod. Phys.*, 1939, **11**, 1–35.
30 E. Fischer, *Personal Life and Early Education*, 2011, vol. 6.
31 D. J. Cram and J. M. Cram, *Science (80-.).*, 1974, **183**, 803–809.
32 Y. H. Ko, I. Hwang, D.-W. Lee and K. Kim, *Isr. J. Chem.*, 2011, **51**, 506–514.
33 U. Boas and P. M. H. Heegaard, *Chem. Soc. Rev.*, 2004, **33**, 43.
34 N. Kishi, M. Akita and M. Yoshizawa, *Angew. Chemie*, 2014, **126**, 3678–3681.
35 C.A. Hunter, *Angewandte International edition – chemie,* 2004, **43**, (40), 5310-5324.
36 G. Wenz, *Clin. Drug Investig.*, 2000, **19**, 21–25.

37 H. Yang, B. Yuan, X. Zhang and O. A. Scherman, *Acc. Chem. Res.*, 2014, **47**, 2106–2115.
38 D. Quane, *Bull. Hist. Chem*, 1990, **7**, 3–13.
39 A. L. McClellan, *J. Chem. Educ.*, 1967, **44**, 547.
40 O. Khakshoor, S. E. Wheeler, K. N. Houk and E. T. Kool, *J. Am. Chem. Soc.*, 2012, **134**, 3154–63.
41 B. Galdino De Oliveira, R. De Cássia and M. Ugulino De Araújo, *6 Hydrogen Bonds and Stacking Interactions on the DNA Structure: A Topological View of Quantum Computing*, .
42 H.-J. Schneider and A. K. Yatsimirsky, *Chem. Soc. Rev.*, 2008, **37**, 263–277.
43 L. Hedstrom, in *Encyclopedia of Life Sciences*, John Wiley & Sons, Ltd, Chichester, UK, 2010.
44 E. T. Kool, *HYDROGEN BONDING, BASE STACKING, AND STERIC EFFECTS IN DNA REPLICATION*, 2001.
45 K. Morokuma, *Acc. Chem. Res.*, 1977, **10**, 294–300.
46 C. A. Schalley and Wiley InterScience (Online service), *Analytical methods in supramolecular chemistry*, Wiley-VCH, 2007.
47 L. Fabbrizzi, *Cryptands and cryptates*, .
48 A. M. (Abel M. oğlu) Mähärrämov, K. T. Mahmudov, M. N. Kopylovich and A. J. L. (Armando J. L. . Pombeiro, *Non-covalent interactions in the synthesis and design of new compounds*, .
49 A. Harada, R. Kobayashi, Y. Takashima, A. Hashidzume and H. Yamaguchi, *Nat. Chem.*, 2011, **3**, 34–37.
50 A. Mateo-Alonso, *Chem. Commun.*, 2010, **46**, 9089.
51 K. Hanada, K. Kumagai, S. Yasuda, Y. Miura, M. Kawano, M. Fukasawa and M. Nishijima, *Nature*, 2003, **426**, 803–809.
52 L. Chen, X. Wang, W. Lu, X. Wu and J. Li, *Chem. Soc. Rev.*, 2016, **45**, 2137–2211.
53 P. A. Monnard and D. W. Deamer, *Minimal Cell Biophys. Cell Compart. Orig. Cell Funct.*, 2011, **207**, 123–151.
54 J. A. A. W. Elemans, A. E. Rowan and R. J. M. Nolte, *J. Mater. Chem.*, 2003, **13**, 2661–2670.
55 G. V. Jensen, R. Lund, J. Gummel, M. Monkenbusch, T. Narayanan and J. S. Pedersen, *J. Am. Chem. Soc.*, 2013, **135**, 7214–7222.
56 A. R. Sapala, S. Dhawan and V. Haridas, *RSC Adv.*, 2017, **7**, 26608–26624.
57 P. L. Yeagle and P. L. Yeagle, *Membr. Cells*, 2016, 219–268.
58 T. Kunitake, *Angew. Chemie Int. Ed. English*, 1992, **31**, 709–726.
59 Y. Huang, H. Yu, L. Guo and Q. Huang, *J. Phys. Chem. B*, 2010, **114**, 7719–26.
60 M. . Hans and A. . Lowman, *Curr. Opin. Solid State Mater. Sci.*, 2002, **6**, 319–327.
61 Viktor Nedovica, * A. K., Verica Manojlovicb, Steva Levica, Branko and Bugarski, *Procedia Food Sci.*, 2011, **1**, 1806 – 1815.
62 J. Seo, J. W. Chung, E.-H. Jo and S. Y. Park, *Chem. Commun.*, 2008, **0**, 2794.
63 N. H. Evans and P. D. Beer, *Angew. Chemie - Int. Ed.*, 2014, **53**, 11716–11754.
64 J. P. Dzoyem and J. N. Eloff, *Toxicol. Surv. African Med. Plants*, 2014, 659–715.
65 N. Busschaert, C. Caltagirone, W. Van Rossom and P. A. Gale, *Chem. Rev.*, 2015, **115**, 8038–8155.
66 P. D. Beer and P. A. Gale, *Angew. Chemie Int. Ed.*, 2001, **40**, 486–516.
67 M. A. Hossain, R. A. Begum, V. W. Day and K. Bowman-James, in *Supramolecular Chemistry*, John Wiley & Sons, Ltd, Chichester, UK, 2012.
68 X.-F. Shang and X.-F. Xu, *Biosystems*, 2009, **96**, 165–171.
69 N. Busschaert, M. Wenzel, M. E. Light, P. Iglesias-Hern Andez, R. P. Erez-Tom and P. A. Gale, *J. Am. Chem. Soc*, 2011, **133**, 14136–14148.
70 J. L. Cook, C. A. Hunter, C. M. R. Low, A. Perez-Velasco and J. G. Vinter, *Angew. Chemie Int. Ed.*, 2007, **46**, 3706–3709.
71 D. Lombardo, M. A. Kiselev, S. Magazù and P. Calandra, *Adv. Condens. Matter Phys.*, 2015, **2015**, 1–22.
72 ScienceStruck Staff, A Detailed Account of Micelle Function, Structure, and its Formation, https://sciencestruck.com/micelle-function-structure-formation, (accessed 4 October 2018).

73 X. Cui, S. Mao, M. Liu, H. Yuan and Y. Du, *Langmuir*, 2008, **24**, 10771–10775.
74 C. O. Rangel-Yagui, A. Pessoa-Jr and D. Blankschtein, *Brazilian J. Chem. Eng.*, 2004, **21**, 531–544.
75 C. O. Rangel-Yagui, A. Pessoa and L. C. Tavares, *J. Pharm. Pharm. Sci.*, 2005, **8**, 147–65.
76 M. Zhang, T. Dai and N. Feng, *Nanoscale Res. Lett.*, 2017, **12**, 274.
77 Bengt Kronberg Krister Holmberg Björn Lindman, in *Surface Chemistry of Surfactants and Polymers*, John Wiley & Sons, Ltd, Chichester, UK, 2014, pp. 1–47.
78 B. E. Rapp and B. E. Rapp, *Microfluid. Model. Mech. Math.*, 2017, 421–444.
79 H. Demissie and R. Duraisamy, *J. Sci. Innov. Res.*, 2016, **5**, 208–214.
80 R. Azarmi and A. Ashjaran, *Available online www.jocpr.com J. Chem. Pharm. Res.*, 2015, **7**, 632–640.
81 C. Wang, Z. Wang and X. Zhang, *Acc. Chem. Res.*, 2012, **45**, 608–618.
82 Célia M.C. Faustino, Calado AR and Luís Garcia-Rio, *J. Colloid Interface Sci.* , 2010, **351**, 472–477.
83 J. R. Hiscock, G. P. Bustone, B. Wilson, K. E. Belsey and L. R. Blackholly, *Soft Matter*, 2016, **12**, 4221–4228.
84 L. J. White, S. N. Tyuleva, B. Wilson, H. J. Shepherd, K. K. L. Ng, S. J. Holder, E. R. Clark and J. R. Hiscock, *Chem. - A Eur. J.*, 2018, **24**, 7761–7773.
85 E. Stratan, N. Ţurcan, V. Crudu, E. Romancenco, T. Cotelea, G. Mihai Niţulescu, C. Chiriţă and L. Moruşciag, *BIOLOGICAL EVALUATION OF NEW 2-PHENETHYLBENZOYL THIOUREA DERIVATIVES AS ANTITUBERCULOSIS AGENTS*, 2018, vol. 66.
86 C. Y. and and K. Mosbach*, *J. Org. Chem*, 1997, **62 (12)**, 4057–4064.
87 S. Ikedu, Y. Nishimura and T. Arai, *J. Phys. Chem. A*, 2011, **115**, 8227–8233.
88 A. A. Bunaciu, E. gabriela Udriştioiu and H. Y. Aboul-Enein, *Crit. Rev. Anal. Chem.*, 2015, **45**, 289–299.
89 J.-P. Zhang, P.-Q. Liao, H.-L. Zhou, R.-B. Lin and X.-M. Chen, *Chem. Soc. Rev.*, 2014, **43**, 5789–5814.
90 *Crystallography: Understanding the Nature of Chemical Bonds and Molecular Structure*, 2014.
91 N. ElBakali-Kassimi, E. F. Archibong and A. J. Thakkar, *J. Mol. Struct. THEOCHEM*, 2002, **591**, 189–197.
92 B. A. Shirley, P. Stanssens, U. Hahn and C. N. Pace, *Biochemistry*, 1992, **31**, 725–732.
93 C. Dalvit and A. Vulpetti, *Che mMedChem*, 2012, **7**, 262–272.
94 C. K. Das and N. S. Das, *J. Chem. Technol. Biotechnol.*, 2007, **32**, 643–649.
95 G. Hildebrandt, *Cryst. Res. Technol.*, 1993, **28**, 747–766.
96 D. Louër, *Encycl. Spectrosc. Spectrom.*, 1999, 1865–1875.
97 A. Chauhan and P. Chauhan, *J. Anal. Bioanal. Tech.*, 2014, **5**, 1–5.
98 Damodara. M. Poojary. and and A. Clearfield*, *Acc. Chem. Res.,* 1997, **30**, pp 414–422.
99 J. C. J. Marta J.K. Flohr, Frank T. Dulong, *X-Ray Powder Diffraction*, 1997.
100 J. G. Dillard, *Chem. Rev.*, 1973, **73**, 589–643.
101 C. S. Ho, C. W. K. Lam, M. H. M. Chan, R. C. K. Cheung, L. K. Law, L. C. W. Lit, K. F. Ng, M. W. M. Suen and H. L. Tai, *Clin. Biochem.*, 2003, **24**, 3–12.
102 P. L. Urban, *Philos. Trans. R. Soc. A Math. Phys. Eng. Sci.*, 2016, **374**, 20150382.
103 T. D. Veenstra, *Electrospray ionization mass spectrometry in the study of biomolecular non-covalent interactions*, 1999, vol. 79.
104 C. C. Liou, H. F. Wu and J. S. Brodbelt, *J. Am. Soc. Mass Spectrom.*, 1994, **5**, 260–273.
105 C. A. Bunton, *MEDIUM EFFECTS OF MICELLES AS MICROREACTORS AND THE SCOPE OF THE HUGHES-INGOLD SOLVENT THEORY*, 1996, vol. 19.
106 J. L. Anderson, V. Pino, E. C. Hagberg, V. V. Sheares and D. W. Armstrong, *Chem. Commun.*, 2003, **0**, 2444.
107 V. M. Wallace, N. R. Dhumal, F. M. Zehentbauer, H. J. Kim and J. Kiefer, *J. Phys. Chem. B*, 2015, **119**, 14780–14789.
108 A. Chand and S. Chowdhuri, *J. Chem. Sci*, 2016, **128**, 991–1001.
109 W. I. Goldburg, *Am. J. Phys.*, 1999, **67**, 1152.

110 Malvern Instruments, *Dynamic Light Scattering: An Introduction in 30 Minutes*, • Worcestershire.
111 L. Øgendal, *Light Scattering a brief introduction*, 2016.
112 T. Provder, *Prog. Org. Coatings*, 1997, **32**, 143–153.
113 S. Bhattacharjee, *Control. Release*, 2016, **235**, 337–351.
114 H. S. Jeffrey Bodycomb, Interpreting and Understanding Dynamic Light Scattering Size Data, https://www.slideshare.net/HORIBA/interpreting-and-understanding-dynamic-light-scattering-size-data, (accessed 14 September 2018).
115 E. J. Cabrita and S. Berger, *Magn. Reson. Chem.*, 2001, **39**, S142–S148.
116 C. B. Minkenberg, L. Florusse, R. Eelkema, G. J. M. Koper and J. H. van Esch, *J. Am. Chem. Soc.*, 2009, **131**, 11274–11275.
117 I. Horman and B. Dreux, *Helv. Chim. Acta*, 1984, **67**, 754–764.
118 A. Macchioni, G. Ciancaleoni, C. Zuccaccia and D. Zuccaccia, *Chem. Soc. Rev.*, 2008, **37**, 479–489.
119 J. P. Patterson, M. P. Robin, C. Chassenieux, O. Colombani and R. K. O'reilly, *Chem. Soc. Rev*, 2014, **43**, 2412.
120 P. Jonkheijm, P. van der Schoot, A. P. H. J. Schenning and E. W. Meijer, *Science*, 2006, **313**, 80–3.
121 C. Kulkarni, E. W. Meijer and A. R. A. Palmans, *Acc. Chem. Res.*, 2017, **50**, 1928–1936.
122 G. Whitesides, J. Mathias, C. Seto and S. V. Kolotuchin, *Science (80-.).*, 1991, **254**, 1312–1319.
123 P. Besenius, *J. Polym. Sci. Part A Polym. Chem.*, 2017, **55**, 34–78.
124 L. K. S. Von Krbek, C. A. Schalley and P. Thordarson, *2622 | Chem. Soc. Rev*, 2017, **46**, 2622.
125 Meijer, BindFit v0.5 | Supramolecular, http://app.supramolecular.org/bindfit/, (accessed 16 September 2018).
126 A. Bhattarai, S. K. Shah and A. K. Yadav, *Nepal J. Sci. Technol.*, 2012, **13**, 89–93.
127 S.-Y. Lin, Y.-Y. Lin, E.-M. Chen, C.-T. Hsu and C.-C. Kwan, *Langmuir*, **1999**, *15* (13), pp 4370–4376
128 Piñeiro A[1], Banquy X, Pérez-Casas S, Tovar E, García A, Villa A, Amigo A, Mark AE, Costas M, J Phys Chem B. 2007 May 3;111(17):4383-92.
129 M. Instruments, *Tech Note: Zeta potential - An introduction in 30 minutes*, .
130 J. D. Clogston and A. K. Patri, in *Methods in molecular biology (Clifton, N.J.)*, 2011, vol. 697, pp. 63–70.
131 R. W. O'Brien, B. R. Midmore, A. Lamb and R. J. Hunter, *Faraday Discuss. Chem. Soc.*, 1990, **90**, 301.
132 H. Ghahremani, A. Moradi, J. Abedini-Torghabeh and S. M. Hassani, *Der Chem. Sin.*, 2011, 212–221.
133 J. K. Ferri and K. J. Stebe, *Adv. Colloid Interface Sci.*, 2000, **85**, 61–97.
134 X. Peng, F. Song, E. Lu, Y. Wang, W. Zhou, J. Fan and Y. Gao, *J. AM. CHEM. SOC*, 2005, **127**, 5.
135 Z. Zhang and S. Achilefu, *Org. Lett.*, 2004, **6**, 2067–70.
136 M. V Sednev, V. N. Belov and S. W. Hell, *Methods Appl. Fluoresc.*, 2015, **3**, 042004.
137 S. J. Sahl, S. W. Hell and S. Jakobs, *Nat. Rev. Mol. Cell Biol.*, 2017, **18**, 685–701.
138 S. V. Rogozhin, E. M. Belavtseva, E. S. Vainerman, L. G. Radchenko, P. P. Pivovarov, T. O. Golovina and F. V. Pertsevoy, *Food/Nahrung*, 1984, **28**, 165–171.
139 S. Shashkova and M. C. Leake, *Biosci. Rep.*, 2017, **37**, 1–19.
140 P. A. Levin, *Methods Microbiol.*, 2002, **31**, 115–132.
141 C. Valgas, S. Machado De Souza, ; Elza, F. A. Smânia and A. Smânia, *Brazilian J. Microbiol.*, 2007, **38**, 369–380.
142 M. Frieri, K. Kumar and A. Boutin, *J. Infect. Public Health*, 2017, **10**, 369–378.
143 M. Carrel, E. N. Perencevich and M. Z. David, *Emerg. Infect. Dis.*, 2015, **21**, 1973–80.
144 I. Sondi and B. Salopek-Sondi, *J. Colloid Interface Sci.*, 2004, **275**, 177–182.
145 A. Mai-Prochnow, M. Clauson, J. Hong and A. B. Murphy, *Sci. Rep.*, 2016, **6**, 38610.
146 J. H. Jorgensen, M. J. Ferraro, J. H. Jorgensen and M. J. Ferraro, *Clin. Infect. Dis.*, 2009, **49**, 1749–1755.
147 Linda Bruslind, *Microbiology*, Open Oregon State, 2017.
148 Raina M.Maier, *Environ. Microbiol.*, 2009, 37–54.
149 Gaurab Karki, Bacterial growth curve -, http://www.onlinebiologynotes.com/bacterial-growth-curve/, (accessed 25 September 2018).

150 W. Schaufeli, C. Maslach and T. Marek, *Professional burnout : recent developments in theory and research*, Taylor & Francis, 1993.
151 Nabel A. Negm, Salah M.Tawfik, *Characterization, surface properties and biological activity of some synthesized anionic surfactants*, J. of Industrial and Engineering Chemistry, 2014, p. 1-10.
152 C. Y. Hachem, J. E. Clarridge, R. Reddy, R. Flamm, D. G. Evans, S. K. Tanaka and D. Y. Graham, *Diagn. Microbiol. Infect. Dis.*, 1996, **24**, 37–41.
153 I. Wiegand, K. Hilpert and R. E. W. Hancock, *Nat. Protoc.*, 2008, **3**, 163–175.
154 Jennifer M.Andrews, *Determination of minimum inhibitory concentrations*, 2001.
155 J. H. Jorgensen, M. J. Ferraro, J. H. Jorgensen and M. J. Ferraro, *Clin. Infect. Dis.*, 2009, **49**, 1749–1755.
156 S. Schwarz, P. Silley, S. Simjee, N. Woodford, E. van Duijkeren, A. P. Johnson and W. Gaastra, *J. Antimicrob. Chemother.*, 2010, **65**, 601–604.
157 H. Niu, R. Yee, P. Cui, L. Tian, S. Zhang, W. Shi, D. Sullivan, B. Zhu, W. Zhang and Y. Zhang, *Pathog. (Basel, Switzerland)*, , DOI:10.3390/pathogens6030044.
158 N. Liu, X.-G. Chen, H.-J. Park, C.-G. Liu, C.-S. Liu, X.-H. Meng and L.-J. Yu, *Carbohydr. Polym.*, 2006, **64**, 60–65.
159 G. M. Sheldrick, *Acta Crystallogr. Sect. C, Struct. Chem.*, 2015, **71**, 3–8.
160 O. V. Dolomanov, L. J. Bourhis, R. J. Gildea, J. A. K. Howard and H. Puschmann, *J. Appl. Crystallogr.*, 2009, **42**, 339–341.

Appendix

Table of contents

Characterisation NMR

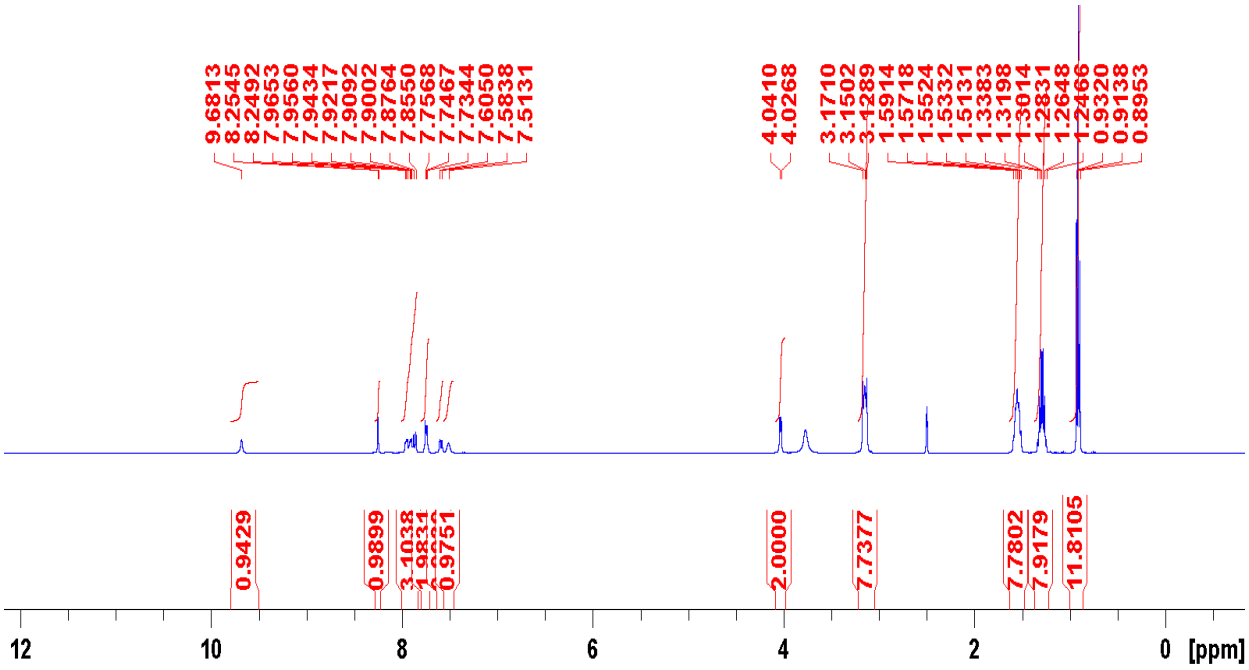

Figure S1: A ^{1}H NMR spectrum of compound **1** in DMSO-d_6 at 298 K.

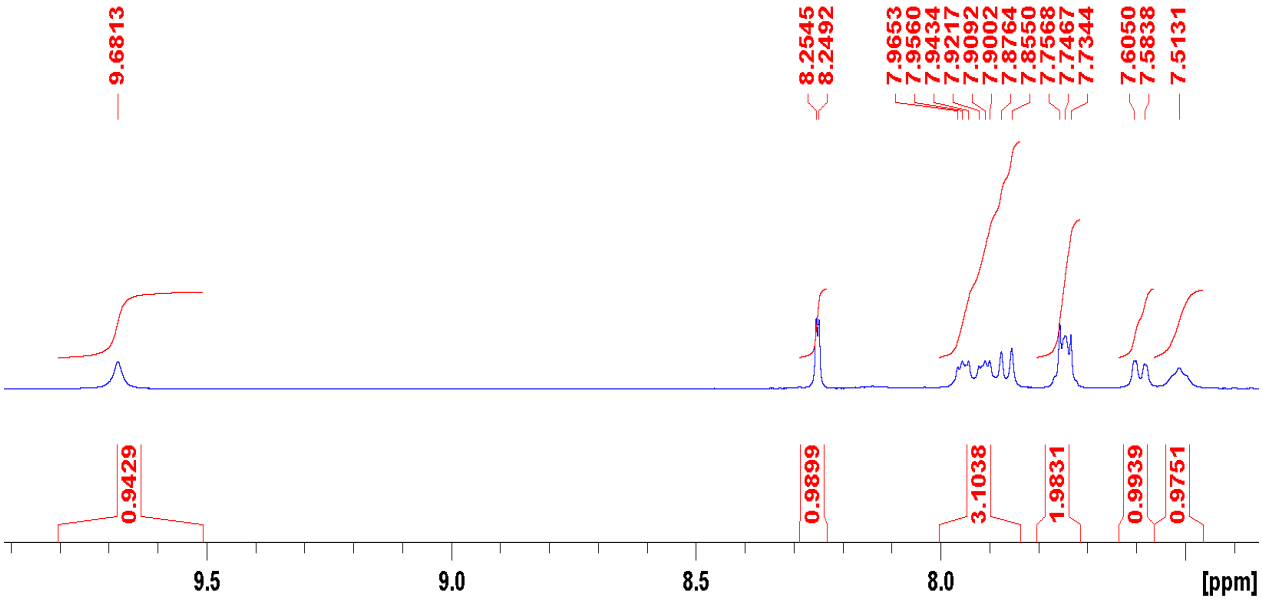

Figure S2: A zoomed in ^{1}H NMR spectrum of compound **1** in DMSO-d_6 at 298 K.

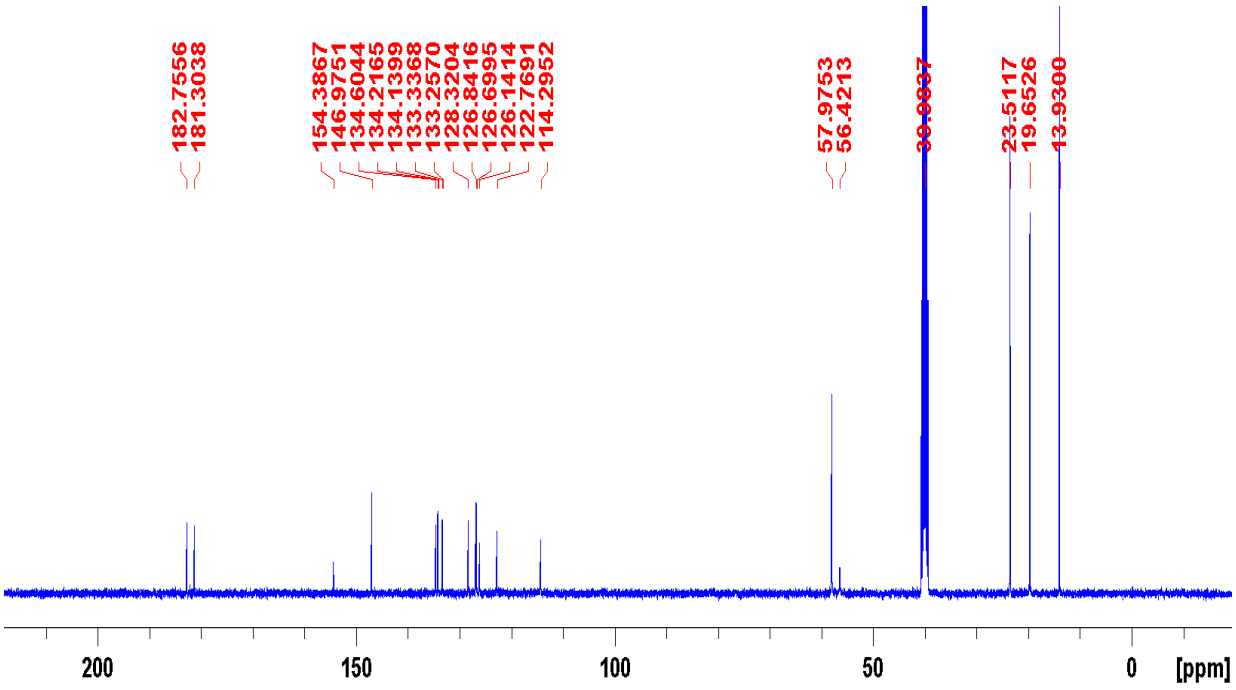

Figure S3: A in ^{13}C NMR spectrum of compound **1** in DMSO-d_6 at 298 K.

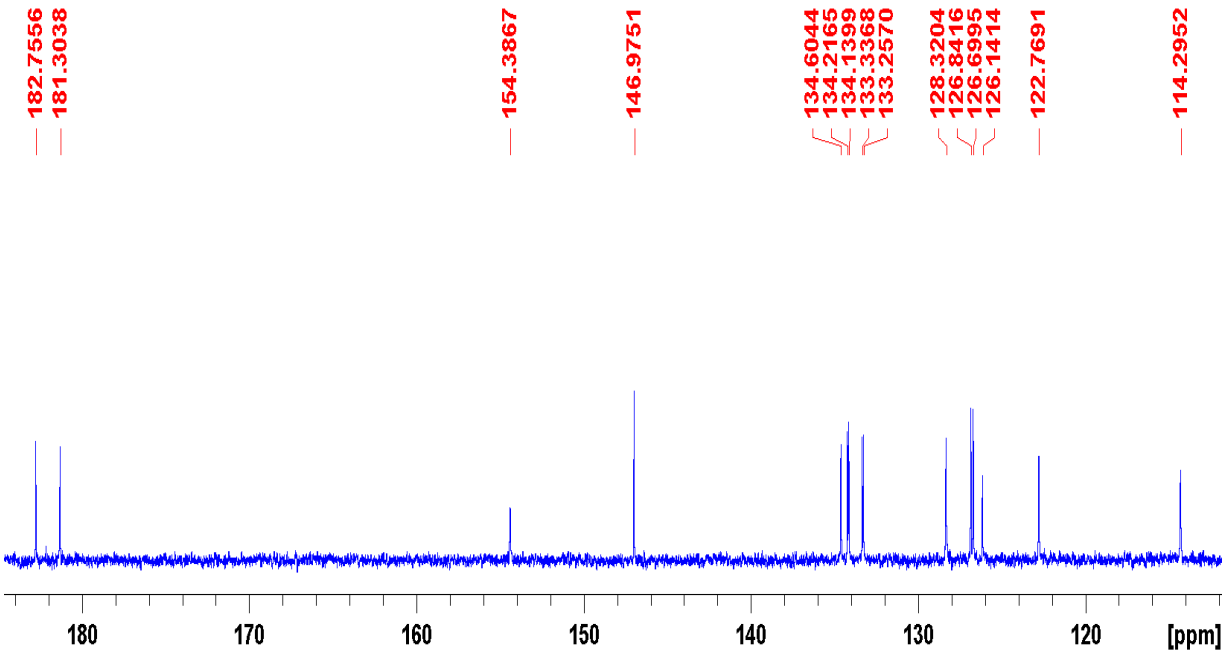

Figure S4: A zoomed in ^{13}C NMR spectrum of compound **1** in DMSO-d_6 at 298 K.

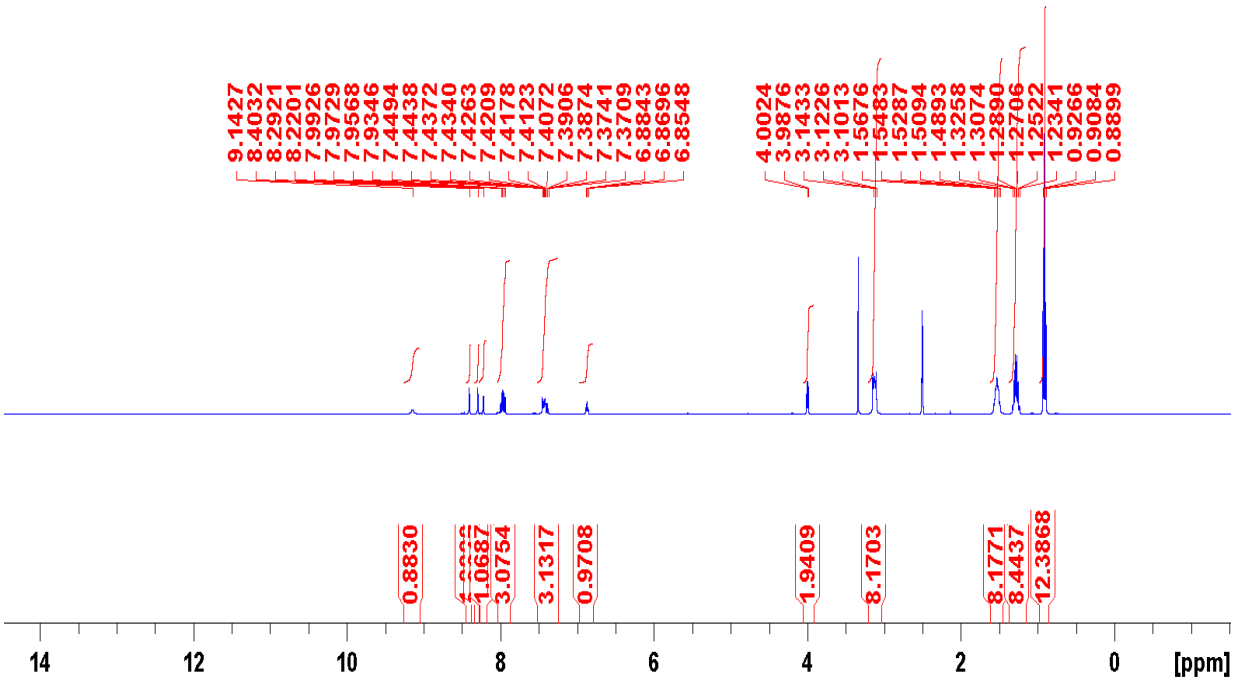

Figure S5: A ^{1}H NMR spectrum of compound **2** in DMSO-d_6 at 298 K.

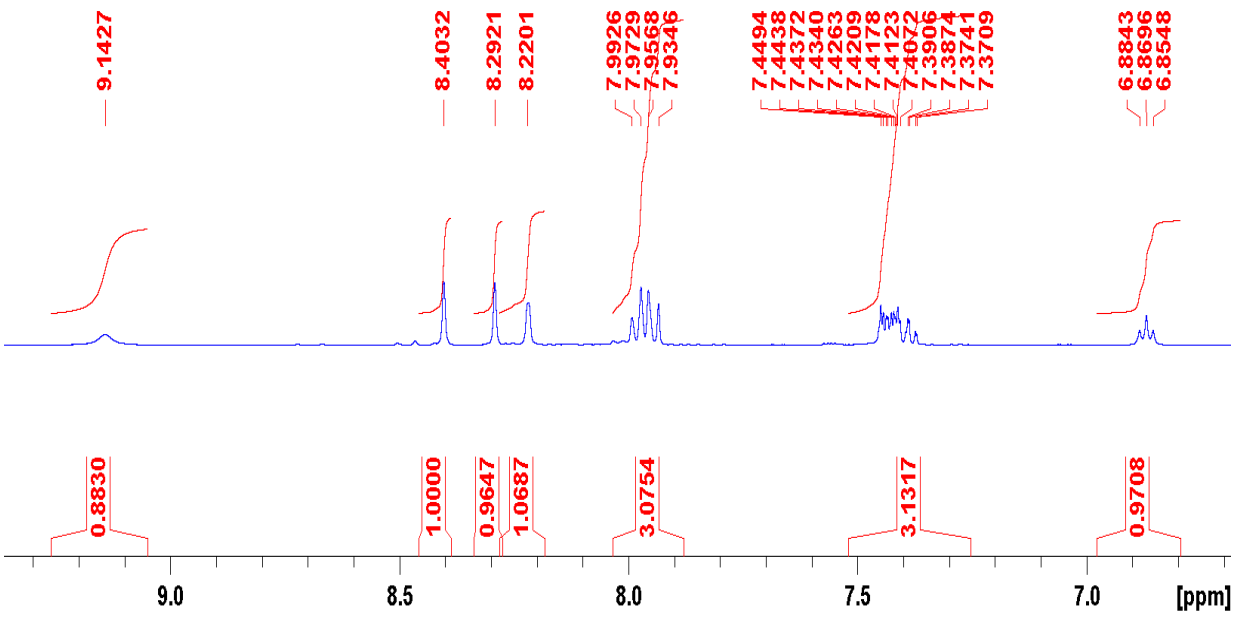

Figure S6: A zoomed in ^{1}H NMR spectrum of compound **2** in DMSO-d_6 at 298 K.

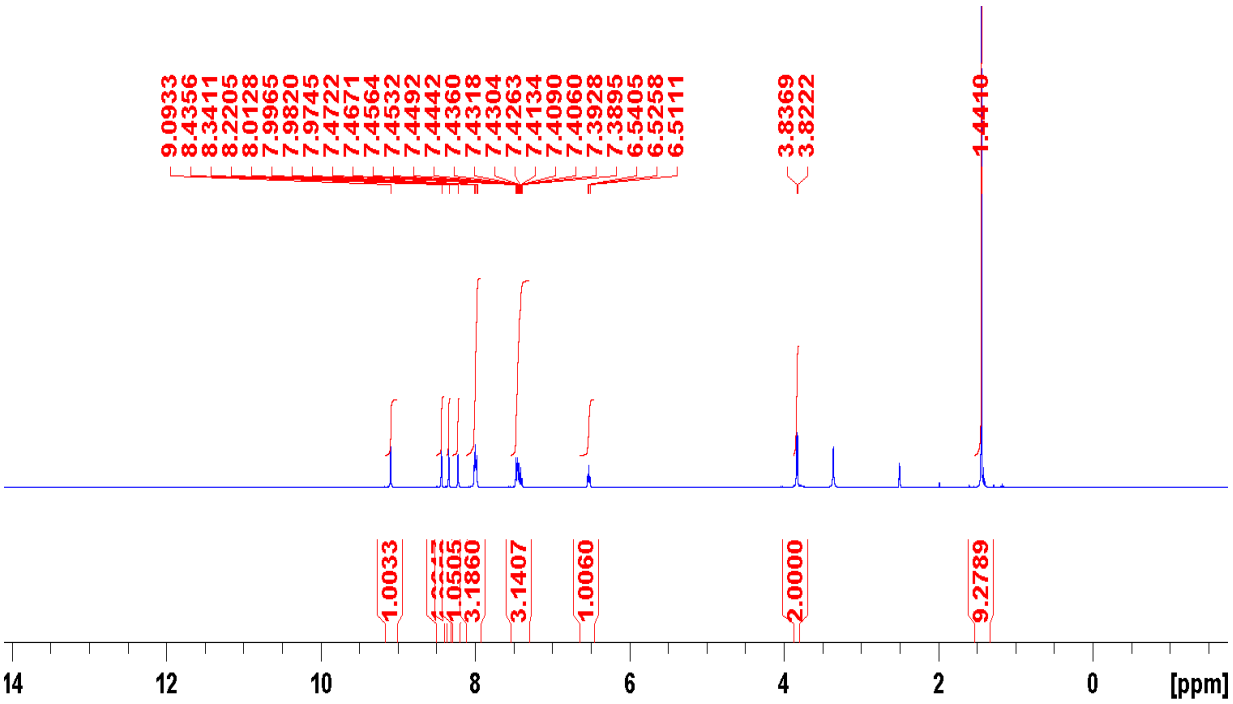

Figure S7: A ^{1}H NMR spectrum of compound **3** in DMSO-d_6 at 298 K.

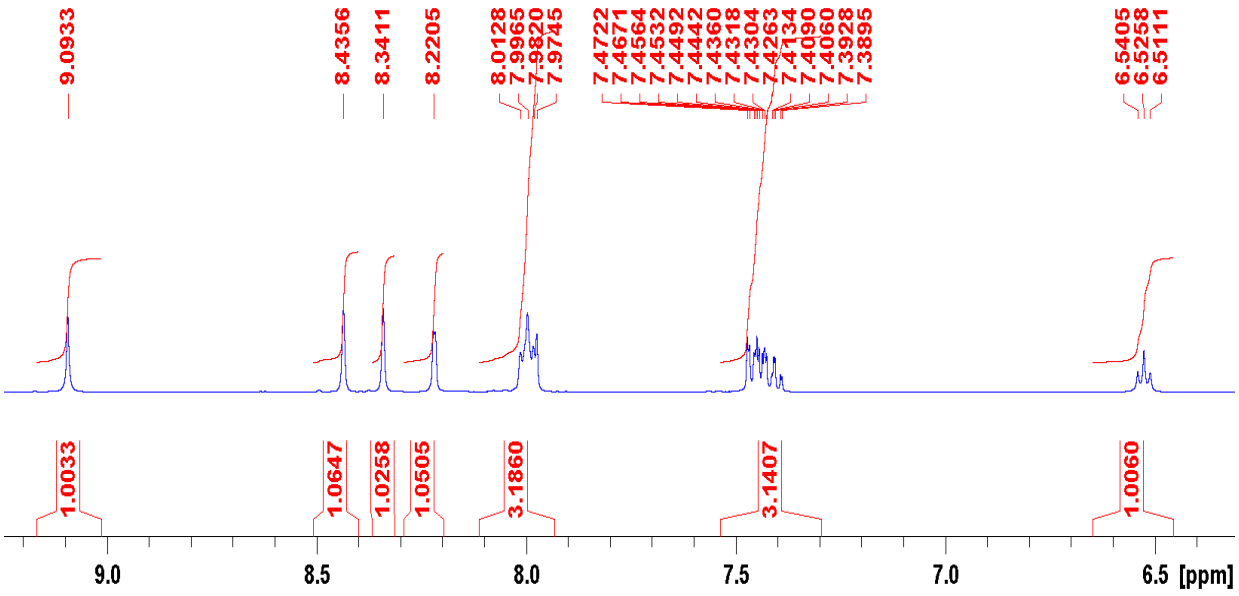

Figure S8: A zoomed in ^{1}H NMR spectrum of compound **3** in DMSO-d_6 at 298 K.

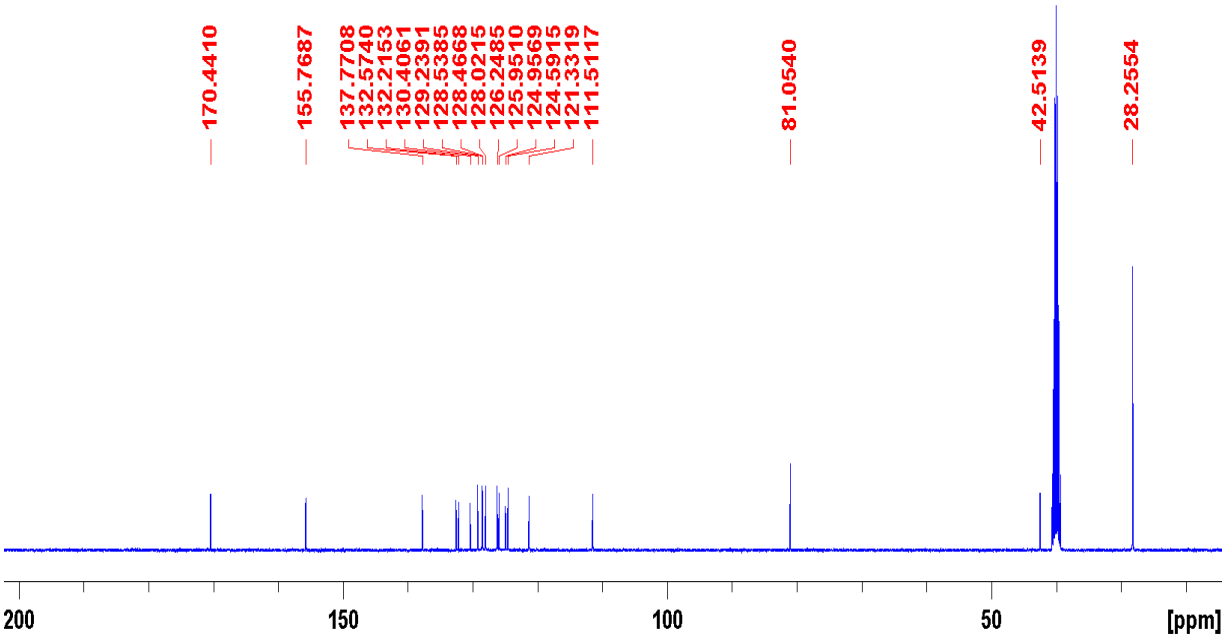

Figure S9: A in ^{13}C NMR spectrum of compound **3** in DMSO-d_6 at 298 K.

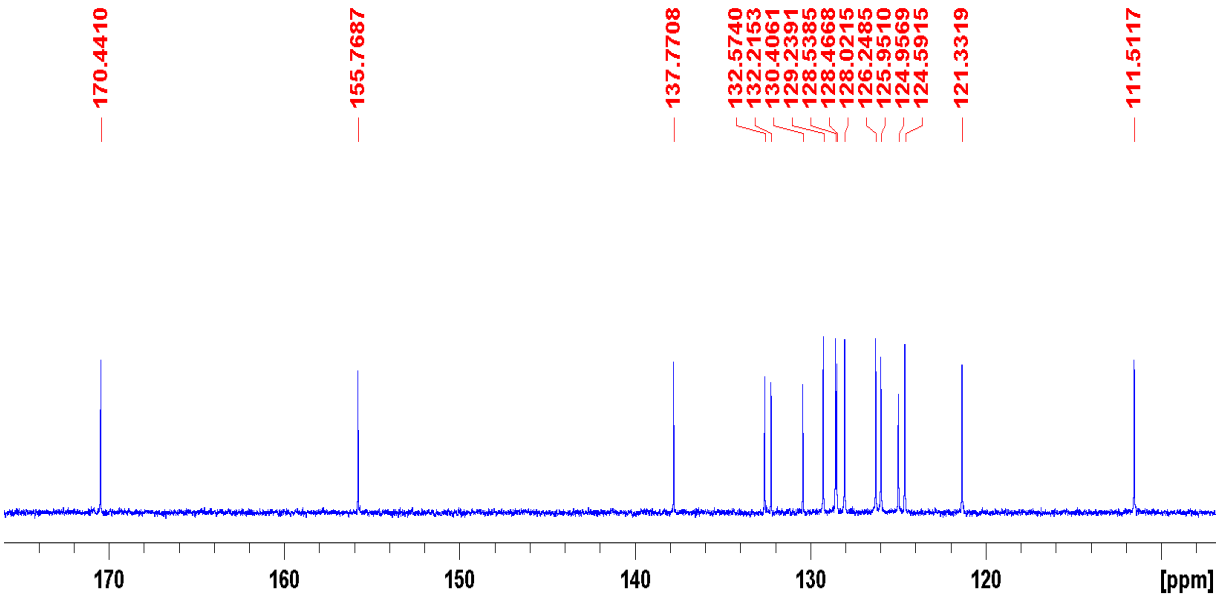

Figure S10: A zoomed in ^{13}C NMR spectrum of compound **3** in DMSO-d_6 at 298 K.

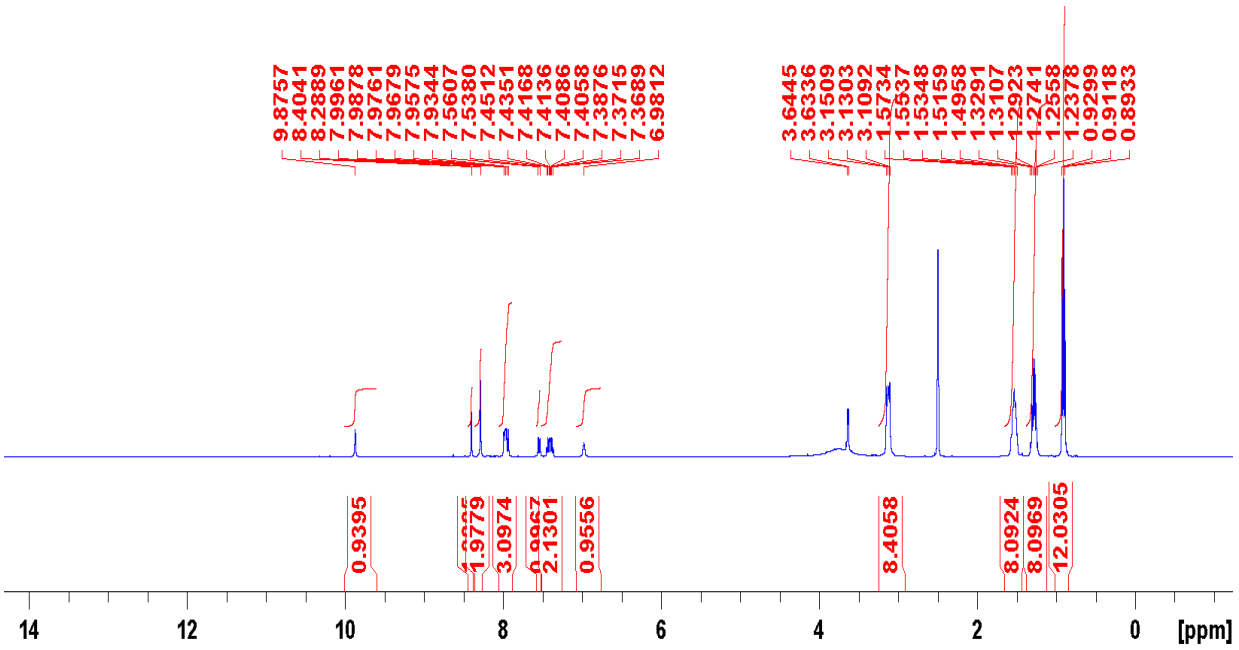

Figure S11: A ^{1}H NMR spectrum of compound **4** in DMSO-d_6 at 298 K.

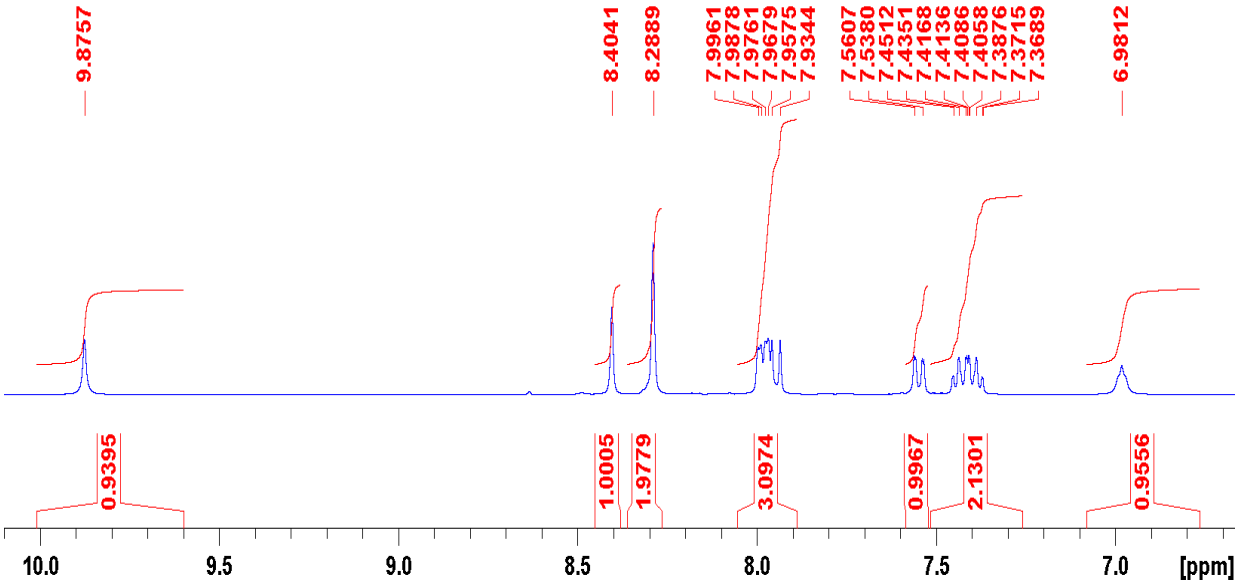

Figure S12: A zoomed in ^{1}H NMR spectrum of compound **4** in DMSO-d_6 at 298 K.

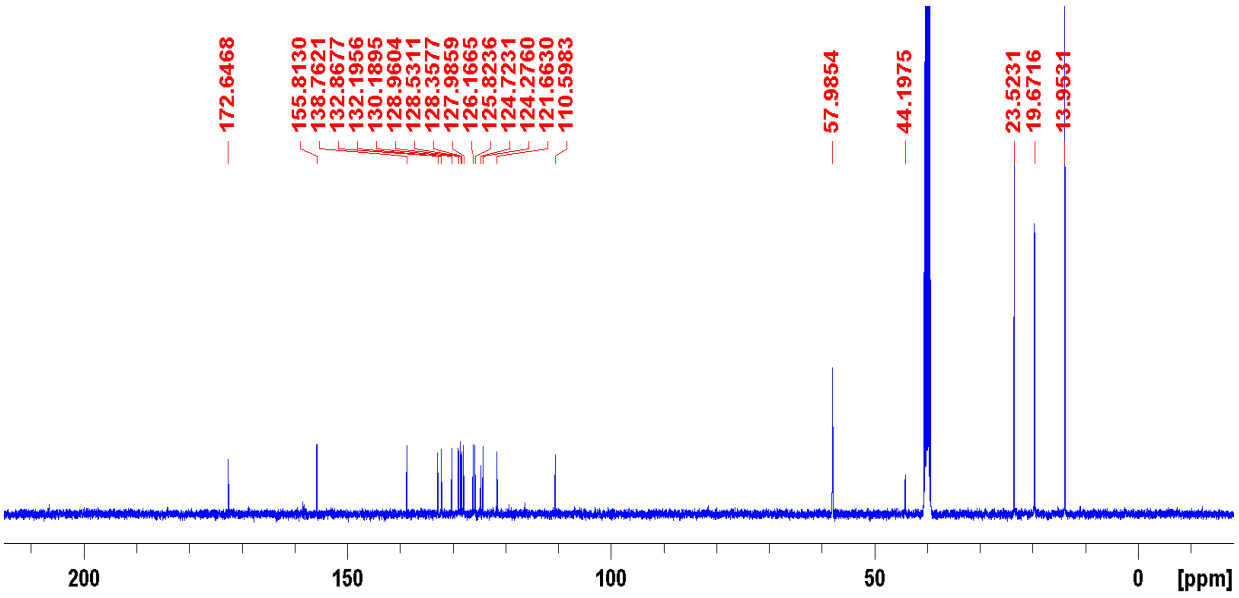

Figure S13: A ^{13}C NMR spectrum of compound **4** in DMSO-d_6 at 298 K.

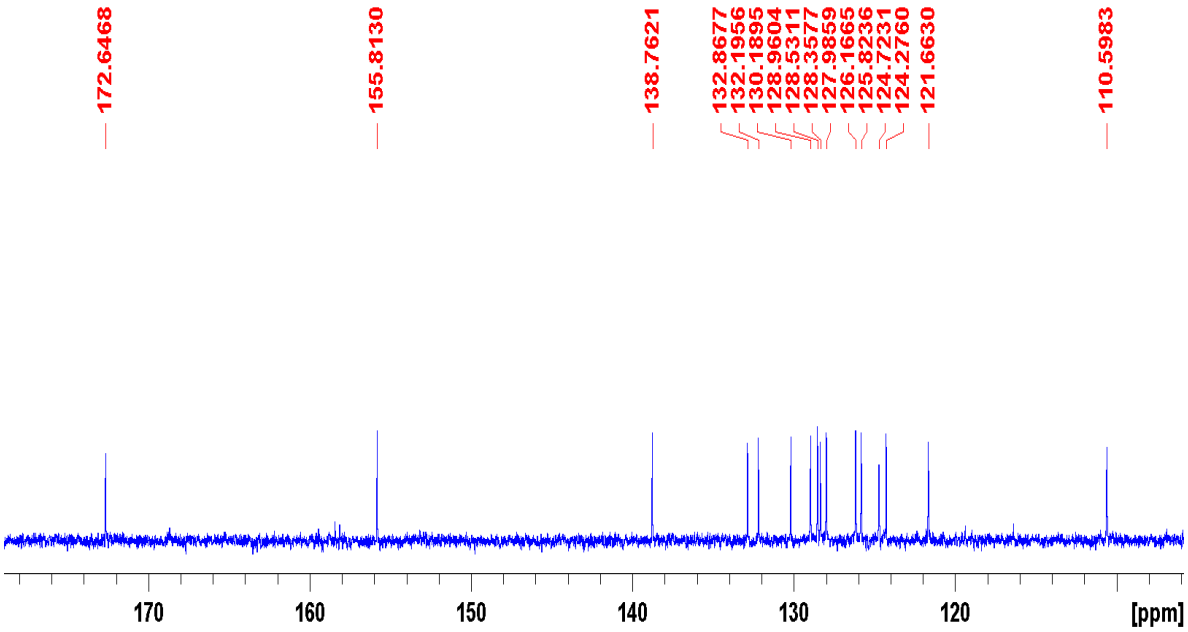

Figure S14: A zoomed in ^{13}C NMR spectrum of compound **4** in DMSO-d_6 at 298 K.

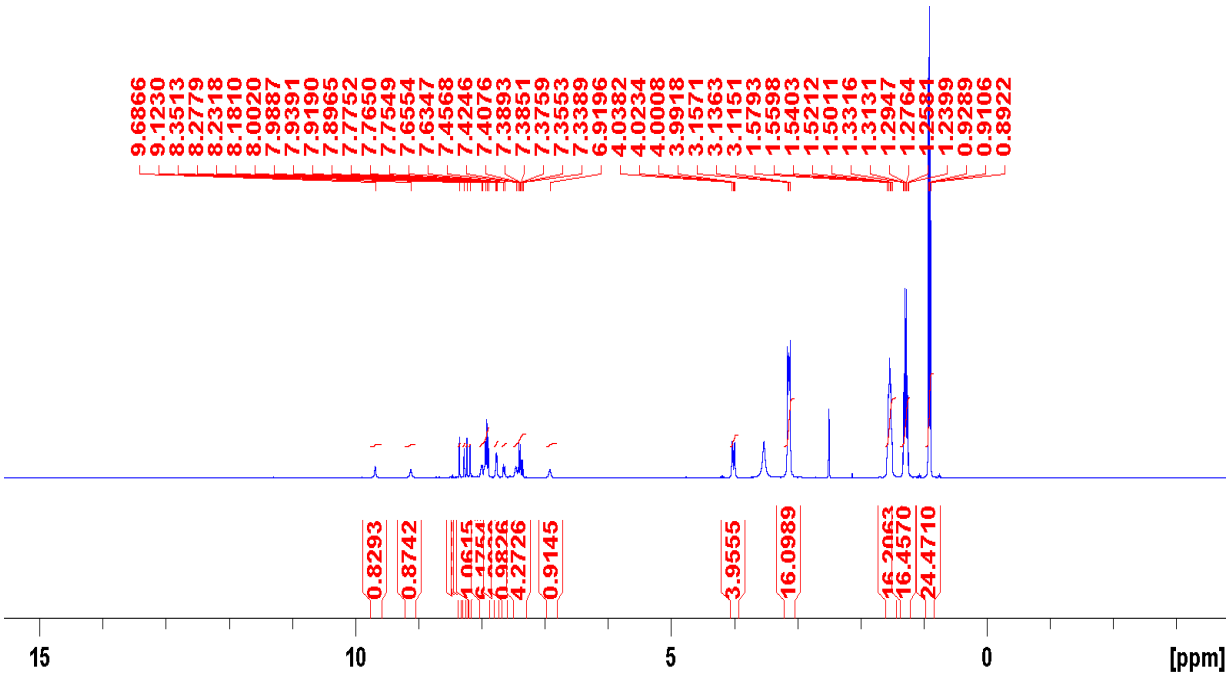

Figure S15: A ^{1}H NMR spectrum of compound **1** and **2** in DMSO-d_6 at 298 K.

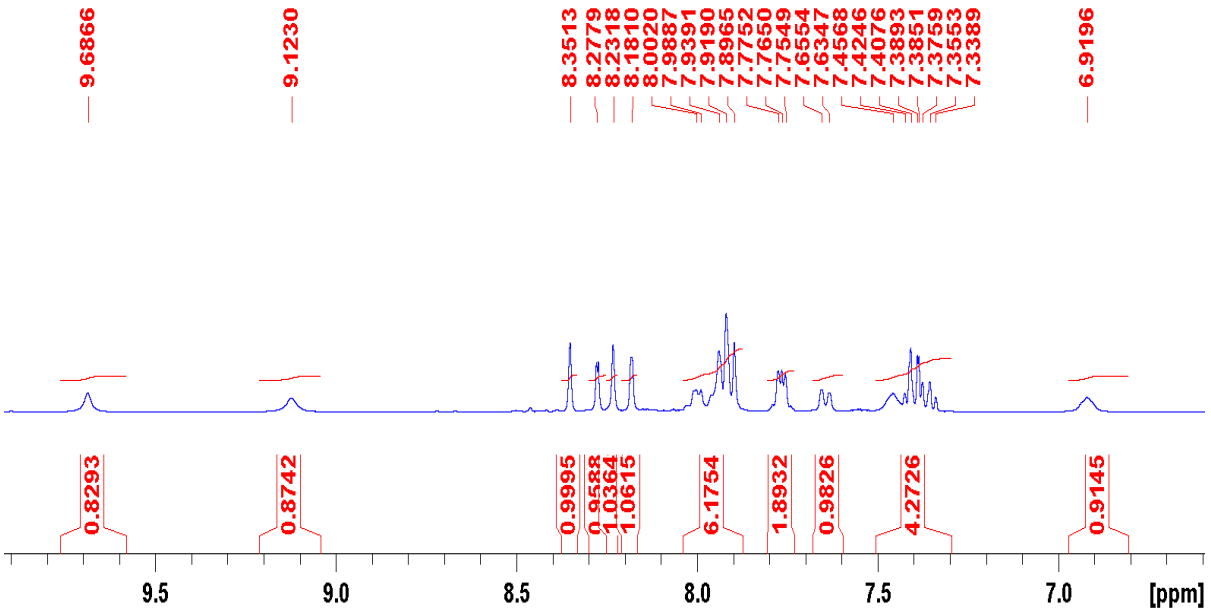

Figure S16: A zoomed in ^{1}H NMR spectrum of compound **1** and **2** in DMSO-d_6 at 298 K.

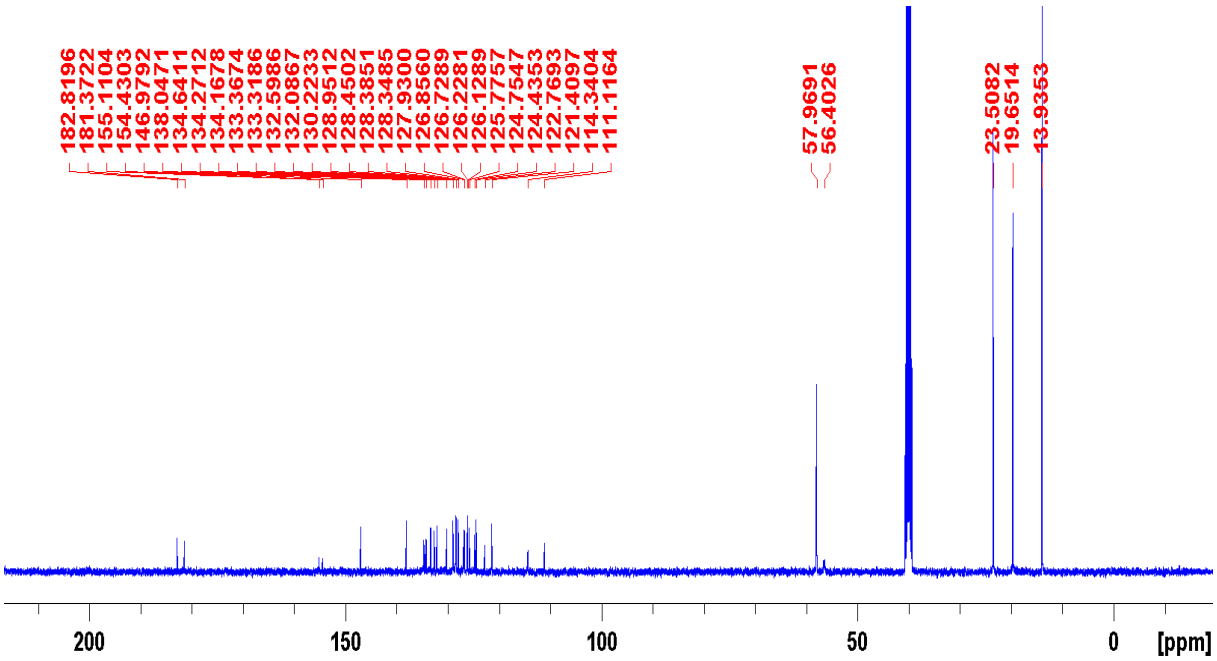

Figure S17: A ^{13}C NMR spectrum of compound **1** and **2** in DMSO-d_6 at 298 K.

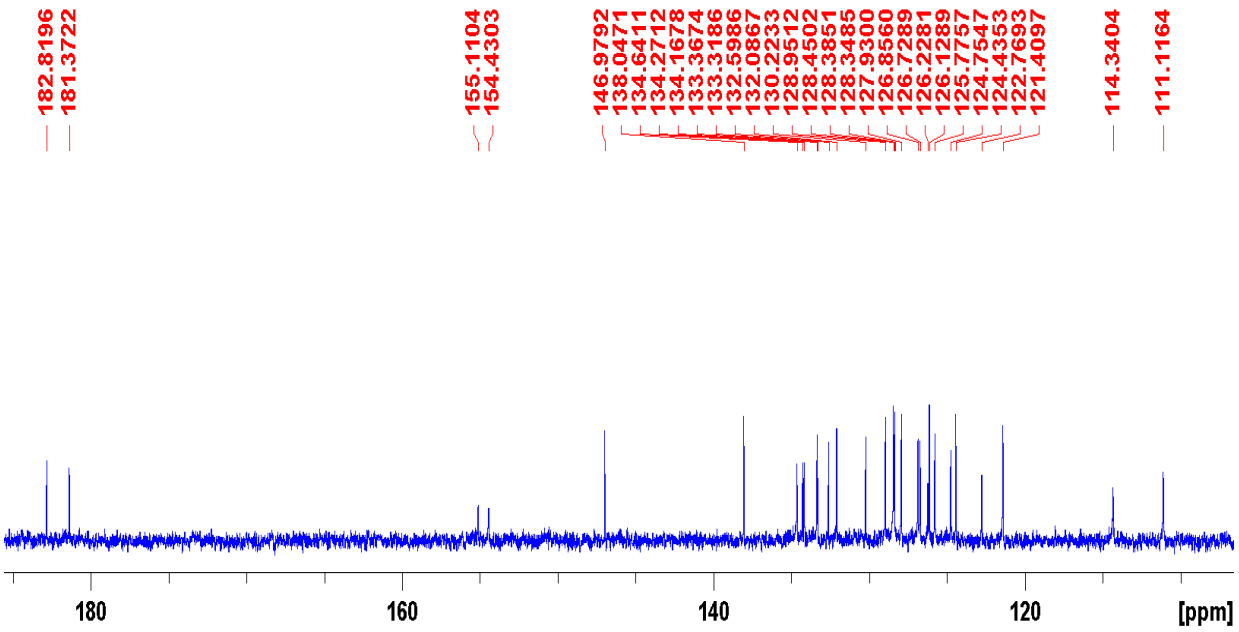

Figure S18: A zoomed in ^{13}C NMR spectrum of compound **1** and **2** in DMSO-d_6 at 298 K.

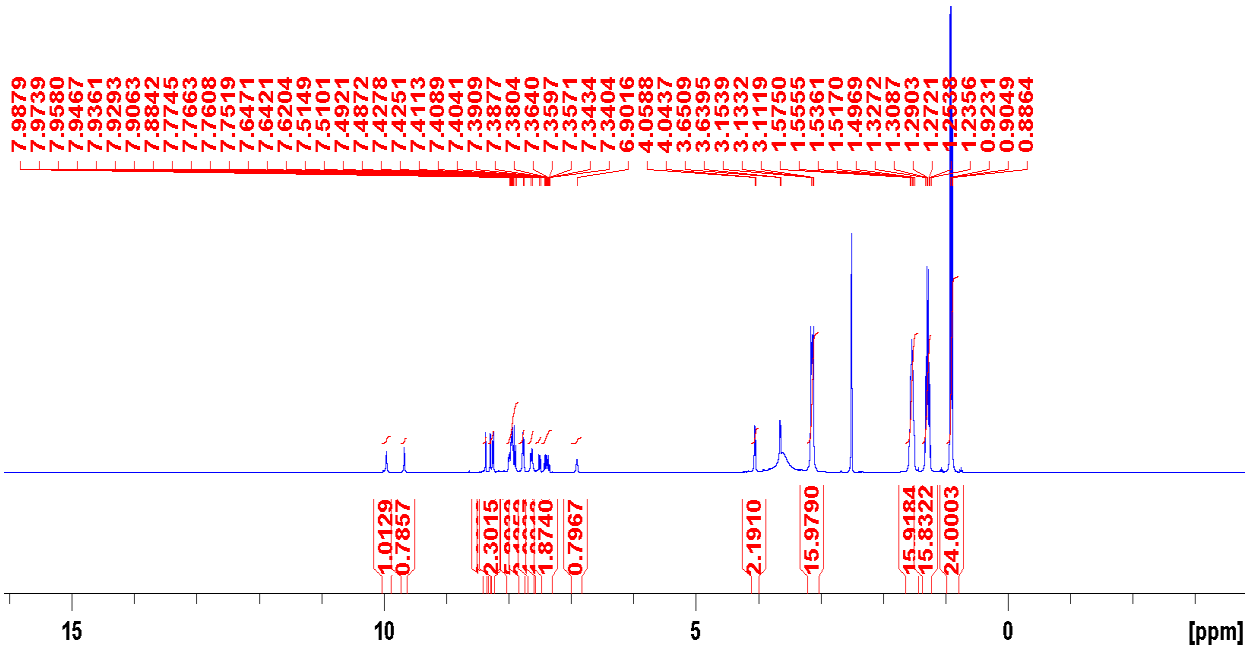

Figure S19: A ^{1}H NMR spectrum of compound **1** and **4** in DMSO-d_6 at 298 K.

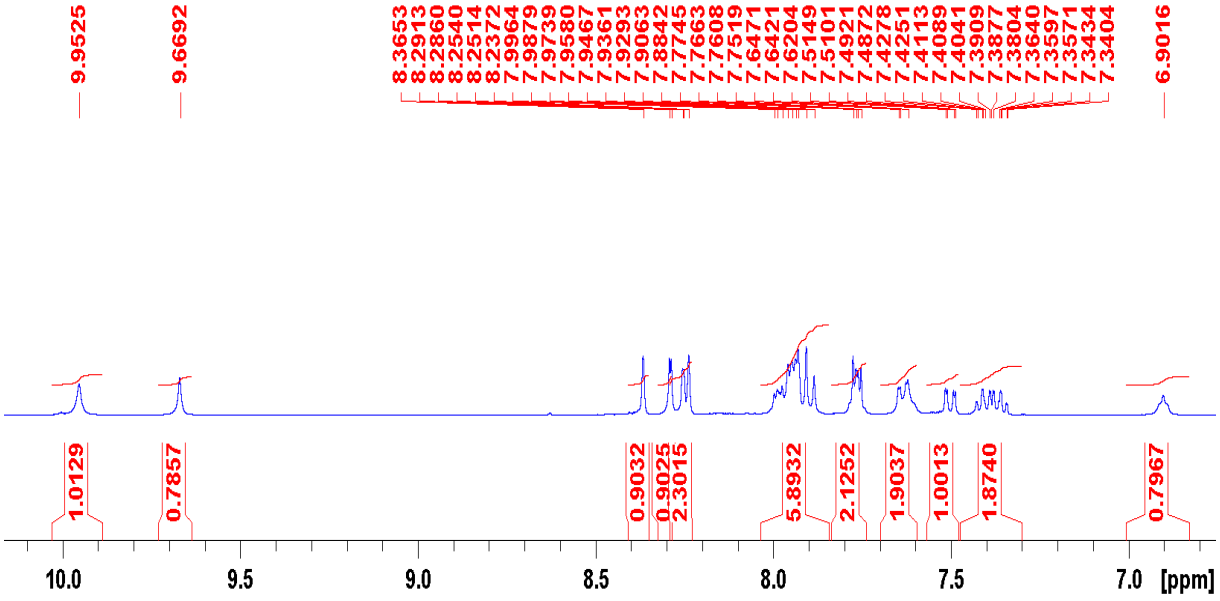

Figure S20: A zoomed in ^{1}H NMR spectrum of compound **1** and **4** in DMSO-d_6 at 298 K.

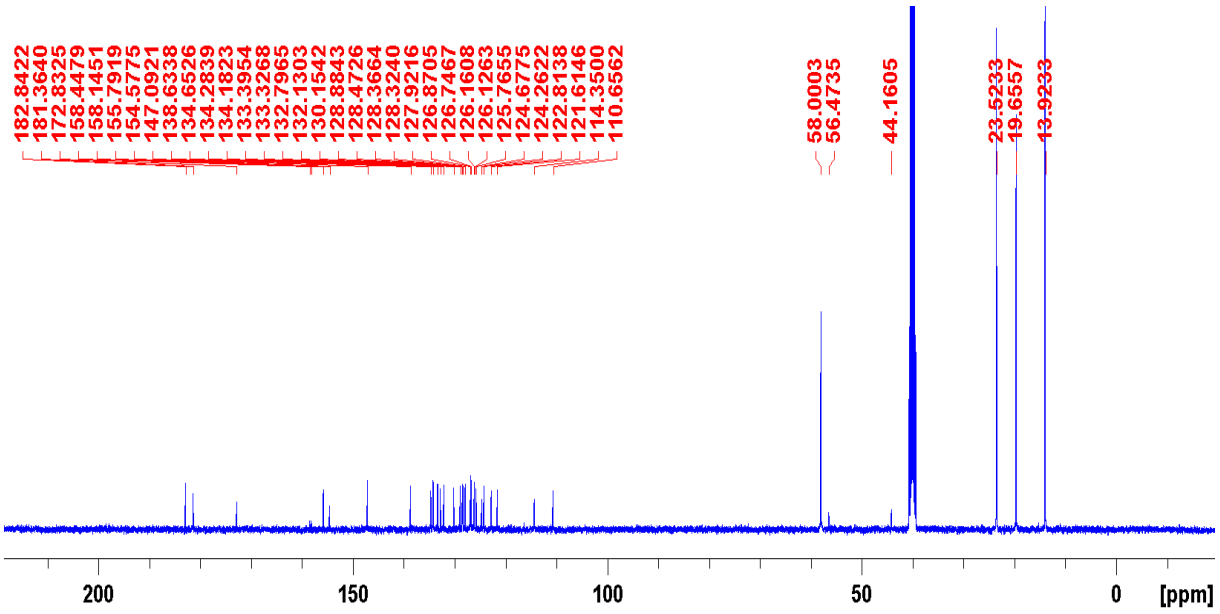

Figure S21: A ^{13}C NMR spectrum of compound **1** and **4** in DMSO-d_6 at 298 K.

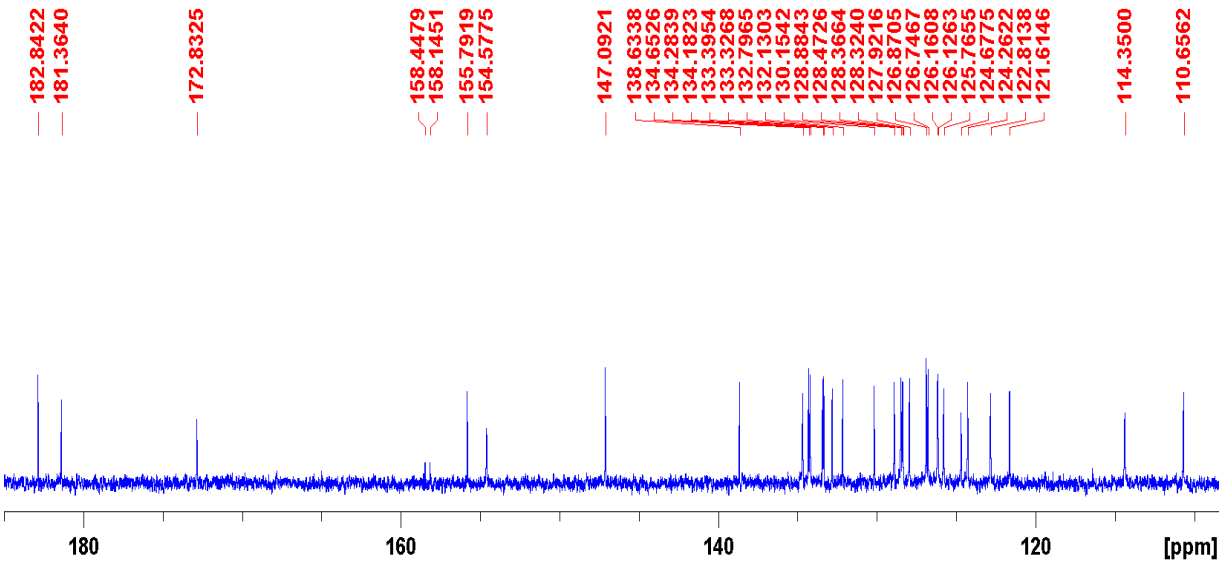

Figure S22: A zoomed in ^{13}C NMR spectrum of compound **1** and **4** in DMSO-d_6 at 298 K.

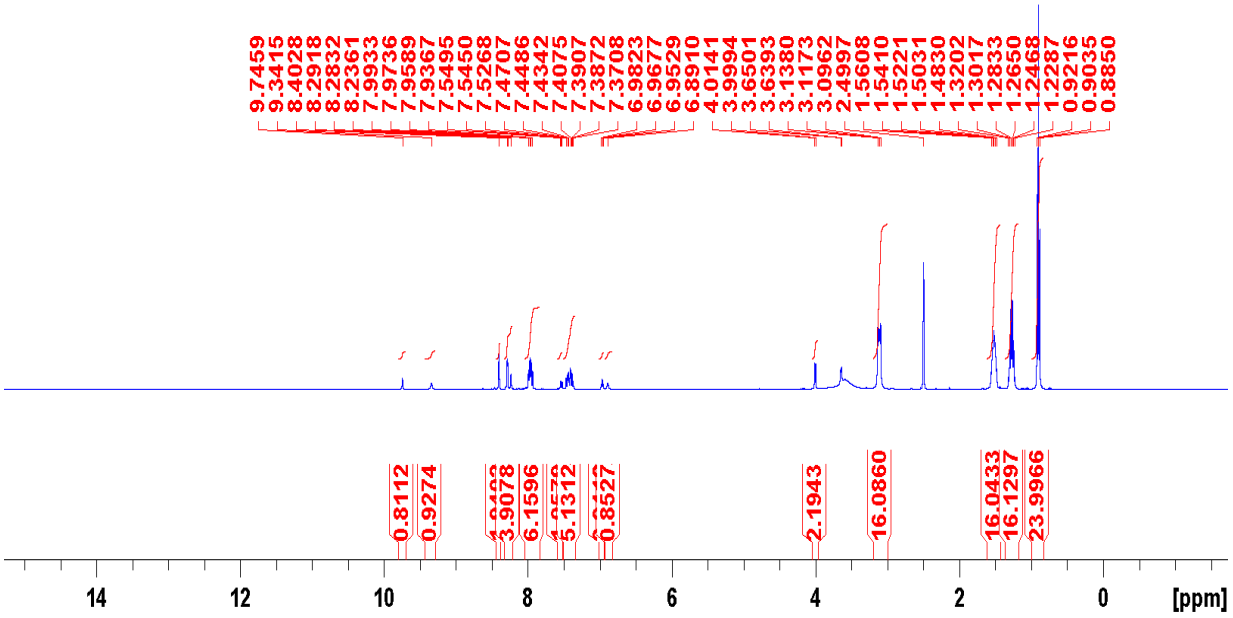

Figure S23: A ^{1}H NMR spectrum of compound **2** and **4** in DMSO-d_6 at 298 K.

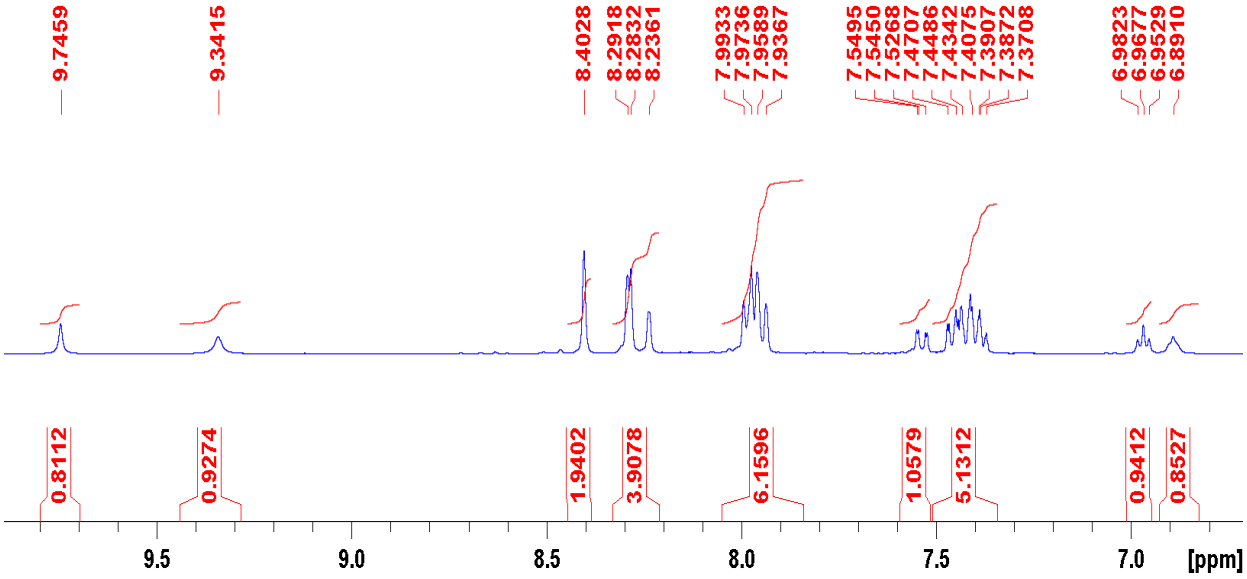

Figure S24: A zoomed in ^{1}H NMR spectrum of compound **2** and **4** in DMSO-d_6 at 298 K.

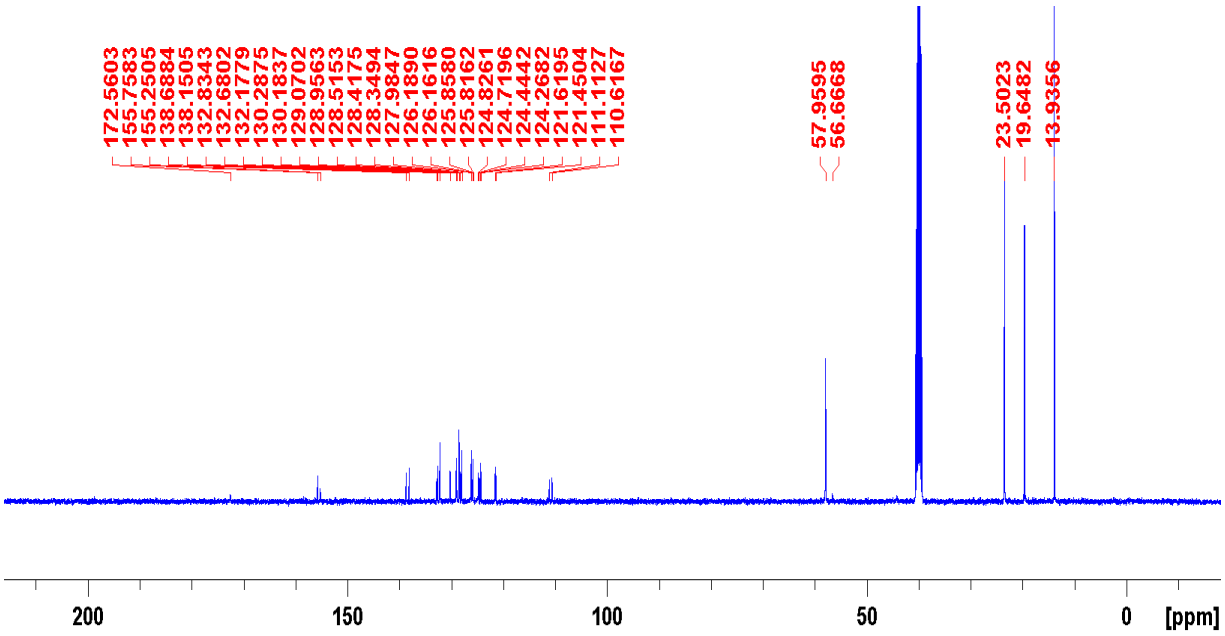

Figure S25: A ^{13}C NMR spectrum of compound **2** and **4** in DMSO-d_6 at 298 K.

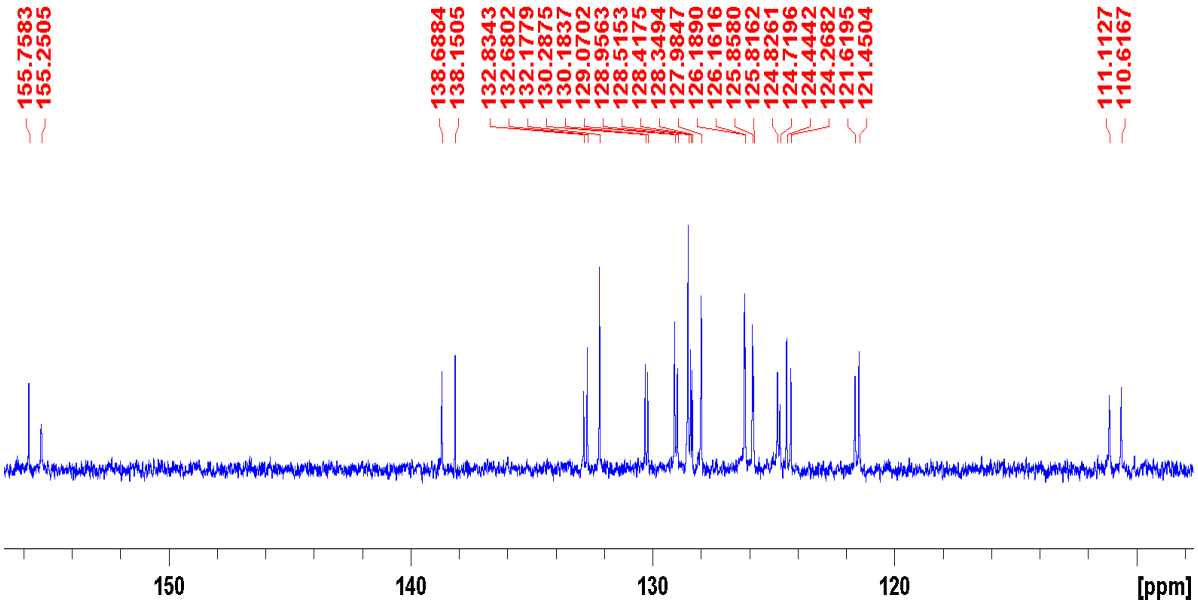

Figure S26: A zoomed in ^{13}C NMR spectrum of compound **2** and **4** in DMSO-d_6 at 298 K.

ESI – MS data

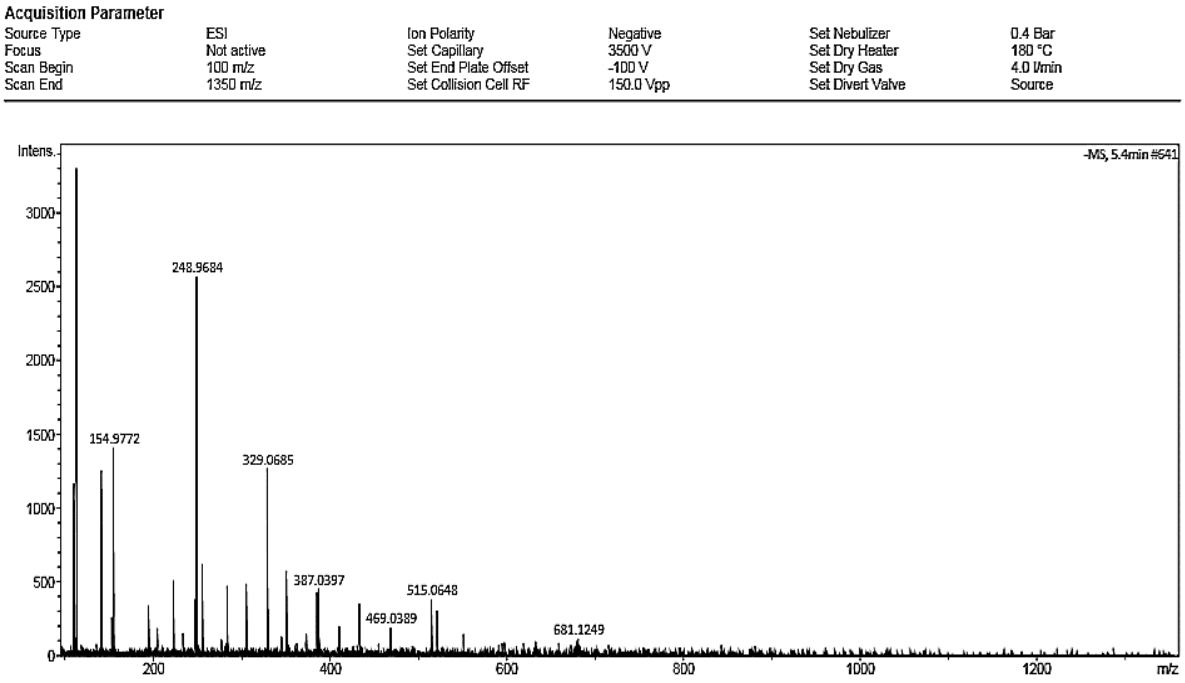

Figure S27: A high resolution mass spectrum (ESI –ve) obtained for compound **2** in methanol.

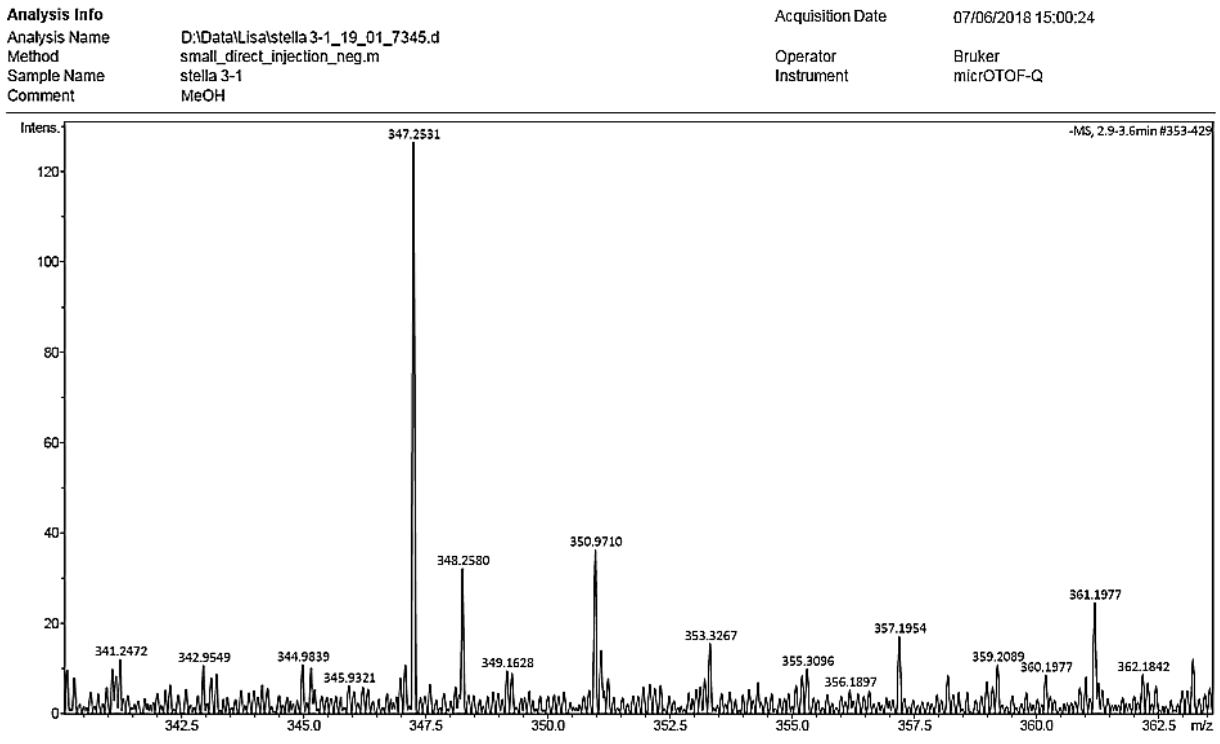

Figure S28: A high resolution mass spectrum (ESI –ve) obtained for compound **3** in methanol.

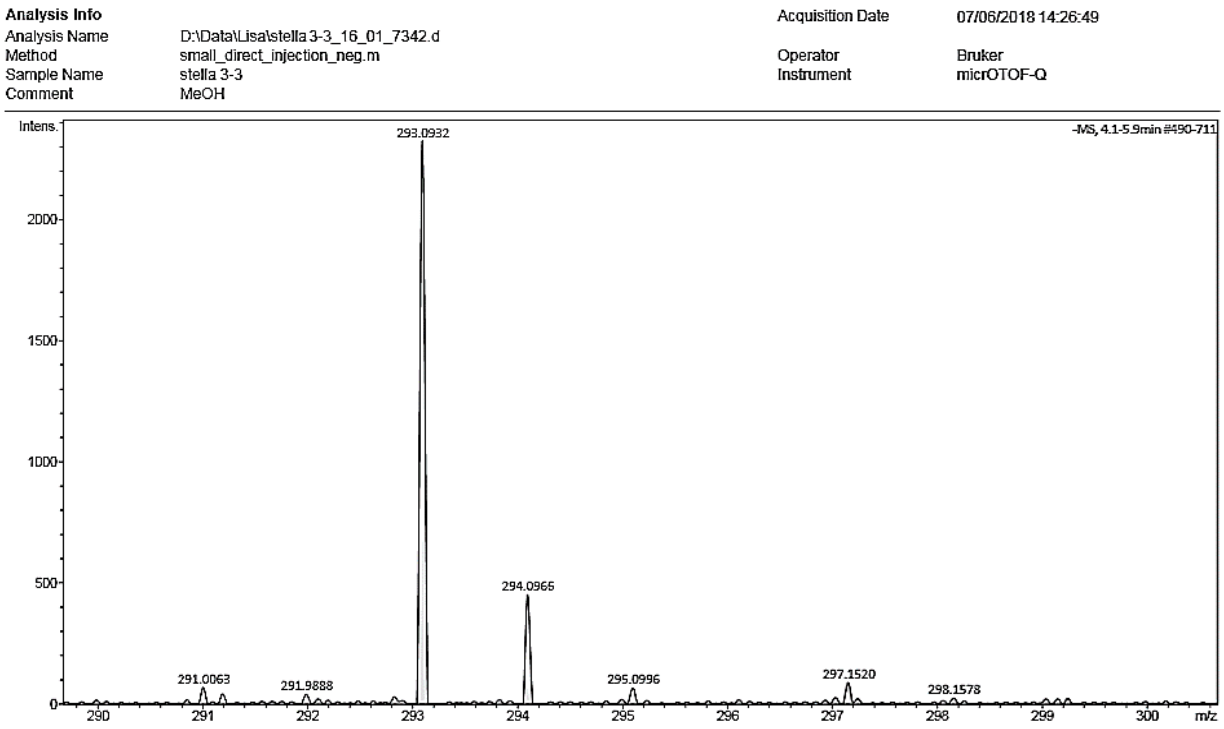

Figure S29: A high resolution mass spectrum (ESI –ve) obtained for compound **4** in methanol.

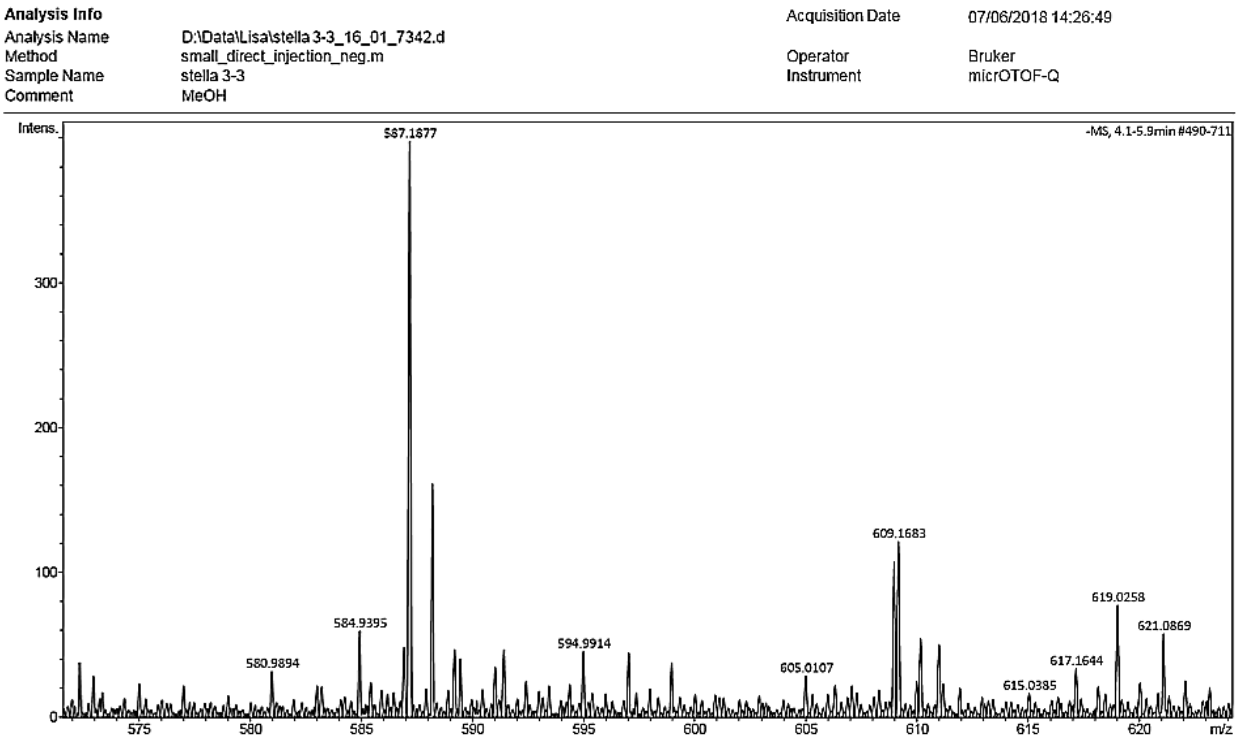

Figure S30: A high resolution mass spectrum (ESI –ve) obtained for compound **4** in methanol.

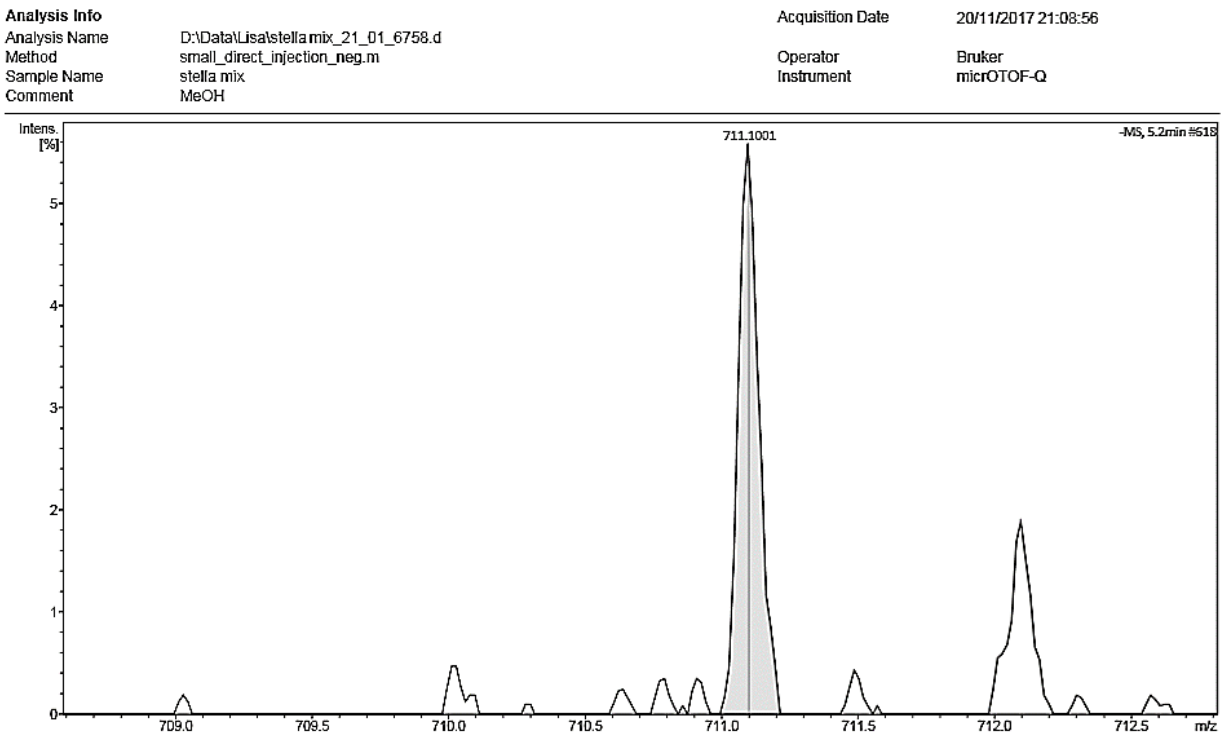

Figure S31: A high resolution mass spectrum (ESI –ve) obtained for compounds **1** and **2** in methanol.

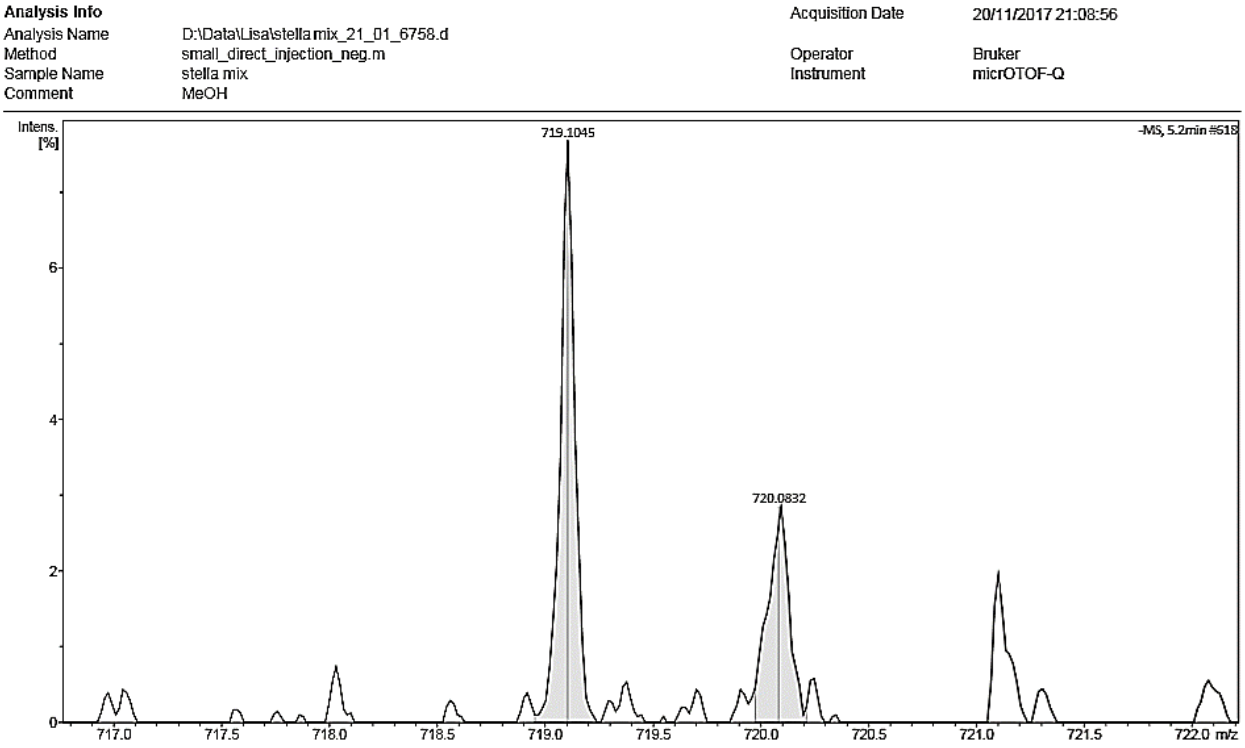

Figure S32: A high resolution mass spectrum (ESI –ve) obtained for compounds **1** and **2** in methanol.

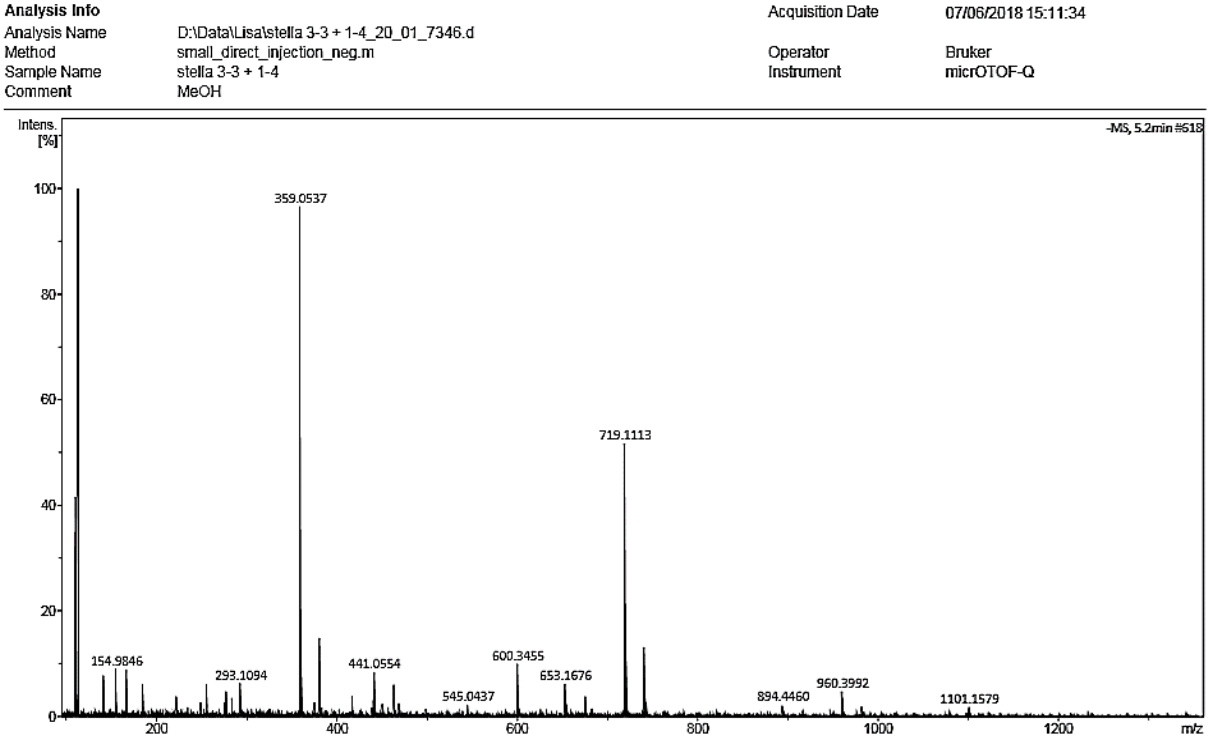

Figure S33: A high resolution mass spectrum (ESI –ve) obtained for compounds **1** and **4** in methanol.

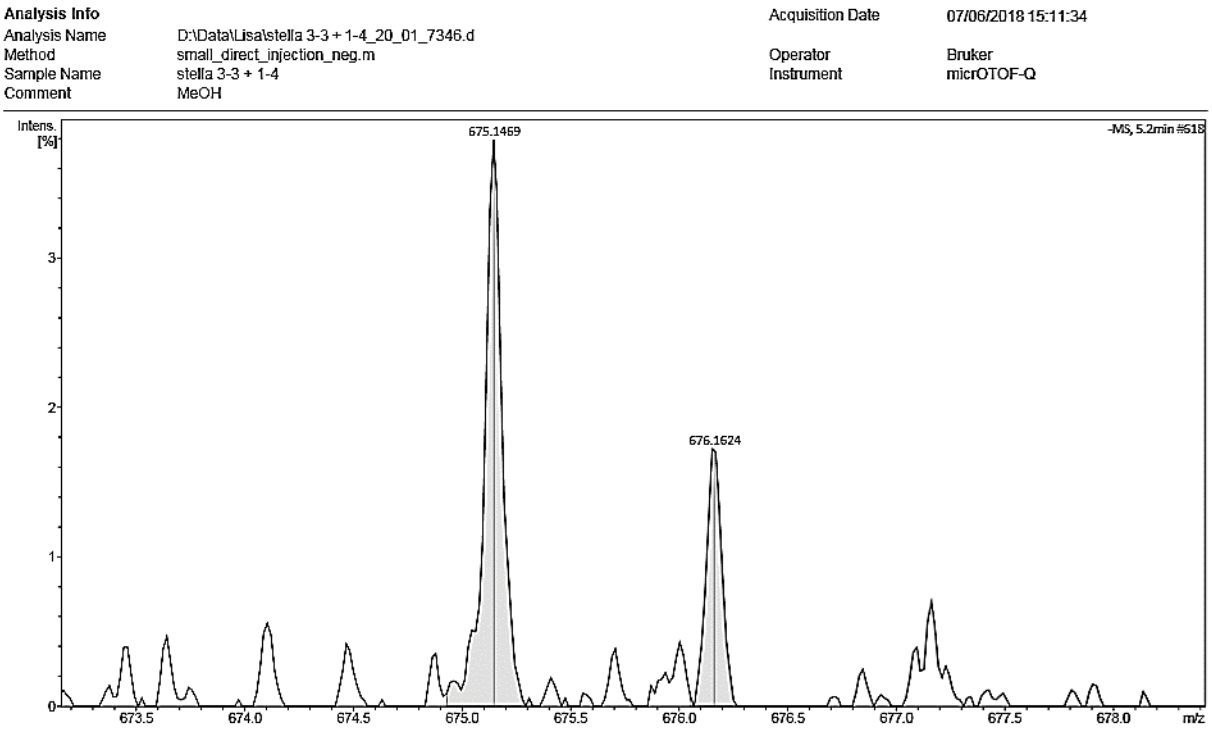

Figure S34: A high resolution mass spectrum (ESI –ve) obtained for compounds **1** and **4** in methanol.

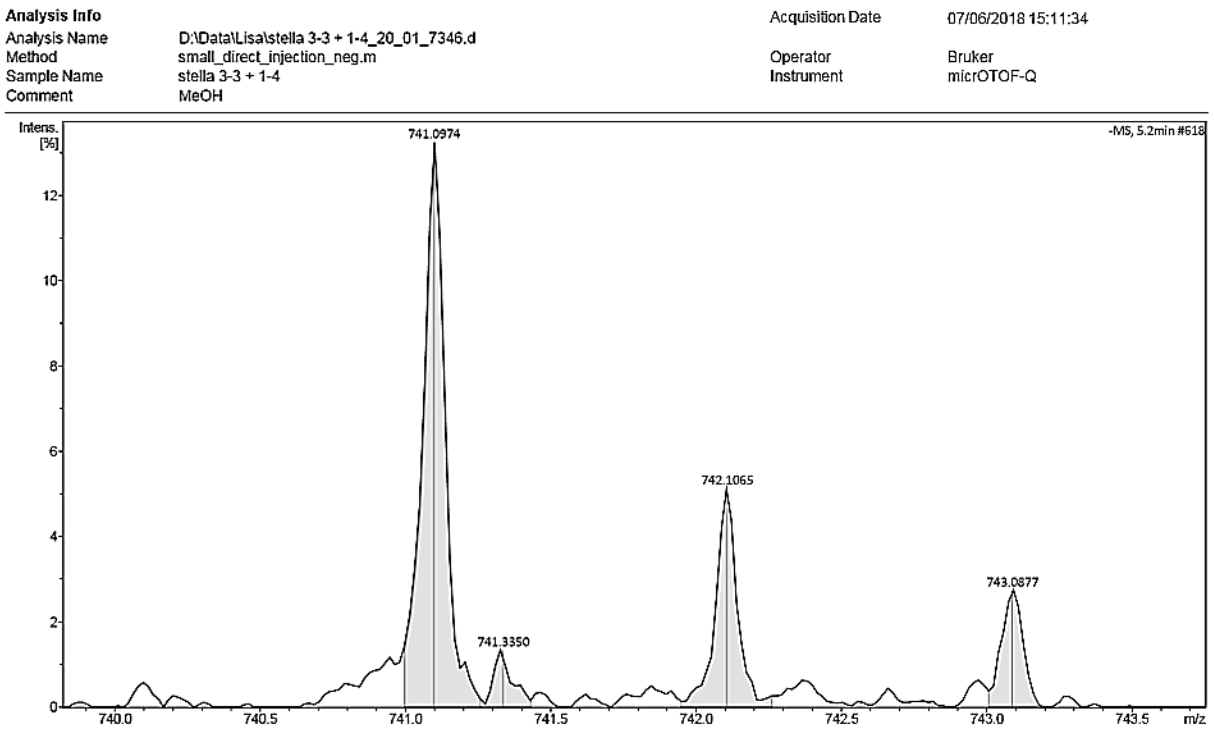

Figure S35: A high resolution mass spectrum (ESI –ve) obtained for compounds **1** and **4** in methanol.

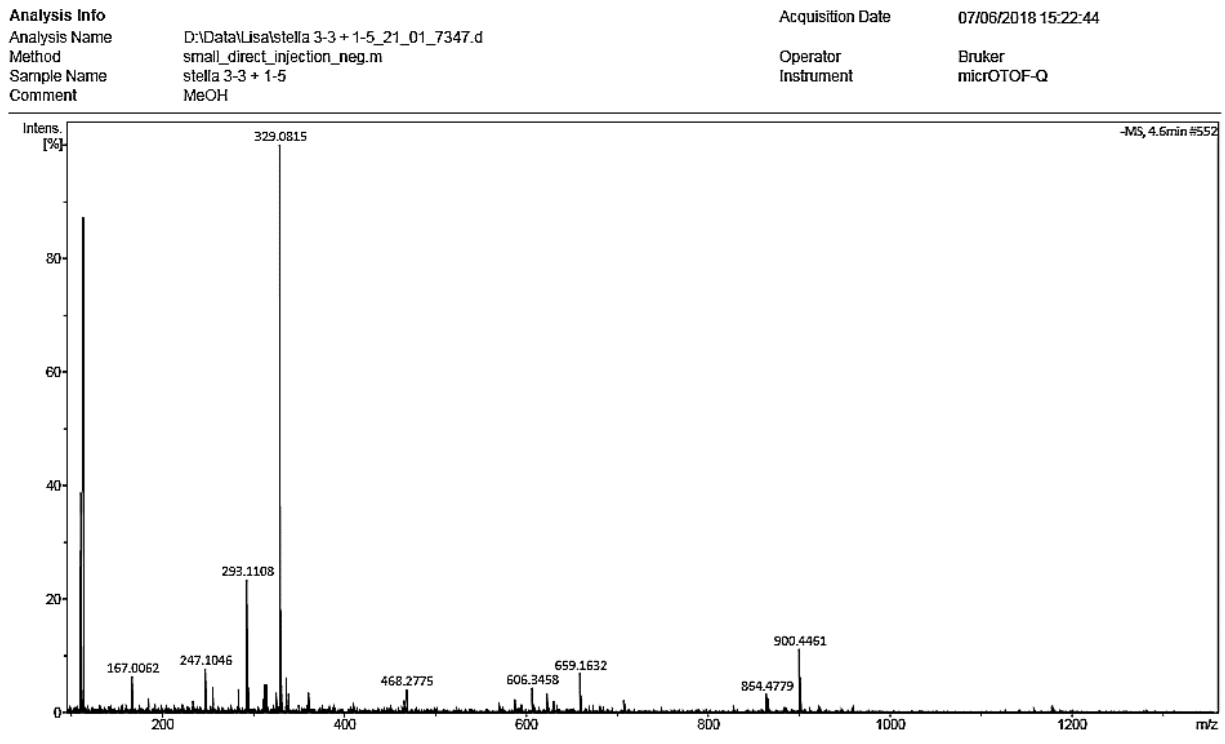

Figure S36: A high resolution mass spectrum (ESI –ve) obtained for compounds **2** and **4** in methanol.

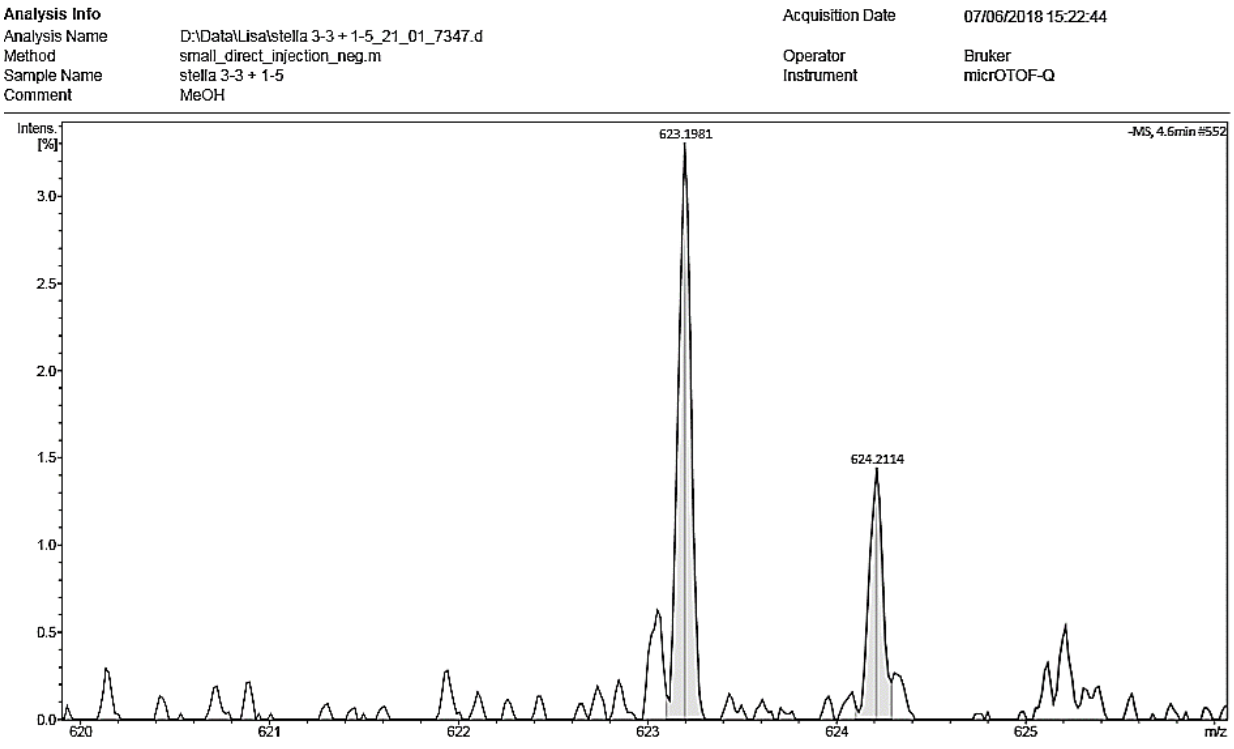

Figure S37: A high resolution mass spectrum (ESI –ve) obtained for compounds **2** and **4** in methanol.

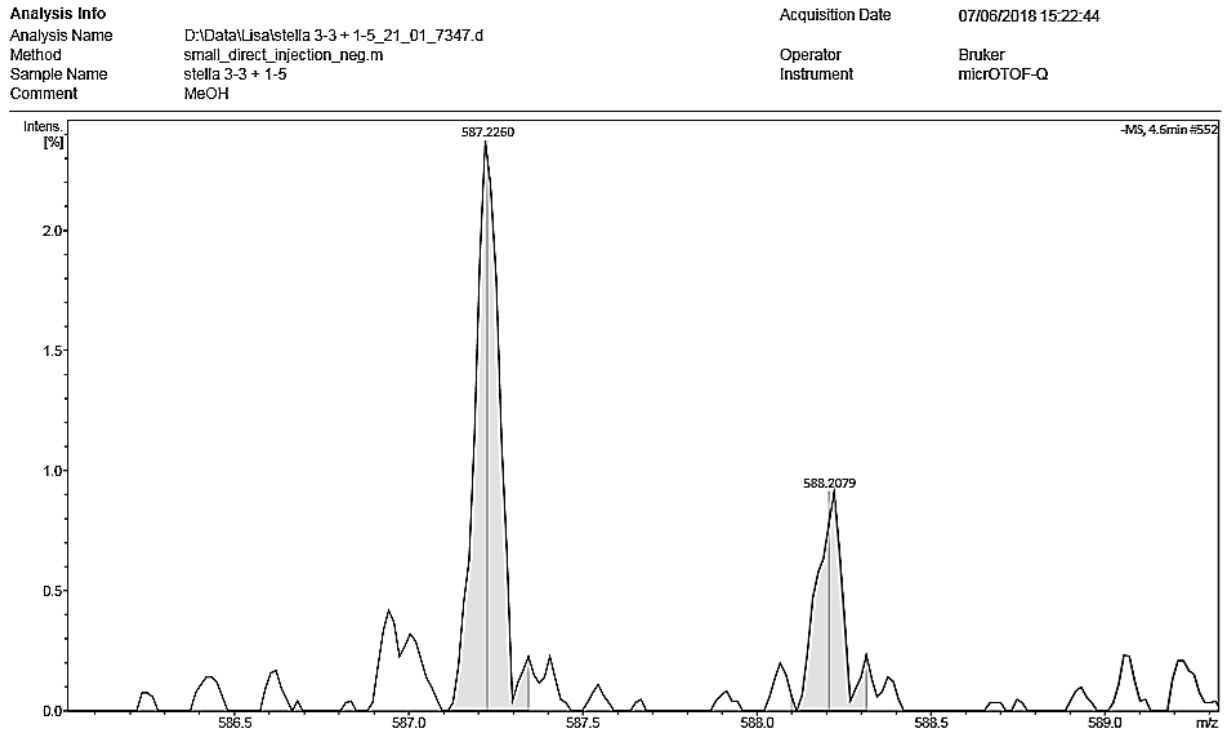

Figure S38: A high resolution mass spectrum (ESI –ve) obtained for compounds **2** and **4** in methanol.

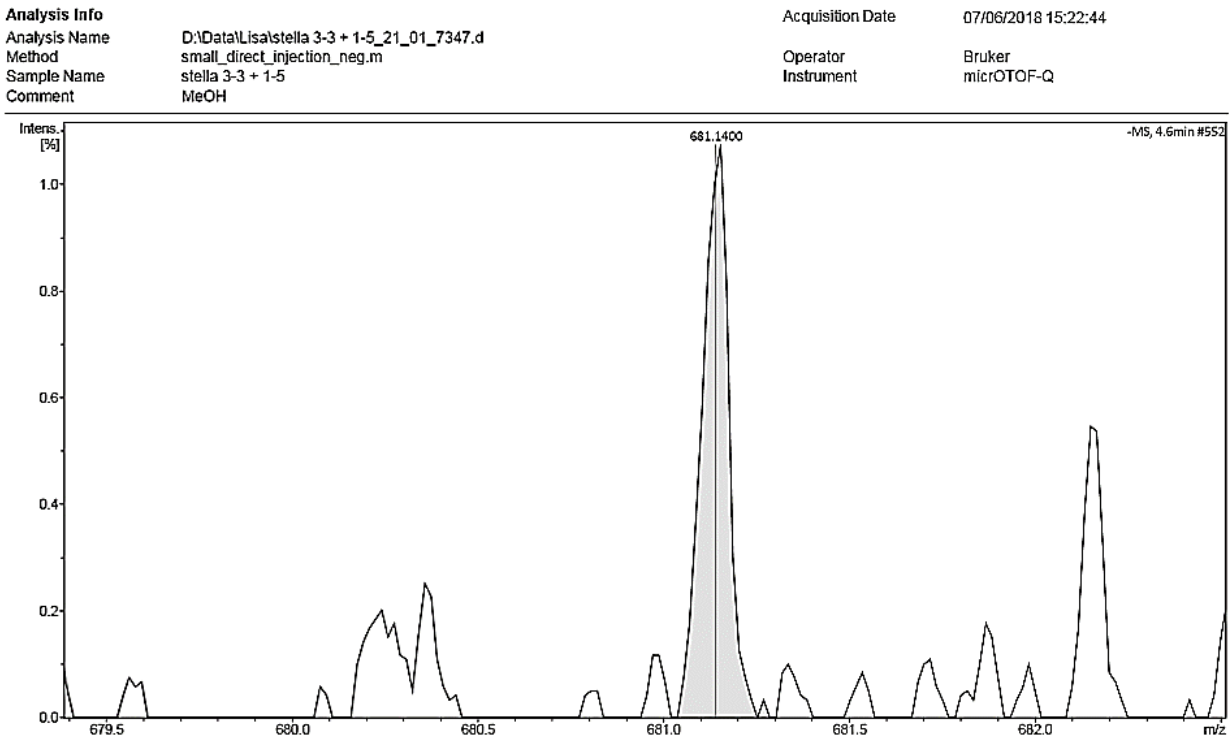

Figure S39: A high resolution mass spectrum (ESI –ve) obtained for compounds **2** and **4** in methanol.

Table S1: An overview of species observed by high resolution ESI -ve mass spectrometry for mixtures containing **1**, **2** and **4** in a 1:1 ratio. Ma and Mb represent the anionic component of that amphiphilic salts contained within the mixtures analysed.

Molecular complex	**1** (M_a) + **4** (M_b)		**2** (M_a) + **4** (M_b)	
	Theoretical *(m/z)*	Actual *(m/z)*	Theoretical *(m/z)*	Actual *(m/z)*
$[M_a]^-$	359.0343	359.0537	329.0602	329.0815
$[M_b]^-$	293.0932	293.1094	293.0932	293.1108
$[M_a+M_b+H]^-$	653.1348	653.1676	623.1607	623.1981
$[M_a+M_b+Na]^-$	675.1167	675.1469	[a]	[a]
$[M_a+M_b+K]^-$	[a]	[a]	[a]	[a]
$[M_a+M_a+H]^-$	719.0759	719.1113	659.1277	659.1632
$[M_a+M_a+Na]^-$	741.0578	741.0974	681.1096	681.1400
$[M_a+M_a+K]^-$	[a]	[a]	[a]	[a]
$[M_b+M_b+H]^-$	[a]	[a]	587.1937	587.2260
$[M_b+M_b+Na]^-$	[a]	[a]	[a]	[a]
$[M_b+M_b+K]^-$	[a]	[a]	[a]	[a]

DLS data

Size distribution graphs (DMSO)

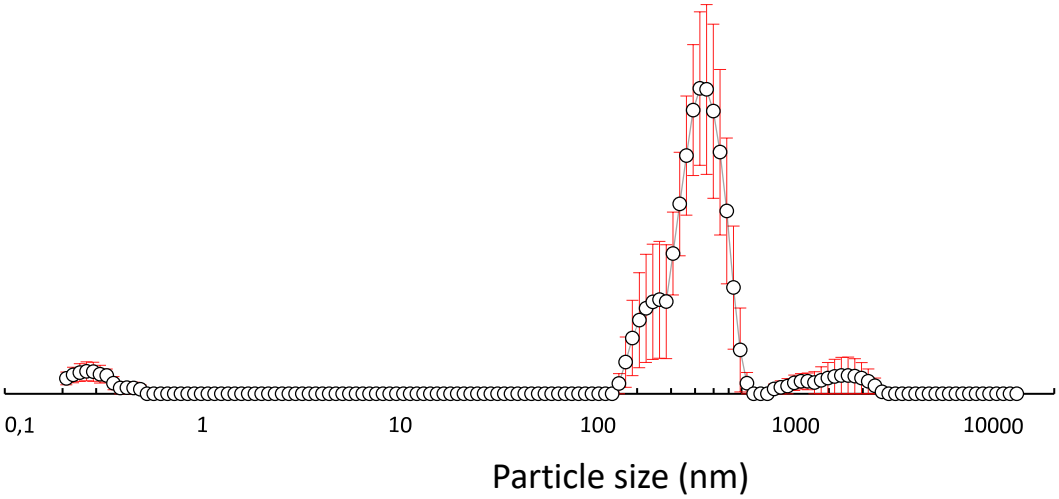

Figure S40: The average intensity particle size distribution for 5 DLS runs of compound **1** (55.56 mM) heated up to 40 °C in a DMSO solution.

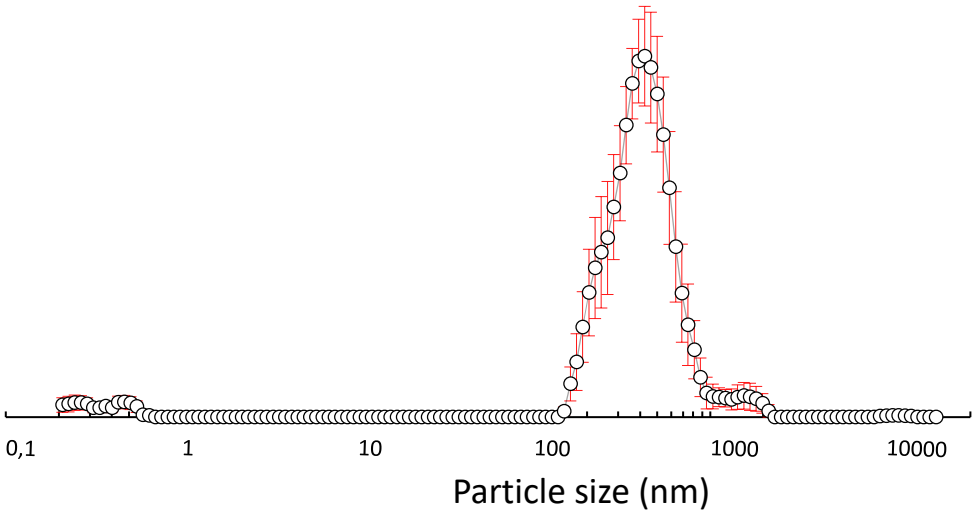

Figure S41: The average intensity particle size distribution for 10 DLS runs of compound **1** (55.56 mM) cooled down to 25 °C in a DMSO solution.

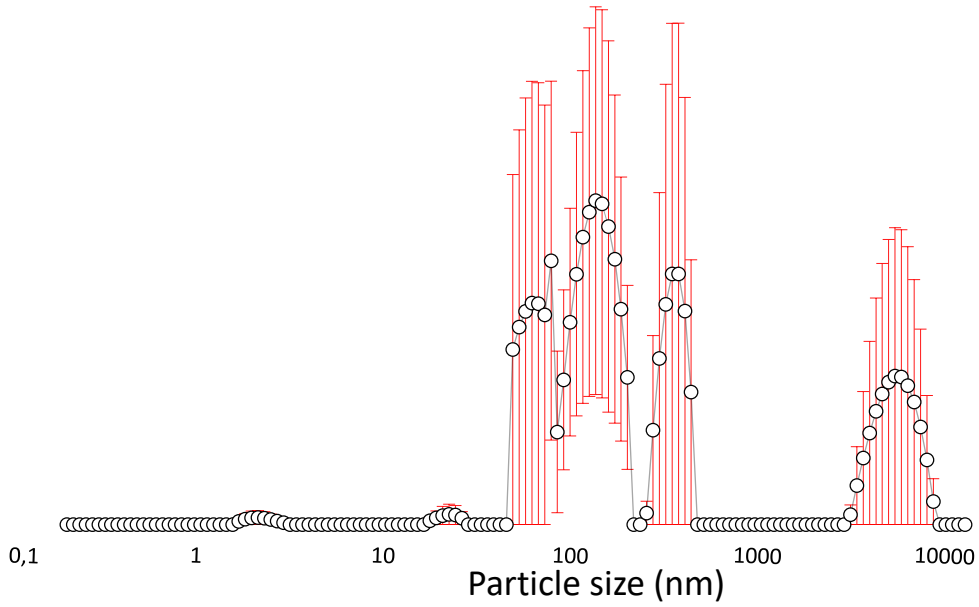

Figure S42: The average intensity particle size distribution for 5 DLS runs of compound **1** (5.56 mM) heated up to 40 °C in a DMSO solution.

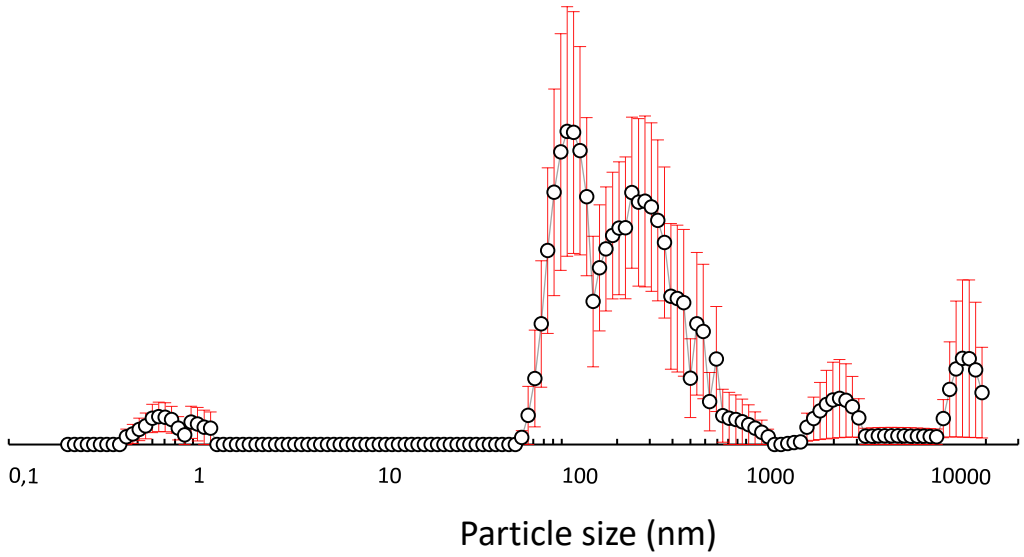

Figure S43: The average intensity particle size distribution for 10 DLS runs of compound **1** (5.56 mM) cooled down to 25 °C in a DMSO solution.

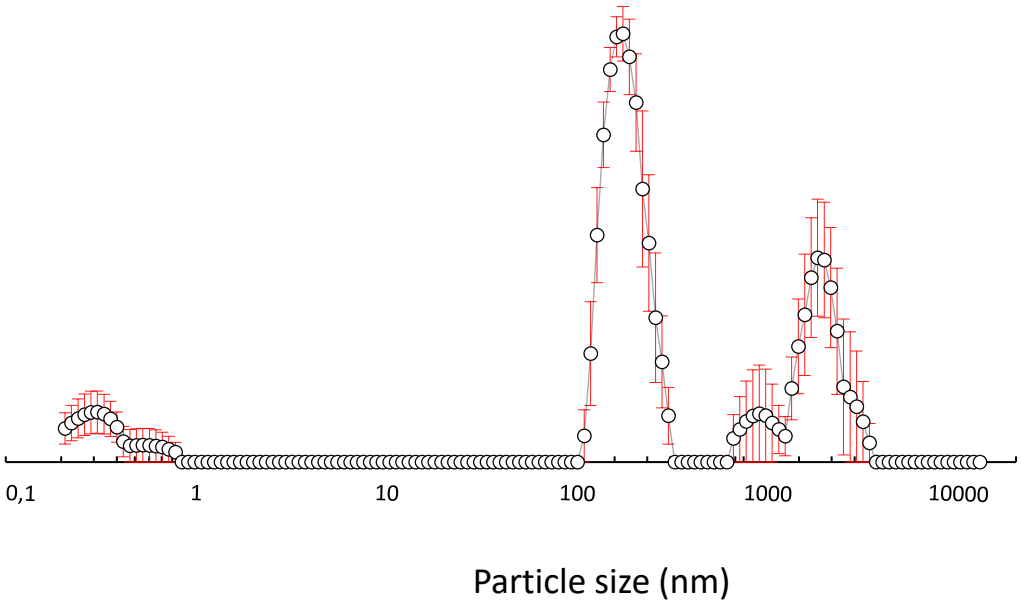

Figure S44: The average intensity particle size distribution for 5 DLS runs of compound **2** (55.56 mM) heated up to 40 °C in a DMSO solution.

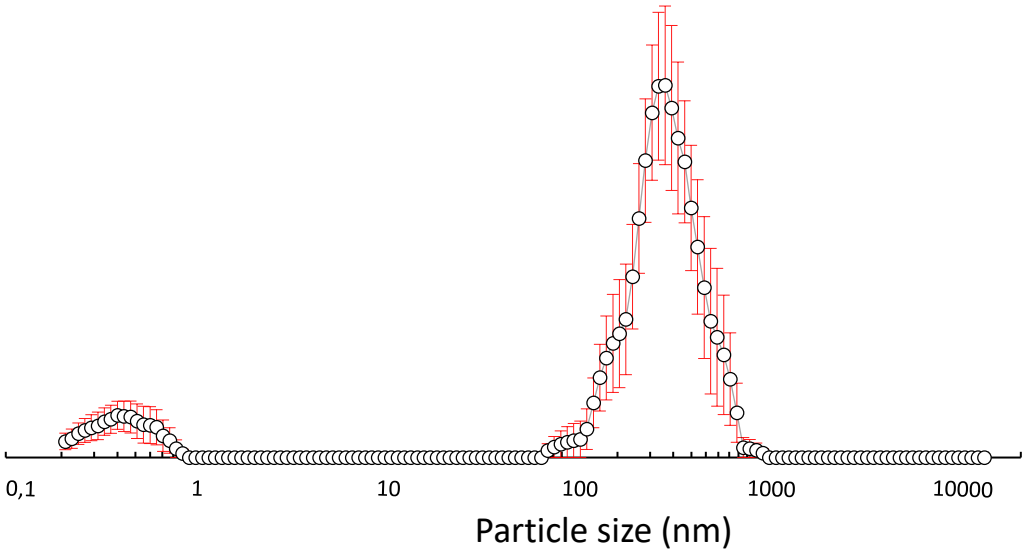

Figure S45: The average intensity particle size distribution for 10 DLS runs of compound **2** (55.56 mM) cooled down to 25 °C in a DMSO solution.

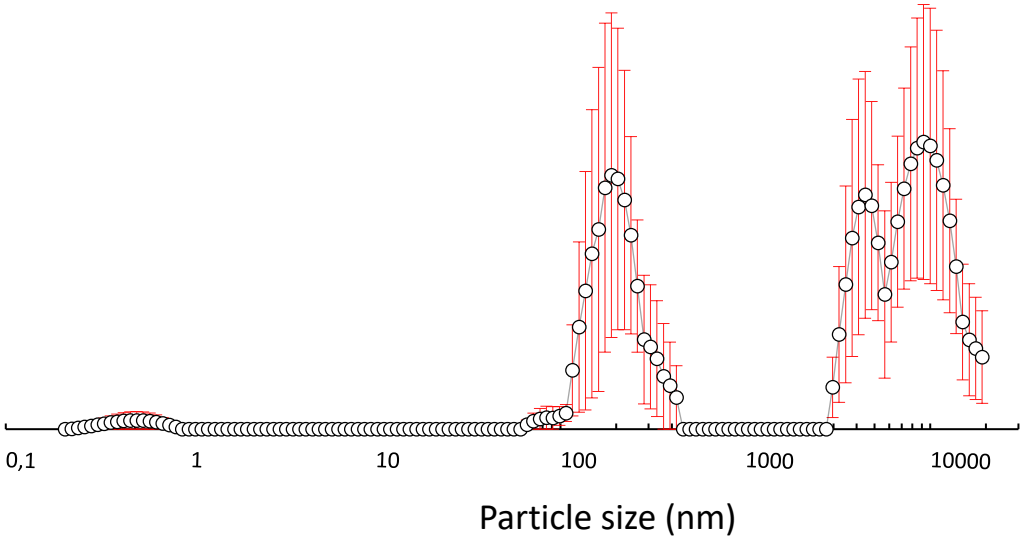

Figure S46: The average intensity particle size distribution for 5 DLS runs of compound **2** (5.56 mM) heated up to 40 °C in a DMSO solution.

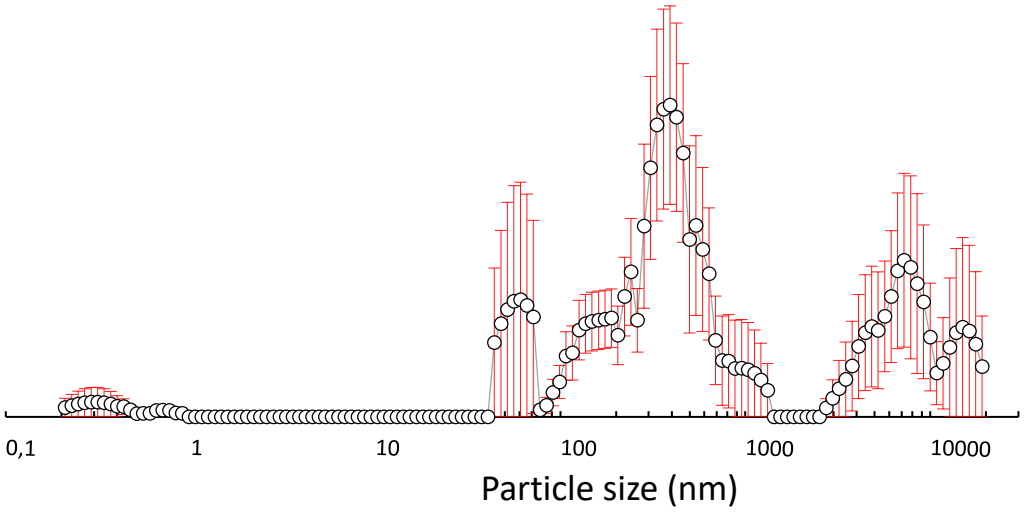

Figure S47: The average intensity particle size distribution for 10 DLS runs of compound **2** (5.56 mM) cooled down to 25 °C in a DMSO solution.

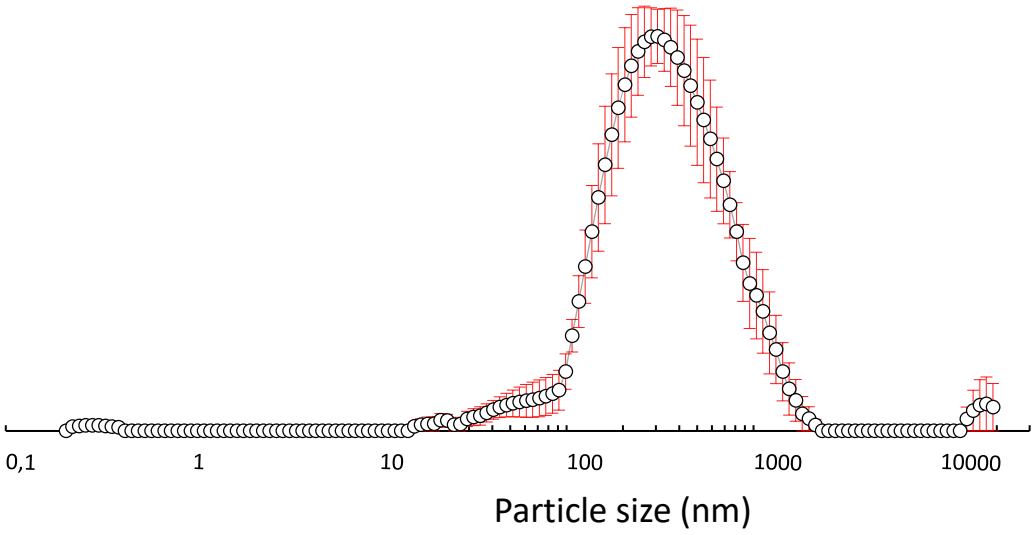

Figure S48: The average intensity particle size distribution for 5 DLS runs of compound **4** (55.56 mM) heated up to 40 °C in a DMSO solution.

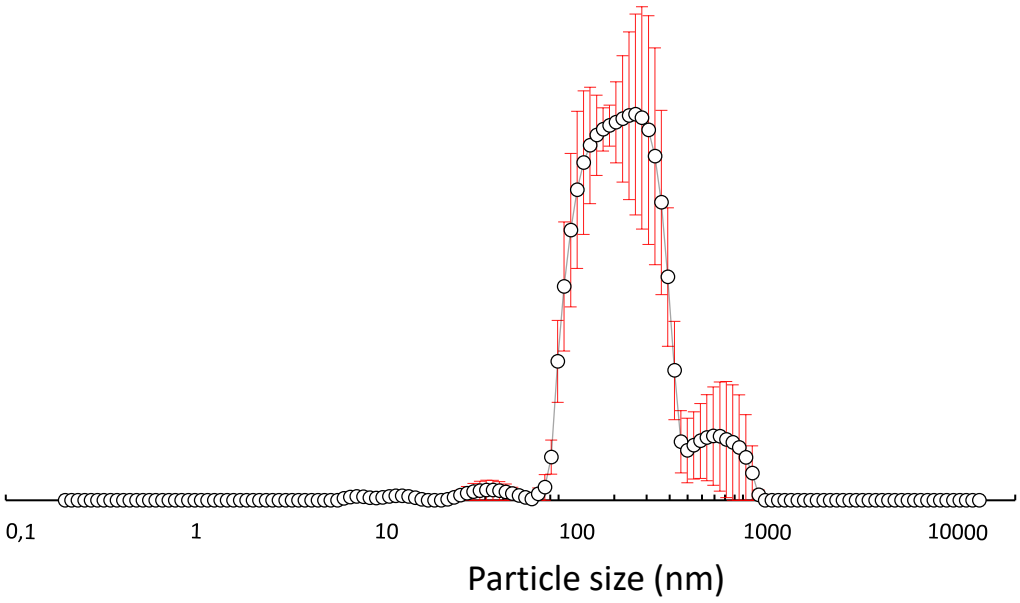

Figure S49: The average intensity particle size distribution for 5 DLS runs of compound **4** (5.56 mM) heated up to 40 °C in a DMSO solution.

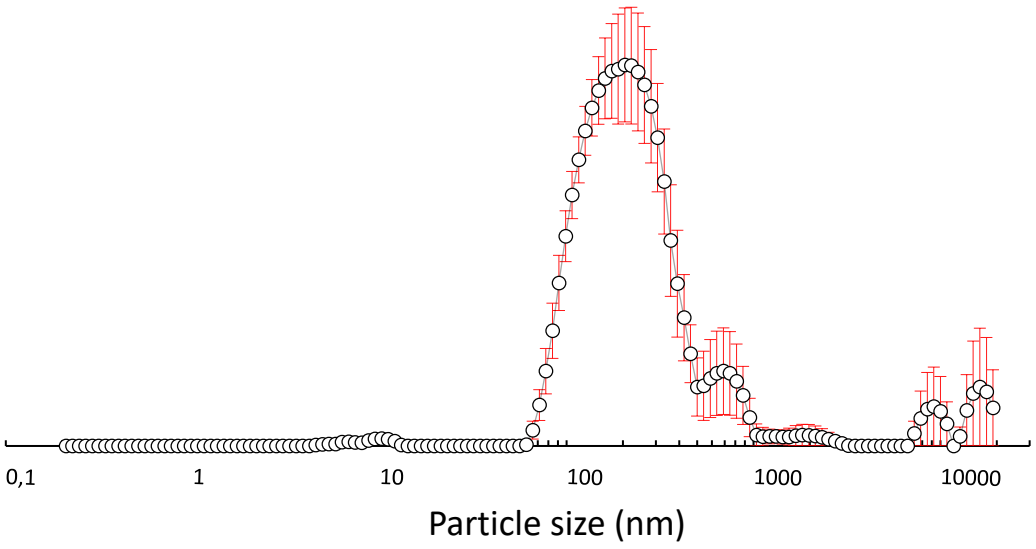

Figure S50: The average intensity particle size distribution for 10 DLS runs of compound **4** (5.56 mM) cooled down to 25 °C in a DMSO solution.

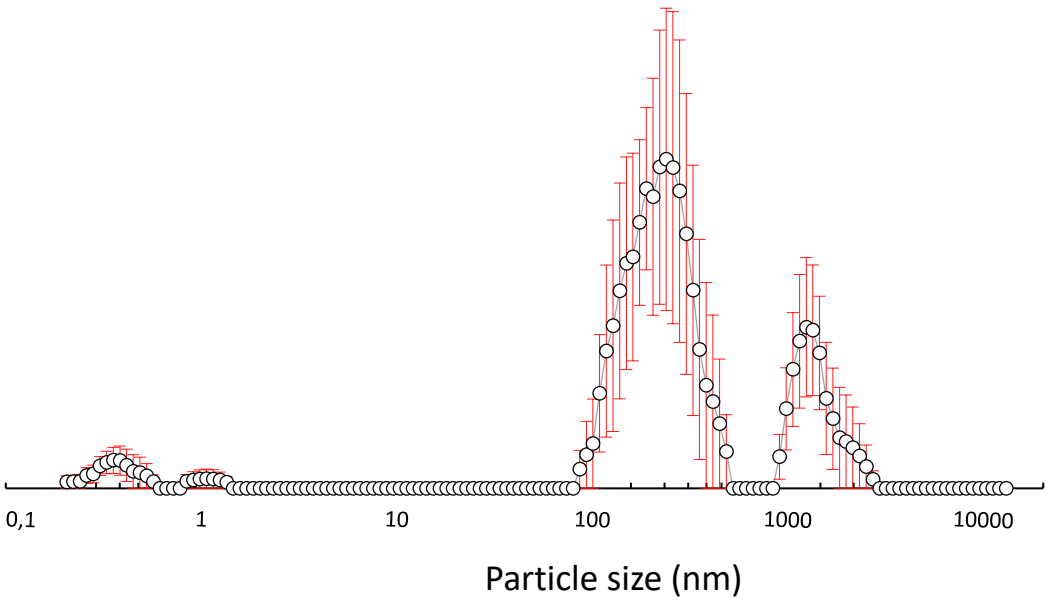

Figure S51: The average intensity particle size distribution for 5 DLS runs of compounds **1** and **2** in a 1:1 mix (total concentration 55.56 mM) heated up to 40 °C of in a DMSO solution.

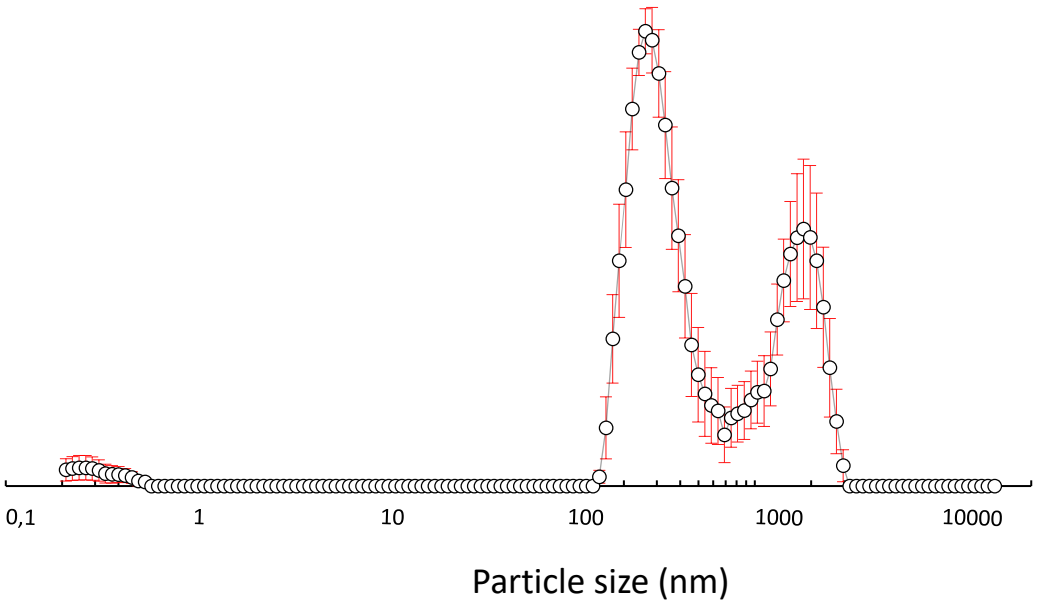

Figure S52: The average intensity particle size distribution for 10 DLS runs of compounds **1** and **2** in a 1:1 mix (total concentration 55.56 mM) cooled down to 25 °C of in a DMSO solution.

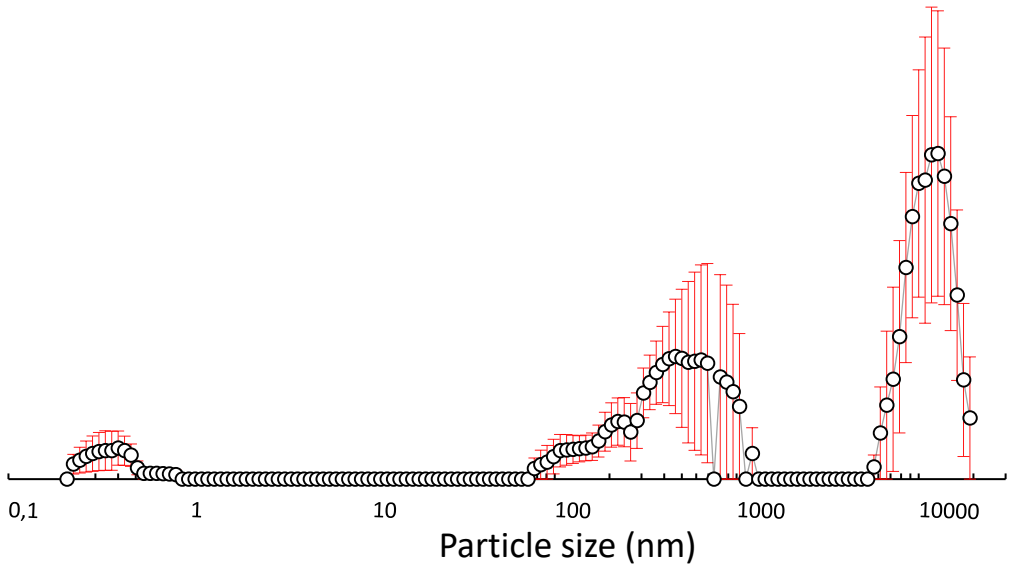

Figure S53: The average intensity particle size distribution for 5 DLS runs of compounds **1** and **2** in a 1:1 mix (total concentration 5.56 mM) heated up to 40 °C of in a DMSO solution.

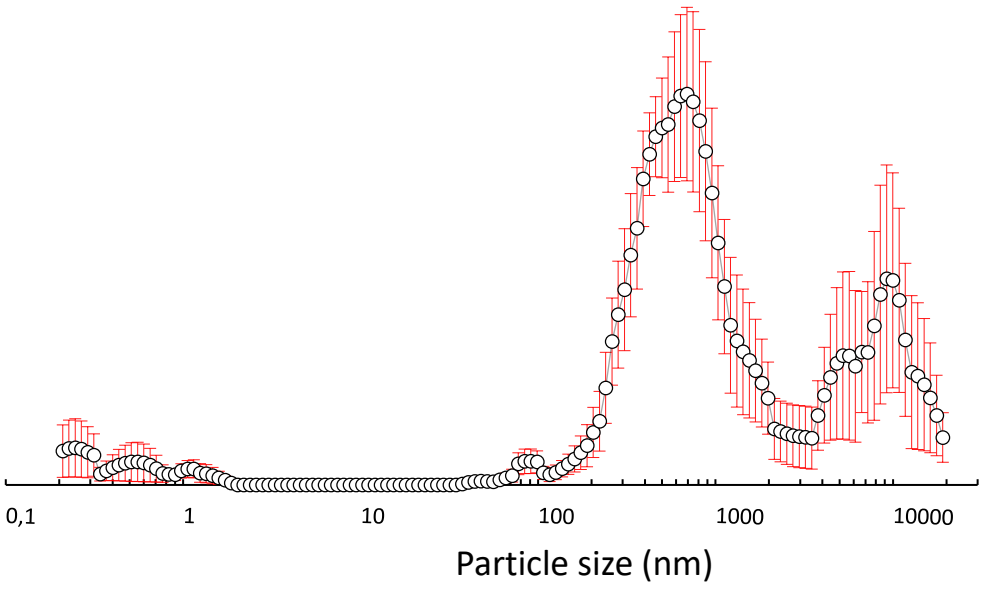

Figure S54: The average intensity particle size distribution for 10 DLS runs of compounds **1** and **2** in a 1:1 mix (total concentration 5.56 mM) cooled down to 25 °C of in a DMSO solution.

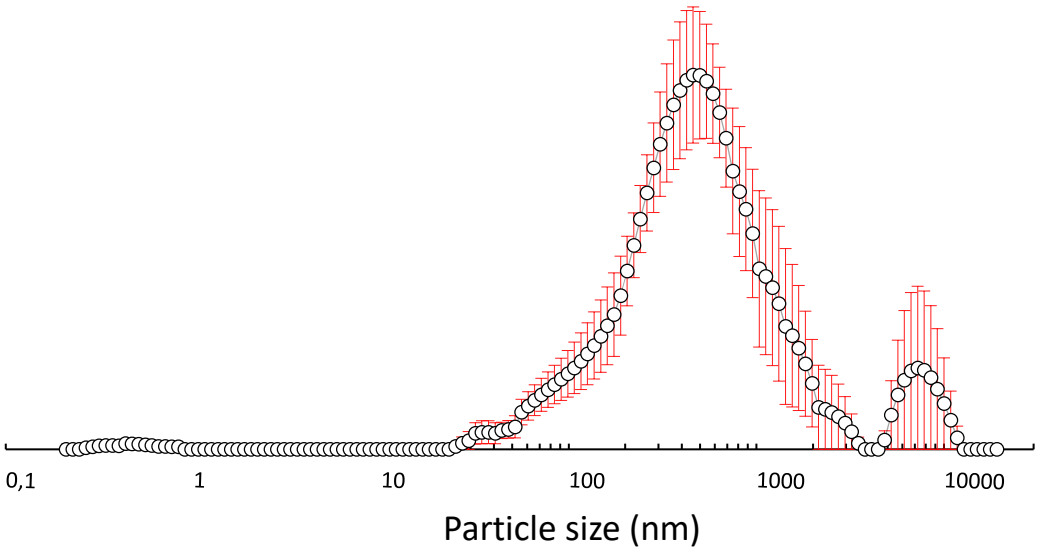

Figure S55: The average intensity particle size distribution for 5 DLS runs of compounds **1** and **4** in a 1:1 mix (total concentration 55.56 mM) heated up to 40 °C of in a DMSO solution.

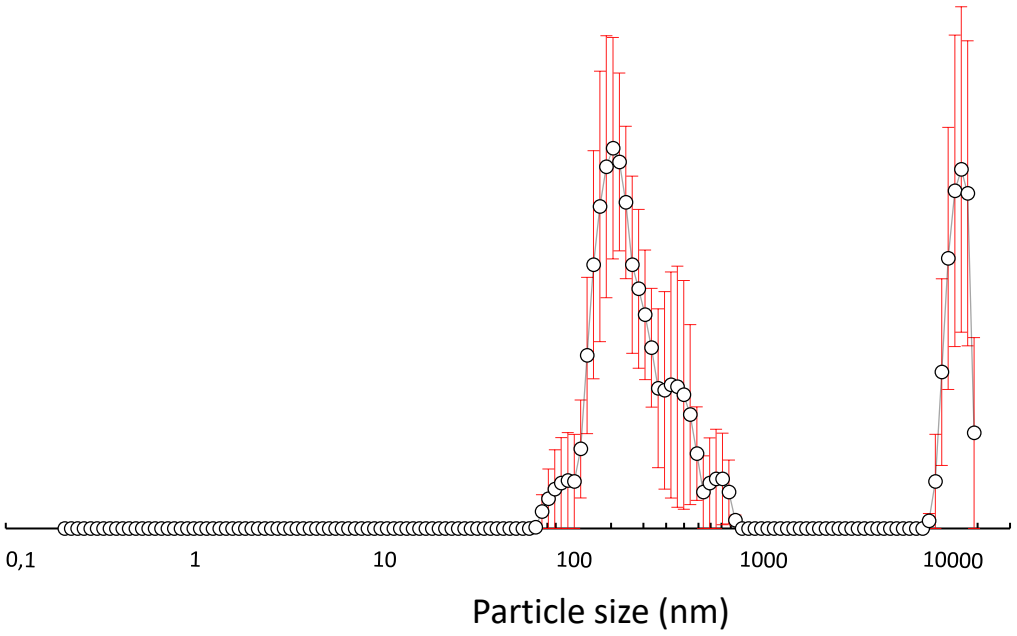

Figure S56: The average intensity particle size distribution for 5 DLS runs of compounds **1** and **4** in a 1:1 mix (total concentration 5.56 mM) heated up to 40 °C of in a DMSO solution.

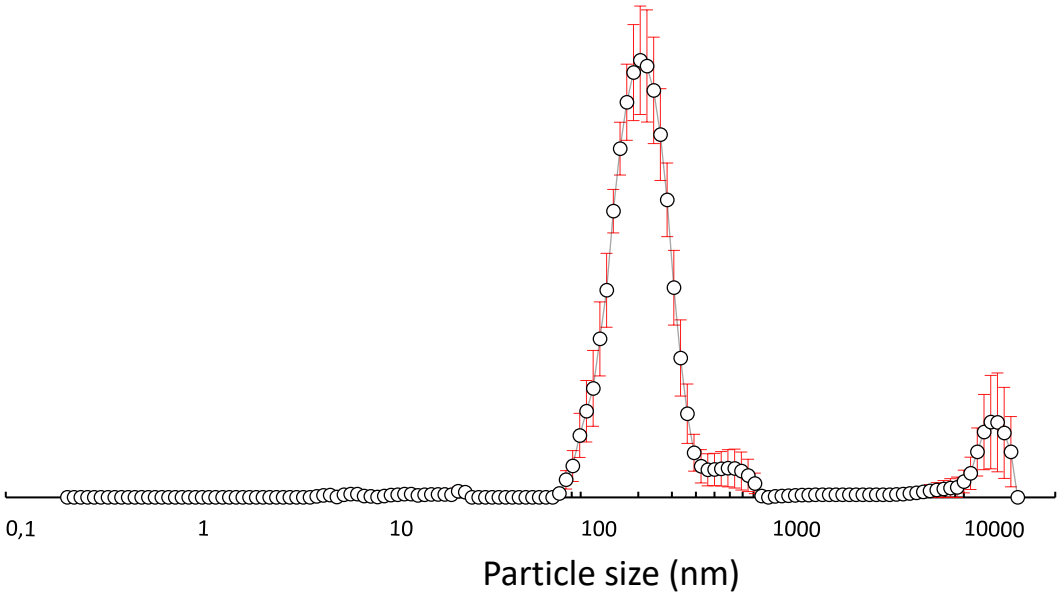

Figure S57: The average intensity particle size distribution for 10 DLS runs of compounds **1** and **4** in a 1:1 mix (total concentration 5.56 mM) cooled down to 25 °C of in a DMSO solution.

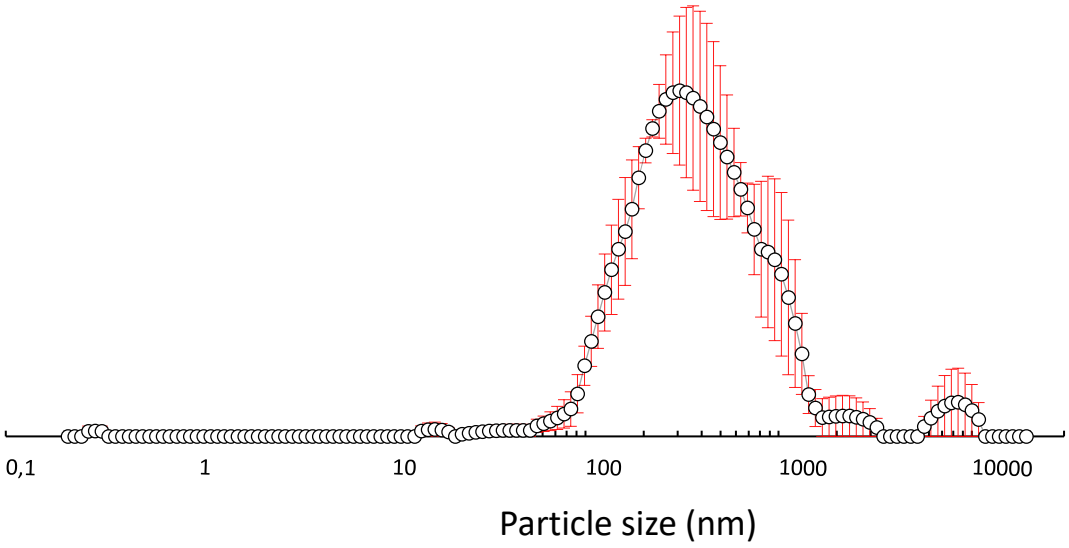

Figure S58: The average intensity particle size distribution for 5 DLS runs of compounds **2** and **4** in a 1:1 mix (total concentration 55.56 mM) heated up to 40 °C of in a DMSO solution.

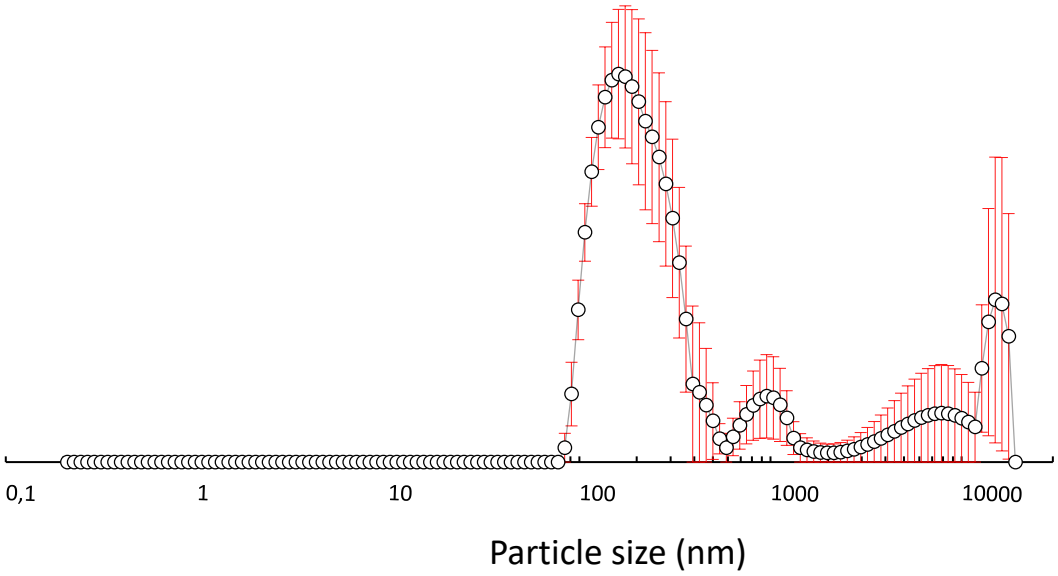

Figure S59: The average intensity particle size distribution for 5 DLS runs of compounds **2** and **4** in a 1:1 mix (total concentration 5.56 mM) heated up to 40 °C of in a DMSO solution.

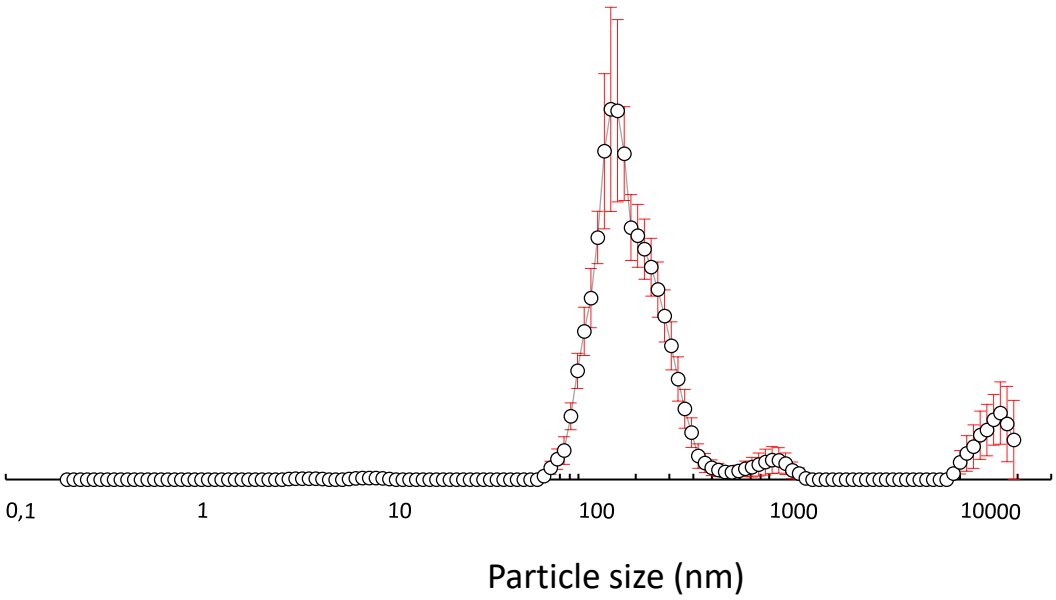

Figure S60: The average intensity particle size distribution for 10 DLS runs of compounds **2** and **4** in a 1:1 mix (total concentration 5.56 mM) cooled down to 25 °C of in a DMSO solution.

Correlation function data (DMSO)

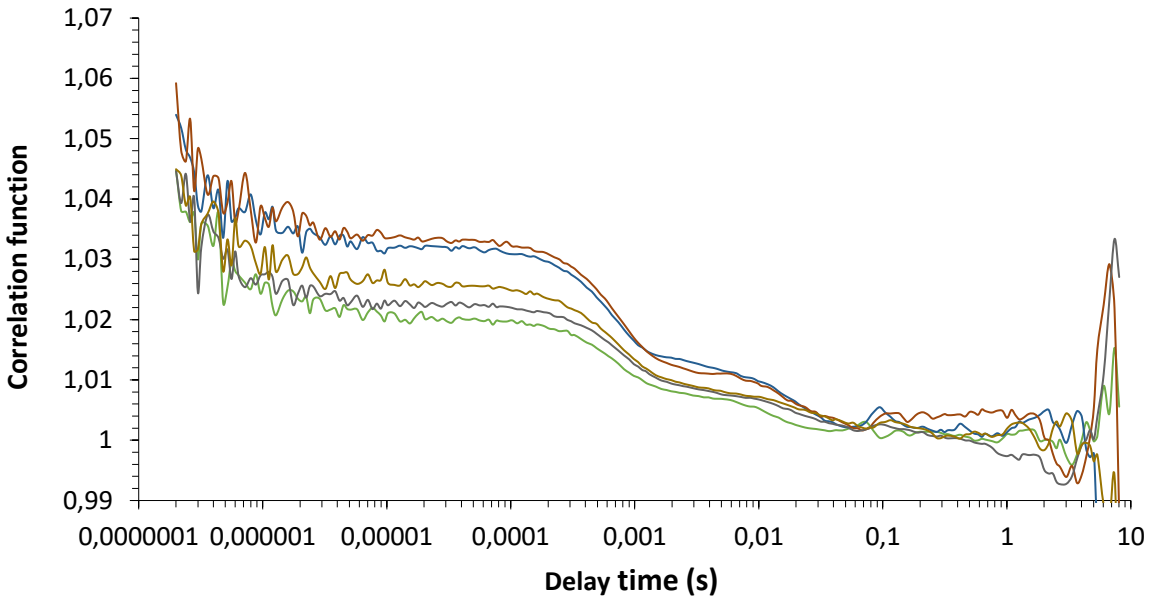

Figure S61: Correlation function data for 5 DLS runs of compound **2** (55.56 mM) heated up to 40 °C in a DMSO solution.

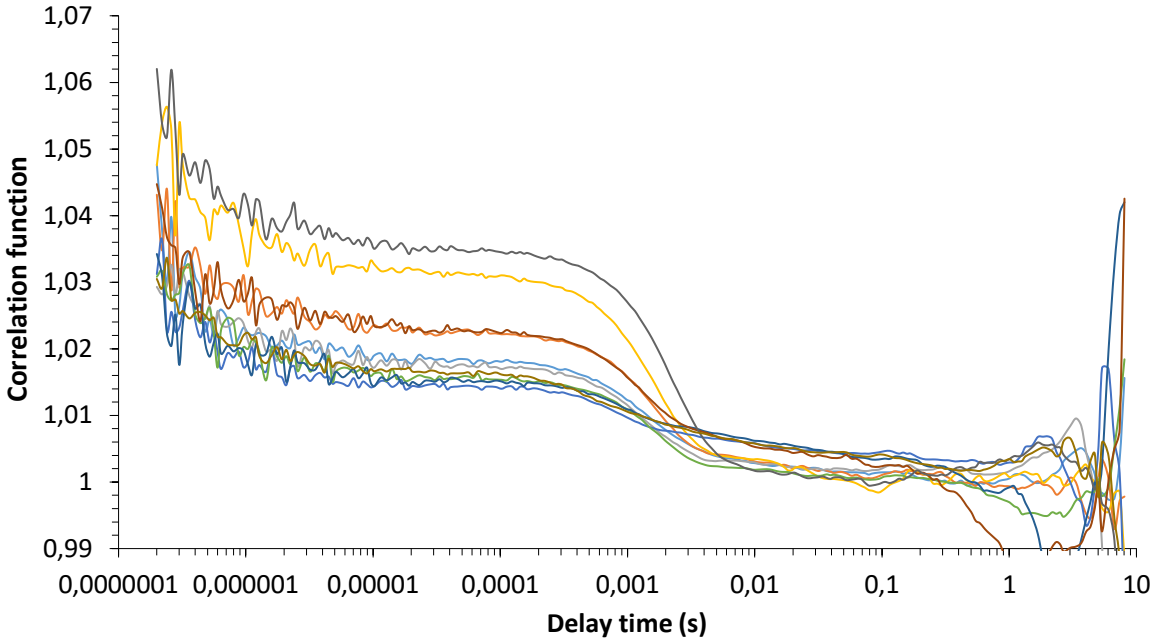

Figure S62: Correlation function data for 10 DLS runs of compound **2** (55.56 mM) cooled down to 25 °C in a DMSO solution.

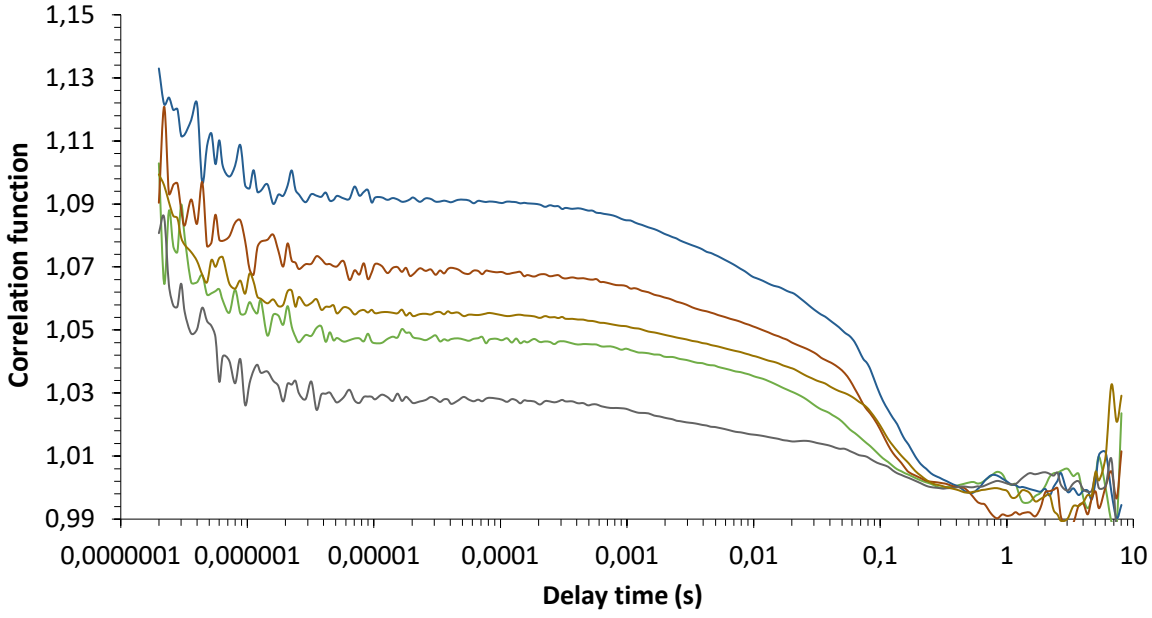

Figure S63: Correlation function data for 5 DLS runs of compound **2** (5.56 mM) heated up to 40 °C in a DMSO solution.

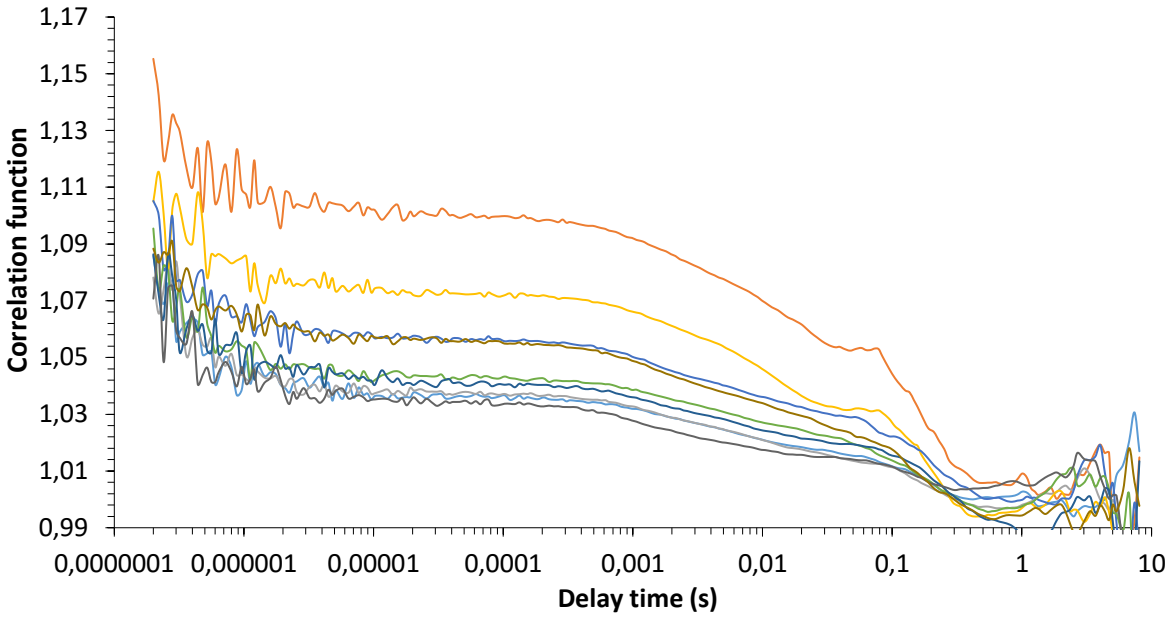

Figure S64: Correlation function data for 10 DLS runs of compound **2** (5.56 mM) cooled down to 25 °C in a DMSO solution.

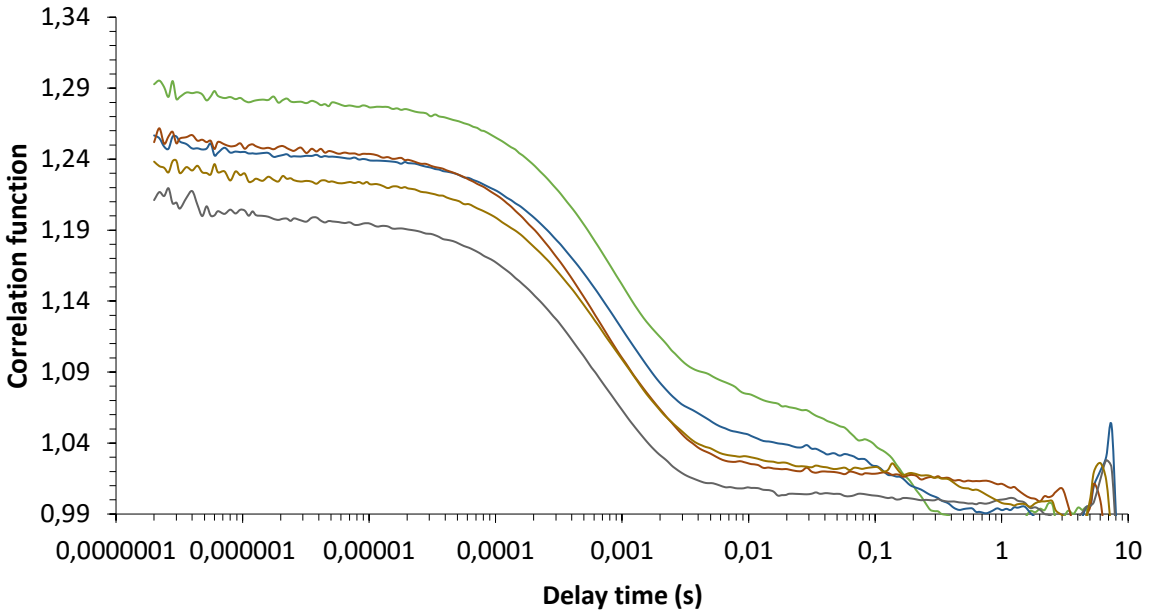

Figure S65: Correlation function data for 5 DLS runs of compound **4** (55.56 mM) heated up to 40 °C in a DMSO solution.

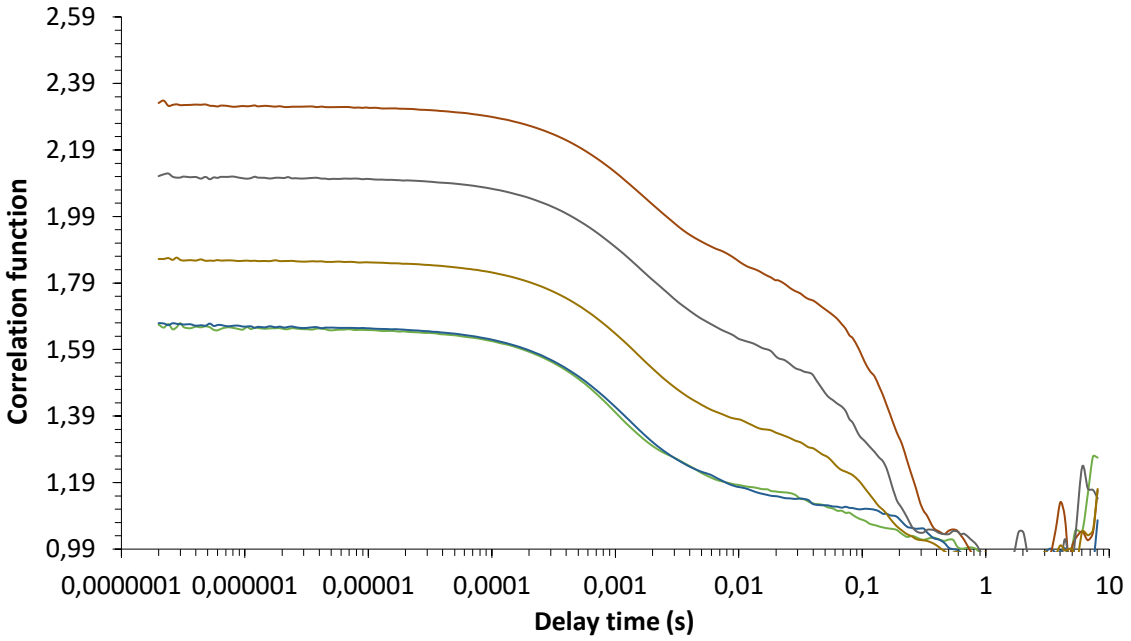

Figure S66: Correlation function data for 5 DLS runs of compound **4** (5.56 mM) heated up to 40 °C in a DMSO solution.

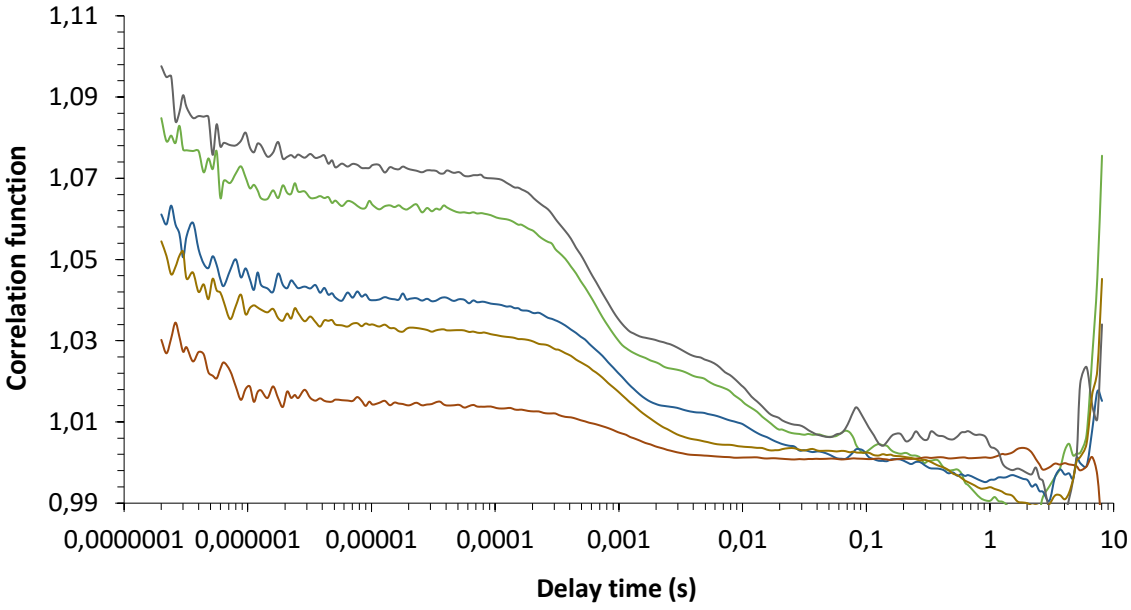

Figure S67: Correlation function data for 5 DLS runs of compounds **1** and **2** in a 1:1 mix (total concentration 55.56 mM) heated up to 40 °C of in a DMSO solution.

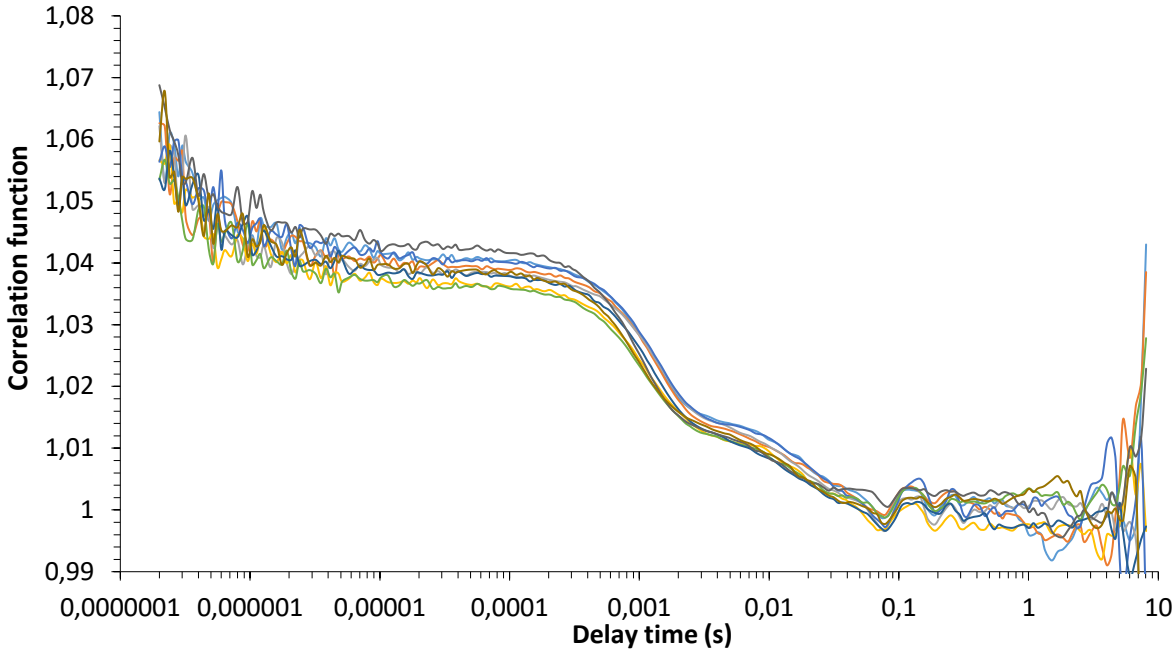

Figure S68: Correlation function data for 10 DLS runs of compounds **1** and **2** in a 1:1 mix (total concentration 55.56 mM) cooled down to 25 °C of in a DMSO solution.

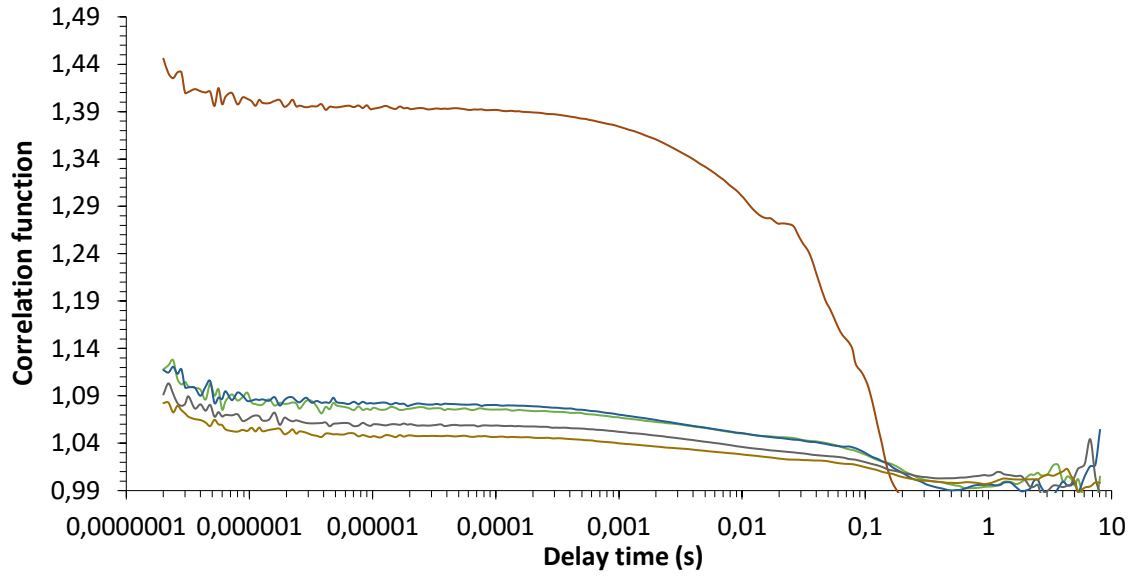

Figure S69: Correlation function data for 5 DLS runs of compounds **1** and **2** in a 1:1 mix (total concentration 5.56 mM) heated up to 40 °C of in a DMSO solution.

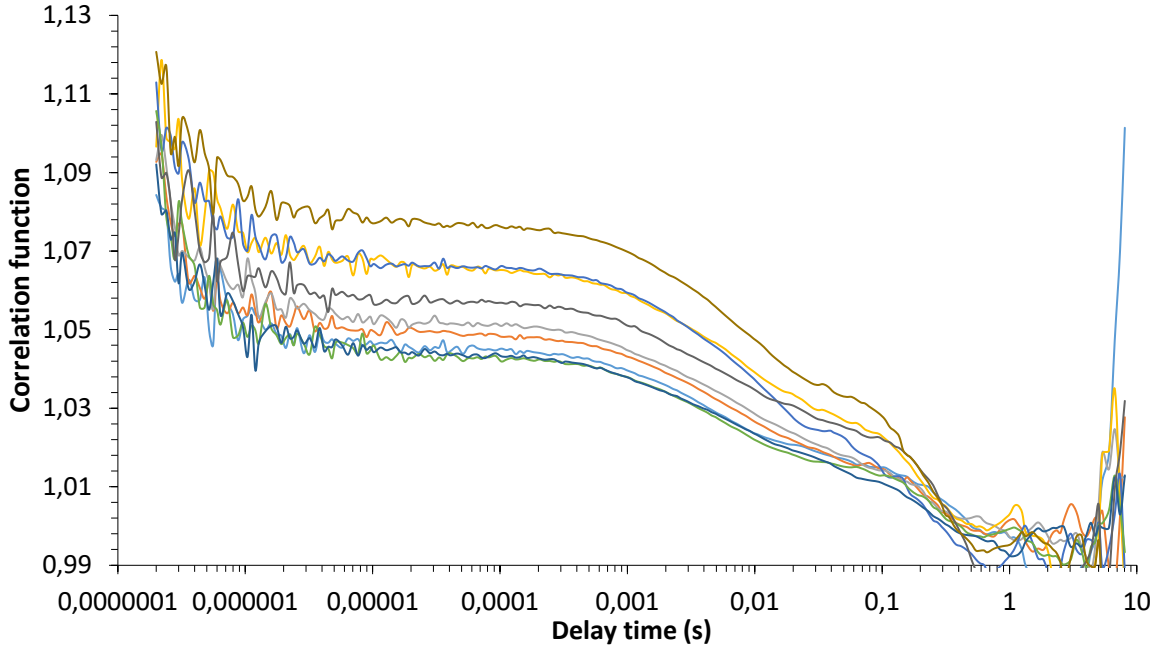

Figure S70: Correlation function data for 10 DLS runs of compounds **1** and **2** in a 1:1 mix (total concentration 5.56 mM) cooled down to 25 °C of in a DMSO solution.

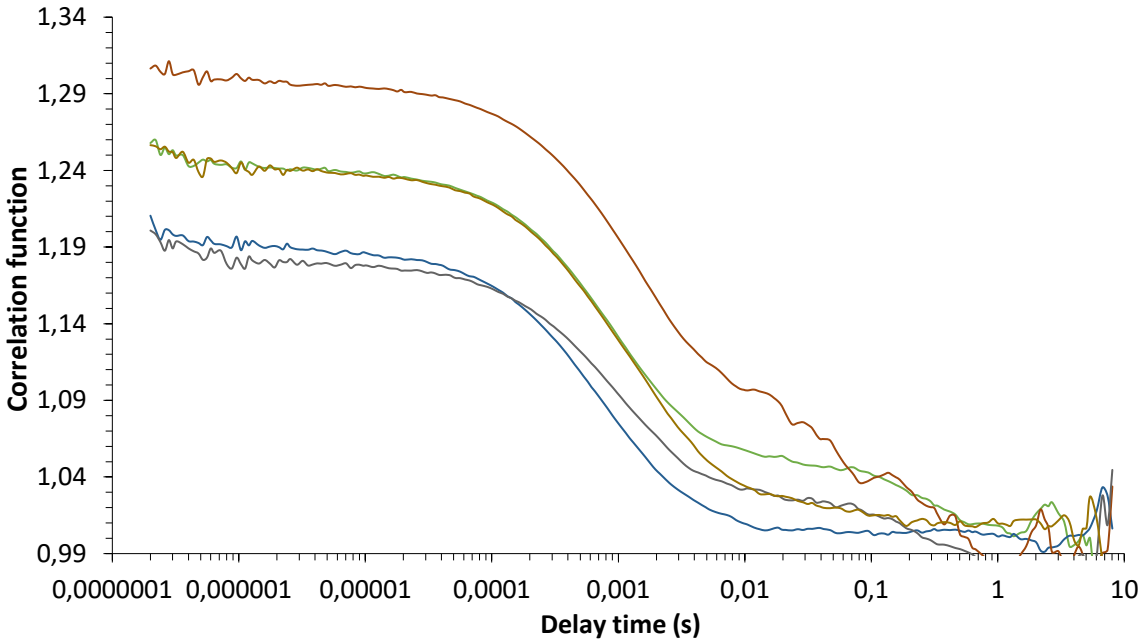

Figure S71: Correlation function data for 5 DLS runs of compounds **1** and **4** in a 1:1 mix (total concentration 55.56 mM) heated up to 40 °C of in a DMSO solution.

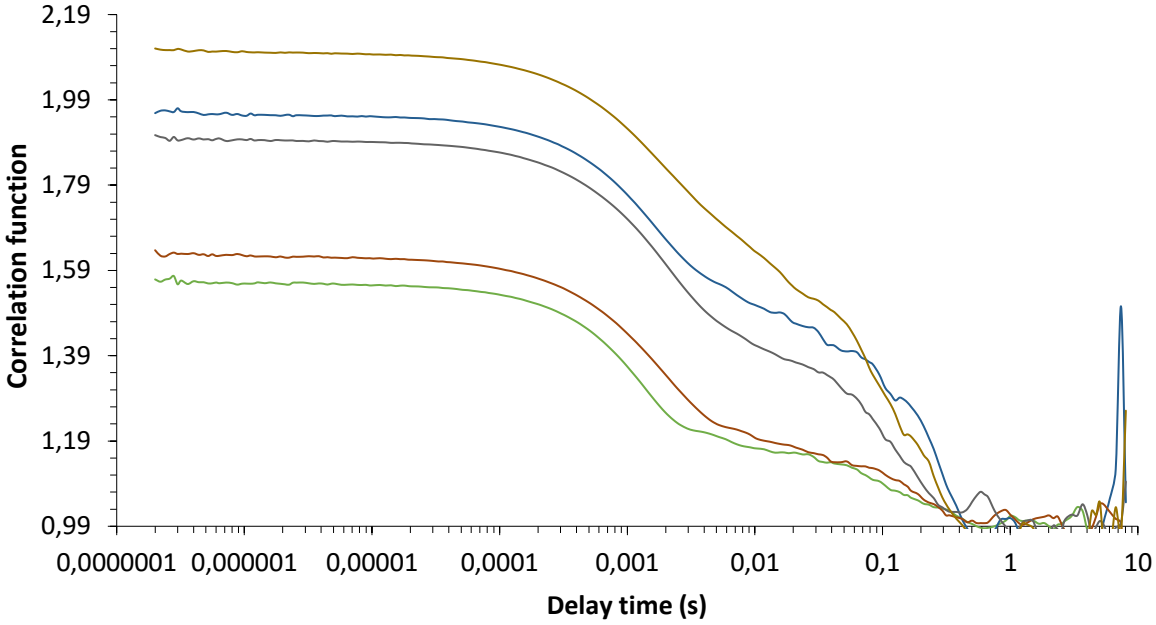

Figure S72: Correlation function data for 5 DLS runs of compounds **1** and **4** in a 1:1 mix (total concentration 5.56 mM) heated up to 40 °C of in a DMSO solution.

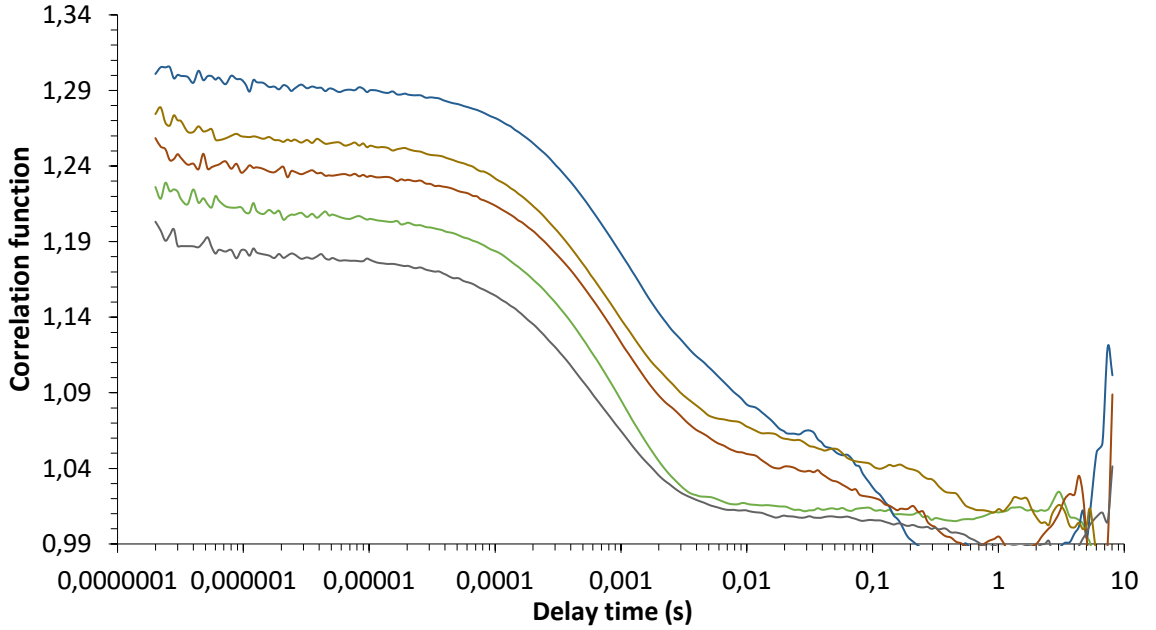

Figure S73: Correlation function data for 5 DLS runs of compounds **2** and **4** in a 1:1 mix (total concentration 55.56 mM) heated up to 40 °C of in a DMSO solution.

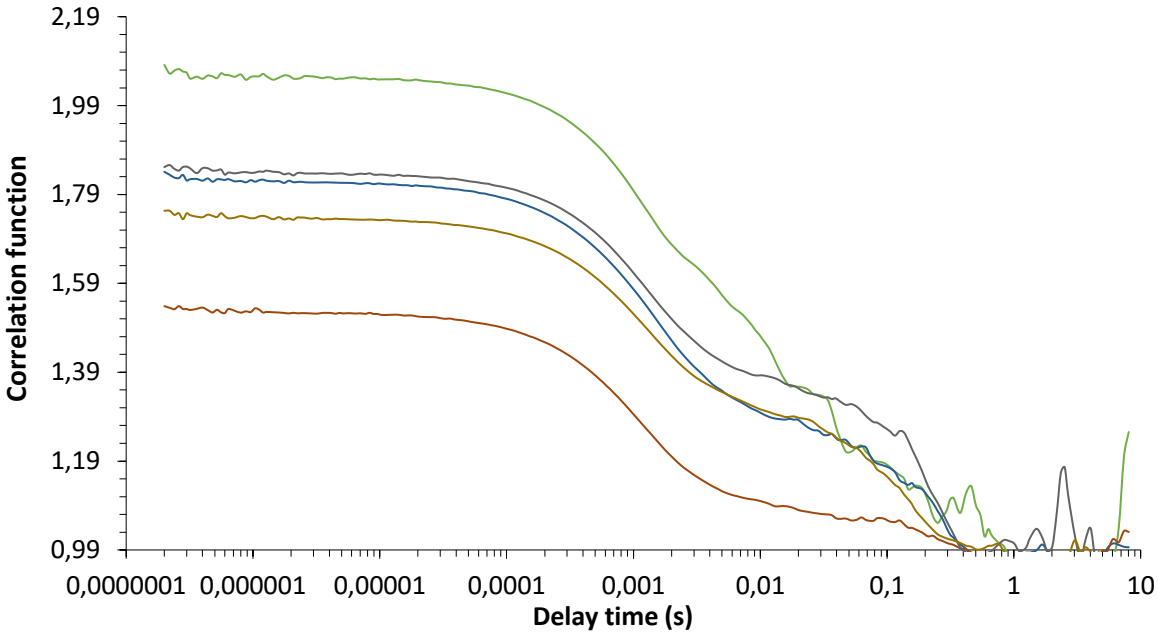

Figure S74: Correlation function data for 5 DLS runs of compounds **2** and **4** in a 1:1 mix (total concentration 5.56 mM) heated up to 40 °C of in a DMSO solution.

Particle size distribution (EtOH: H_2O 1:19)

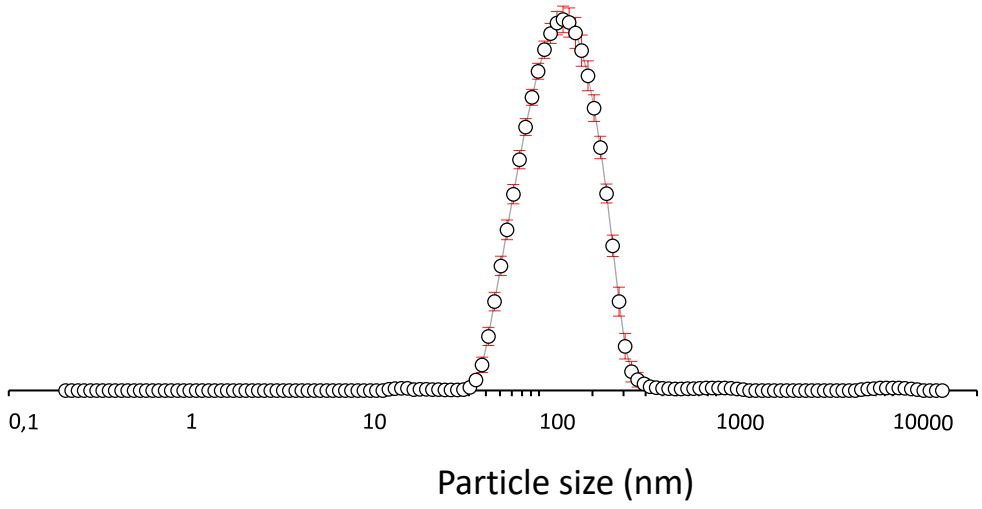

Figure S75: Illustrating the average intensity particle size distribution of compound **1** at 5.56 mM in EtOH: H_2O (1: 19) which was calculated using 10 DLS runs at a temperature of 25 ^{o}C.

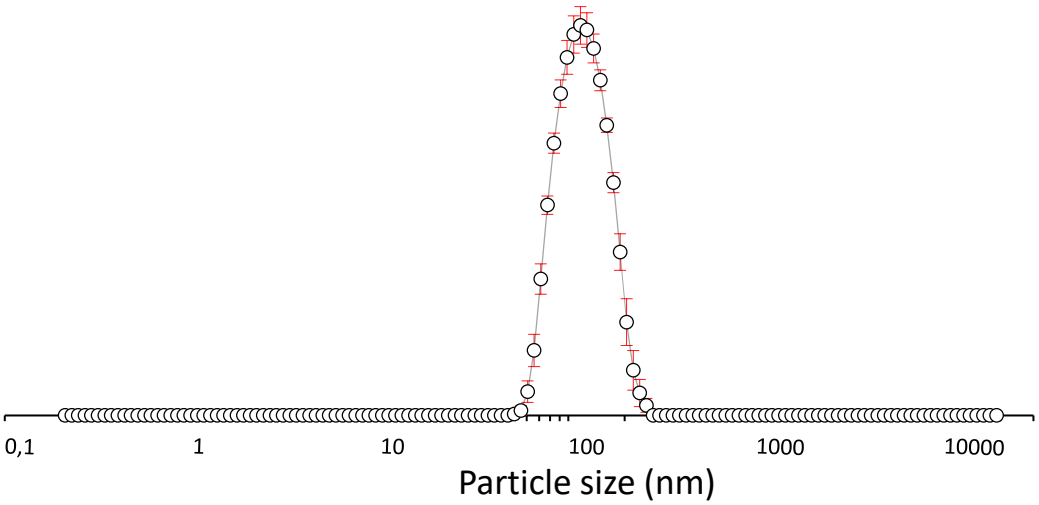

Figure S76: Illustrating the average intensity particle size distribution of compound **1** at 0.56 mM in EtOH: H_2O (1: 19) which was calculated using 10 DLS runs at a temperature of 25 ^oC.

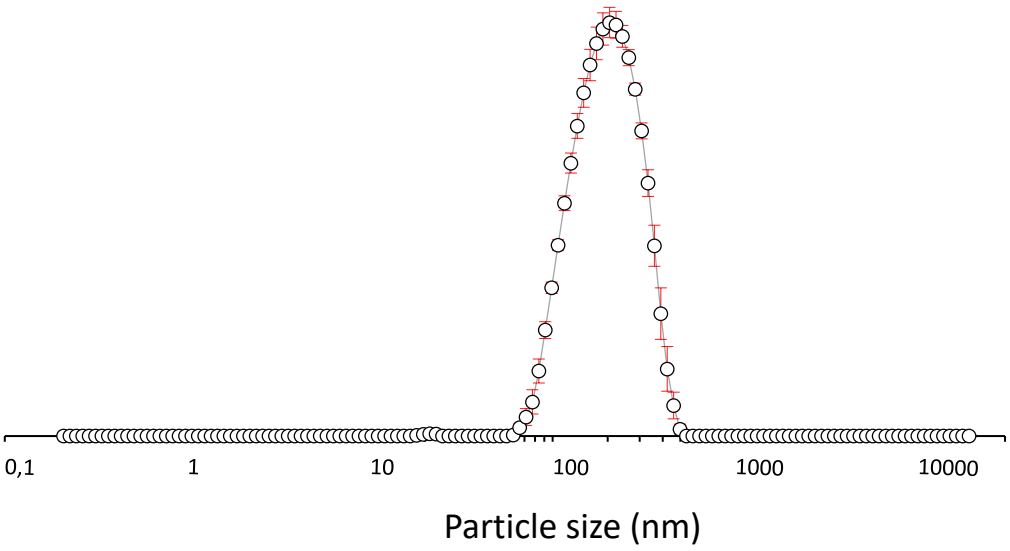

Figure S77: Illustrating the average intensity particle size distribution of compound **2** at 5.56 mM in EtOH: H_2O (1: 19) which was calculated using 10 DLS runs at a temperature of 25 ^oC.

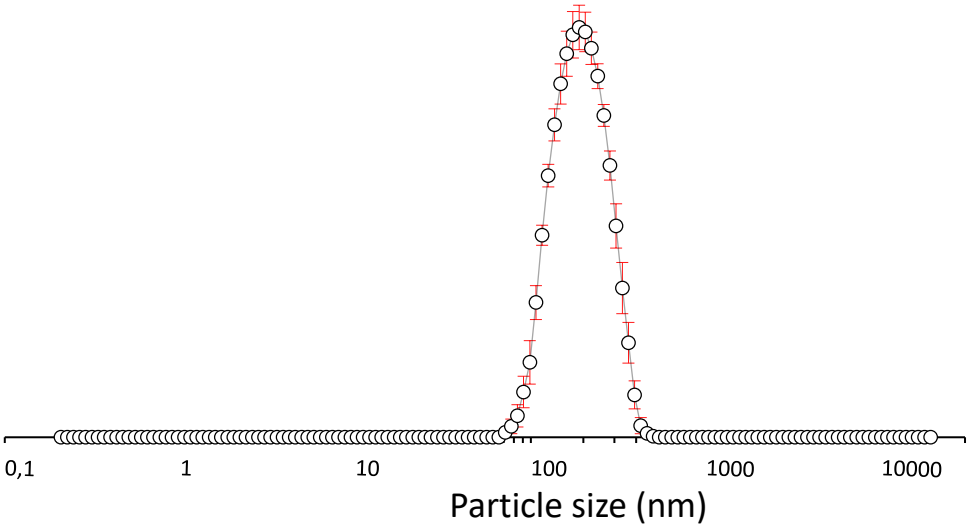

Figure S78: Illustrating the average intensity particle size distribution of compound **2** at 0.56 mM in EtOH: H_2O (1: 19) which was calculated using 10 DLS runs at a temperature of 25 ^oC.

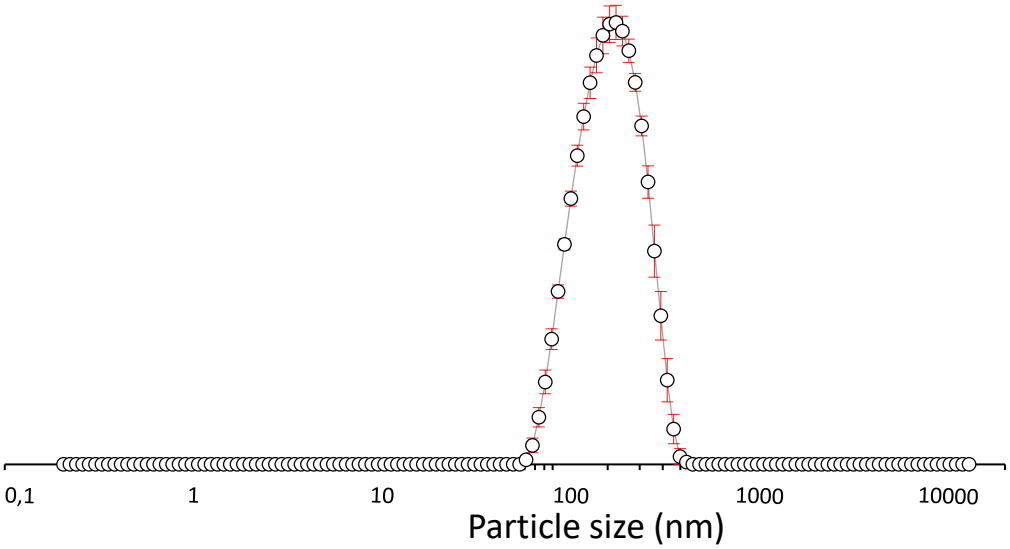

Figure S79: Illustrating the average intensity particle size distribution of compound **4** at 5.56 mM in EtOH: H_2O (1: 19) which was calculated using 10 DLS runs at a temperature of 25 ^oC.

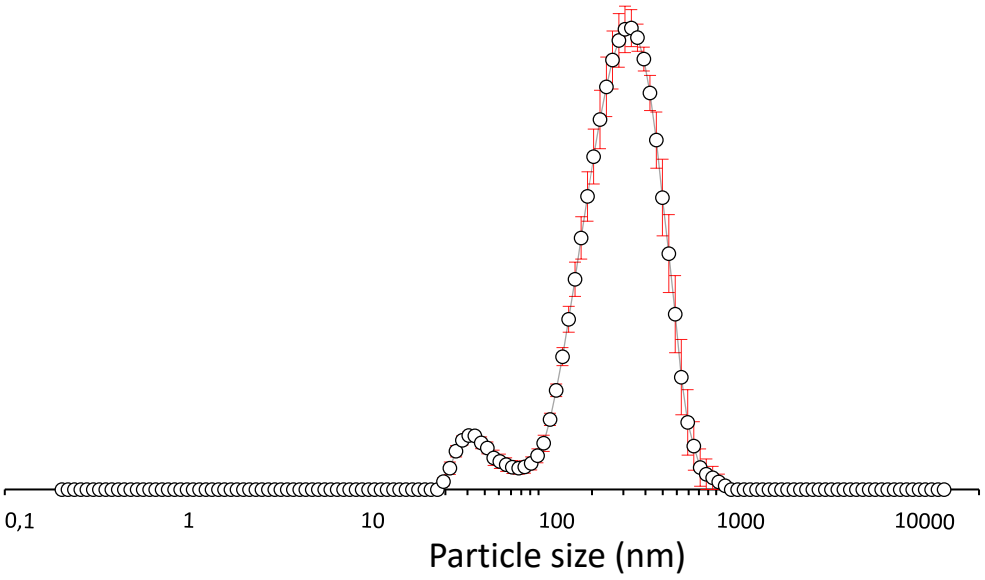

Figure S80: Illustrating the average intensity particle size distribution of compound **4** at 0.56 mM in EtOH: H_2O (1: 19) which was calculated using 10 DLS runs at a temperature of 25 ^oC.

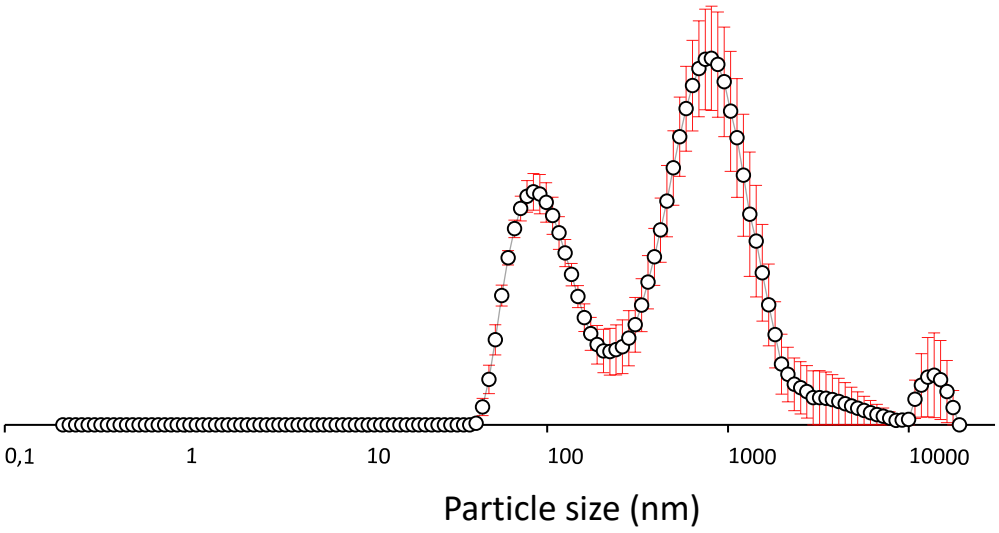

Figure S81: Illustrating the average intensity particle size distribution of compound **1** and **2** (mix) at 5.56 mM in EtOH: H_2O (1: 19) which was calculated using 10 DLS runs at a temperature of 25 ^oC.

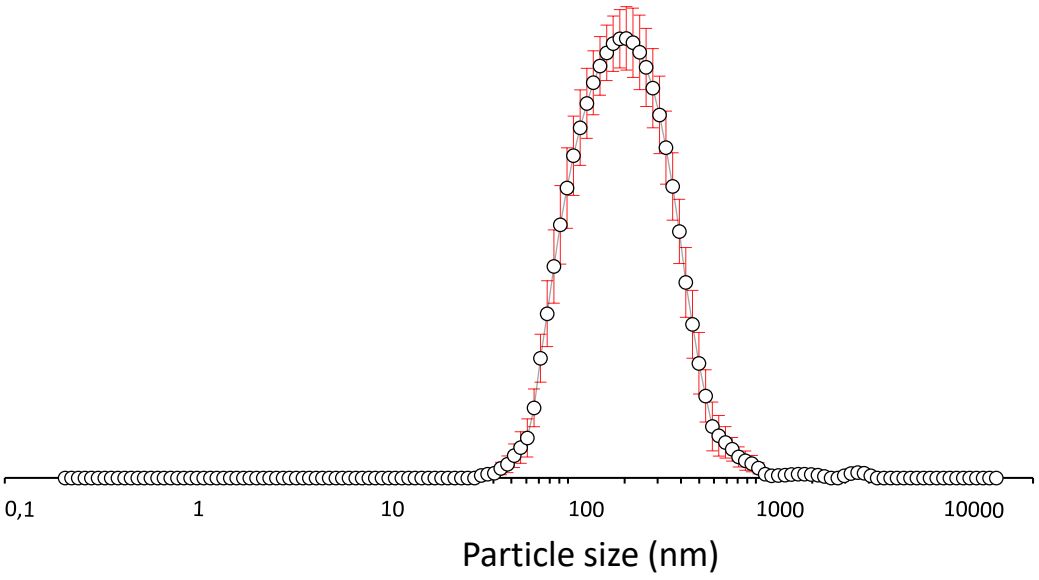

Figure S82: Illustrating the average intensity particle size distribution of compound **1** and **2** (mix) at 0.56 mM in EtOH: H_2O (1: 19) which was calculated using 10 DLS runs at a temperature of 25 ^oC.

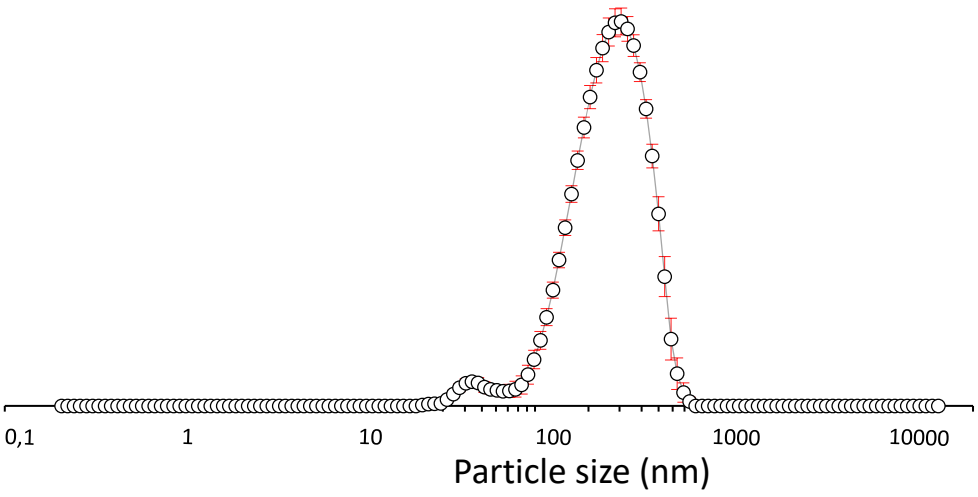

Figure S83: Illustrating the average intensity particle size distribution of compound **1** and **4** (mix) at 5.56 mM in EtOH: H_2O (1: 19) which was calculated using 10 DLS runs at a temperature of 25 ^oC.

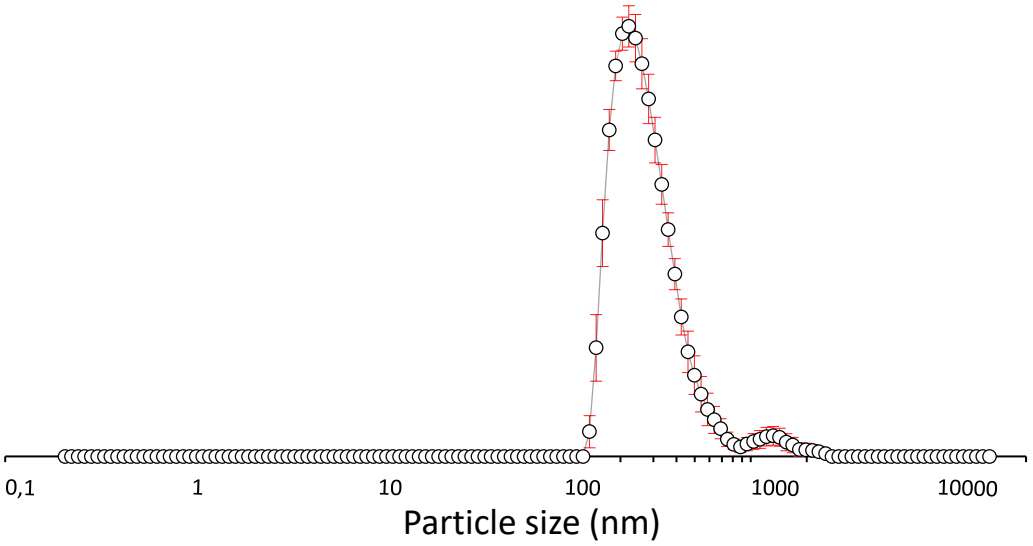

Figure S84: Illustrating the average intensity particle size distribution of compound **1** and **4** (mix) at 0.56 mM in EtOH: H_2O (1: 19) which was calculated using 10 DLS runs at a temperature of 25 ^oC.

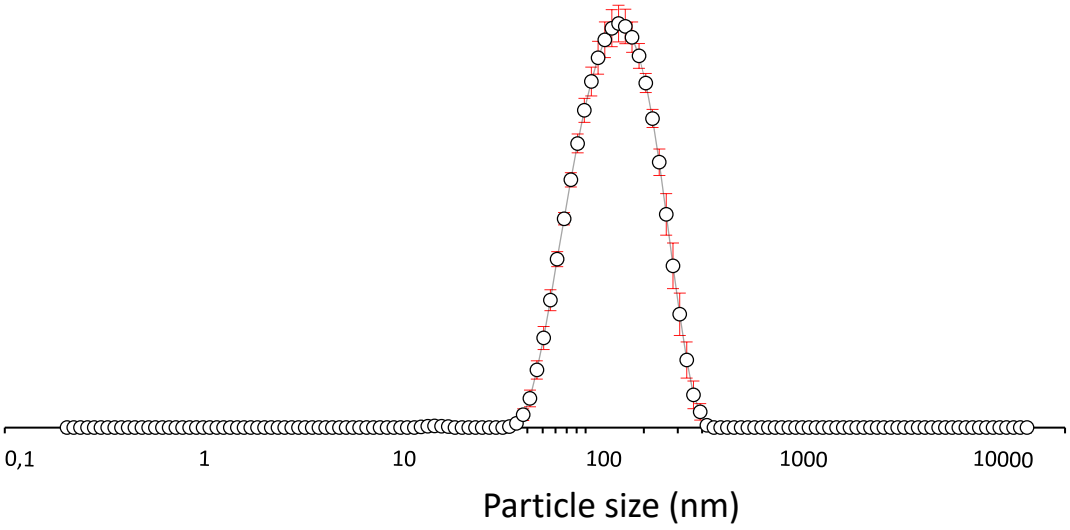

Figure S85: Illustrating the average intensity particle size distribution of compound **2** and **4** (mix) at 5.56 mM in EtOH: H_2O (1: 19) which was calculated using 10 DLS runs at a temperature of 25 ^oC.

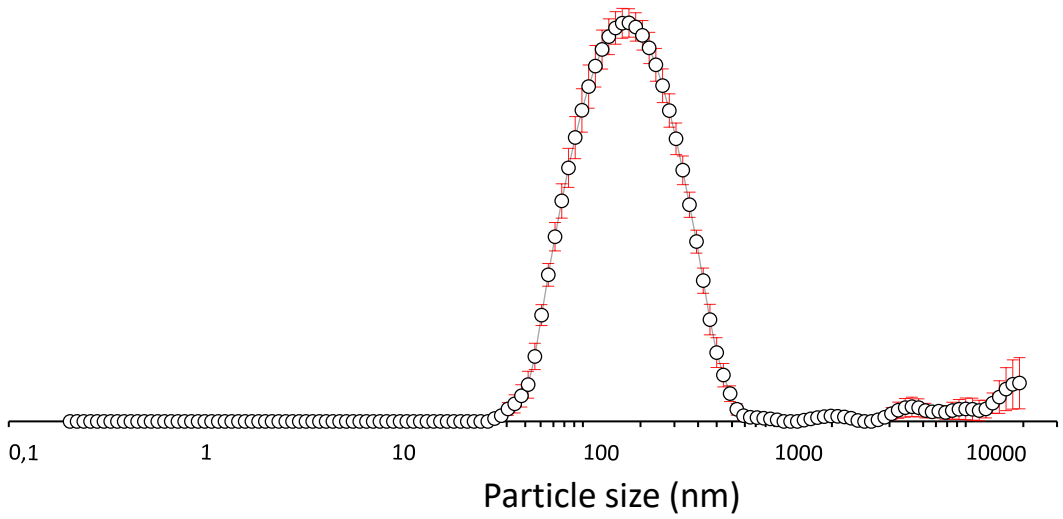

Figure S86: Illustrating the average intensity particle size distribution of compound **2** and **4** (mix) at 0.56 mM in EtOH: H_2O (1: 19) which was calculated using 10 DLS runs at a temperature of 25 ^{o}C.

Correlation function data (EtOH: H_2O 1:19)

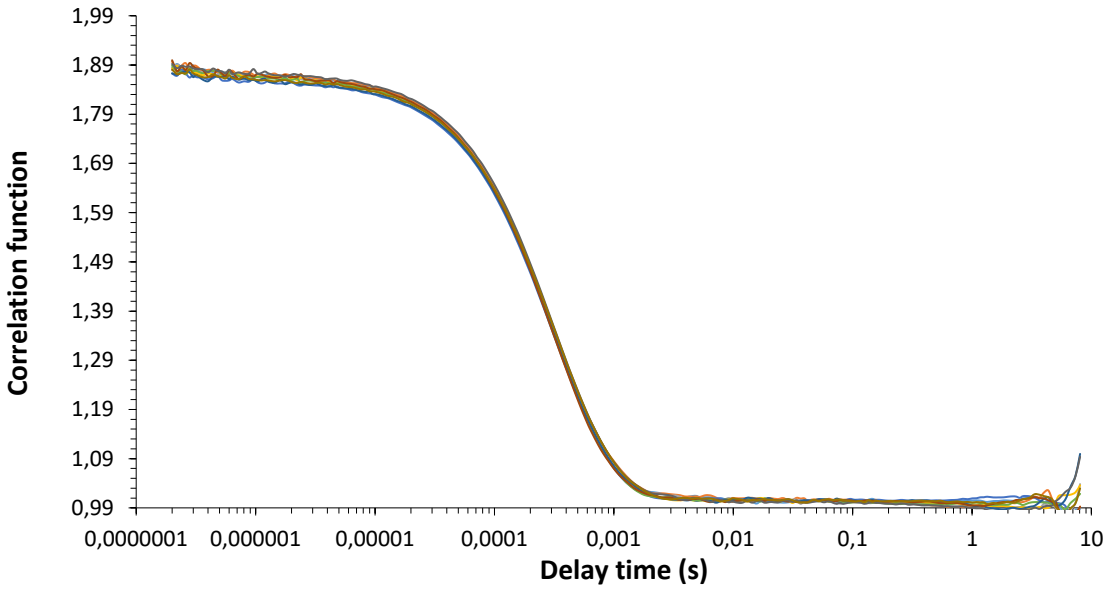

Figure S87: Correlation function data of compound **1** at 5.56 mM in EtOH: H_2O (1: 19) which was calculated using 10 DLS runs at a temperature of 25 °C.

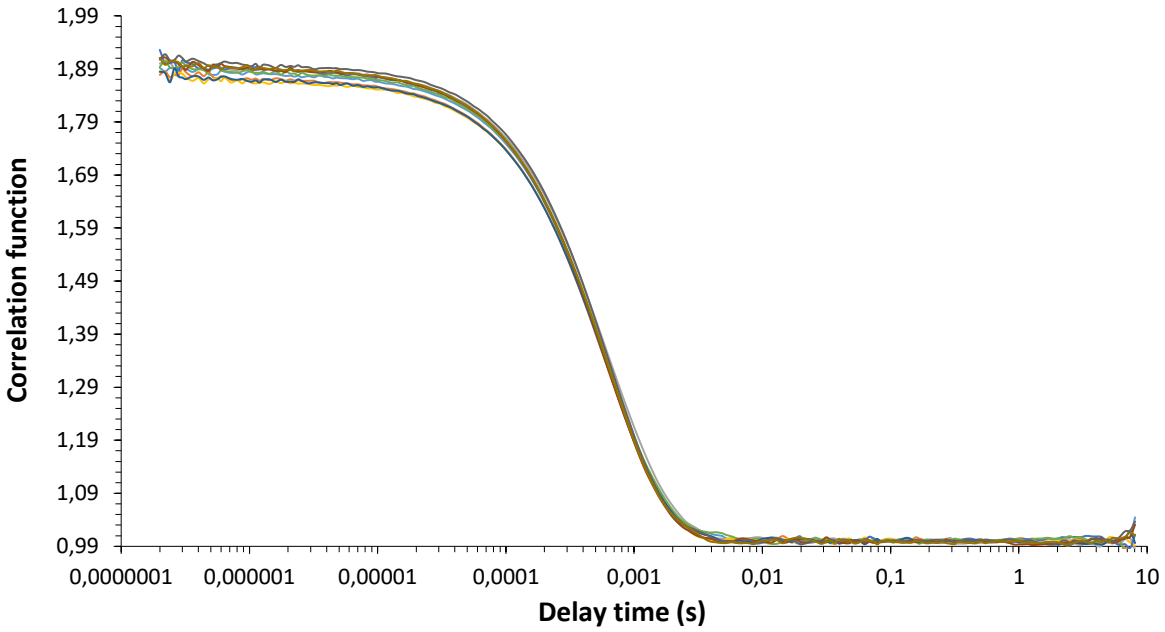

Figure S88: Correlation function data of compound **1** at 0.56 mM in EtOH: H_2O (1: 19) which was calculated using 10 DLS runs at a temperature of 25 °C.

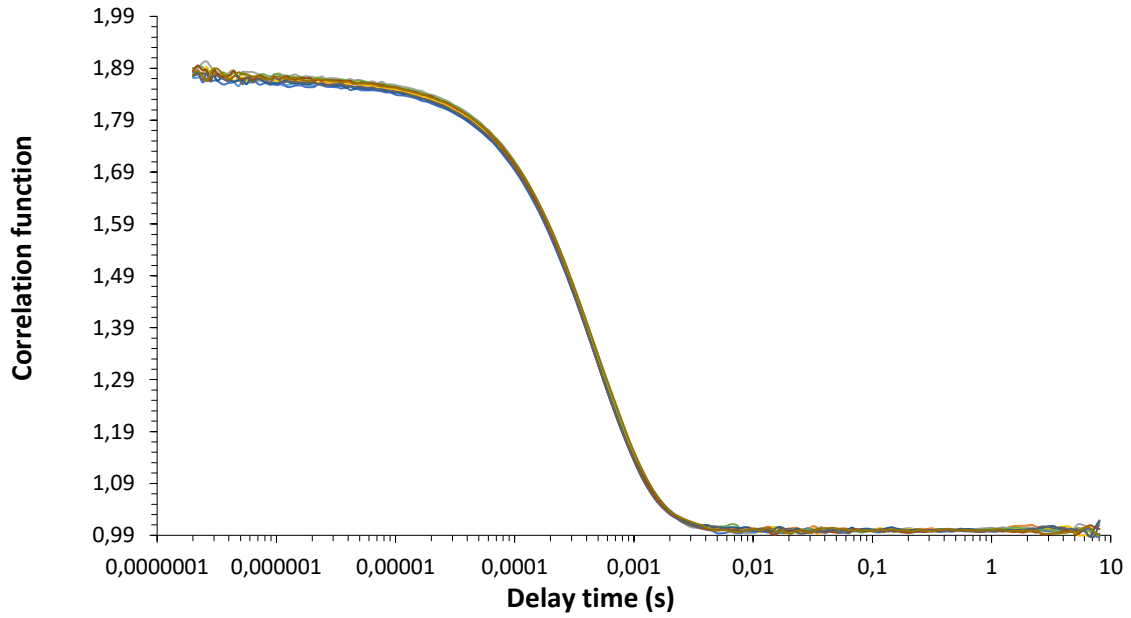

Figure S89: Correlation function data of compound **2** at 5.56 mM in EtOH: H_2O (1: 19) which was calculated using 10 DLS runs at a temperature of 25 °C.

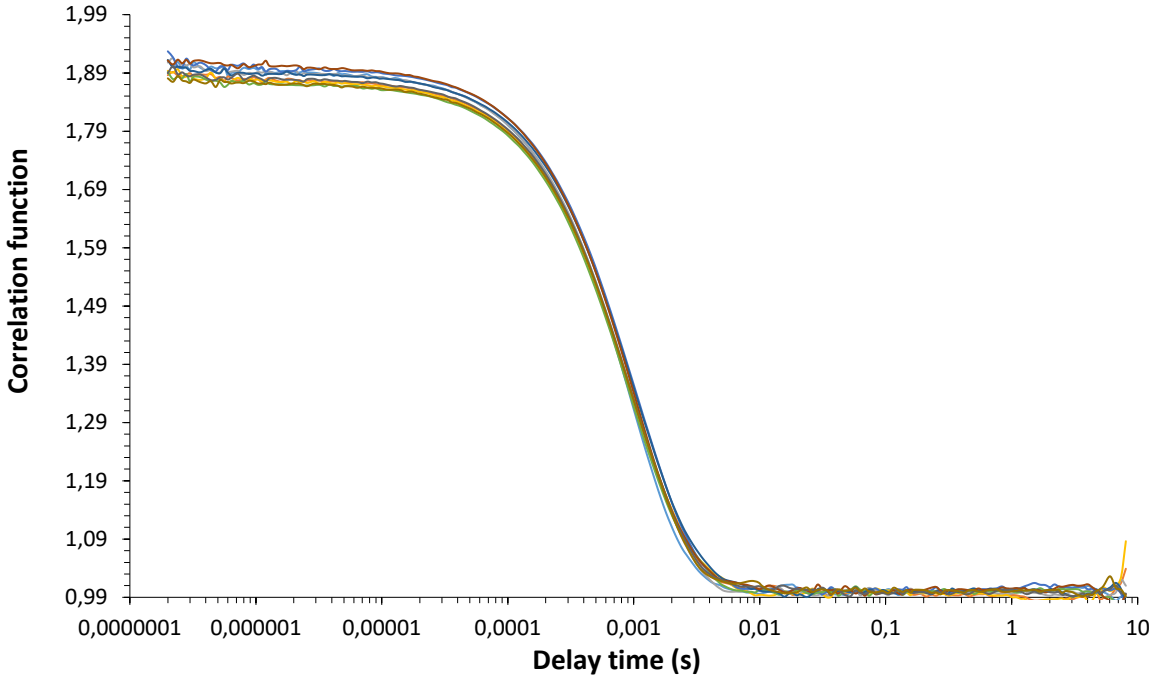

Figure S90: Correlation function data of compound **2** at 0.56 mM in EtOH: H_2O (1: 19) which was calculated using 10 DLS runs at a temperature of 25 °C.

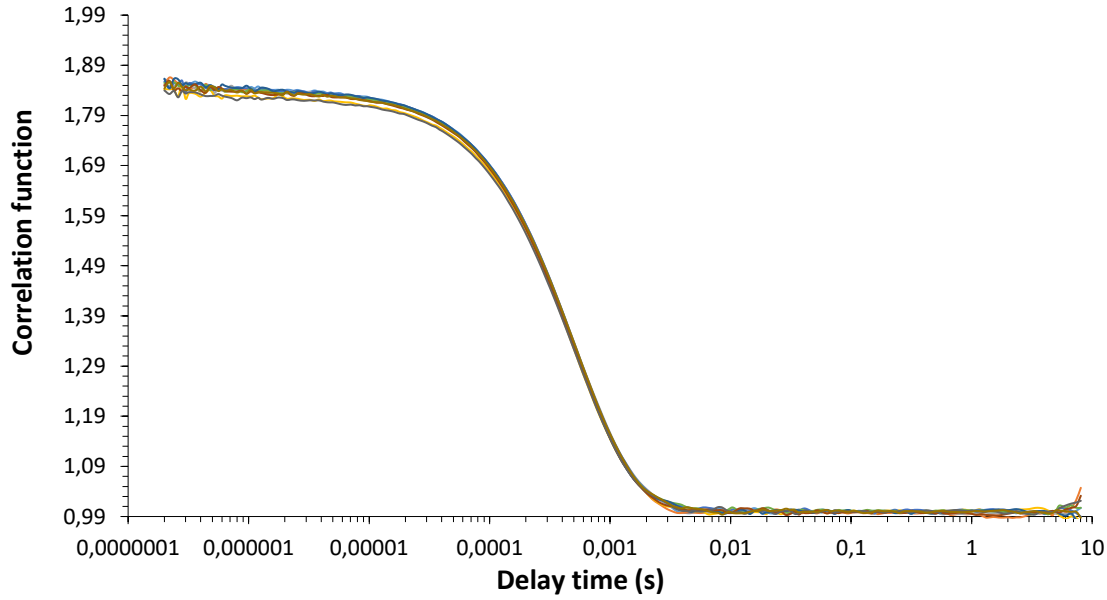

Figure S91: Correlation function data of compound **4** at 5.56 mM in EtOH: H_2O (1: 19) which was calculated using 10 DLS runs at a temperature of 25 °C.

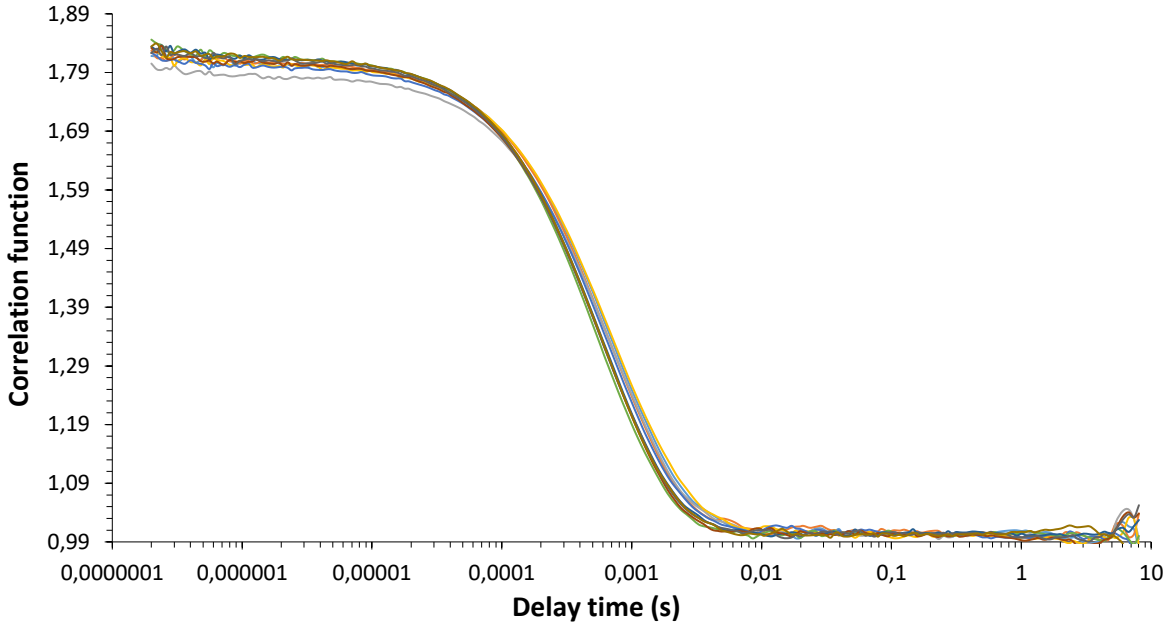

Figure S92: Correlation function data of compound **4** at 0.56 mM in EtOH: H_2O (1: 19) which was calculated using 10 DLS runs at a temperature of 25 °C.

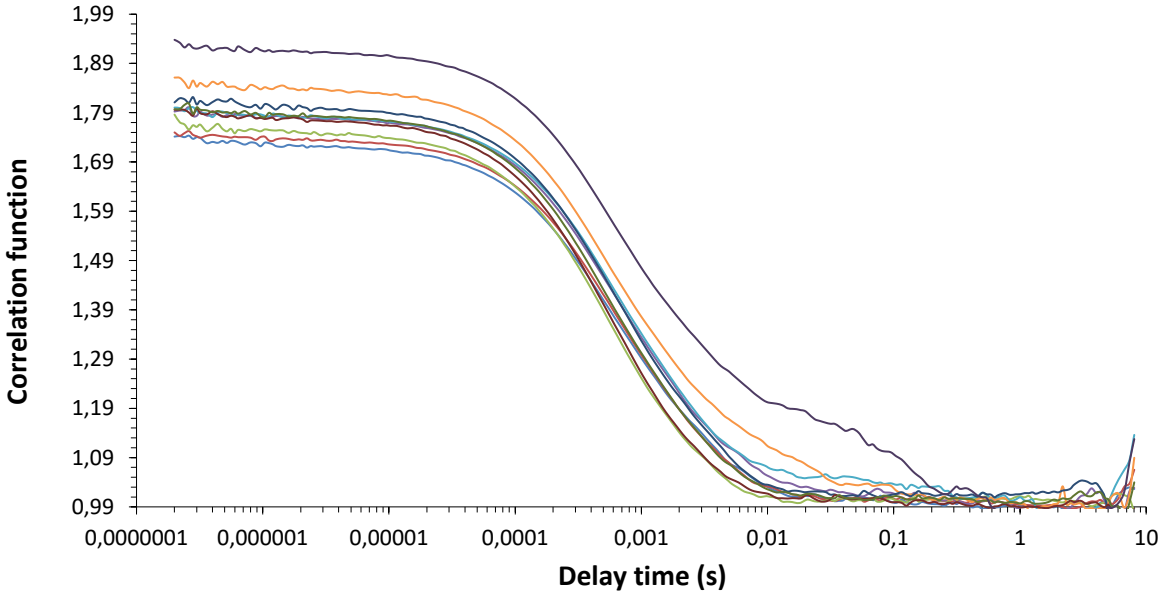

Figure S93: Correlation function data of compound **1** and **2** (mix) at 5.56 mM in EtOH: H_2O (1: 19) which was calculated using 10 DLS runs at a temperature of 25 °C.

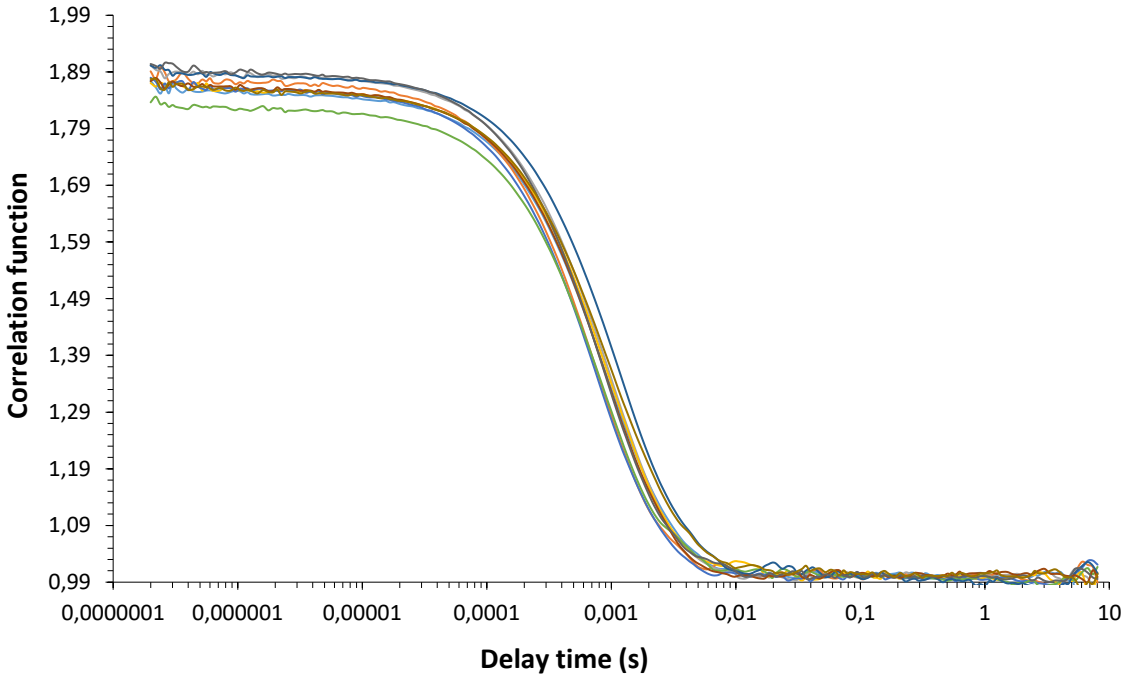

Figure S94: Correlation function data of compound **1** and **2** (mix) at 0.56 mM in EtOH: H_2O (1: 19) which was calculated using 10 DLS runs at a temperature of 25 °C.

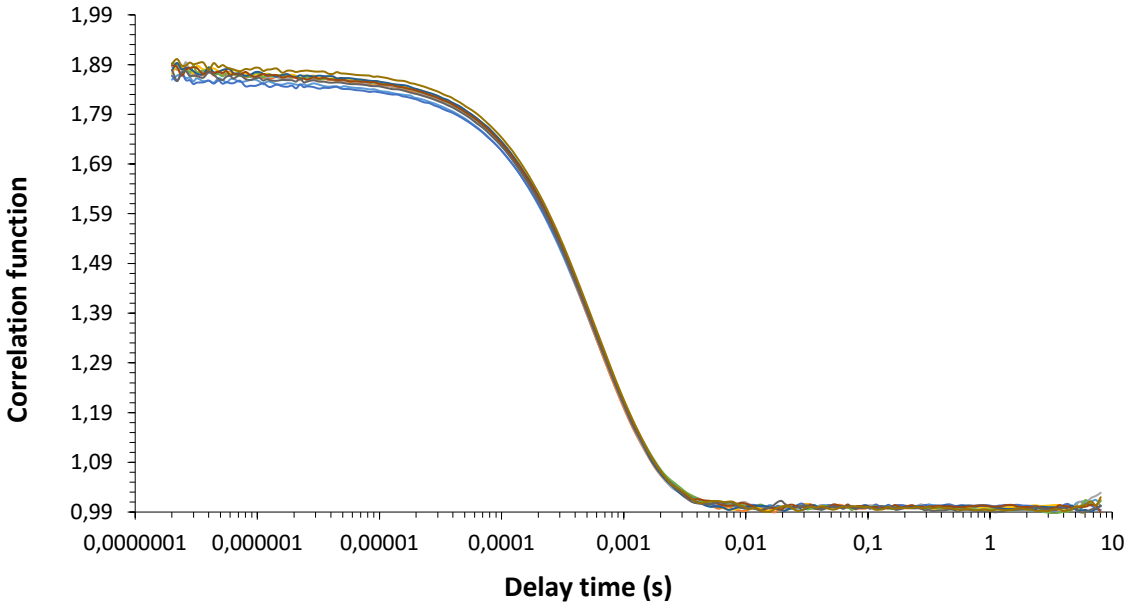

Figure S95: Correlation function data of compound **1** and **4** (mix) at 5.56 mM in EtOH: H_2O (1: 19) which was calculated using 10 DLS runs at a temperature of 25 °C.

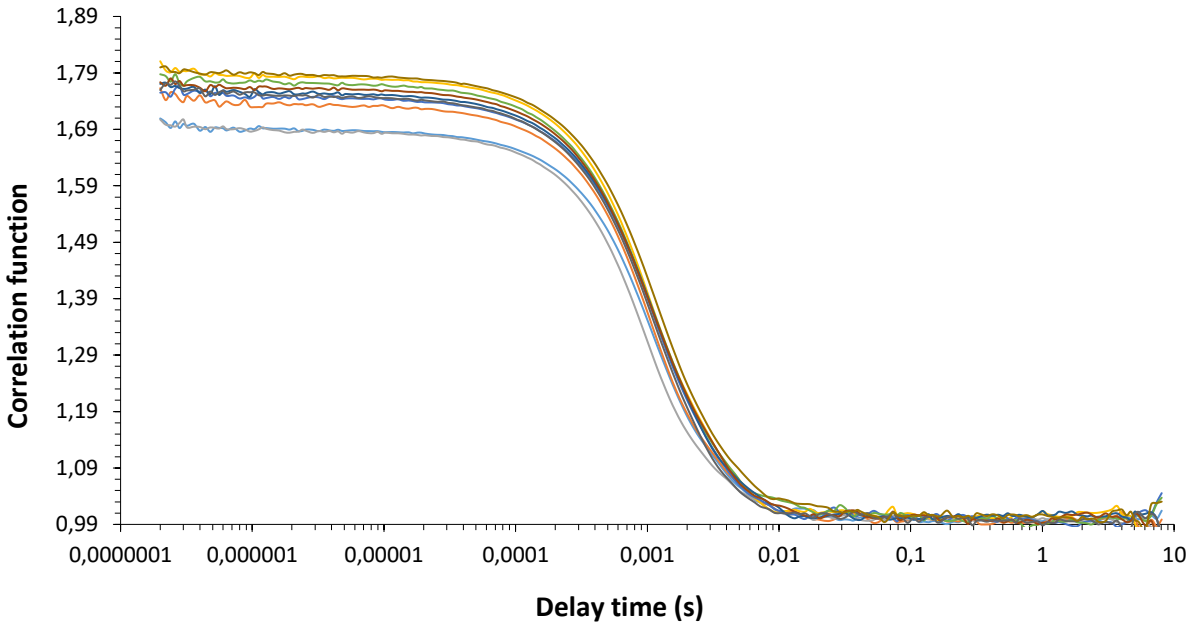

Figure S96: Correlation function data of compound **1** and **4** (mix) at 0.56 mM in EtOH: H_2O (1: 19) which was calculated using 10 DLS runs at a temperature of 25 °C.

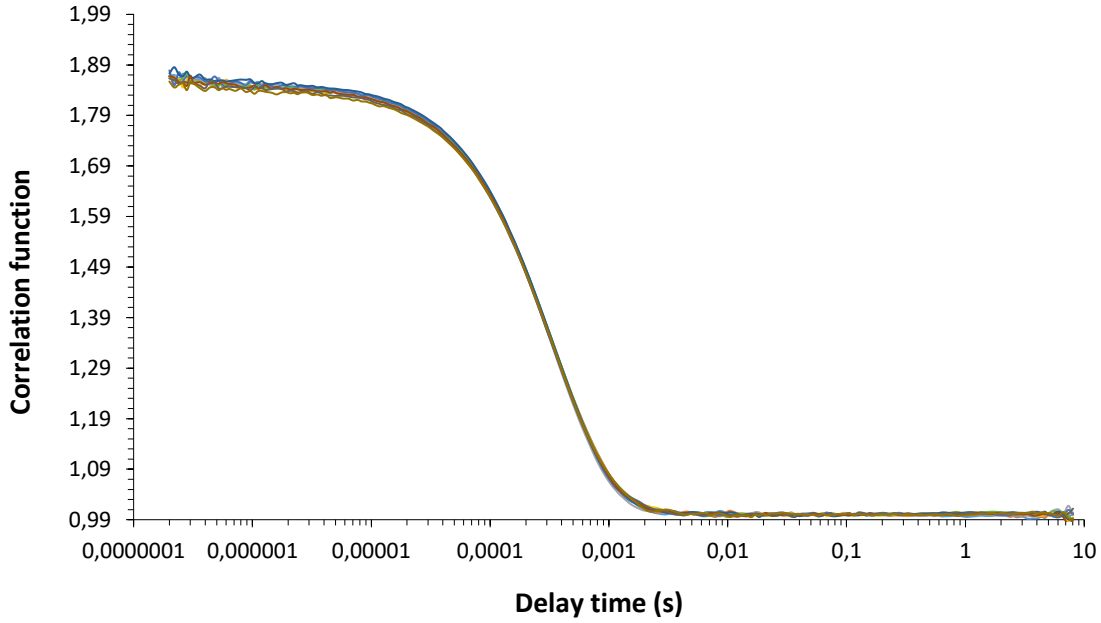

Figure S97: Correlation function data of compound **2** and **4** (mix) at 5.56 mM in EtOH: H_2O (1: 19) which was calculated using 10 DLS runs at a temperature of 25 °C.

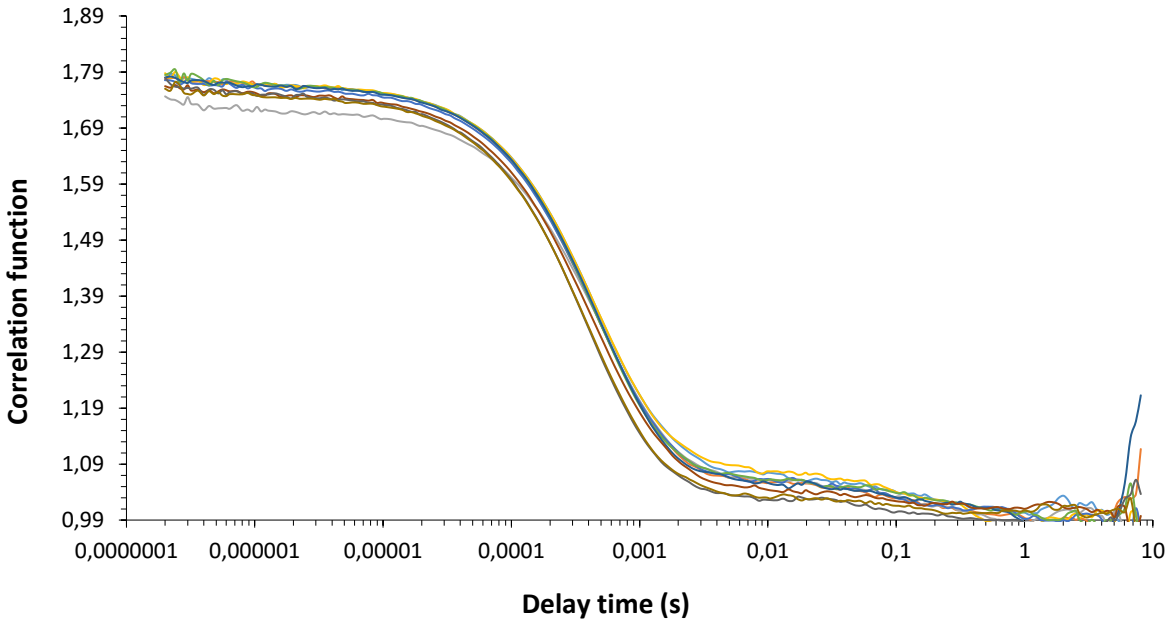

Figure S98: Correlation function data of compound **2** and **4** (mix) at 0.56 mM in EtOH: H_2O (1: 19) which was calculated using 10 DLS runs at a temperature of 25 °C.

Table S2: Showing the average intensity particle size distribution values for compounds **1** ,**2** and mixture **1** and **2** calculated using 10 DLS runs in DMSO at concentrations of 55.56 mM and 5.56 mM at 25 °C. The samples were initially heated up to 40 °C and then cooled down to 25 °C. Samples were prepared in series, with an aliquot of the most concentrated solution undergoing serial dilution.

* - data obtained determined to be unreliable

!- Only 9 runs were used in the calculations for compound **1** and **2** at 5.56 mM. A measurement was taken but it did not show when processing the data.

	DMSO		
Amphiphile	Concentration (mM)	Peak maxima (nm)	Polydispersity (%)
1	55.56	421 (± 32.35)	29 (± 3.23)
	5.56*	1910 (± 1353.94)*	263 (± 122.92)*
2	55.56	378 (± 38.74)	45 (± 4.55)
	5.56*	4099 (± 1406.91)*	101 (± 35.98)*
1 and **2**	55.56	651 (± 223.017)	199 (± 31.21)
	5.56*	3396(±1211.28)*!	104 (± 58.16)*

Quantitative ^{1}H NMR data

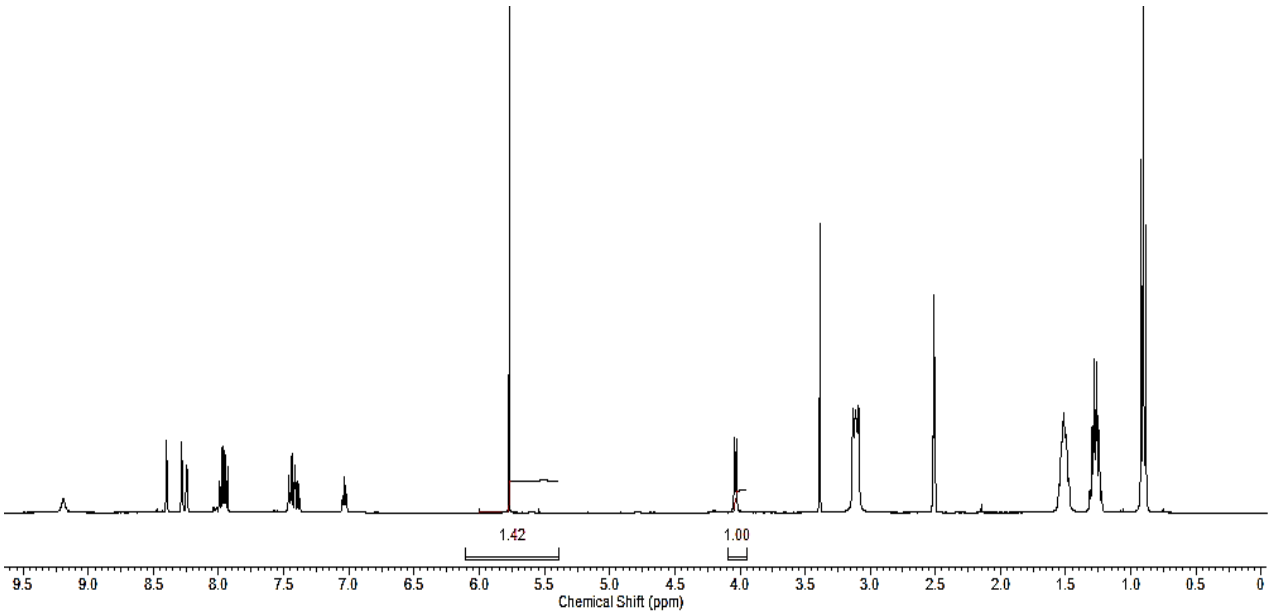

Figure S99: A ^{1}H NMR spectrum of compound **2** (31.73 mg, 0.055 mM) in a solution of DMSO-d_6 (0.495 mL) and dichloromethane (5 µl, 0.078 mM) with a delay (d_1 = 60 s). No apparent loss of compound observed.

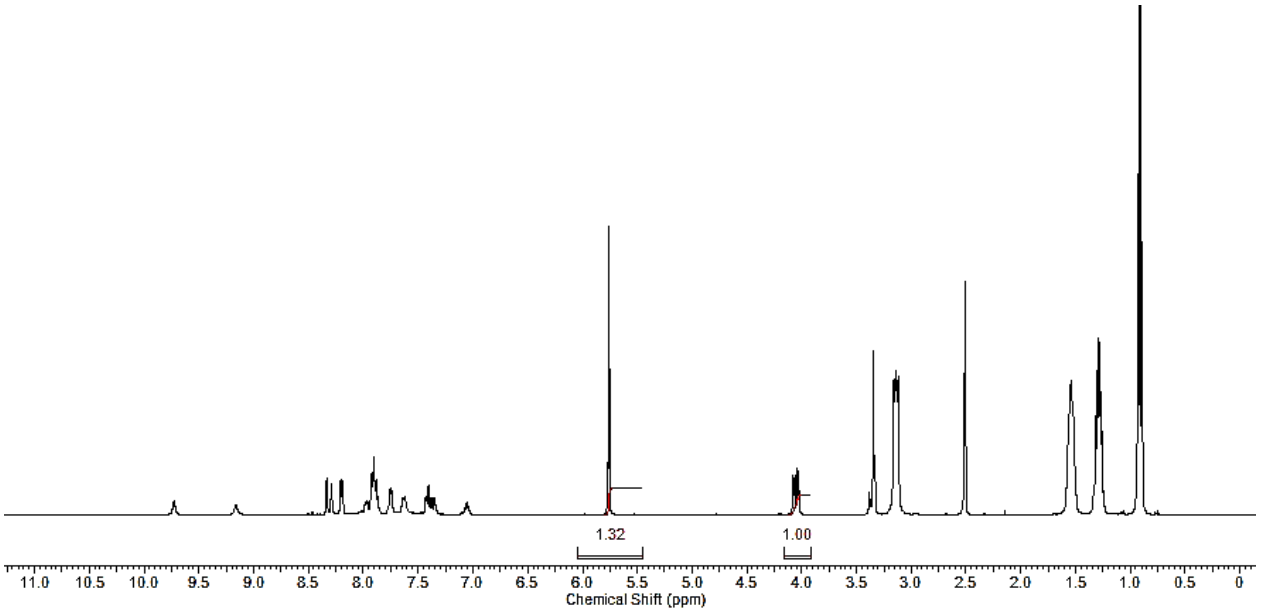

Figure S100: A ^{1}H NMR spectrum of compound **1** and **2** (mix) (compound **1** (16.73 mg, 0.028 mM and compound **2** (15.86 mg, 0.028 mM (both together 32.59 mg, 0.056 mM) in a solution of DMSO-d_6 (0.495 mL) and dichloromethane (5 µl, 0.078 mM) solution with a delay (d_1 = 60 s). No apparent loss of compound observed.

DOSY data

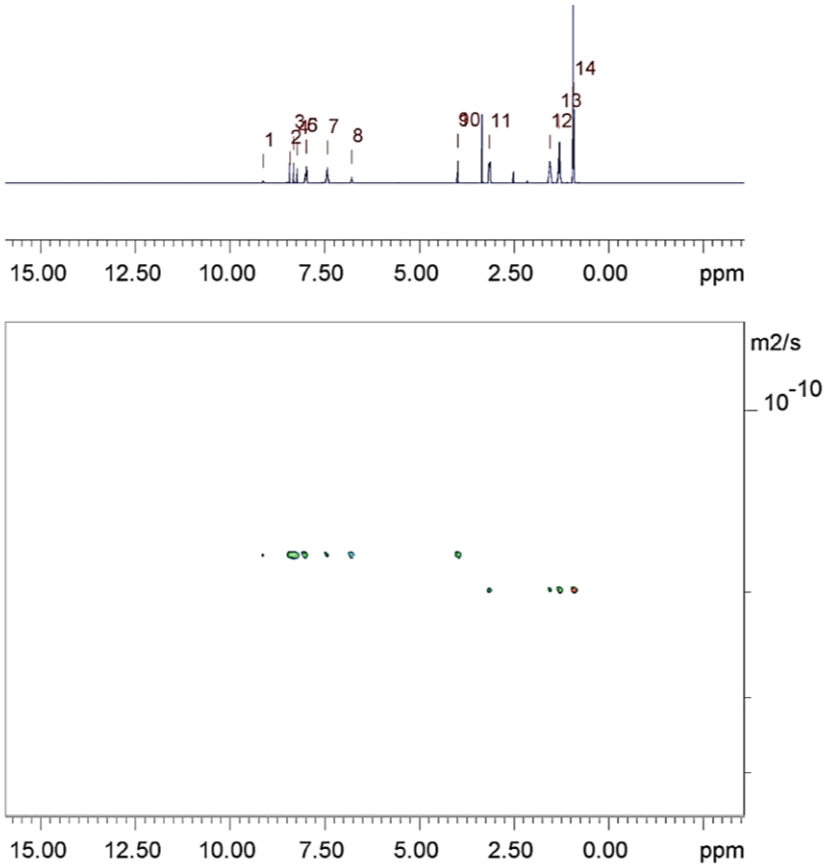

Peak name	F2 [ppm]	Io	error	D [m2/s]	error
1	9.121	3.43e+06	9331	1.73e-10	1.024e-12
2	8.422	3.23e+07	9343	1.74e-10	1.094e-13
3	8.316	3.20e+07	9341	1.74e-10	1.104e-13
4	8.221	2.33e+07	9348	1.74e-10	1.520e-13
5	7.990	2.66e+07	9332	1.73e-10	1.322e-13
6	7.976	2.63e+07	9334	1.73e-10	1.338e-13
7	7.421	2.43e+07	9335	1.74e-10	1.447e-13
8	6.781	1.03e+07	9339	1.74e-10	3.420e-13
9	3.987	3.48e+07	9334	1.73e-10	1.012e-13
10	3.972	3.50e+07	9349	1.74e-10	1.014e-13
11	3.142	3.20e+07	9698	1.99e-10	1.295e-13
12	1.547	3.43e+07	9699	1.99e-10	1.208e-13
13	1.305	6.44e+07	9700	1.99e-10	6.442e-14
14	0.925	2.80e+08	9703	1.99e-10	1.485e-14

Figure S101: Showing ^{1}H DOSY of compound **2** (15.87 mg, 0.028 mM) at a concentration of 55.56 mM (stock) in DMSO-d_6 (0.500 mL) conducted at 298K and a table representing the values for the diffusion constant for each peak used for calculating the hydrodynamic diameter (d_H = 1.26 nm). This does not include the TBA peaks. Peaks 1-10 correspond to the anionic component of **2** while peaks 11-14 correspond to the cationic component of **2**.

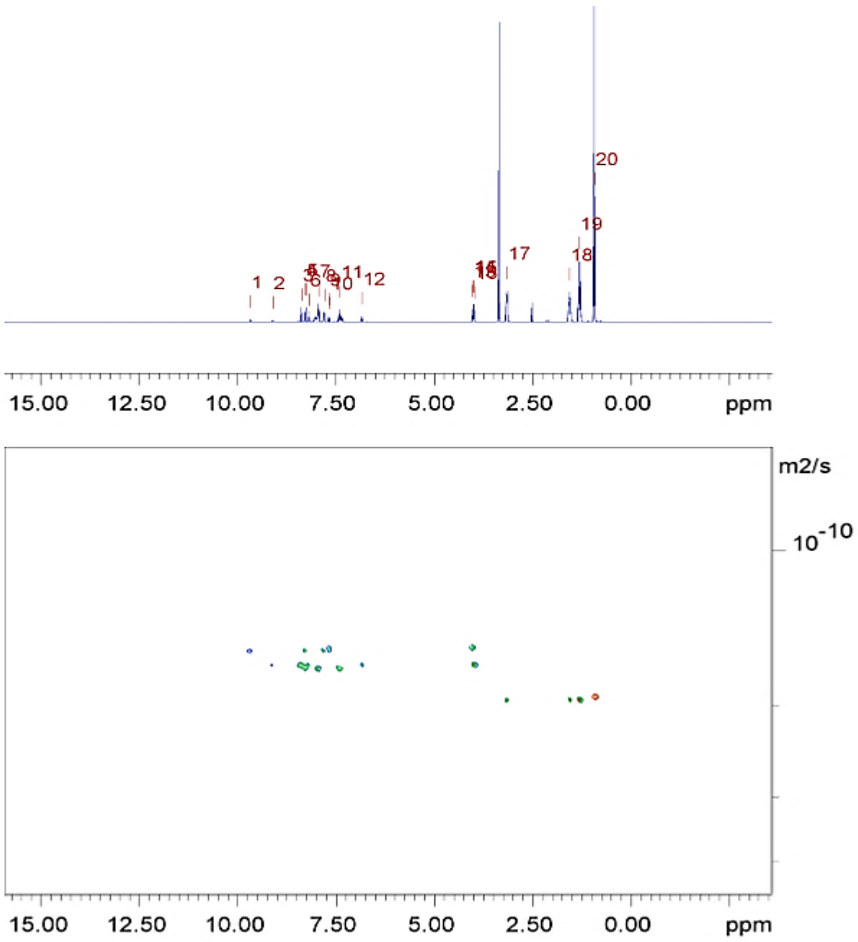

Peak name	F2 [ppm]	Io	error	D [m2/s]	error
1	9.672	3.27e+06	9041	1.56e-10	9.666e-13
2	9.111	2.28e+06	9210	1.67e-10	1.499e-12
3	8.378	2.04e+07	9210	1.67e-10	1.677e-13
4	8.280	1.41e+07	9045	1.56e-10	2.245e-13
5	8.264	2.02e+07	9222	1.68e-10	1.703e-13
6	8.189	1.51e+07	9214	1.68e-10	2.276e-13
7	7.945	2.55e+07	9233	1.69e-10	1.355e-13
8	7.794	1.17e+07	9040	1.56e-10	2.703e-13
9	7.683	6.39e+06	9024	1.55e-10	4.898e-13
10	7.661	5.55e+06	9042	1.56e-10	5.691e-13
11	7.394	1.76e+07	9229	1.69e-10	1.958e-13
12	6.840	7.83e+06	9211	1.67e-10	4.369e-13
13	4.025	1.84e+07	9004	1.54e-10	1.687e-13
14	4.010	1.89e+07	9024	1.55e-10	1.653e-13
15	3.992	2.53e+07	9185	1.66e-10	1.335e-13
16	3.978	2.53e+07	9201	1.67e-10	1.348e-13
17	3.150	3.88e+07	9609	1.95e-10	1.058e-13
18	1.555	4.13e+07	9605	1.95e-10	9.903e-14
19	1.309	8.35e+07	9590	1.94e-10	4.868e-14
20	0.925	4.51e+08	9583	1.93e-10	8.979e-15

Figure S102: Showing ^{1}H DOSY of compound **1** (8.38 mg, 0.014 mM) and **2** (7.93 mg, 0.014 mM) (mix) at a concentration of 55.56 mM (stock) in DMSO-d_6 (0.500 mL) conducted at 298K and a table representing the values for the diffusion constant for each peak used for calculating the hydrodynamic diameter (d_{H1} = 1.41 nm and d_{H2} = 1.31 nm). This does not include the TBA peaks. Peaks 1-16 correspond to the anionic component of **1** and **2** while peaks 17-20 correspond to the cationic component of **1** and **2**.

Zeta potential data

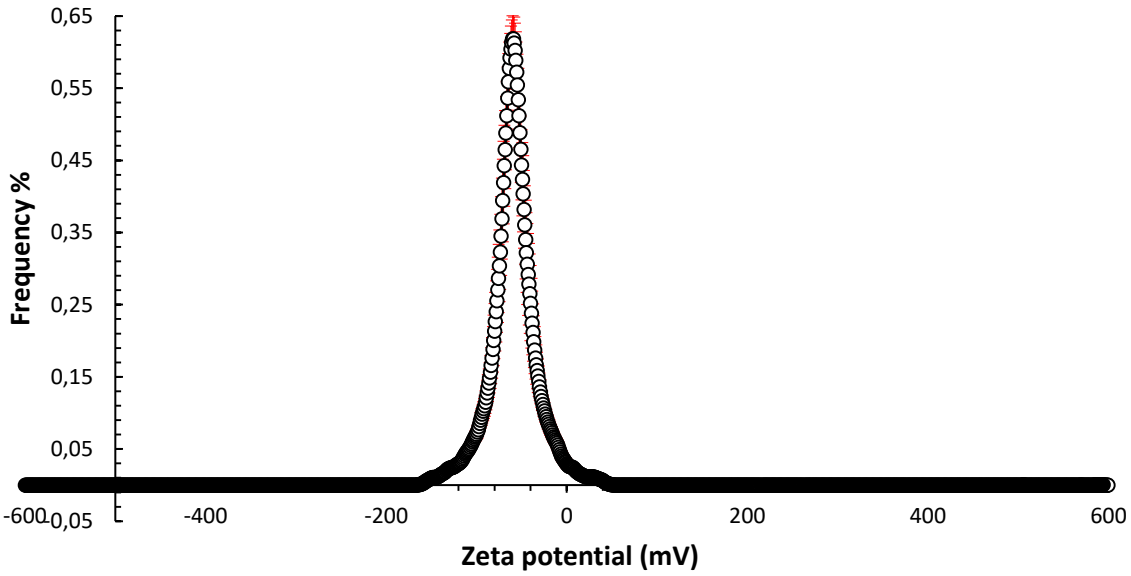

Figure S103: The average zeta potential distribution calculated using 10 DLS runs for compound **1** (5.56 mM) in an EtOH: H_2O (1:19) solution at 298 K.

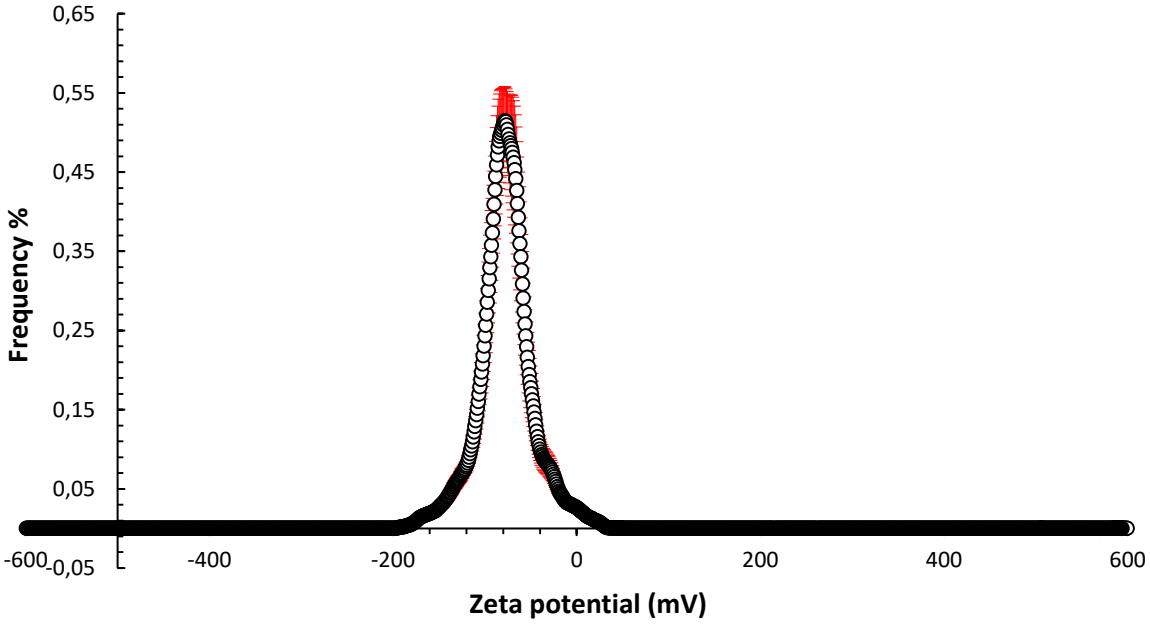

Figure S104: The average zeta potential distribution calculated using 10 DLS runs for compound **1** (0.56 mM) in an EtOH: H_2O (1:19) solution at 298 K.

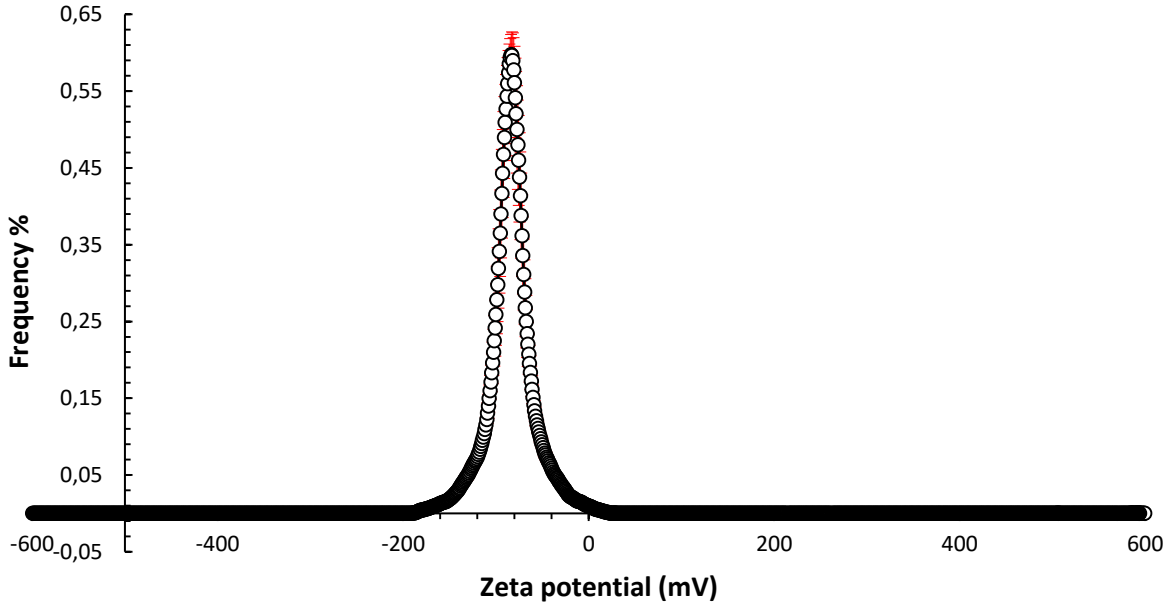

Figure S105: The average zeta potential distribution calculated using 10 DLS runs for compound **2** (5.56 mM) in an EtOH: H_2O (1:19) solution at 298 K.

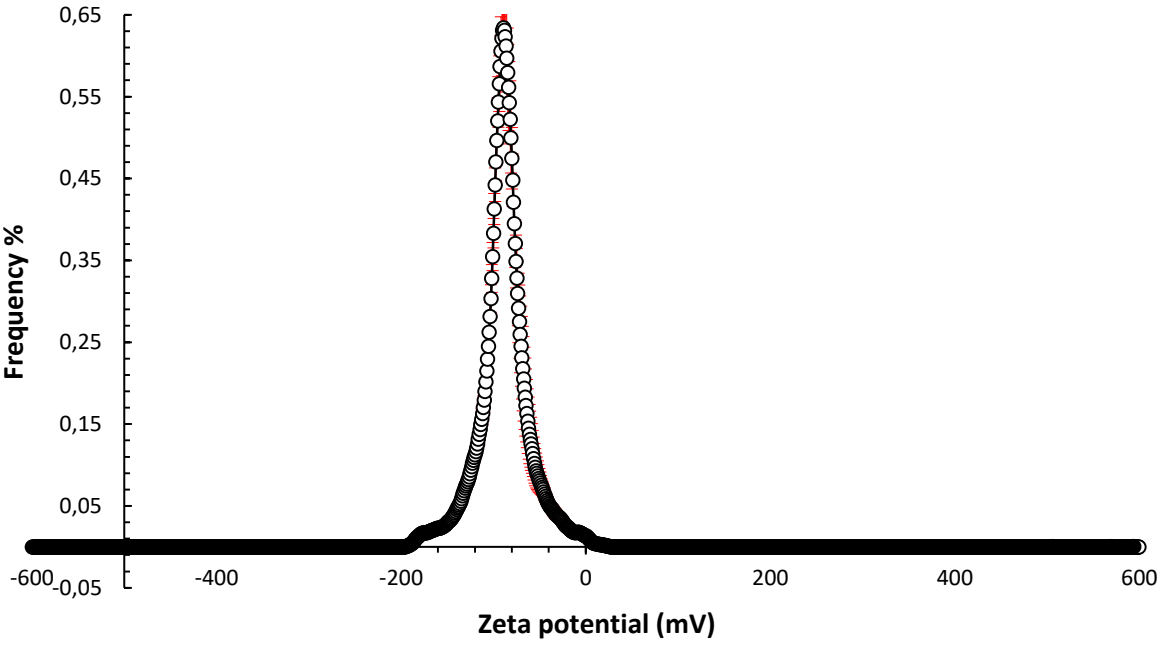

Figure S106: The average zeta potential distribution calculated using 10 DLS runs for compound **2** (0.56 mM) in an EtOH: H_2O (1:19) solution at 298 K.

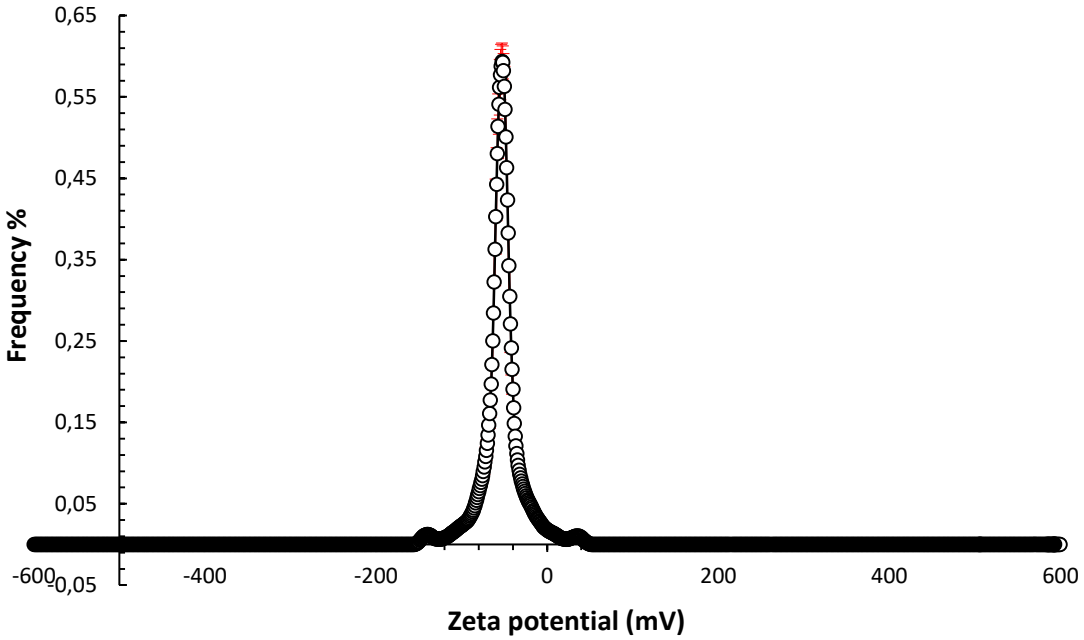

Figure S107: The average zeta potential distribution calculated using 10 DLS runs for compound **4** (5.56 mM) in an EtOH: H_2O (1:19) solution at 298 K.

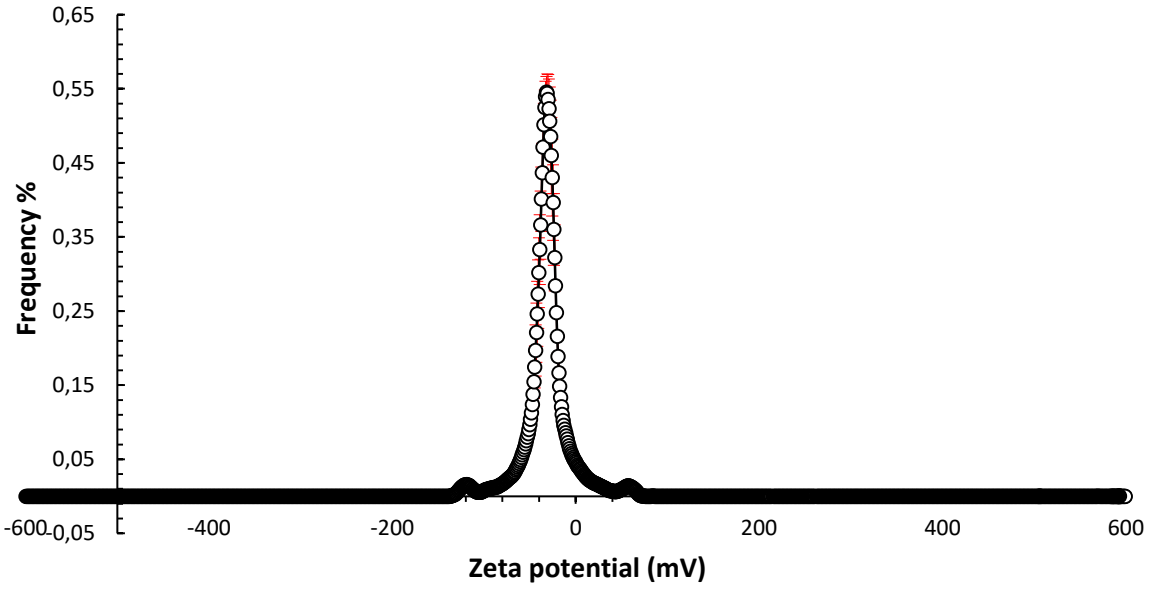

Figure S108: The average zeta potential distribution calculated using 10 DLS runs for compound **4** (0.56 mM) in an EtOH: H_2O (1:19) solution at 298 K.

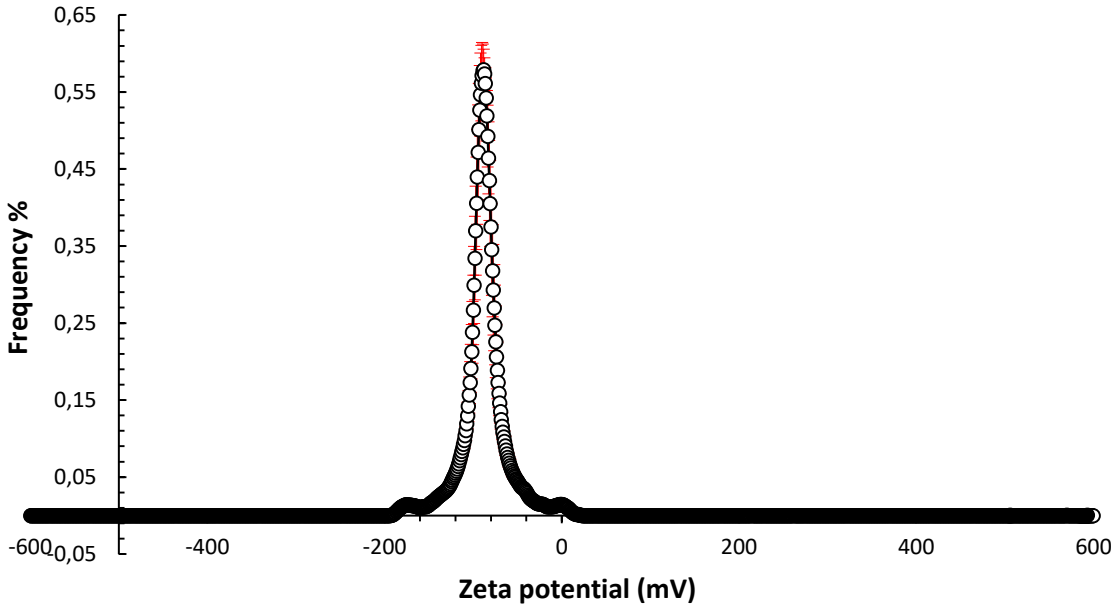

Figure S109: The average zeta potential distribution calculated using 10 DLS runs for compounds **1** and **2** in a 1:1 mixture (total concentration 0.56 mM) in an EtOH: H_2O (1:19) solution at 298 K. An analogous experiment could not be run at the comparative 5.56 mM concentration due to compound solubility.

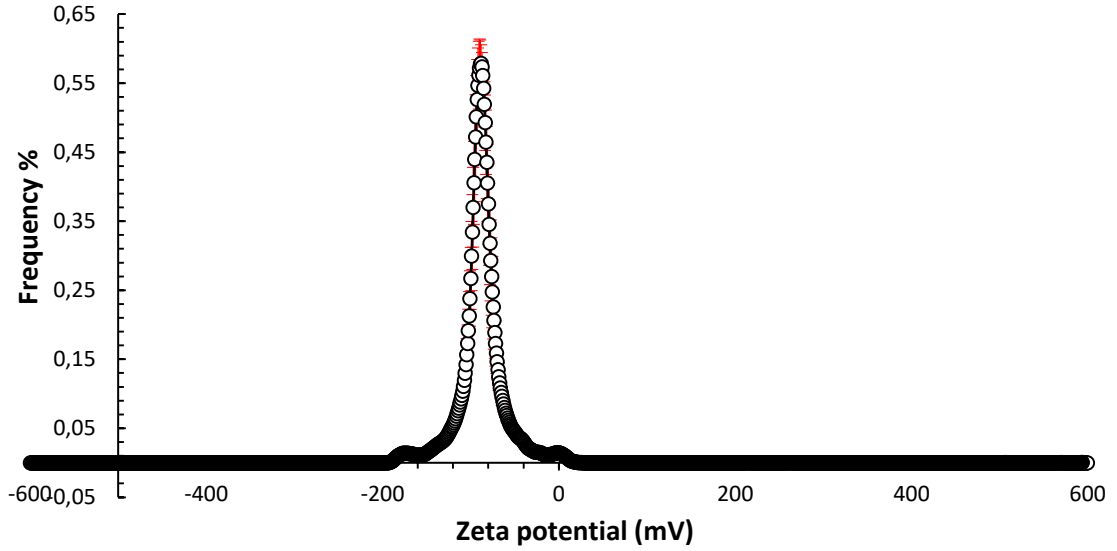

Figure S110: The average zeta potential distribution calculated using 10 DLS runs for compounds **1** and **2** in a 1:1 mixture (total concentration 0.56 mM) in an EtOH: H_2O (1:19) solution at 298 K. An analogous experiment could not be run at the comparative 5.56 mM concentration due to compound solubility.

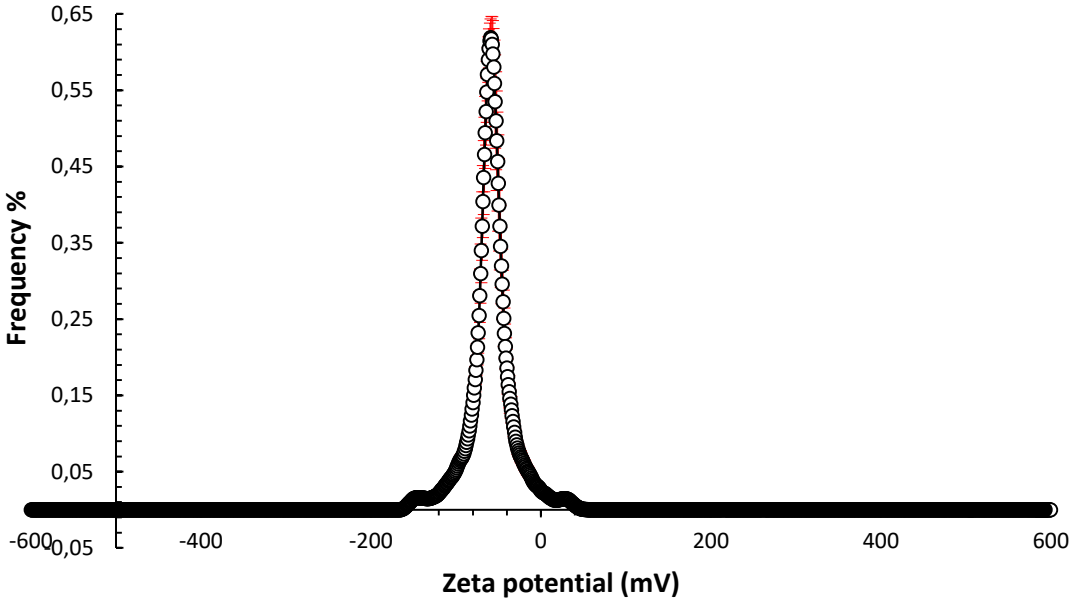

.

Figure S111: The average zeta potential distribution calculated using 10 DLS runs for compounds **1** and **4** in a 1:1 mixture (total concentration 5.56 mM) in an EtOH: H_2O (1:19) solution at 298 K.

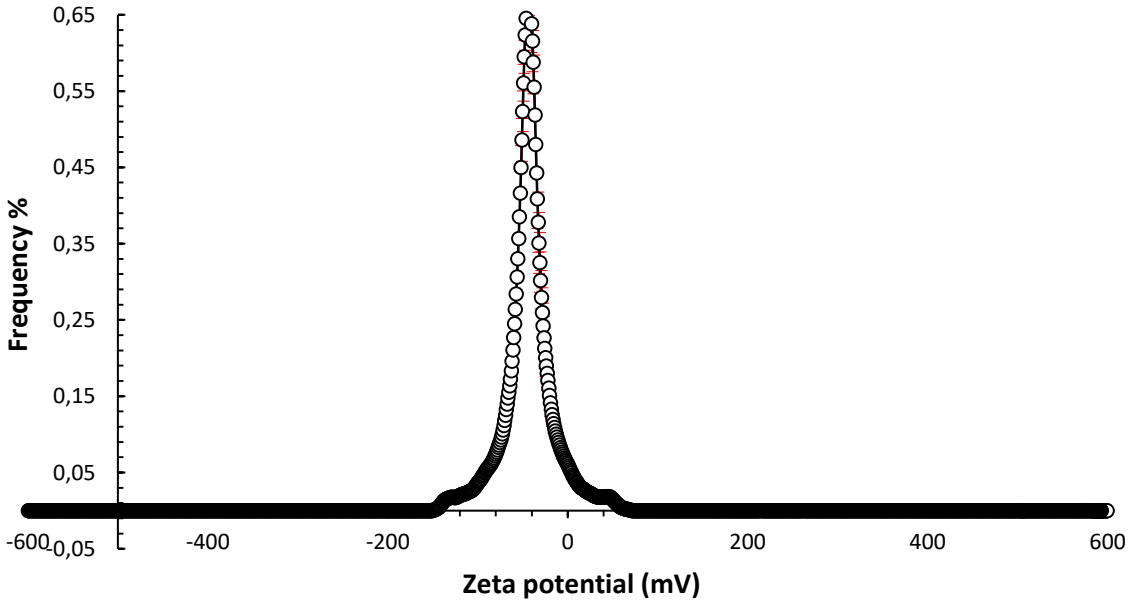

Figure S112: The average zeta potential distribution calculated using 10 DLS runs for compounds **1** and **4** in a 1:1 mixture (total concentration 0.56 mM) in an EtOH: H_2O (1:19) solution at 298 K.

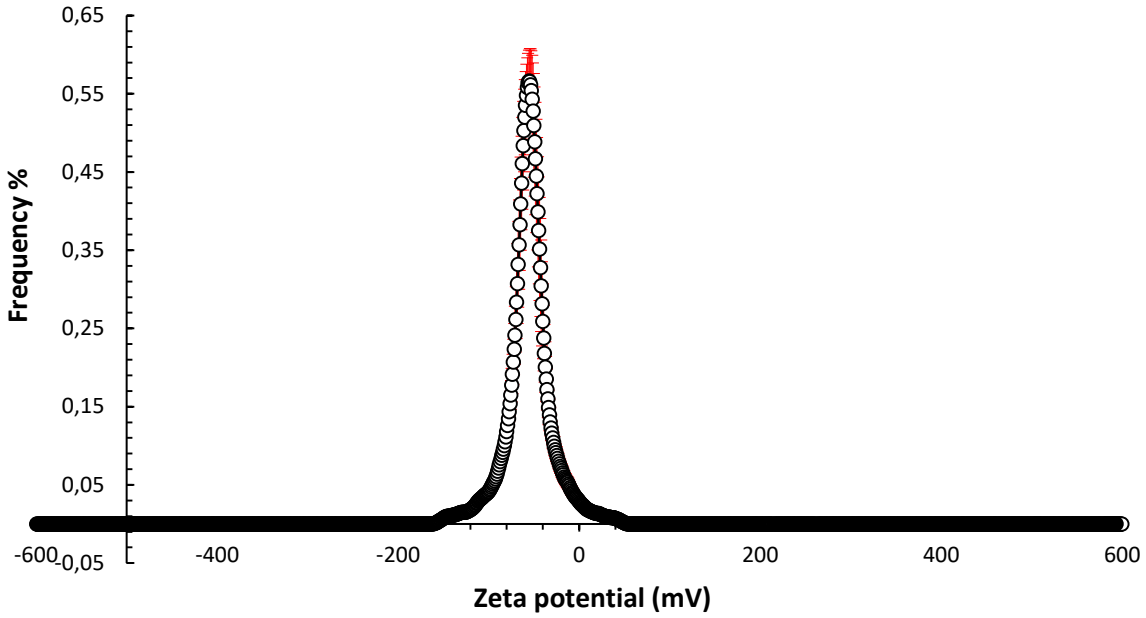

Figure S113: The average zeta potential distribution calculated using 10 DLS runs for compounds **2** and **4** in a 1:1 mixture (total concentration 5.56 mM) in an EtOH: H_2O (1:19) solution at 298 K.

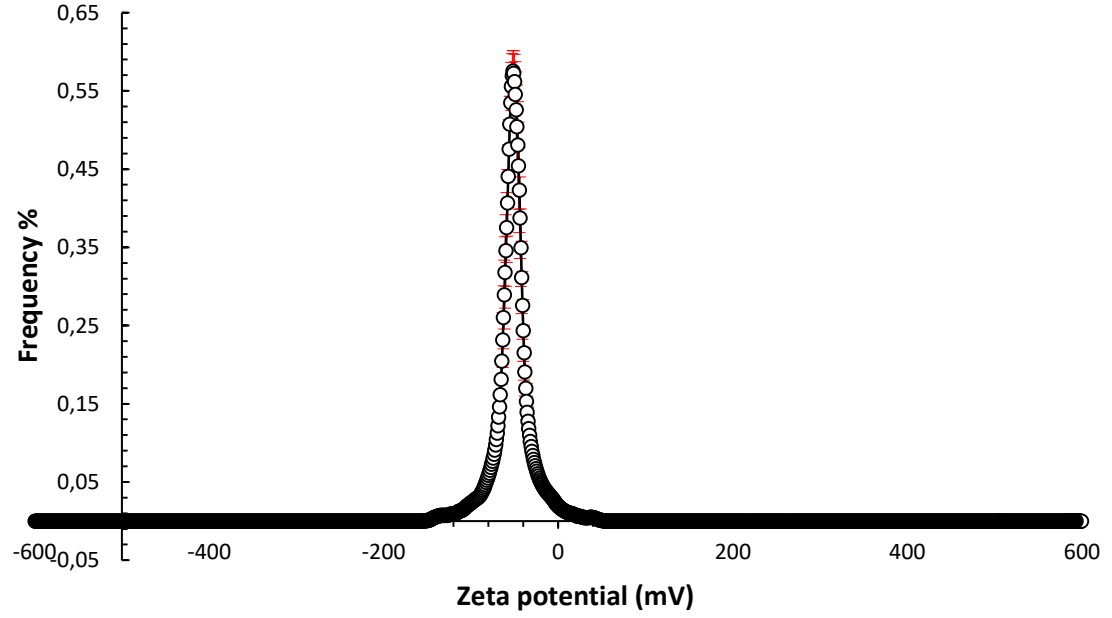

Figure S114: The average zeta potential distribution calculated using 10 DLS runs for compounds **2** and **4** in a 1:1 mixture (total concentration 0.56 mM) in an EtOH: H_2O (1:19) solution at 298 K.

Surface tension measurements and CMC calculations

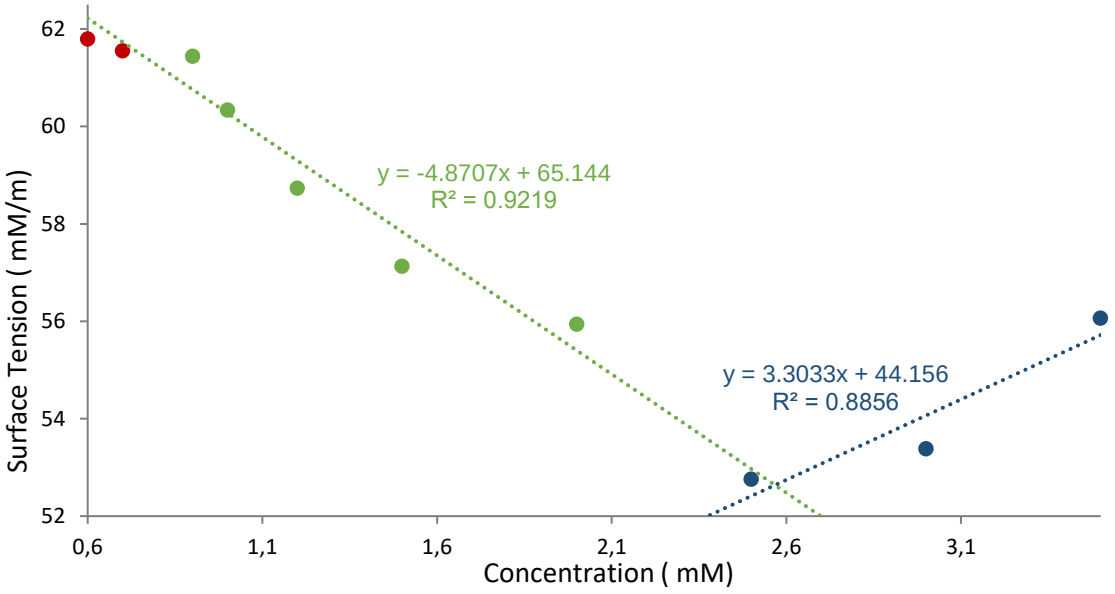

Figure S115: Calculation of CMC (**2.57 mM**) for compound **4** in an EtOH: H_2O (1:19) mixture using surface tension measurements.

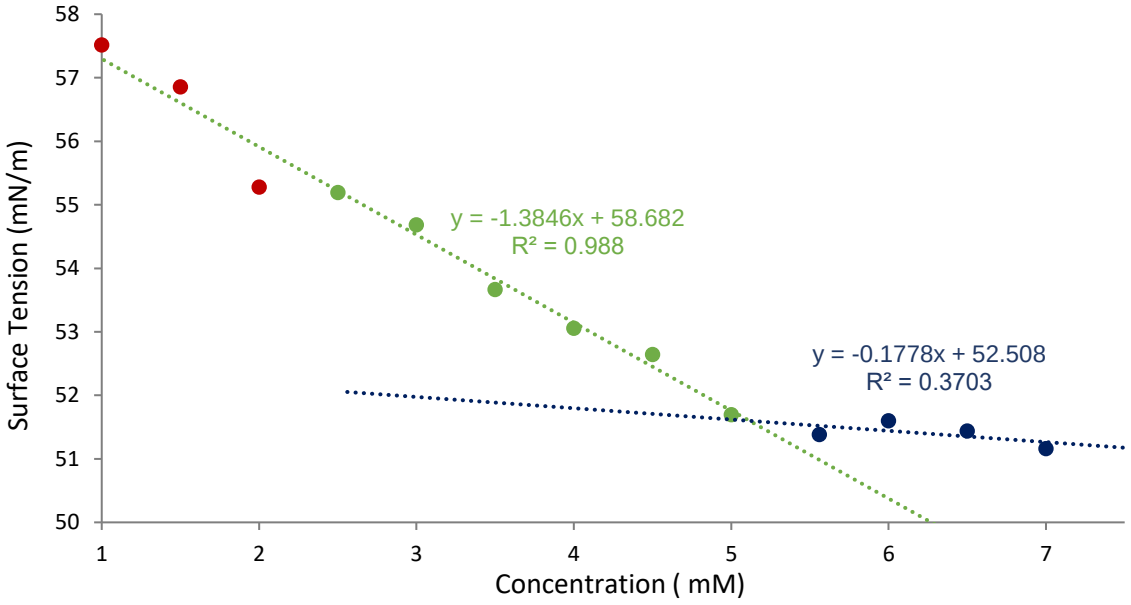

Figure S116: Calculation of CMC (**5.12 mM**) for compound **1** and **4** (1:1 mix) in an EtOH: H_2O (1:19) mixture using surface tension measurements.

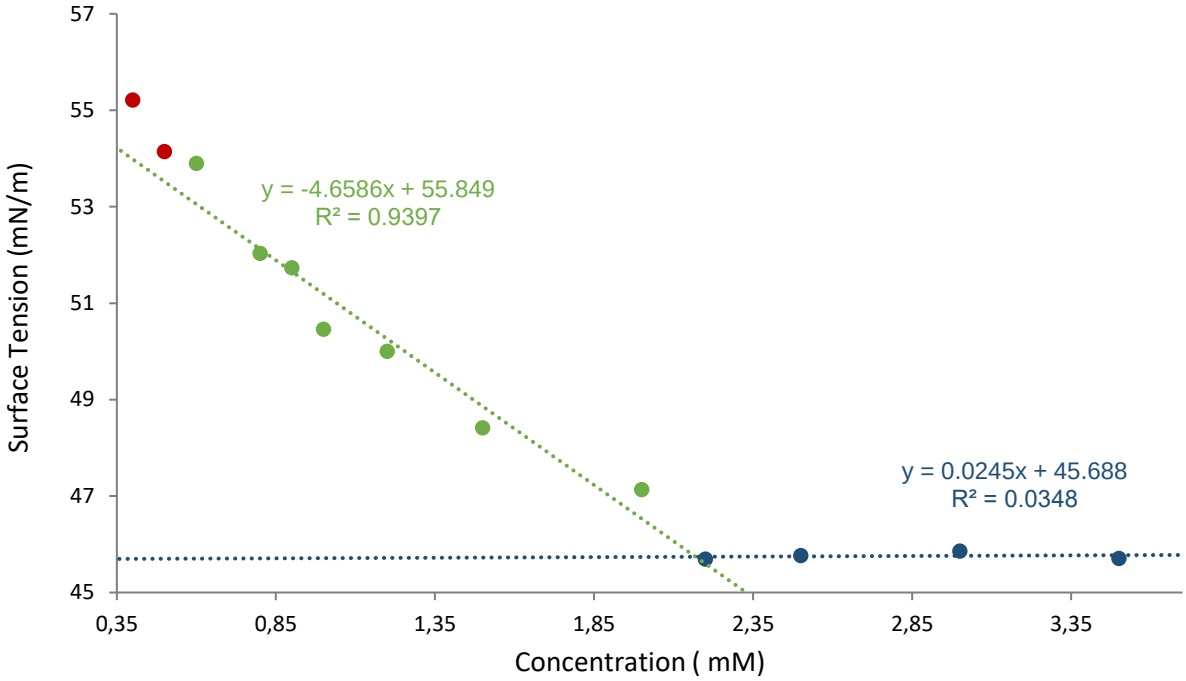

Figure S117: Calculation of CMC (**2.17 mM**) for compound **2** and **4** (1:1 mix) in an EtOH: H_2O (1:19) mixture using surface tension measurements.

UV-Vis data

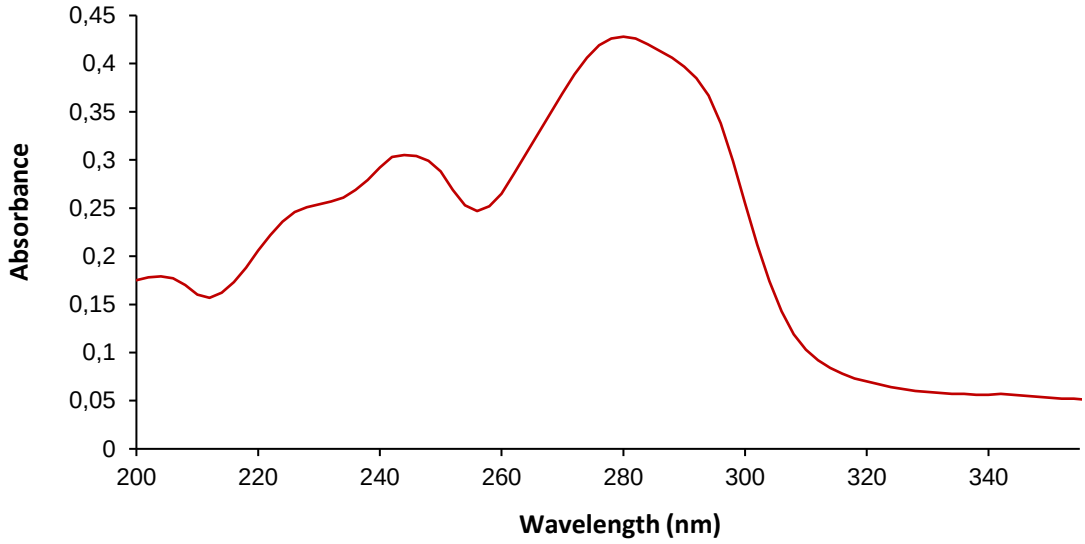

Figure S118: UV-Vis spectra of compound **1** at a concentration of 0.01 mM in EtOH: H_2O (1: 19).

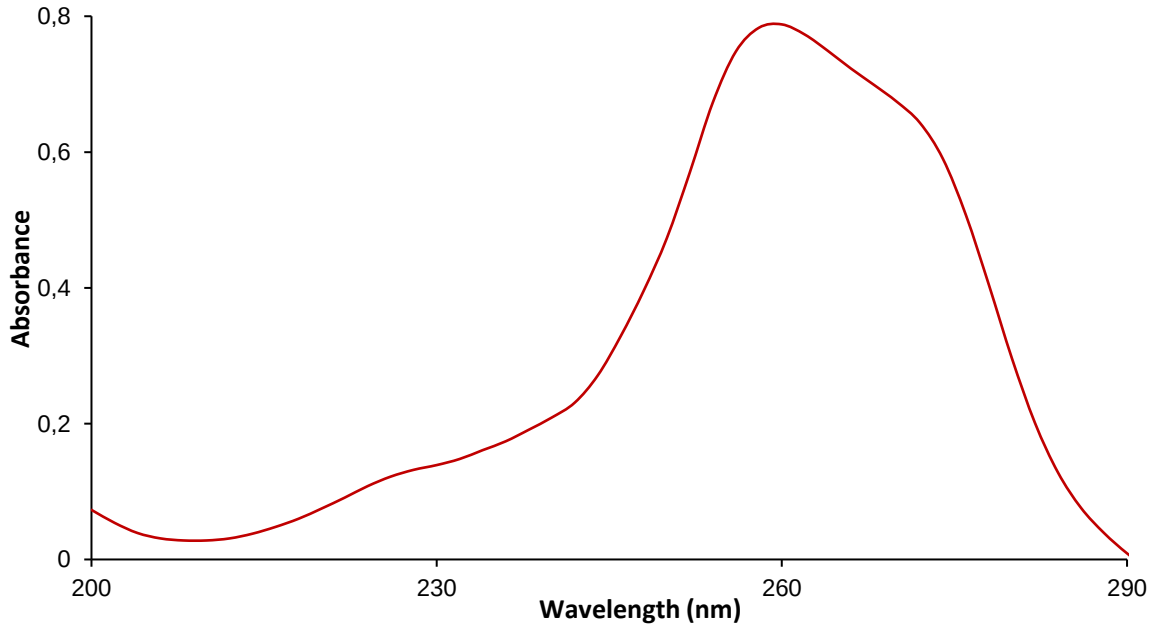

Figure S119: UV-Vis spectra of compound **4** at a concentration of 0.01 mM in EtOH: H_2O (1: 19).

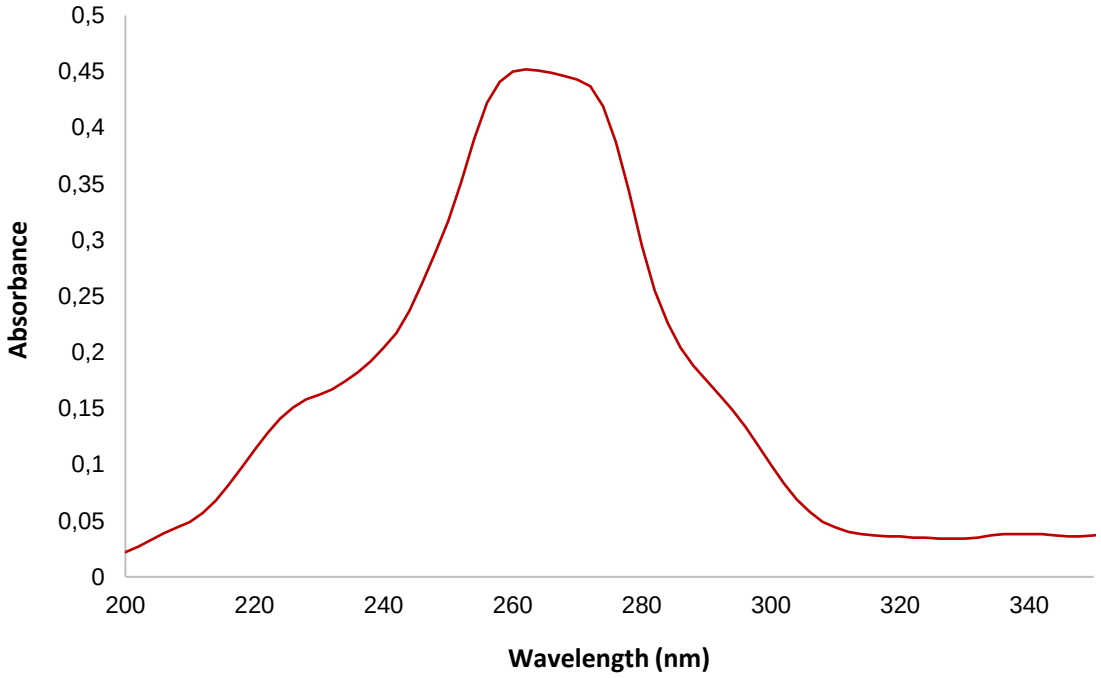

Figure S120: UV-Vis spectra of compound **1** and **2** (mix) at a concentration of 0.01 mM in EtOH: H_2O (1: 19)

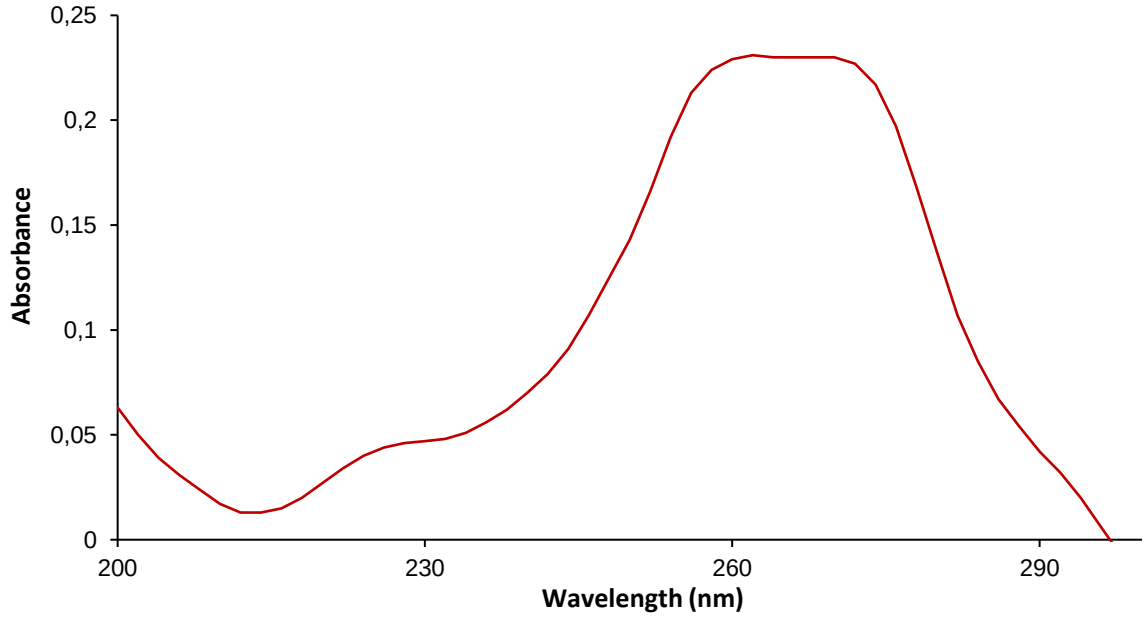

Figure S121: UV-Vis spectra of compound **1** and **4** at a concentration 0.01 mM in EtOH: H_2O (1: 19).

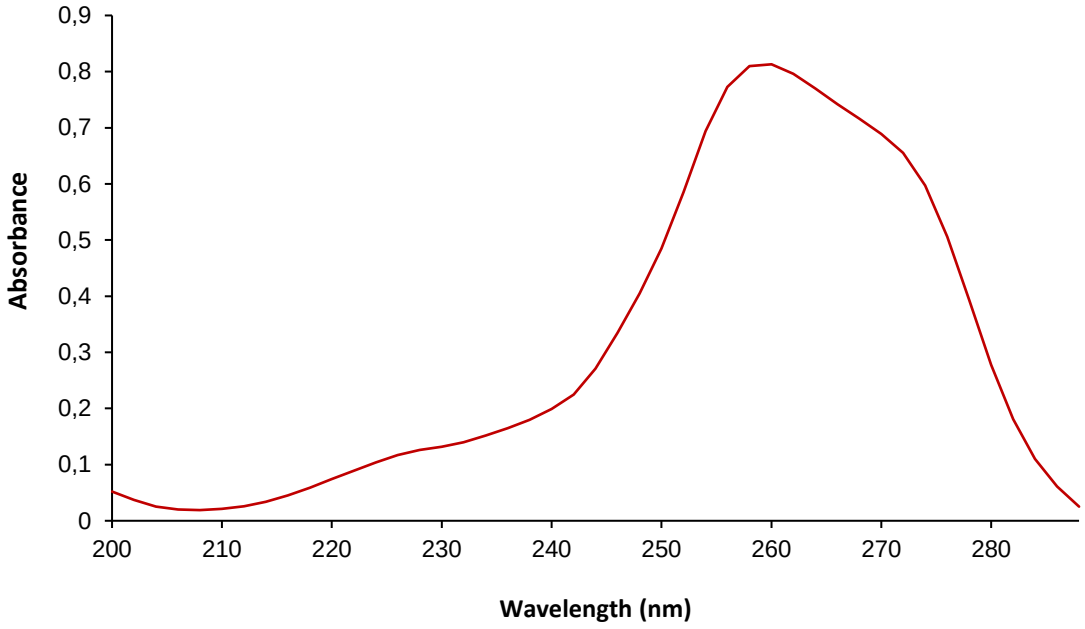

Figure S122: UV-Vis spectra of compound **2** and **4** at a concentration 0.03 mM in EtOH: H_2O (1: 19).

Fluorescence data

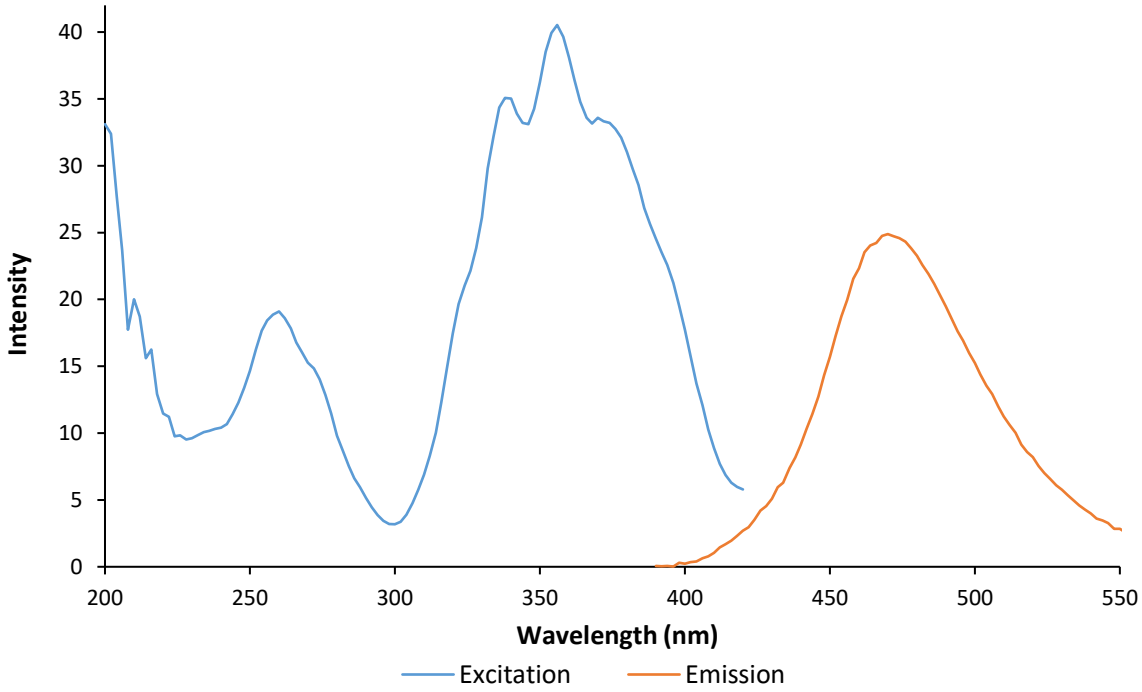

Figure S123: Fluorescence emission and excitation spectra of compound **1** (0.5 mM) and **4** (0.5 mM) in EtOH: H_2O (1: 19).

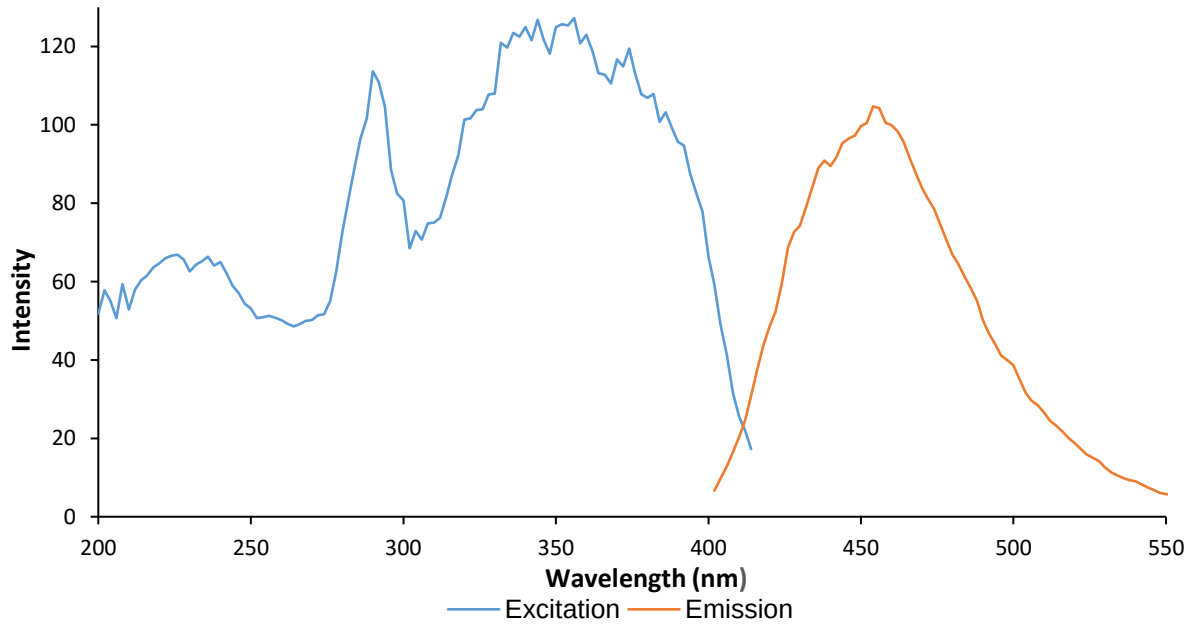

Figure S124: Fluorescence emission and excitation spectra of compound **2** (0.5 mM) and **4** (0.5 mM) in EtOH: H_2O (1: 19).

Microscopy images

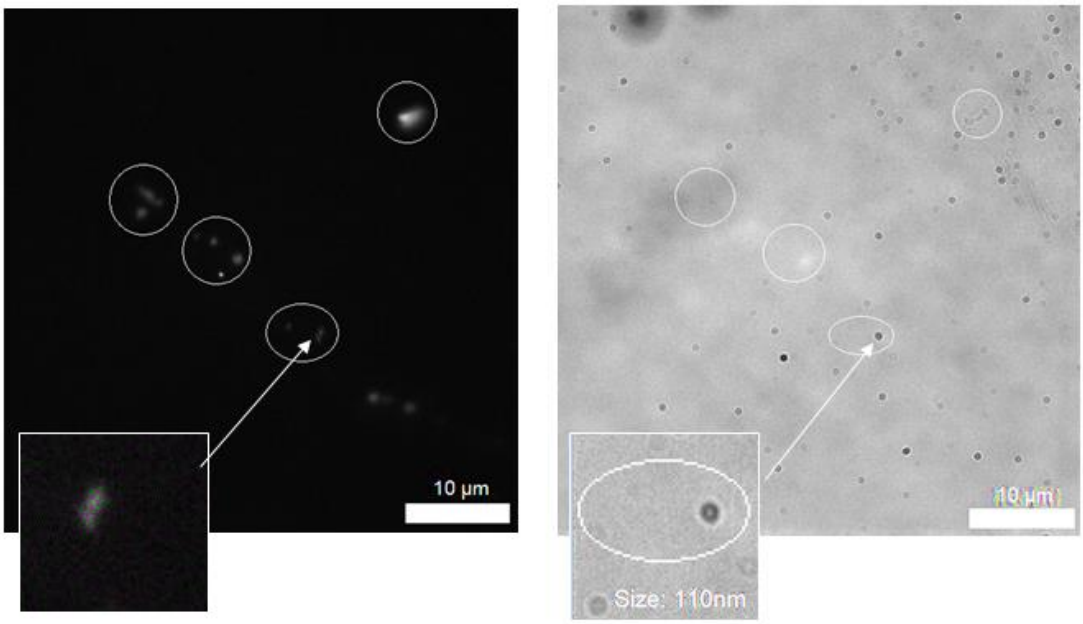

Figure S125: Left: a DAPI filtered fluorescence microscopy image of compound **1** (1 mM) in an EtOH: H_2O (1: 19) solution. Right: an analogous transmitted light microscopy image. Evidence of aggregated spherical structures are circled for clarity. Photo bleaching during the imaging process resulted in loss of fluorescence emission intensity, as a result some aggregates could not be captured in the fluorescence microscopy image. Only clearly visible spherical structures which appeared in both images were measured. Shape variation can be due to individual aggregation and or moving structures.

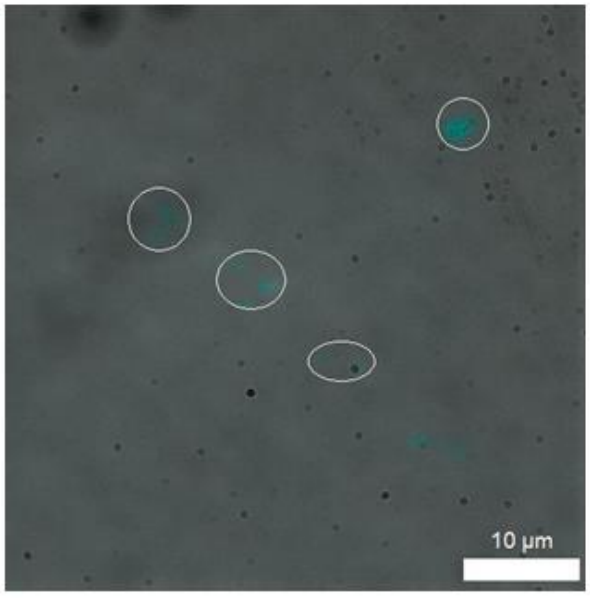

Figure S126: An overlaid image of those shown in Figure S125 (left and right) image. Clear evidence of aggregated spherical structures of compound **1** are circled for clarity.

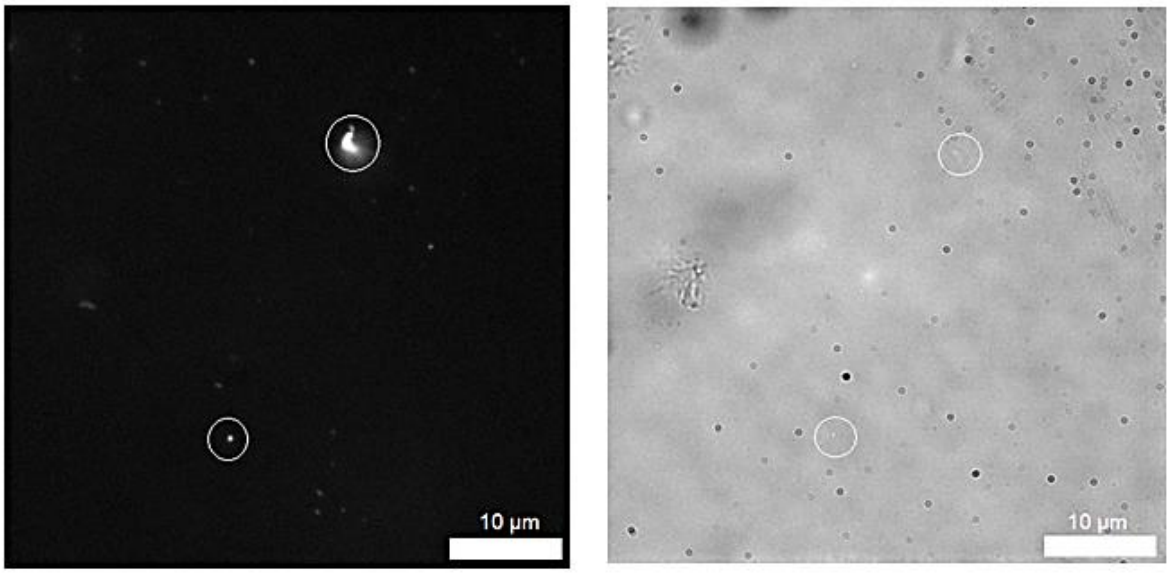

Figure S127: Left: a DAPI filtered fluorescence microscopy image of compound **1** (0.56 mM) in an EtOH: H_2O (1: 19) solution. Right: an analogous transmitted light microscopy image. Evidence of aggregated spherical structures are circled for clarity. Photo bleaching during the imaging process resulted in loss of fluorescence emission intensity, as a result some aggregates could not be captured in the fluorescence microscopy image. Only clearly visible spherical structures which appeared in both images were measured. Shape variation can be due to individual aggregation and or moving structures.

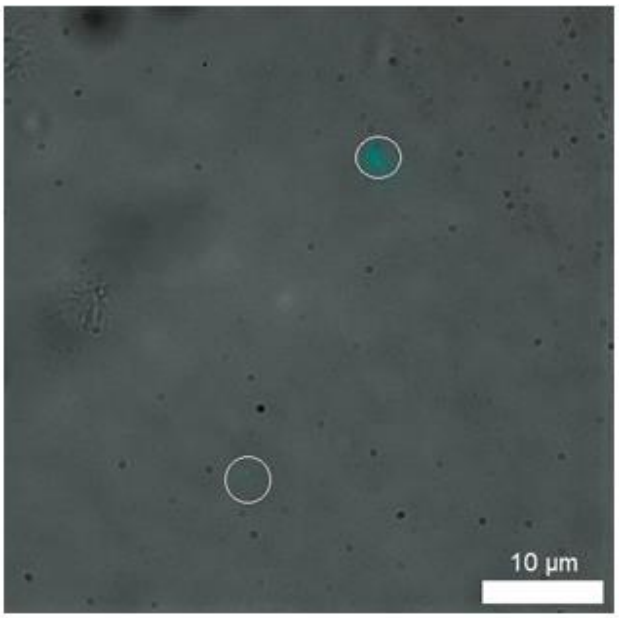

Figure S128: An overlaid image of those shown in Figure S127 (left and right) image. Clear evidence of aggregated spherical structures of compound **1** are circled for clarity.

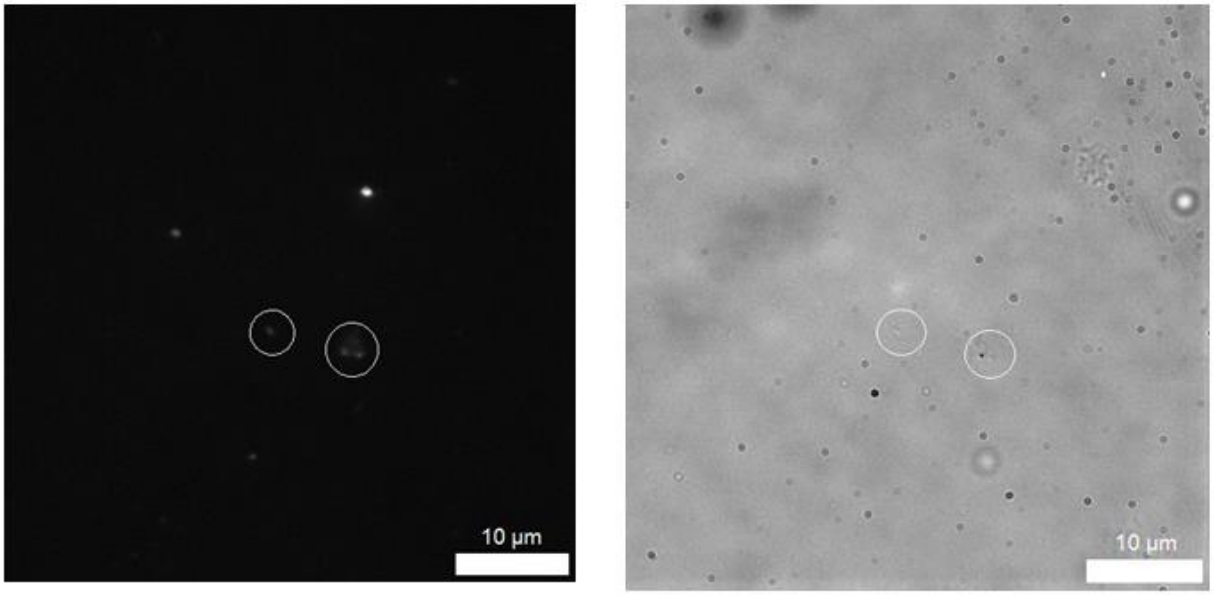

Figure S129: Left: a DAPI filtered fluorescence microscopy image of compound **1** (0.56 mM) in an EtOH: H_2O (1: 19) solution. Right: an analogous transmitted light microscopy image. Evidence of aggregated spherical structures are circled for clarity. Photo bleaching during the imaging process resulted in loss of fluorescence emission intensity, as a result some aggregates could not be captured in the fluorescence microscopy image. Only clearly visible spherical structures which appeared in both images were measured. Shape variation can be due to individual aggregation and or moving structures.

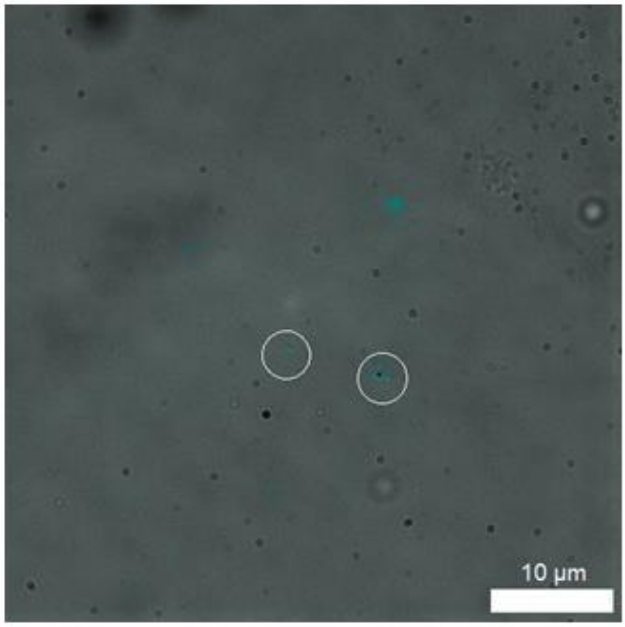

Figure S130: An overlaid image of those shown in Figure S129 left and right) image. Clear evidence of aggregated spherical structures of compound **1** are circled for clarity.

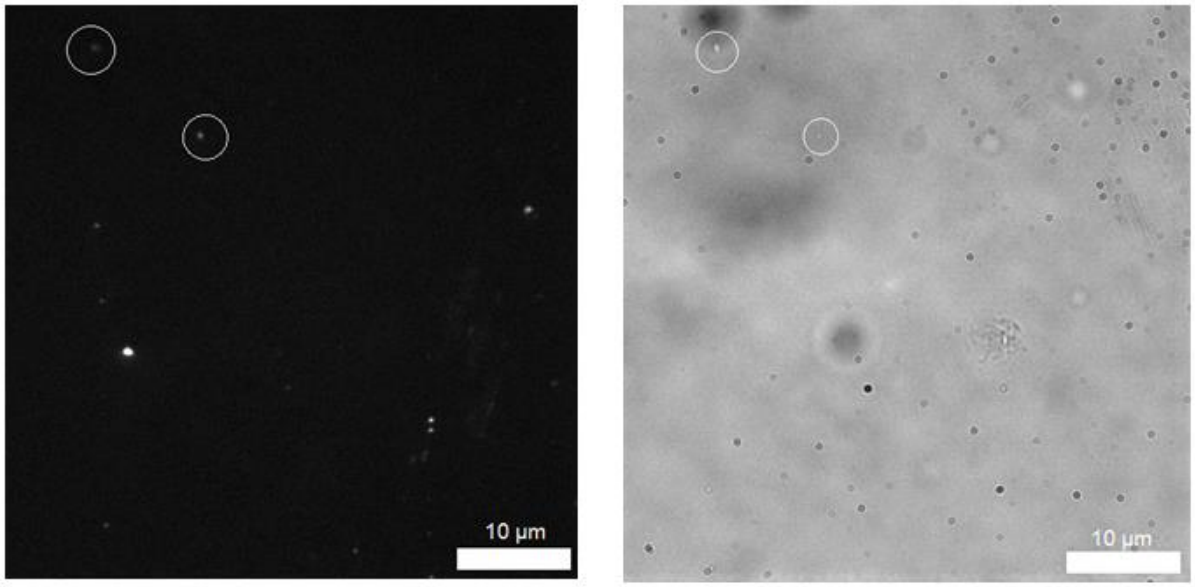

Figure S131: Left: a DAPI filtered fluorescence microscopy image of compound **1** (0.56 mM) in an EtOH: H_2O (1: 19) solution. Right: an analogous transmitted light microscopy image. Evidence of aggregated spherical structures are circled for clarity. Photo bleaching during the imaging process resulted in loss of fluorescence emission intensity, as a result some aggregates could not be captured in the fluorescence microscopy image. Only clearly visible spherical structures which appeared in both images were measured. Shape variation can be due to individual aggregation and or moving structures.

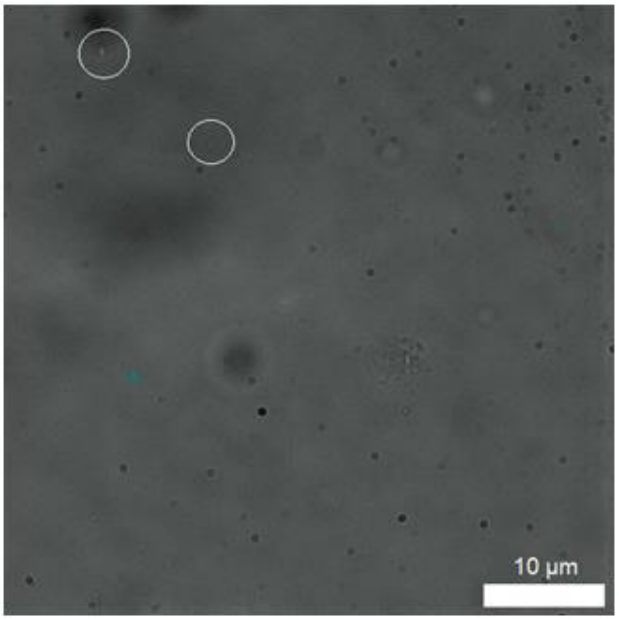

Figure S132: An overlaid image of those shown in Figure S131 (left and right) image. Clear evidence of aggregated spherical structures of compound **1** are circled for clarity

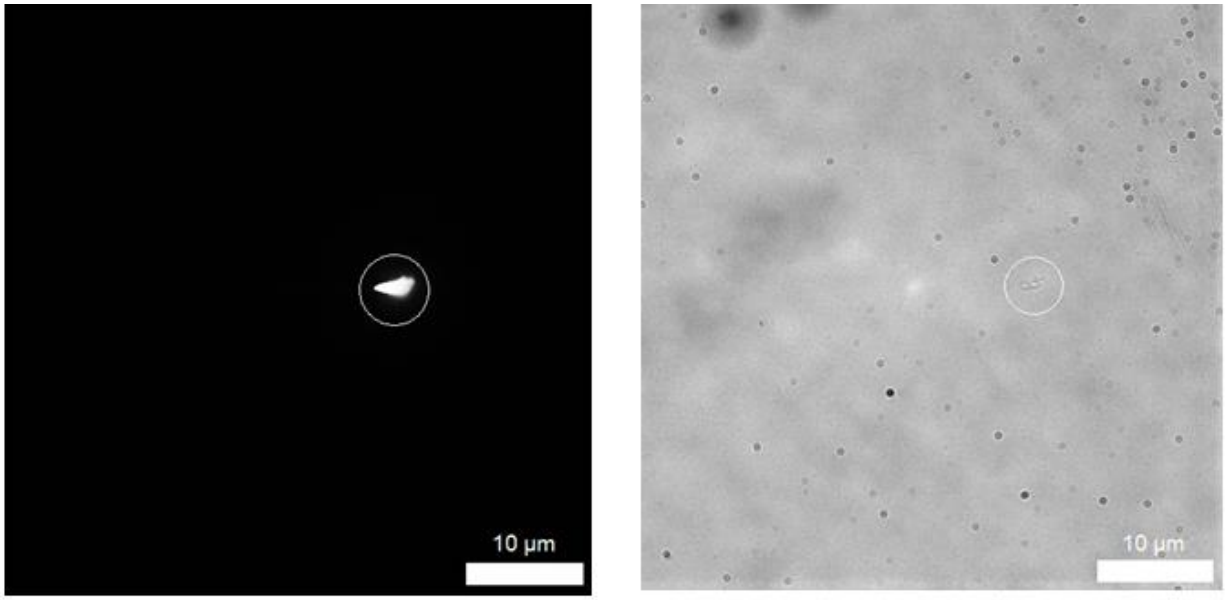

Figure S133: Left: a DAPI filtered fluorescence microscopy image of compound **2** (1 mM) in an EtOH: H_2O (1: 19) solution. Right: an analogous transmitted light microscopy image. Evidence of aggregated spherical structures are circled for clarity. Photo bleaching during the imaging process resulted in loss of fluorescence emission intensity, as a result some aggregates could not be captured in the fluorescence microscopy image. Only clearly visible spherical structures which appeared in both images were measured. Shape variation can be due to individual aggregation and or moving structures.

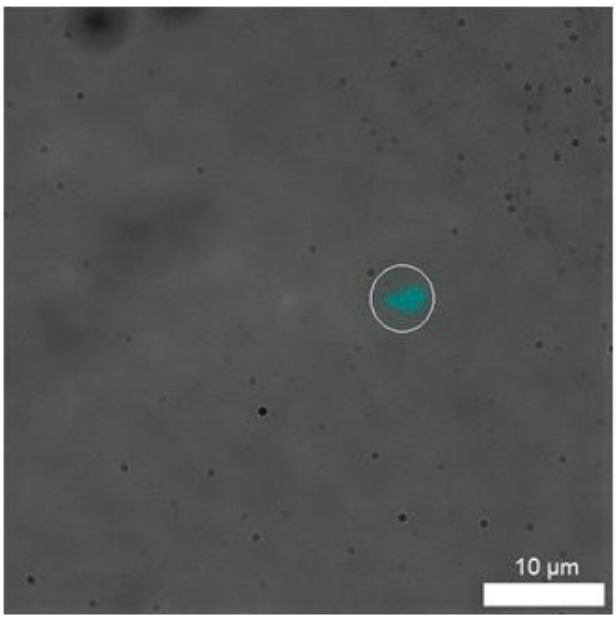

Figure S134: An overlaid image of those shown in Figure S133 (left and right) image. Clear evidence of aggregated spherical structures of compound **2** are circled for clarity.

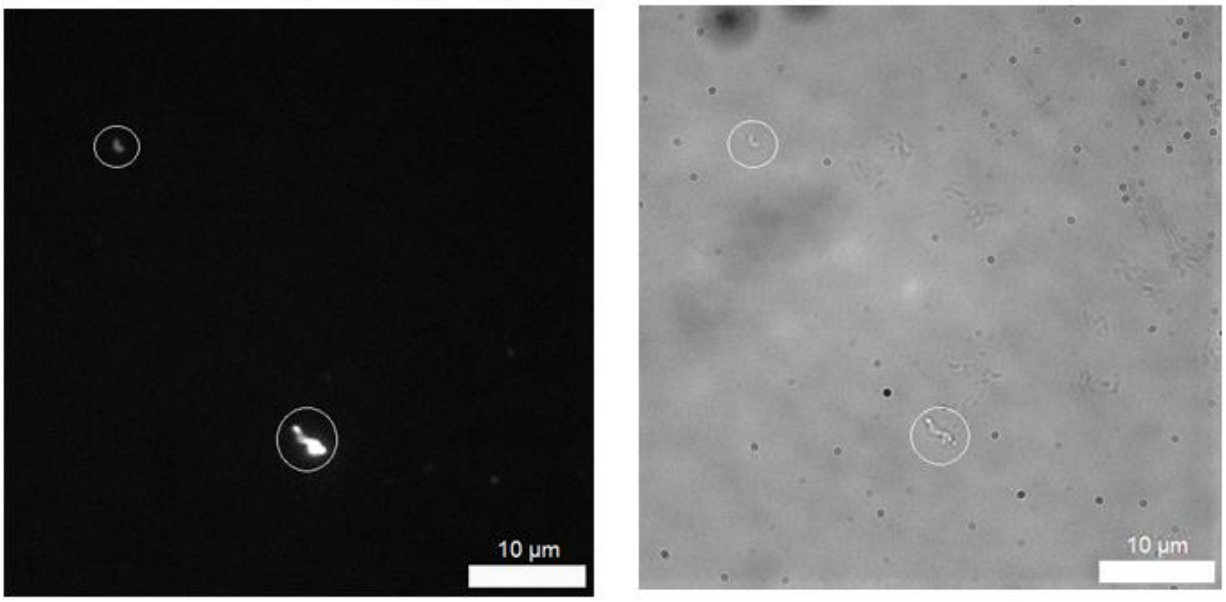

Figure S135: Left: a DAPI filtered fluorescence microscopy image of compound **2** (0.56 mM) in an EtOH: H_2O (1: 19) solution. Right: an analogous transmitted light microscopy image. Evidence of aggregated spherical structures are circled for clarity. Photo bleaching during the imaging process resulted in loss of fluorescence emission intensity, as a result some aggregates could not be captured in the fluorescence microscopy image. Only clearly visible spherical structures which appeared in both images were measured. Shape variation can be due to individual aggregation and or moving structures.

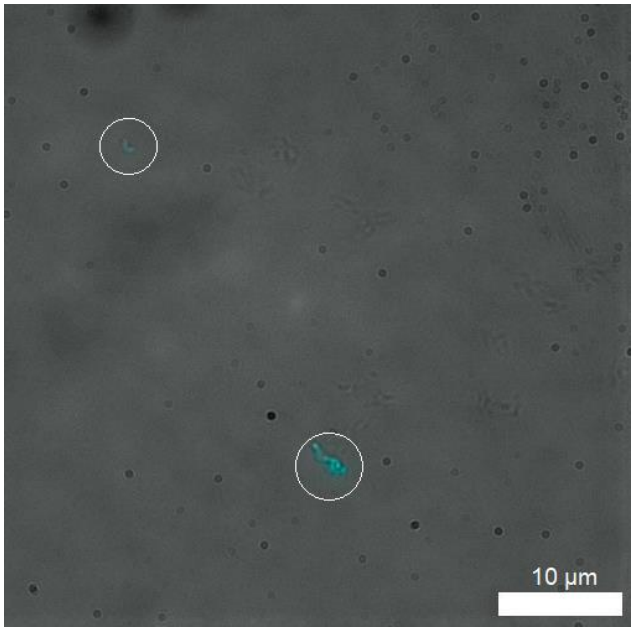

Figure S136: An overlaid image of those shown in Figure S135 (left and right) image. Clear evidence of aggregated spherical structures of compound **2** are circled for clarity.

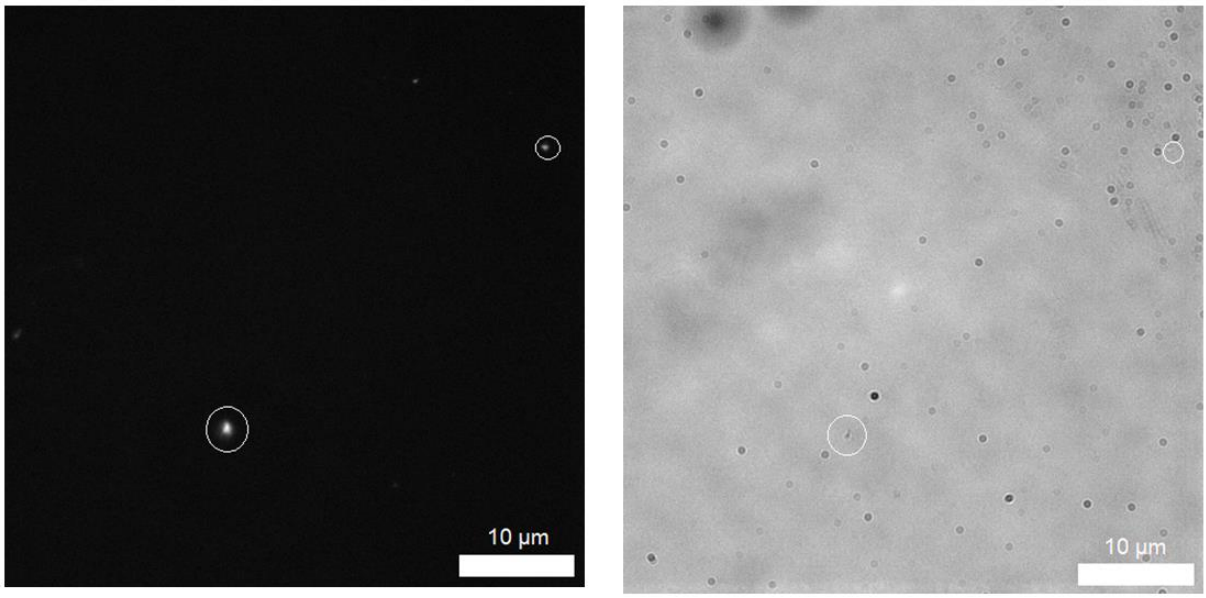

Figure S137: Left: a DAPI filtered fluorescence microscopy image of compound **2** (0.56 mM) in an EtOH: H_2O (1: 19) solution. Right: an analogous transmitted light microscopy image. Evidence of aggregated spherical structures are circled for clarity. Photo bleaching during the imaging process resulted in loss of fluorescence emission intensity, as a result some aggregates could not be captured in the fluorescence microscopy image. Only clearly visible spherical structures which appeared in both images were measured. Shape variation can be due to individual aggregation and or moving structures.

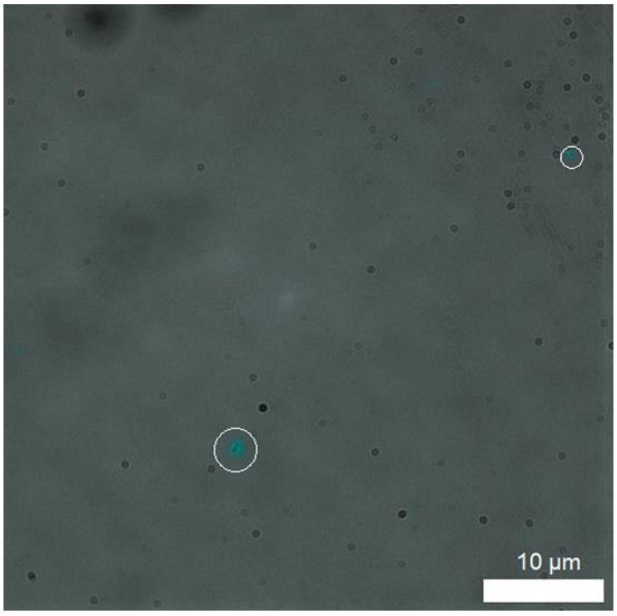

Figure S138: An overlaid image of those shown in Figure S137 (left and right) image. Clear evidence of aggregated spherical structures of compound **2** are circled for clarity.

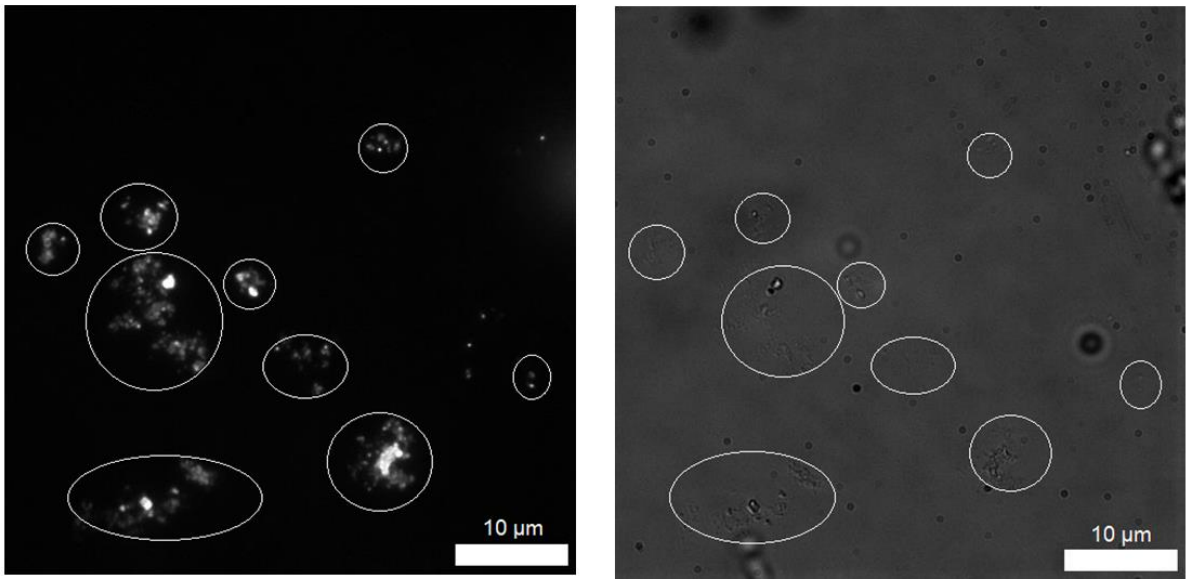

Figure S139: Left: a DAPI filtered fluorescence microscopy image of compound **4** (1 mM) in an EtOH: H_2O (1: 19) solution. Right: an analogous transmitted light microscopy image. Evidence of aggregated spherical structures are circled for clarity. Photo bleaching during the imaging process resulted in loss of fluorescence emission intensity, as a result some aggregates could not be captured in the fluorescence microscopy image. Only clearly visible spherical structures which appeared in both images were measured. Shape variation can be due to individual aggregation and or moving structures.

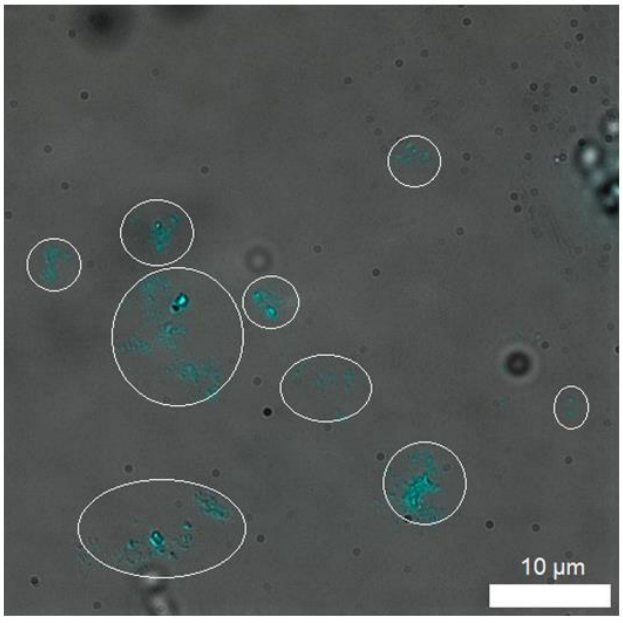

Figure S140: An overlaid image of those shown in Figure S139 (left and right) image. Clear evidence of aggregated spherical structures of compound **4** are circled for clarity.

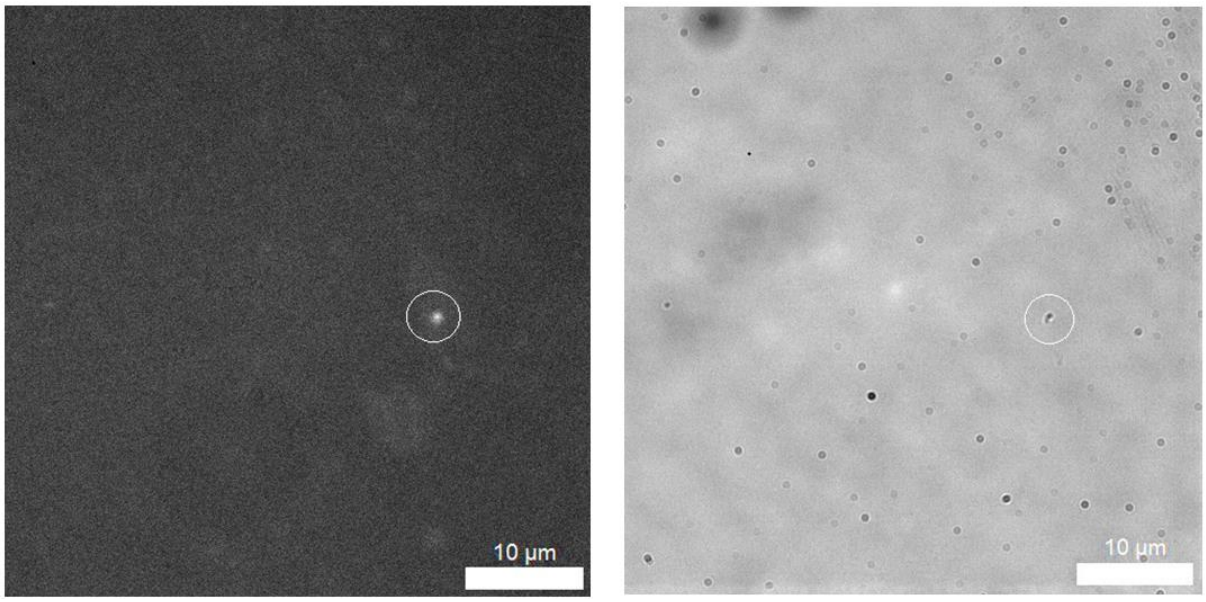

Figure S141: Left: a DAPI filtered fluorescence microscopy image of compound **4** (1 mM) in an EtOH: H_2O (1: 19) solution. Right: an analogous transmitted light microscopy image. Evidence of aggregated spherical structures are circled for clarity. Photo bleaching during the imaging process resulted in loss of fluorescence emission intensity, as a result some aggregates could not be captured in the fluorescence microscopy image. Only clearly visible spherical structures which appeared in both images were measured. Shape variation can be due to individual aggregation and or moving structures.

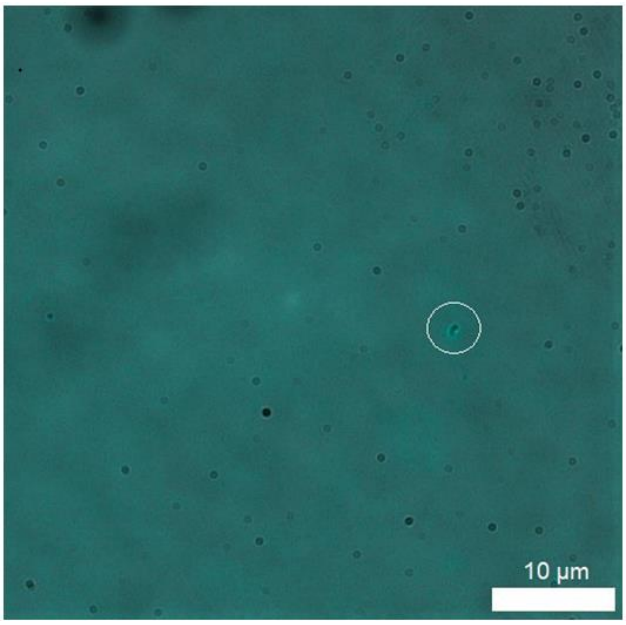

Figure S142: An overlaid image of those shown in Figure S141 (left and right) image. Clear evidence of aggregated spherical structures of compound **4** are circled for clarity.

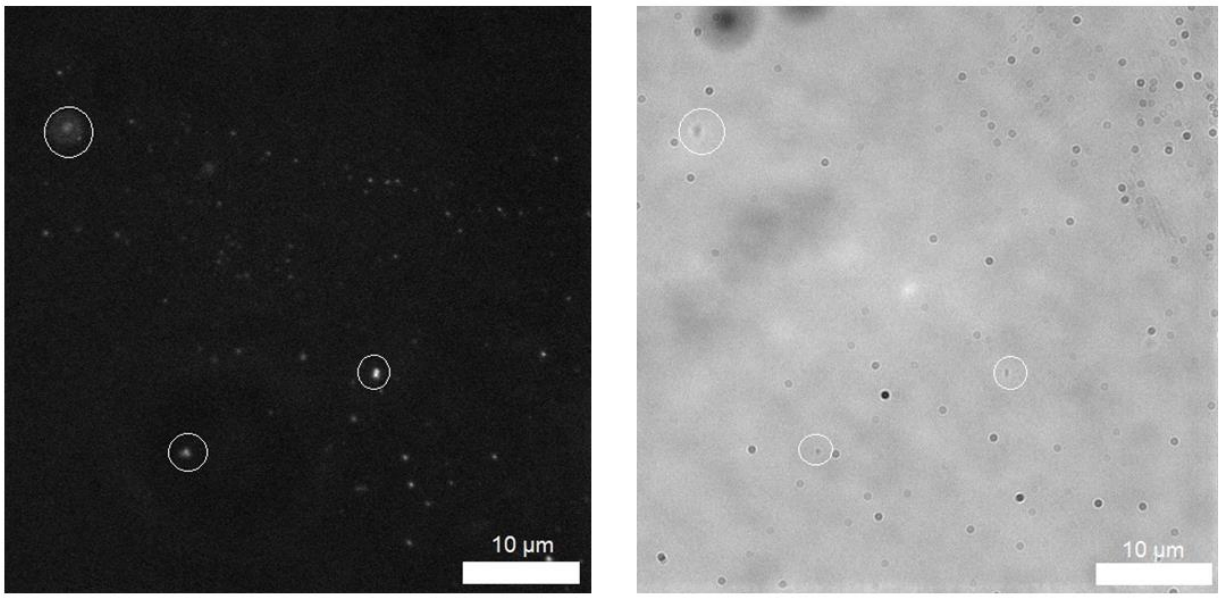

Figure S143: Left: a CFP filtered fluorescence microscopy image of compound **4** (0.56 mM) in an EtOH: H_2O (1: 19) solution. Right: an analogous transmitted light microscopy image. Evidence of aggregated spherical structures are circled for clarity. Photo bleaching during the imaging process resulted in loss of fluorescence emission intensity, as a result some aggregates could not be captured in the fluorescence microscopy image. Only clearly visible spherical structures which appeared in both images were measured. Shape variation can be due to individual aggregation and or moving structures.

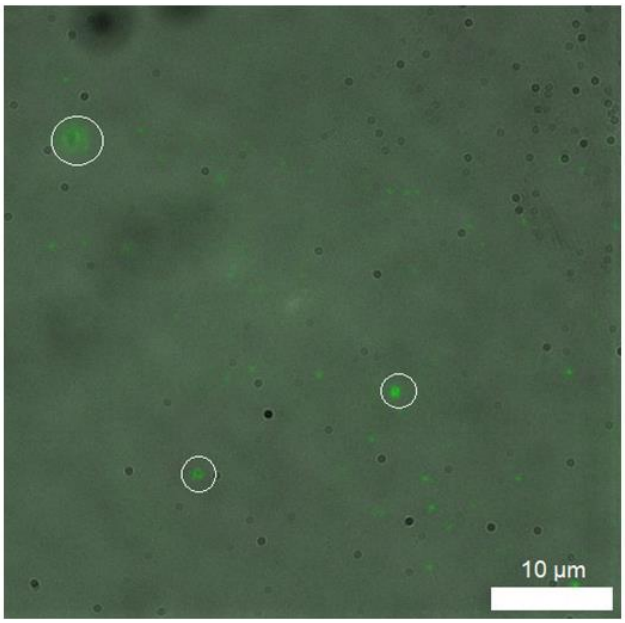

Figure S144: An overlaid image of those shown in Figure S143 (left and right) image. Clear evidence of aggregated spherical structures of compound **4** are circled for clarity.

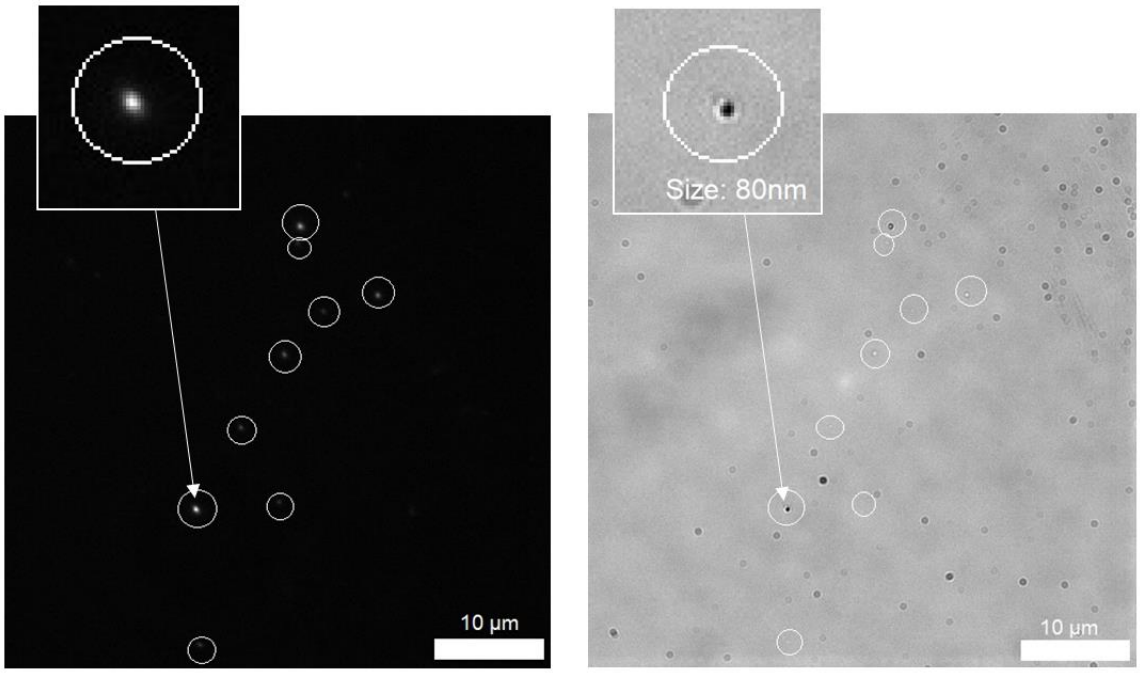

Figure S145: Left: a CFP filtered fluorescence microscopy image of compound **4** (0.56 mM) in an EtOH: H_2O (1: 19) solution. Right: an analogous transmitted light microscopy image. Evidence of aggregated spherical structures are circled for clarity. Photo bleaching during the imaging process resulted in loss of fluorescence emission intensity, as a result some aggregates could not be captured in the fluorescence microscopy image. Only clearly visible spherical structures which appeared in both images were measured. Shape variation can be due to individual aggregation and or moving structures.

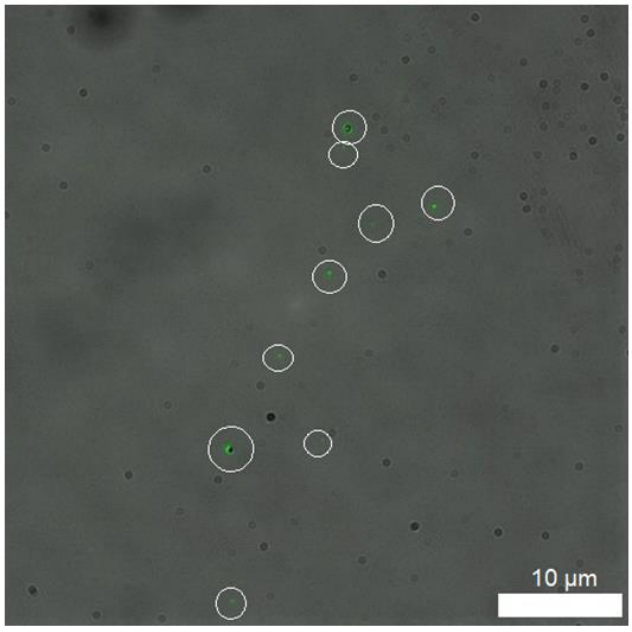

Figure S146: An overlaid image of those shown in Figure S145 (left and right) image. Clear evidence of aggregated spherical structures of compound **4** are circled for clarity.

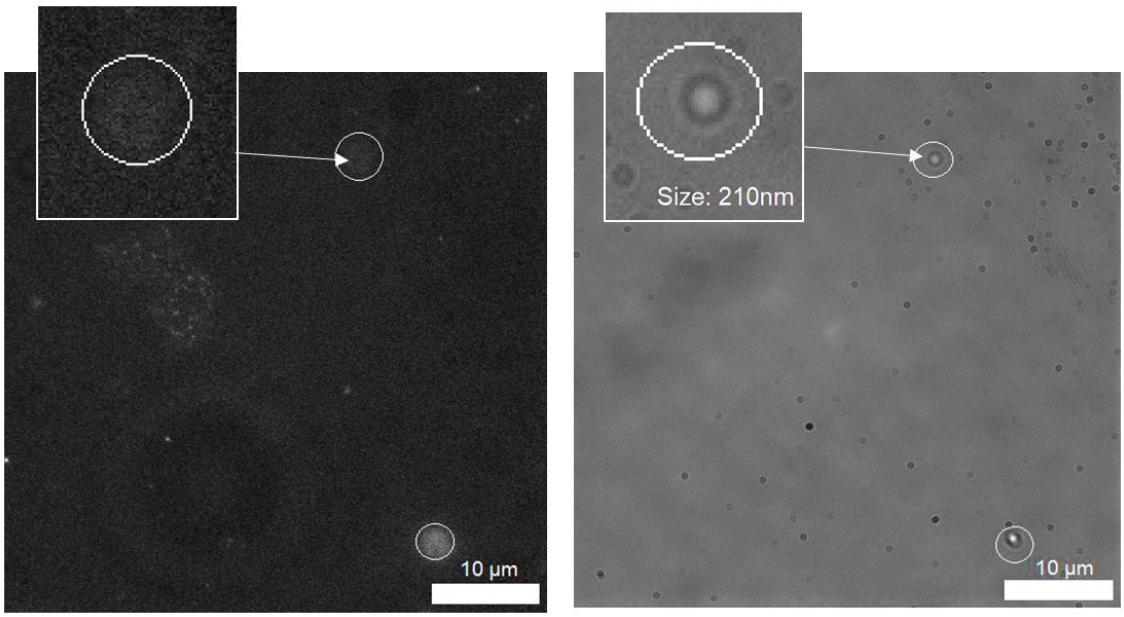

Figure S147: Left: a CFP filtered fluorescence microscopy image of compound **4** (0.56 mM) in an EtOH: H_2O (1: 19) solution. Right: an analogous transmitted light microscopy image. Evidence of aggregated spherical structures are circled for clarity. Photo bleaching during the imaging process resulted in loss of fluorescence emission intensity, as a result some aggregates could not be captured in the fluorescence microscopy image. Only clearly visible spherical structures which appeared in both images were measured. Shape variation can be due to individual aggregation and or moving structures.

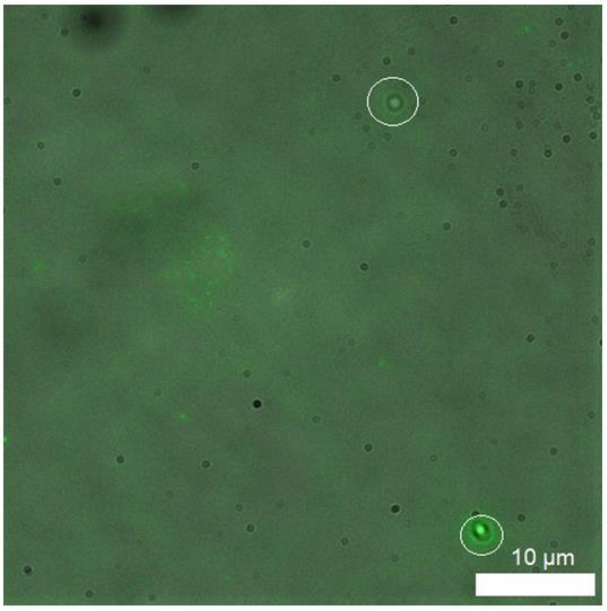

Figure S148: An overlaid image of those shown in Figure S147 (left and right) image. Clear evidence of aggregated spherical structures of compound **4** are circled for clarity.

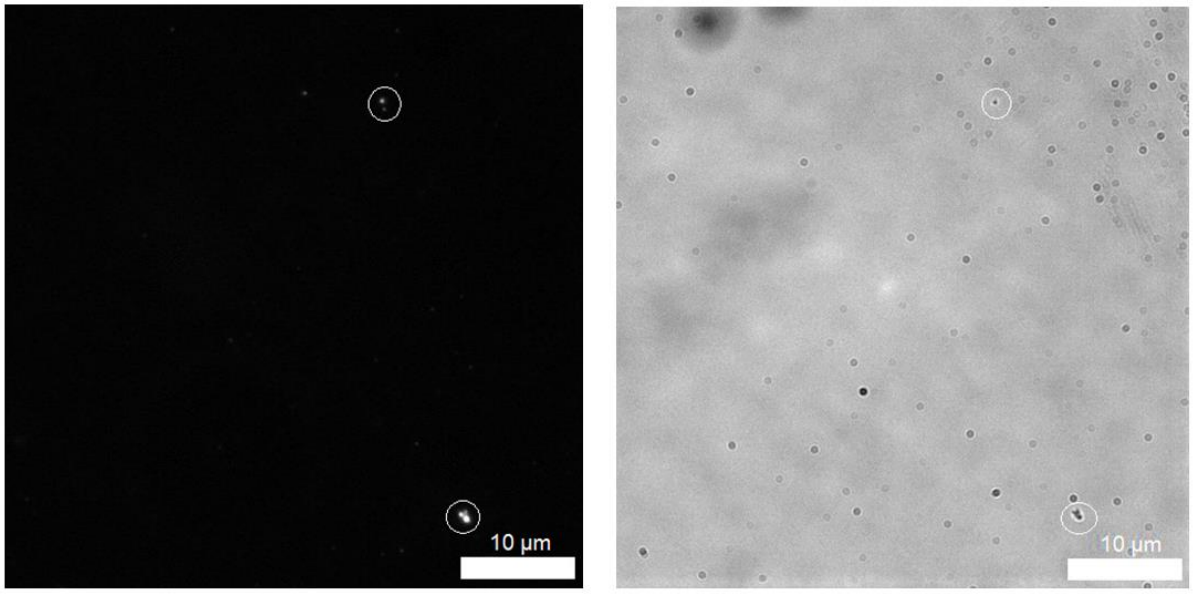

Figure S149: Left: a CFP filtered fluorescence microscopy image of compound **4** (0.56 mM) in an EtOH: H_2O (1: 19) solution. Right: an analogous transmitted light microscopy image. Evidence of aggregated spherical structures are circled for clarity. Photo bleaching during the imaging process resulted in loss of fluorescence emission intensity, as a result some aggregates could not be captured in the fluorescence microscopy image. Only clearly visible spherical structures which appeared in both images were measured. Shape variation can be due to individual aggregation and or moving structures.

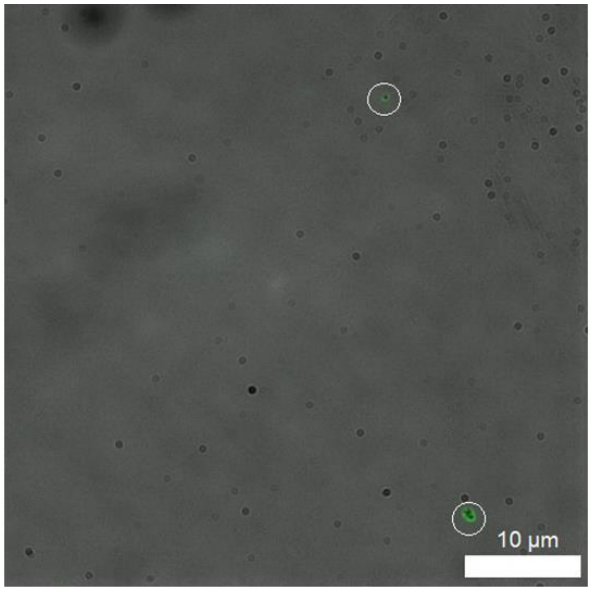

Figure S150: An overlaid image of those shown in Figure S149 (left and right) image. Clear evidence of aggregated spherical structures of compound **3** are circled for clarity.

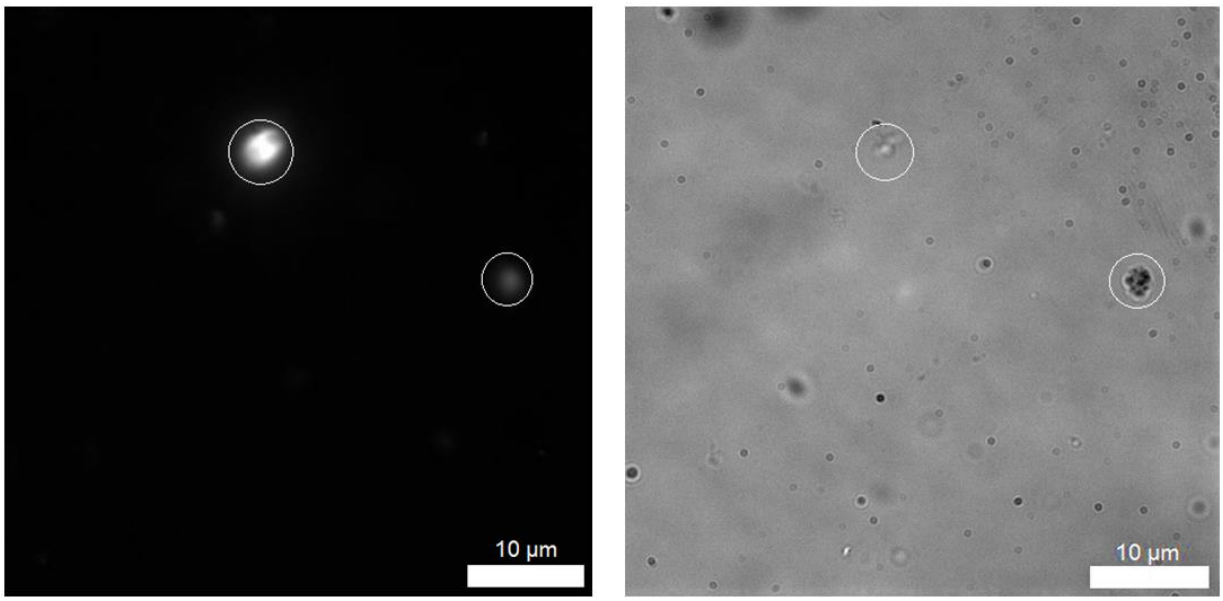

Figure S151: Left: a DAPI filtered fluorescence microscopy image of compound **1** and **2** (1:1 mix) (total concentration 1 mM) in an EtOH: H_2O (1: 19) solution. Right: an analogous transmitted light microscopy image. Evidence of aggregated spherical structures are circled for clarity. Photo bleaching during the imaging process resulted in loss of fluorescence emission intensity, as a result some aggregates could not be captured in the fluorescence microscopy image. Only clearly visible spherical structures which appeared in both images were measured. Shape variation can be due to individual aggregation and or moving structures.

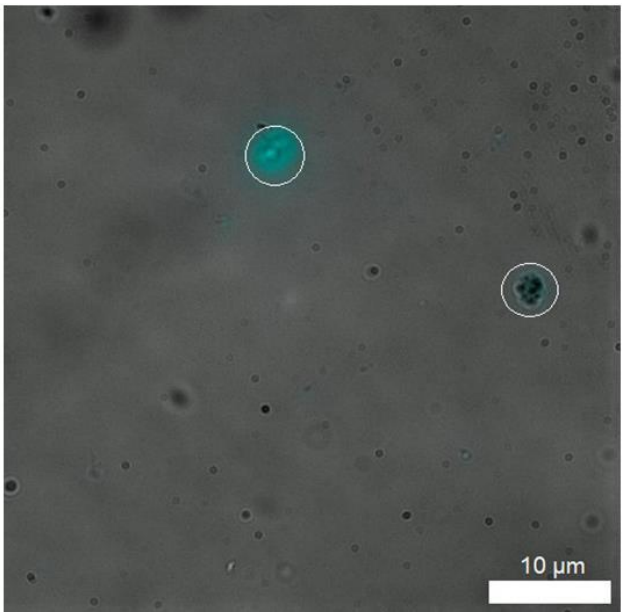

Figure S152: An overlaid image of those shown in Figure S151 (left and right) image. Clear evidence of aggregated spherical structures of compound **1** and **2** (1:1 mix) (total concentration 1 mM) are circled for clarity.

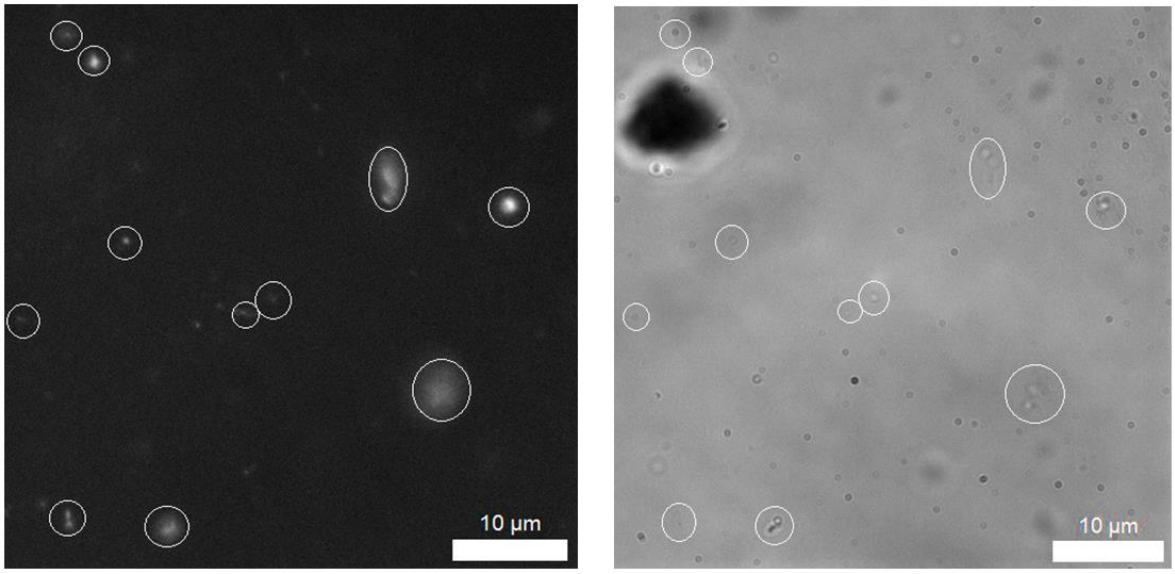

Figure S153: Left: a DAPI filtered fluorescence microscopy image of compound **1** and **2** (1:1 mix) (total concentration 1 mM) in an EtOH: H_2O (1: 19) solution. Right: an analogous transmitted light microscopy image. Evidence of aggregated spherical structures are circled for clarity. Photo bleaching during the imaging process resulted in loss of fluorescence emission intensity, as a result some aggregates could not be captured in the fluorescence microscopy image. Only clearly visible spherical structures which appeared in both images were measured. Shape variation can be due to individual aggregation and or moving structures.

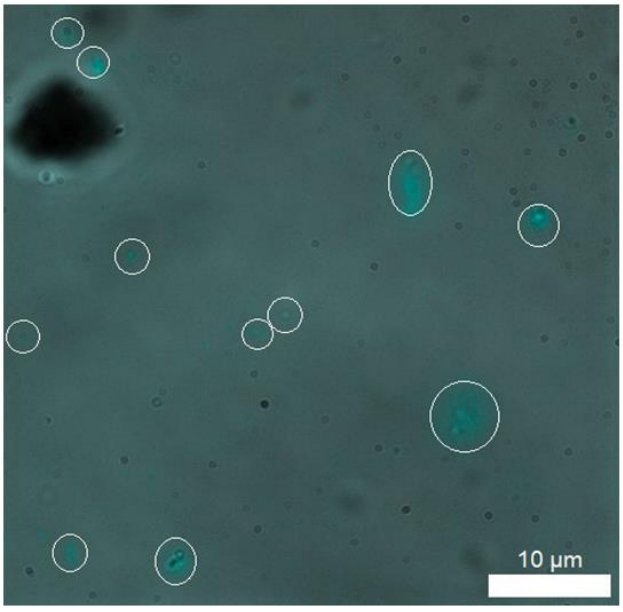

Figure S154: An overlaid image of those shown in Figure S153 (left and right) image. Clear evidence of aggregated spherical structures of compound **1** and **2** (1:1 mix) (total concentration 1 mM) are circled for clarity.

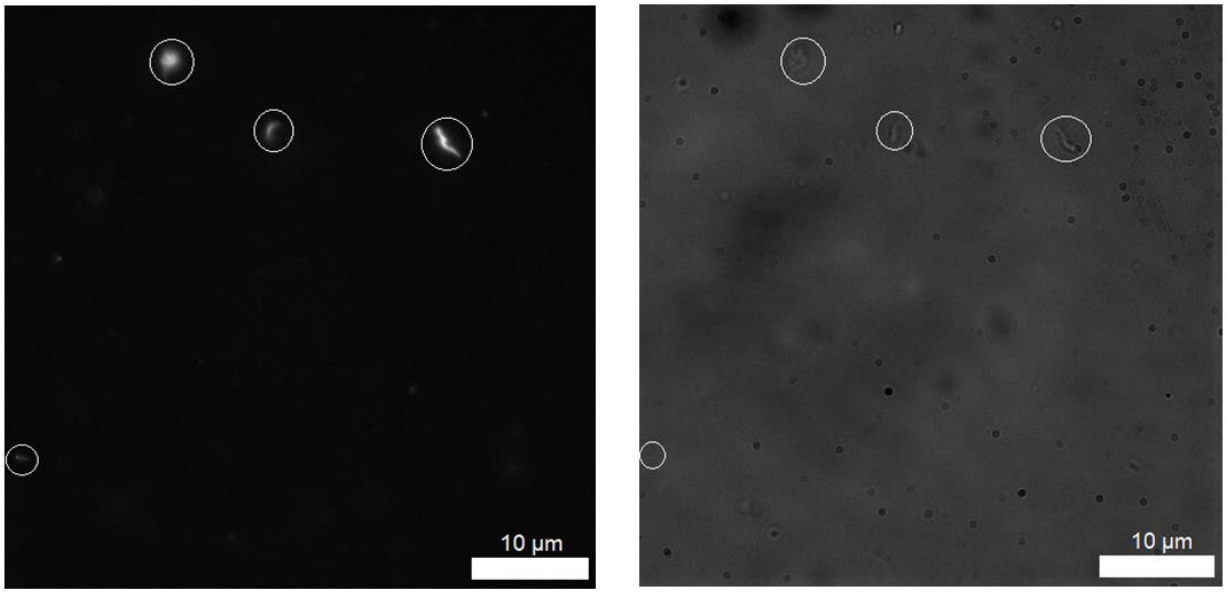

Figure S155: Left: a DAPI filtered fluorescence microscopy image of compound **1** and **2** (1:1 mix) (total concentration 1 mM) in an EtOH: H_2O (1: 19) solution. Right: an analogous transmitted light microscopy image. Evidence of aggregated spherical structures are circled for clarity. Photo bleaching during the imaging process resulted in loss of fluorescence emission intensity, as a result some aggregates could not be captured in the fluorescence microscopy image. Only clearly visible spherical structures which appeared in both images were measured. Shape variation can be due to individual aggregation and or moving structures.

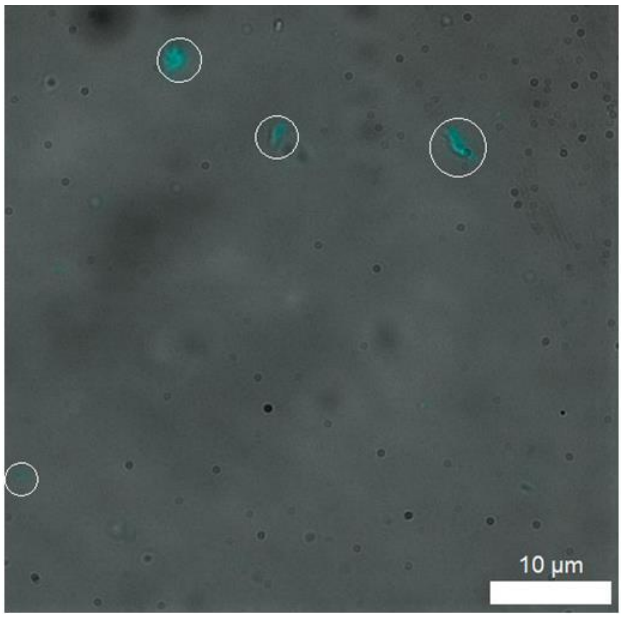

Figure S156: An overlaid image of those shown in Figure S155 (left and right) image. Clear evidence of aggregated spherical structures of compound **1** and **2** (1:1 mix) (total concentration 1 mM) are circled for clarity.

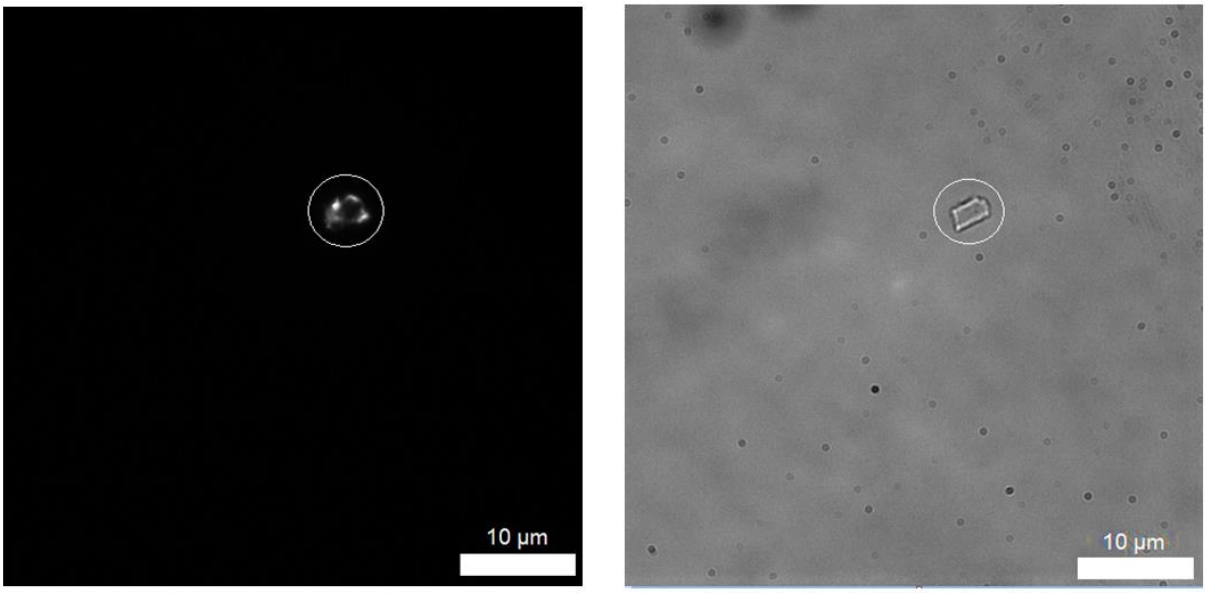

Figure S157: Left: a DAPI filtered fluorescence microscopy image of compound **1** and **2** (1:1 mix) (total concentration 0.56 mM) in an EtOH: H_2O (1: 19) solution. Right: an analogous transmitted light microscopy image. Evidence of aggregated spherical structures are circled for clarity. Photo bleaching during the imaging process resulted in loss of fluorescence emission intensity, as a result some aggregates could not be captured in the fluorescence microscopy image. Only clearly visible spherical structures which appeared in both images were measured. Shape variation can be due to individual aggregation and or moving structures.

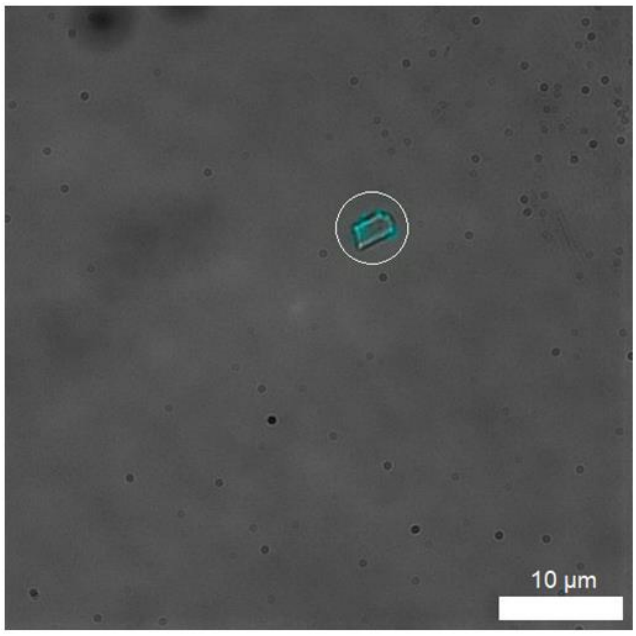

Figure S158: An overlaid image of those shown in Figure S157 (left and right) image. Clear evidence of aggregated spherical structures of compound **1** and **2** (1:1 mix) (total concentration 0.56 mM) are circled for clarity.

MIC_{50} data for *S.aureus*

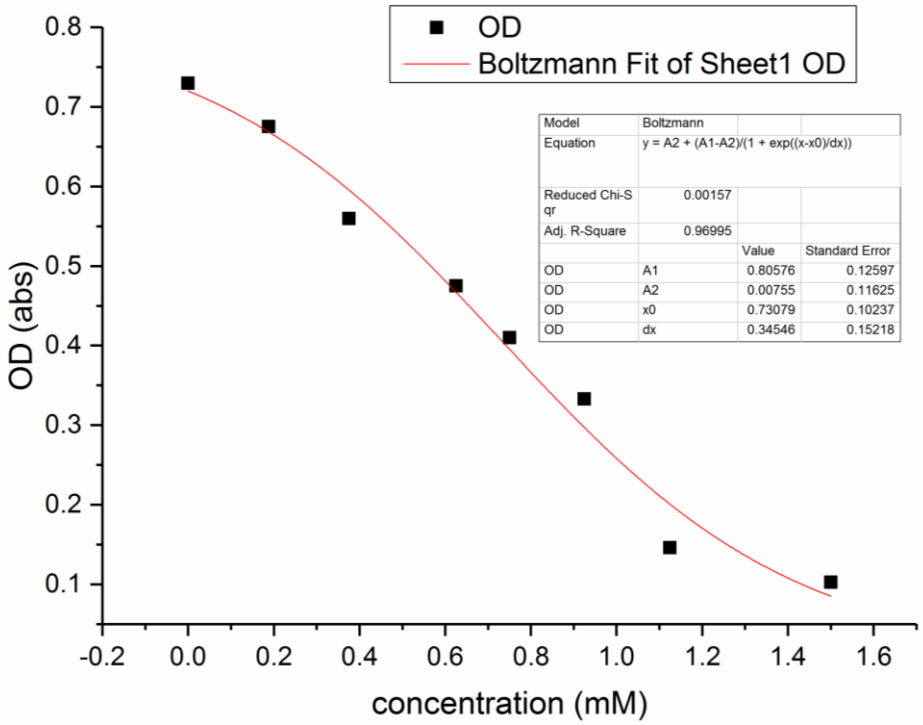

Figure S159: Data obtained from average growth curves with compound **1** at 900 mins and fitted using a Boltzmann fit. This fit was used to calculate the reported MIC_{50} value.

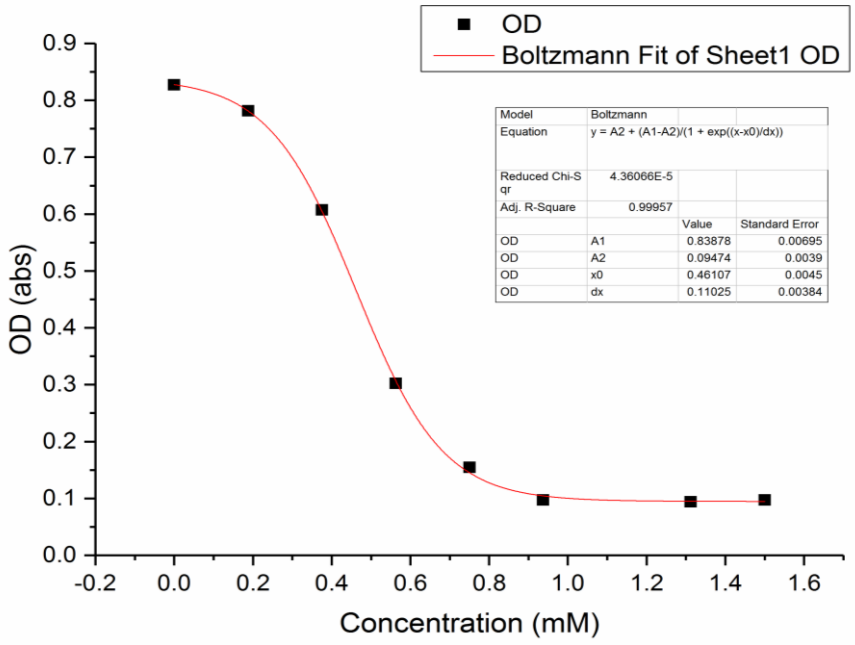

Figure S160: Data obtained from average growth curves with compound **2** at 900 mins and fitted using a Boltzmann fit. This fit was used to calculate the reported MIC_{50} value.

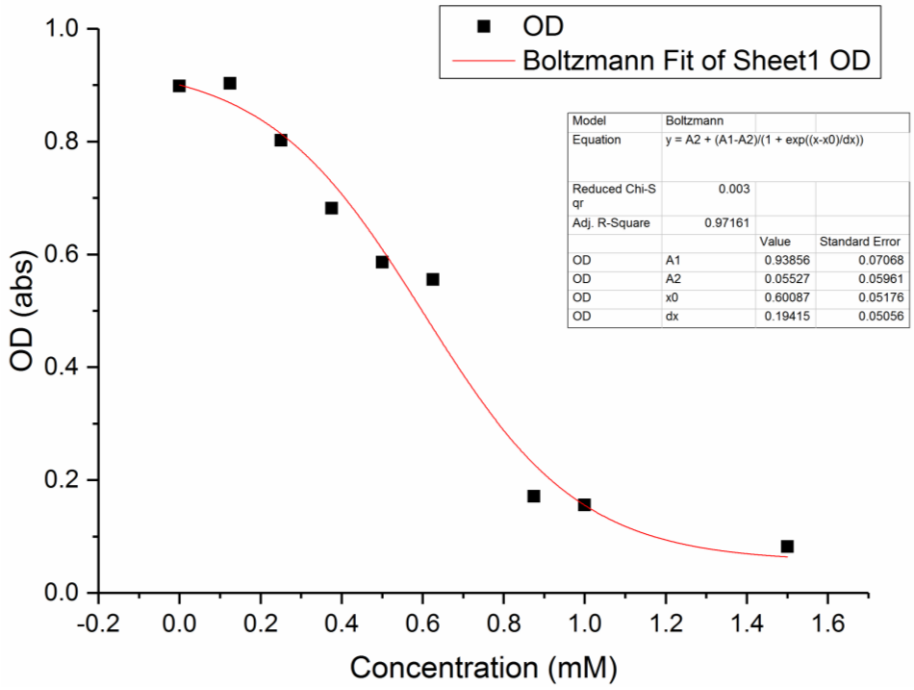

Model	Boltzmann		
Equation	y = A2 + (A1-A2)/(1 + exp((x-x0)/dx))		
Reduced Chi-Sqr	0.003		
Adj. R-Square	0.97161		
		Value	Standard Error
OD	A1	0.93856	0.07068
OD	A2	0.05527	0.05961
OD	x0	0.60087	0.05176
OD	dx	0.19415	0.05056

Figure S161: Data obtained from average growth curves with compound **4** at 900 mins and fitted using a Boltzmann fit. This fit was used to calculate the reported MIC_{50} value.

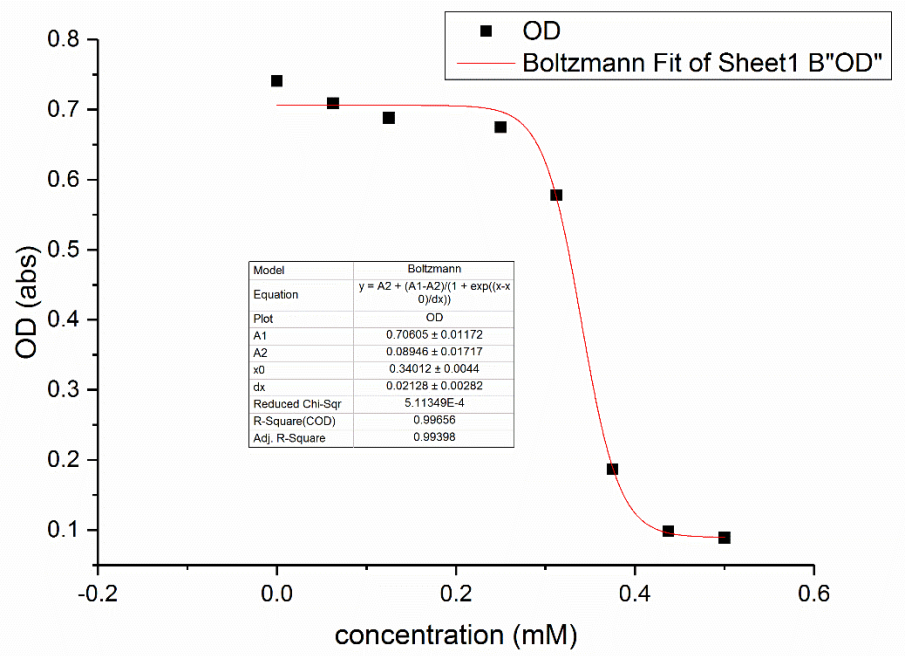

Model	Boltzmann
Equation	y = A2 + (A1-A2)/(1 + exp((x-x0)/dx))
Plot	OD
A1	0.70605 ± 0.01172
A2	0.08946 ± 0.01717
x0	0.34012 ± 0.0044
dx	0.02128 ± 0.00282
Reduced Chi-Sqr	5.11349E-4
R-Square(COD)	0.99656
Adj. R-Square	0.99398

Figure S162: Data obtained from average growth curves with compounds **1** and **2** in a 1:1 mix at 900 mins and fitted using a Boltzmann fit. This fit was used to calculate the reported MIC_{50} value.

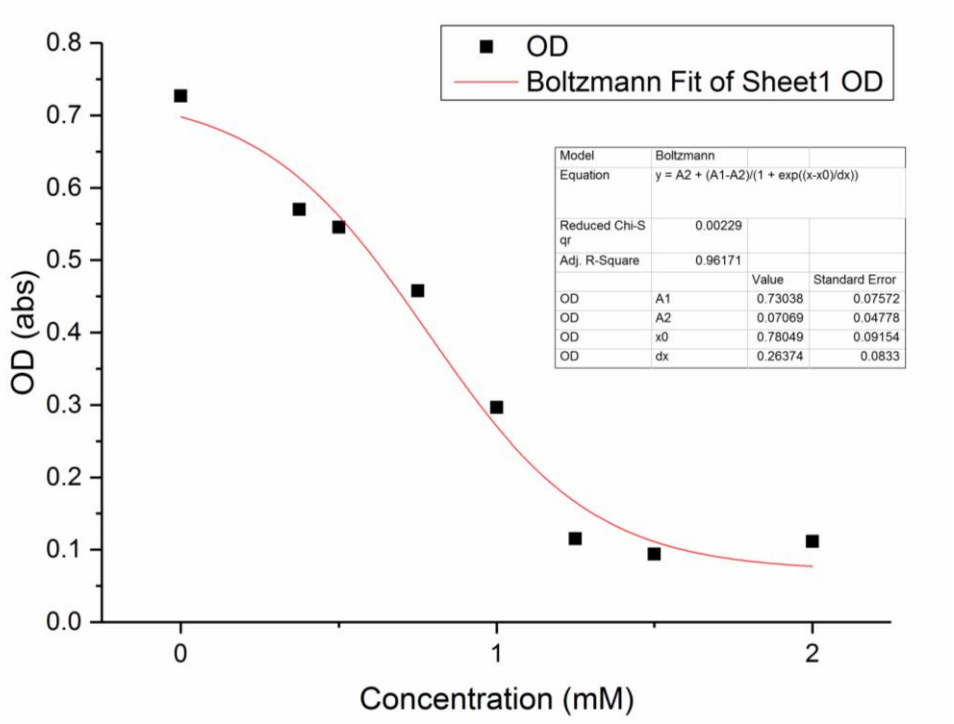

Figure S163: Data obtained from average growth curves with compounds **1** and **4** in a 1:1 mix at 900 mins and fitted using a Boltzmann fit. This fit was used to calculate the reported MIC_{50} value.

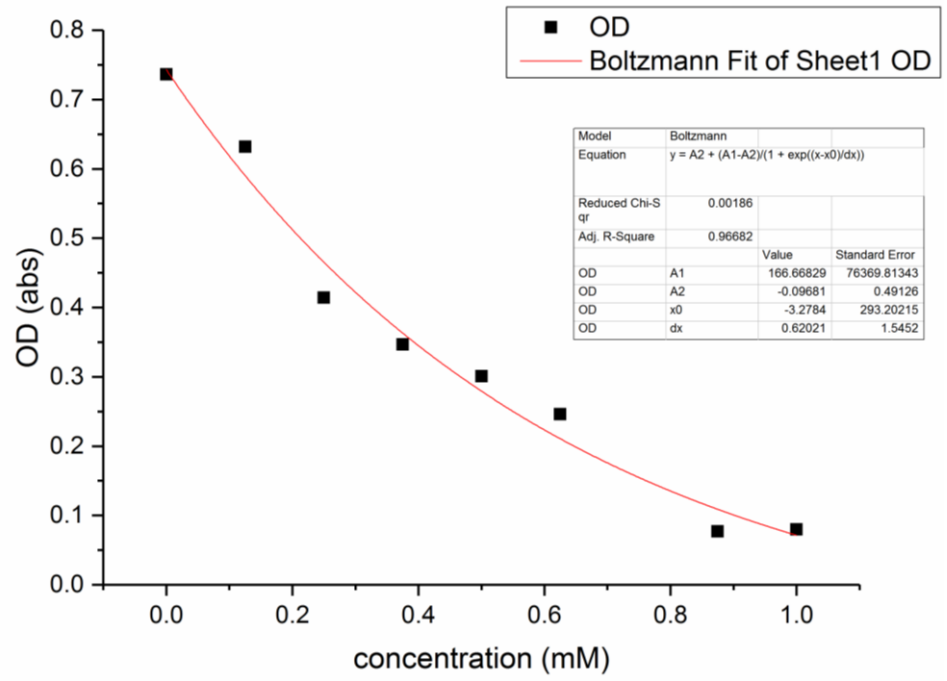

Figure S164: Data obtained from average growth curves with compounds **2** and **4** in a 1:1 mix at 900 mins and fitted using a Boltzmann fit. This fit was used to calculate the reported MIC_{50} value.

Average growth curve graphs (*E.coli*)

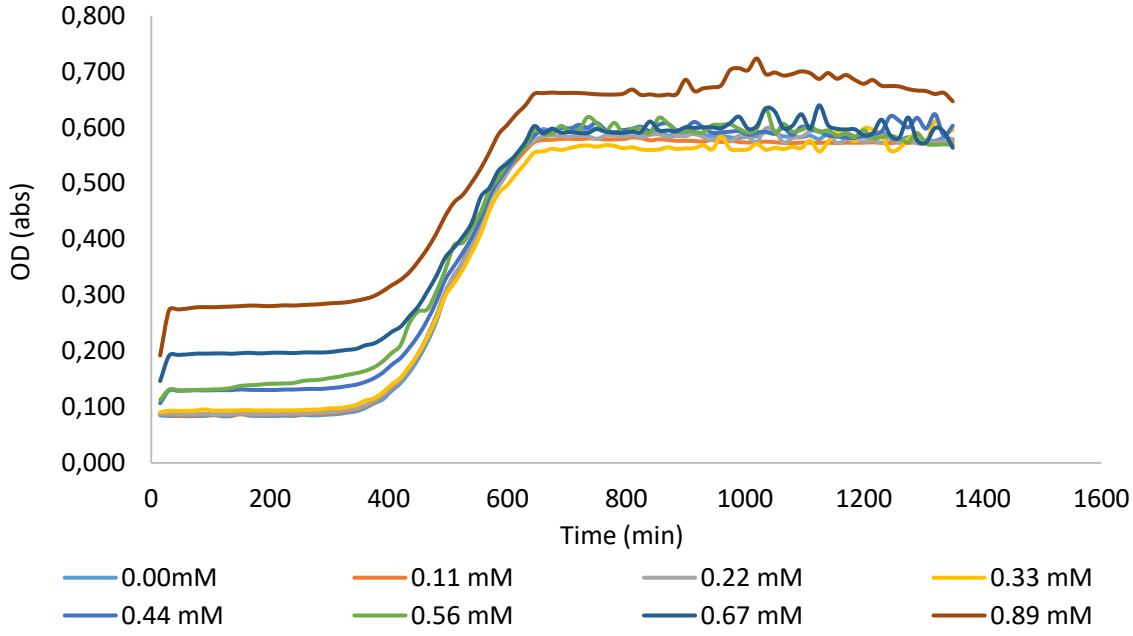

Figure S165: Average growth curves obtained for *E.coli* in the presence of compounds **2** at eight different concentrations. Optical density (OD) relates to the number of cells present.

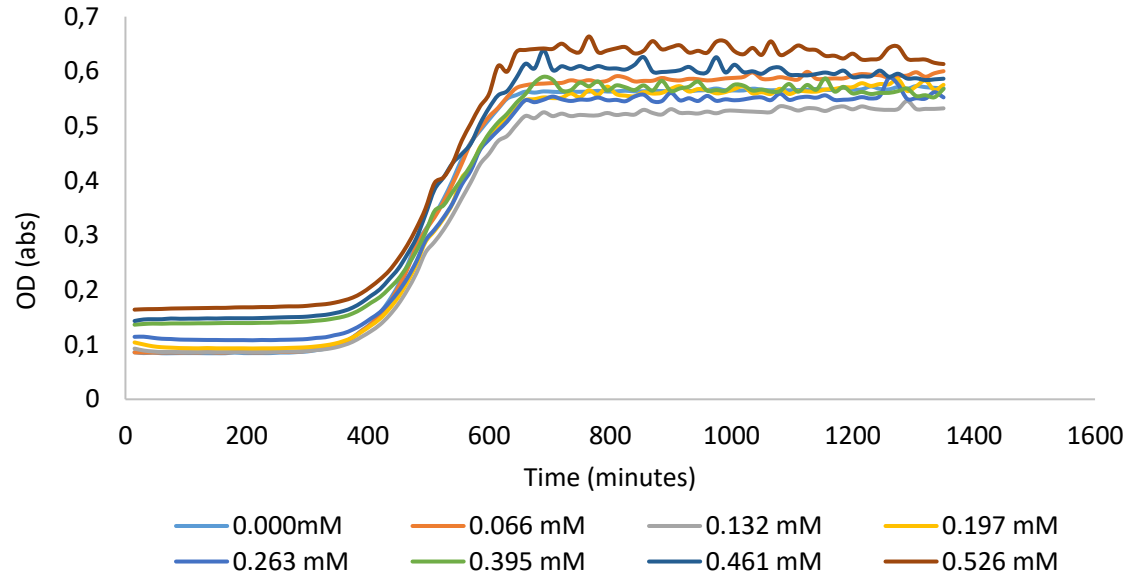

Figure S166: Average growth curves obtained for *E.coli* in the presence of compounds **4** at eight different concentrations. Optical density (OD) relates to the number of cells present.

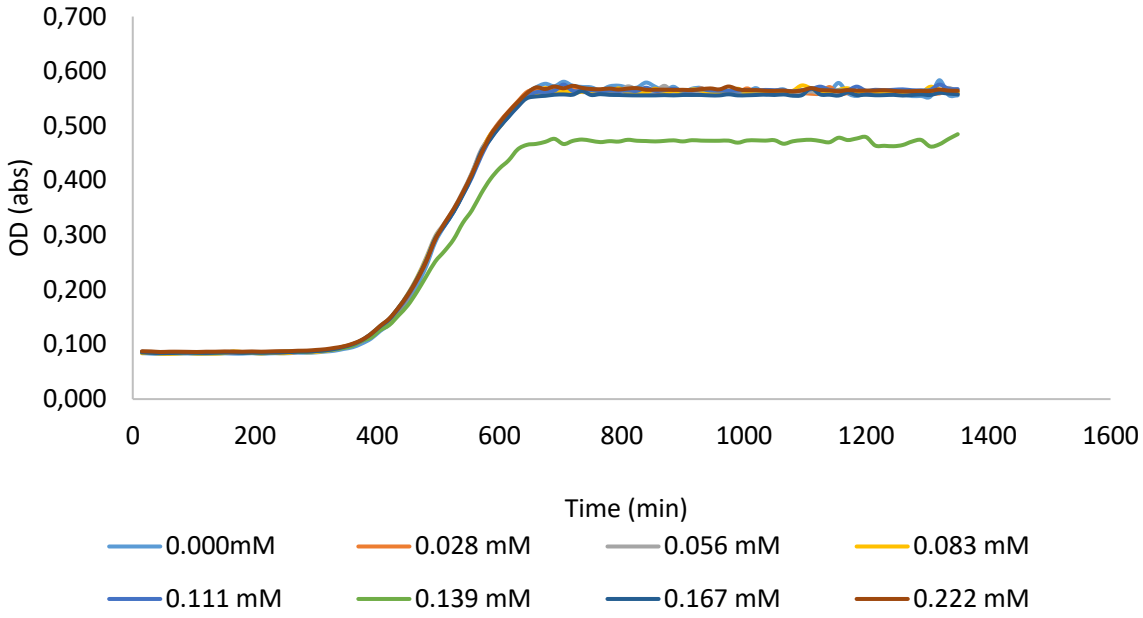

Figure S167: Average growth curves obtained for *E.coli* in the presence of compounds **1** and **2** (1:1 mixture) at eight different concentrations. Optical density (OD) relates to the number of cells present.

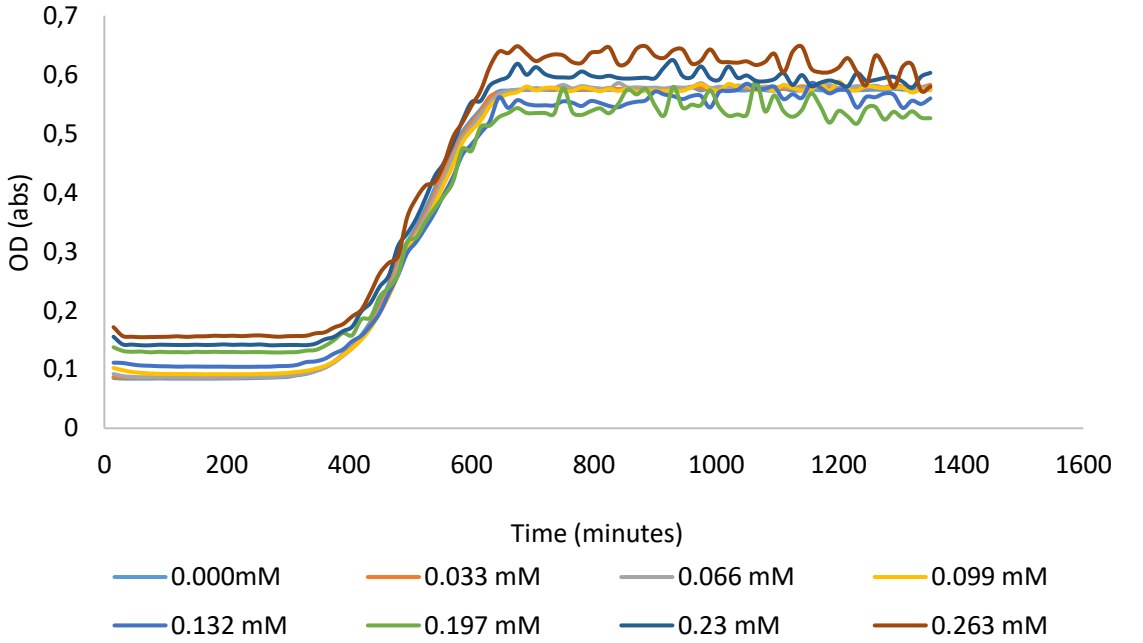

Figure S168: Average growth curves obtained for *E.coli* in the presence of compounds **1** and **4** (1:1 mixture) at eight different concentrations. Optical density (OD) relates to the number of cells present.

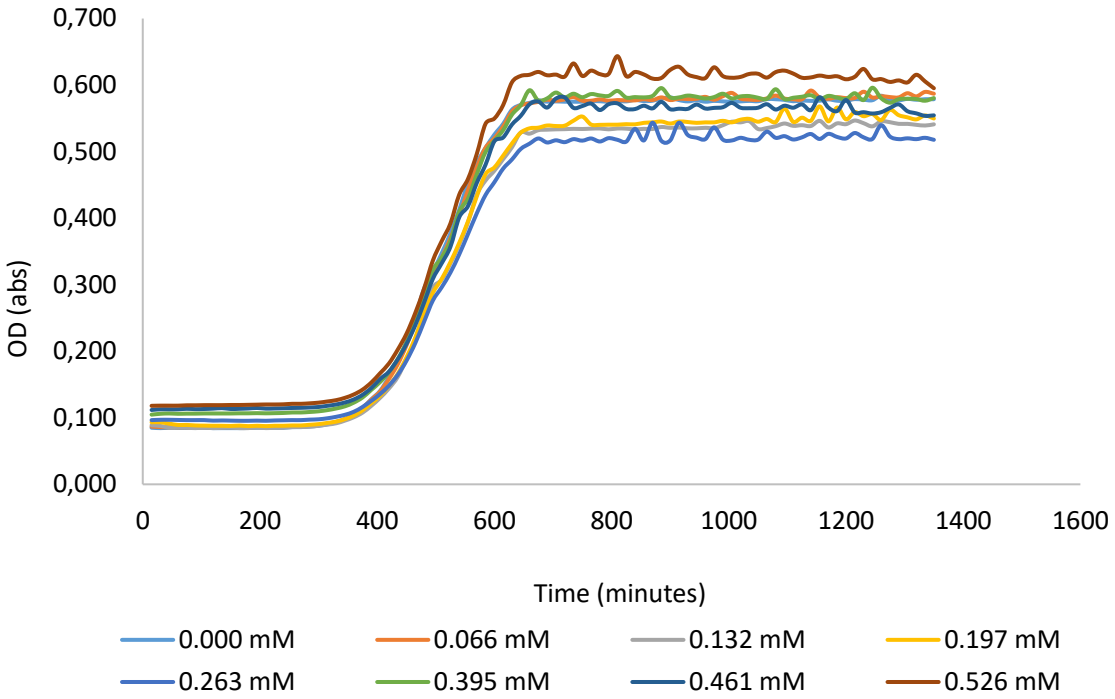

Figure S169: Average growth curves obtained for *E.coli* in the presence of compounds **2** and **4** (1:1 mixture) at eight different concentrations. Optical density (OD) relates to the number of cells present.

References:

2. L. J. White, N. J. Wells, L. R. Blackholly, H. J. Shepherd, B. Wilson, G. P. Bustone, T. J. Runacres and J. R. Hiscock, *Chem. Sci.*, 2017, **8**, 7620–7630.

35. C.A. Hunter, *Angewandte International edition – chemie,* 2004, **43**, (40), 5310-5324.

128. Piñeiro A[1], Banquy X, Pérez-Casas S, Tovar E, García A, Villa A, Amigo A, Mark AE, Costas M, J Phys Chem B. 2007 May 3;111(17):4383-92

140. P.A.Levin, Light microscopy techniques for bacterial cell biology, *In Methods in Microbiology*, Philippe Sansonetti, Arturo Zychlinsky (ed.), 2002, **31**, p.115-132